THERMODYNAMIC STABILITY STUDIES OF RACEMIC AND CONGLOMERATE ENANTIOMERIC CRYSTALS

by

Robert A. Marriott

Submitted in partial fulfillment of the requirements
for the degree of Doctor of Philosophy

at

Dalhousie University
Halifax, Nova Scotia
August 2004

© Copyright by Robert A. Marriott, 2004

National Library
of Canada

Acquisitions and
Bibliographic Services

395 Wellington Street
Ottawa ON K1A 0N4
Canada

Bibliothèque nationale
du Canada

Acquisisitons et
services bibliographiques

395, rue Wellington
Ottawa ON K1A 0N4
Canada

Your file Votre référence
ISBN: 0-612-94047-0
Our file Notre référence
ISBN: 0-612-94047-0

The author has granted a non-exclusive licence allowing the National Library of Canada to reproduce, loan, distribute or sell copies of this thesis in microform, paper or electronic formats.

The author retains ownership of the copyright in this thesis. Neither the thesis nor substantial extracts from it may be printed or otherwise reproduced without the author's permission.

L'auteur a accordé une licence non exclusive permettant à la Bibliothèque nationale du Canada de reproduire, prêter, distribuer ou vendre des copies de cette thèse sous la forme de microfiche/film, de reproduction sur papier ou sur format électronique.

L'auteur conserve la propriété du droit d'auteur qui protège cette thèse. Ni la thèse ni des extraits substantiels de celle-ci ne doivent être imprimés ou aturement reproduits sans son autorisation.

In compliance with the Canadian Privacy Act some supporting forms may have been removed from this dissertation.

While these forms may be included in the document page count, their removal does not represent any loss of content from the dissertation.

Conformément à la loi canadienne sur la protection de la vie privée, quelques formulaires secondaires ont été enlevés de ce manuscrit.

Bien que ces formulaires aient inclus dans la pagination, il n'y aura aucun contenu manquant.

Canada

DALHOUSIE UNIVERSITY

To comply with the Canadian Privacy Act the National Library of Canada has requested that the following pages be removed from this copy of the thesis:

Preliminary Pages
    Examiners Signature Page (pii)
    Dalhousie Library Copyright Agreement (piii)

Appendices
    Copyright Releases (if applicable)

With all my love for Lea, Gavin and Mason

Table of Contents

List of Tables x

List of Figures xiii

Abstract xviii

List of Abbreviations and Symbols Used xix

1 Introduction 1

1.1 Optical activity and molecular dissymmetry 1

1.2 Conglomerate crystals 4

1.3 Racemic crystals 7

1.4 Thesis objectives 10

2 Current understanding of the relative stability of conglomerate and racemic crystals 13

2.1 Packing enantiomers into crystal structures 13

2.1.1 Crystallographic and volumetric considerations 13

2.1.2 Interaction potentials and computational insights 21

2.2 Thermodynamic mixtures and their phase diagrams 29

2.2.1 Thermodynamic definitions required to discuss phase stability 29

2.2.2 Melting point phase diagrams of conglomerate crystals 32

2.2.3 Melting point phase diagrams of racemic crystals 36

2.3 Thermodynamic cycles for investigating the formation of a racemic crystal from a conglomerate 40

3 Estimation of ideal gas thermodynamic properties 56

3.1 Introduction to classical and empirical estimation methods 56

3.2 Additivity 58

3.3 Statistical mechanical methods 60

3.3.1 Rotation and translation 60
3.3.2 Internal vibration and the harmonic oscillator approximation 62
3.3.3 An example of an anharmonic effect: internal rotation 63
3.3.4 An example of computation using fundamental vibrational frequencies 65
3.4 Introduction to exploratory *ab initio* calculations 69
3.5 *Ab initio* results and discussion 70
3.5.1 Piperidine 70
3.5.2 A comparison to various estimated and literature ideal gas heat capacities ... 72
3.5.3 The *n*-alkanes from ethane to decane 76
3.5.3.1 An uncoupled internal rotator model 76
3.5.3.2 Semi-empirical equations for estimating ideal gas heat capacities 83
3.6 Conclusions 88

4 Condensed phase heat capacities 90
4.1 Introduction 90
4.2 Crystal heat capacities 92
4.2.1 Simple crystals and harmonic centre-of-mass modes 92
4.2.2 Molecular crystals 96
4.3 Liquid heat capacities 103
4.4 Fusion entropies and empirical relationships 104
4.5 An empirical equation for estimating the heat capacity of fusion 109
4.5.1 Objective 109
4.5.2 Correlation scheme 110
4.5.3 Discussion 113
4.6 Returning to racemic and conglomerate crystal stability 116

5 The mandelic acids 125
5.1 Introduction 125
5.2 Experimental methods 131
5.2.1 Characterisation techniques 131
5.2.2 Preparation 133
5.3 Results and discussion 140
5.3.1 Spectroscopy 140
5.3.2 Thermal analysis 147
5.3.3 Crystal structures and first derivative properties 154
5.3.3.1 X-ray structures and hydrogen-bonding patterns 154
5.3.3.2 Thermal expansion 171
5.3.3.3 Isothermal compressibility 178
5.4 Conclusions 178

6 Internal vibrational modes 181
6.1 Introduction 181
6.2 Assignment tools 182
6.2.1 Symmetry considerations 182
6.2.2 Useful literature 183
6.2.2.1 Vibrational optical activity 183
6.2.2.2 Substituted benzenes 184
6.2.3 *Ab initio* calculations 188
6.2.4 Deuterated mandelic acids 190
6.3 Assignment tables and density of internal vibrational states 192
6.4 Discussion 197
6.4.1 Phenyl ring modes 197

6.4.2 Carbine and hydroxyl modes 199
6.4.3 Backbone modes 201
6.5 Conclusions 202

7 Experimental heat capacities 203
7.1 Introduction 203
7.2 Experimental techniques 204
7.2.1 Differential scanning calorimeter (DSC) 204
7.2.2 Adiabatic calorimeter 208
7.2.3 Relaxation calorimeter 212
7.3 Evaluations of calorimetric techniques 217
7.3.1 Addenda materials 217
7.3.1.1 Aluminium 217
7.3.1.2 Apiezon N 220
7.3.2 Calorimetry standard materials 222
7.3.2.1 Sapphire 222
7.3.2.2 Copper 224
7.3.2.3 Benzoic acid 226
7.3.2.4 Indium 231
7.3.3 Conclusion for calorimetric standards 232
7.4 Heat capacity measurements for mandelic acids 235
7.4.1 Heat capacity data 235
7.4.2 Uncertainty and data assessment 242
7.4.3 Contributions to constant pressure heat capacities 251
7.4.4 Debye analysis 262

7.4.5 Thermodynamic analysis and cycles 263

7.5 Conclusions 273

8 Conclusions and future directions 276

8.1 Thermodynamics of forming a racemic crystal from a conglomerate 276

8.1.1 Introduction 276

8.1.2 Calorimetric techniques 277

8.1.3 The mandelic acids 277

8.1.4 Liquid-solid heat capacity differences 280

8.1.5 Conclusions 281

8.2 *Ab initio* tools and ideal gas heat capacities 282

8.3 Future directions 283

8.3.1 Experimental studies 283

8.3.2 Theoretical explorations 285

8.4 Final comment 287

Appendix A The full Schröder-van Laar equation and an extended Prigogine and Defay equation 288

Appendix B Lists of chemical names and cross references to CA information 290

References 297

List of Tables

Table 2.1 The 14 structural pairs studied by Marthi *et al.*(59) showing similar packing modes. 19

Table 2.2 Some reported enthalpies of enantiomer mixing at $x_R = 0.50 \pm 0.01$. 34

Table 2.3 Some reported excess volumes of enantiomer mixing at $x_R = 0.50 \pm 0.01$. 35

Table 2.4 Speculations of possible conditions where conglomerate crystal formation would be spontaneous versus spontaneous racemic crystal formation. 41

Table 3.1 Examples of the symmetry numbers used in the additivity scheme of Benson and Buss.(93). 59

Table 3.2 Frequency scaling factors and root-mean-square deviations of Scott and Radom.(119). 70

Table 3.3 Relative error in % of some estimated ideal gas heat capacities. 74

Table 4.1 Experimental and internal vibrational heat capacities for the 48 molecules compiled by Neau and Flynn.(91). 100

Table 4.2 Experimental fusion entropies and heat capacities differences for the 53 molecules used for testing correlation equations. 112

Table 4.3 The thermodynamic fusion and racemic crystal formation data for some racemic and conglomerate crystal pairs. 119

Table 5.1 Some physical properties of the halogen-substituted mandelic acids and 3-phenylhydracrylic acids. 127

Table 5.2 ^{13}C chemical shifts for mandelic acid and the *ortho*-halogen-substituted mandelic acids. 141

Table 5.3 Specific optical rotations for *R*-(-)-mandelic acid, *R*-(-)-*o*-fluoromandelic acid and *R*-(-)-*o*-chloromandelic acid. 146

Table 5.4 Experimental fusion values for benzoic, mandelic acid, *o*-fluoromandelic acid, *o*-chloromandelic acid and *o*-bromomandelic acid. 150

Table 5.5 Summary of X-ray structure and refinement results for *Rac*-mandelic acid. 154

Table 5.6 Summary of X-ray structure and refinement results for *R*-(-)-mandelic acid. 155

Table 5.7 Summary of X-ray structure and refinement results for *Rac*-*o*-fluoromandelic acid. 163

Table 5.8 Summary of X-ray structure and refinement results for *R*-(-)-*o*-fluoromandelic acid. 164

Table 5.9 Summary of X-ray structure and refinement results for *R*-(-)-*o*-chloromandelic acid. 168

Table 5.10 The estimated linear and volumetric expansion properties of mandelic acid, *o*-fluoromandelic acid and *o*-chloromandelic acid crystals, and resulting values of $(C_p\text{-}C_V)$.. 176

Table 6.1 Frequencies for *mono*- and *ortho*-substituted benzene molecules as assigned by Varsányi.(262) 187

Table 6.2 The *ab initio* vibrational analysis for mandelic acid and *o*-fluoromandelic acid. 189

Table 6.3 Assignments of the vibrational spectra for *Rac*-mandelic acid and *R*-(-)-mandelic acid. 193

Table 6.4 Assignments of the vibrational spectra for *Rac*-*o*-fluoromandelic acid and *R*-(-)-*o*-fluoromandelic acid. 194

Table 6.5 Assignments of the vibrational spectra for *R*-(-)-*o*-chloromandelic acid and racemic *o*-bromomandelic acid. 195

Table 7.1 Experimental heat capacities for *Rac*-mandelic acid. 236

Table 7.2 Experimental heat capacities for *R*-(-)-mandelic acid. 237

Table 7.3 Experimental heat capacities for *Rac*-*o*-fluoromandelic acid. 239

Table 7.4 Experimental heat capacities for *R*-(-)-*o*-fluoromandelic acid. 240

Table 7.5 Experimental heat capacities of *R*-(-)-*o*-chloromandelic acid. 241

Table 7.6 Smoothed constant pressure heat capacities, constant volume heat capacities, internal vibrational heat capacities and external constant volume heat capacities for mandelic acid. 252

Table 7.7 Smoothed constant pressure heat capacities, constant volume heat capacities, internal vibrational heat capacities and external constant volume heat capacities for *o*-fluoromandelic acid. 253

Table 7.8 Smoothed constant pressure heat capacities, constant volume heat capacities, internal vibrational heat capacities and external constant volume heat capacities for *R*-(-)-*o*-chloromandelic acid. 255

Table 7.9 Thermodynamic functions for mandelic acid crystals. 264

Table 7.10 Thermodynamic functions for *o*-fluoromandelic acid crystals. 265

Table 7.11 Thermodynamic functions for *R*-(-)-*o*-chloromandelic acid. 267

Table 7.12 The enthalpy changes and entropy changes for forming *Rac*-mandelic acid or *Rac*-*o*-fluoromandelic acid from their corresponding conglomerate crystals..... 272

Table 8.1 Preliminary experimental fusion values for pentafluoromandelic acid and the disubstituted fluoromandelic acids.. 284

Table B.1 Chemical names cited listed with Chemical Abstract, CA, nomenclature. 291

List of Figures

Figure 1.1 A typical melting point phase diagram for a conglomerate enantiomeric mixture. 5

Figure 1.2 A typical melting point phase diagram for an enantiomeric mixture which forms a racemic crystal 8

Figure 2.1 Histogram of relative molar volumes from table 1 of Brock *et al.*(51) 17

Figure 2.2 The (6-12) Lennard-Jones potential function 22

Figure 2.3 The Buckingham 6-exp potential function 24

Figure 2.4 A binary mixture model using homochiral and heterochiral Lennard-Jones interaction potentials 26

Figure 2.5 A test of the Prigogine and Defay equation for racemic crystals 38

Figure 2.6 Experimental heat capacities of three racemic crystal forming systems:(85) 39

Figure 2.7 A Gibbs energy schematic of solid and liquid enantiomers and enantiomer mixtures 44

Figure 2.8 Thermodynamic cycles for calculating the Gibbs energy change for forming a racemic crystal from a conglomerate 47

Figure 2.9 The Gibbs energy change for forming racemic crystals from conglomerate crystals versus their differences in fusion temperature 49

Figure 2.10 The calculated enthalpy, entropy and Gibbs energy changes for forming racemic crystals from conglomerate crystals versus their differences in fusion temperature. 51

Figure 2.11 Histogram of $\Delta_{\mathrm{fus}}C_p$ from the literature.(85,91) 54

Figure 3.1 A schematic of the Pitzer internal rotator potential and the calculated constant volume heat capacities of two internal rotators.(103) 64

Figure 3.2 The ideal heat capacity of piperidine. 65

Figure 3.3 The effect of frequency uncertainty of $\delta\nu = 50\ \mathrm{cm}^{-1}$ on the error in vibrational heat capacity, $\delta C_{V,\mathrm{vib}}$, for various modes of piperidine.. 67

Figure 3.4 Results for piperidine heat capacity as a function of temperature. 72

Figure 3.5 Relative error of heat capacities for 27 organic compounds calculated by three additivity schemes(97) and from present *ab initio* results. 75

Figure 3.6 The relative error of calculated heat capacities and entropies for some n-alkanes at $T = 298.15$, 500, 700 and 1000 K. 77

Figure 3.7 Calculated activation energies for methyl rotation for ethane through decane. . 78

Figure 3.8 The calculated potential energy surface for the methyl rotations of propane..... 81

Figure 3.9 Two calculated paths across the calculated potential energy surface of n-butane. 82

Figure 3.10 The relative heat capacity errors from equation 3.20 for some n-alkanes at $T = 298.15$, 500, 700 and 1000 K. 85

Figure 3.11 The relative heat capacity errors from equation 3.21 for some n-alkanes at $T = 298.15$, 500, 700 and 1000 K. 87

Figure 3.12 A histogram of 68 $C_{p,\mathrm{exp}} - C_{\mathrm{V,vib}}$ values for the harmonic oscillator approximation at the B3LYP/6-31G(d) theory level. 89

Figure 4.1 The Debye and Einstein heat capacity functions. 94

Figure 4.2 A Schematic of transverse vibrational modes along one lattice direction for a crystal with two atoms per unit cell. 95

Figure 4.3 Experimental constant pressure, internal constant volume and external constant pressure heat capacities for 20 molecular organic crystals over a large temperature range.. 98

Figure 4.4 Histograms of the external constant pressure heat capacities at the fusion temperature for molecular organic compounds. 101

Figure 4.5 External constant pressure heat capacities at the fusion temperature for 48 molecular organic compounds plotted against the fusion temperatures. 102

Figure 4.6 Histogram of $\Delta_{\mathrm{fus}}S$ for 428 organic molecular solids. 105

Figure 4.7 Fusion entropies versus solid-liquid heat capacity differences at the fusion temperature... 109

Figure 4.8 Experimental solid-liquid heat capacity differences at the fusion temperature versus the estimated values. 113

Figure 4.9 The *ab initio* calculated potential energy surfaces of mandelic acid and *o*-fluoromandelic acid. 115

Figure 4.10 The calculated melting point phase diagrams of the 1-*X*-2',6'-pipecoloxylidides. 118

Figure 4.11 The calculated enthalpy, entropy and Gibbs energy changes for forming racemic crystals from conglomerate crystals versus their differences in fusion temperature. 122

Figure 5.1 The calculate binary phase diagrams for selected halogen-substituted mandelic acids using the fusion data of Collet and Jacques.(196) 128

Figure 5.2 The calculated phase diagrams for selected halogen-substituted 3-phenylhydracrylic acids using the data of Collet and Jacques.(197) 129

Figure 5.3 DSC calibration factors using benzoic acid and indium over three days of operation. 132

Figure 5.4 Standard mandelic acid preparation. 134

Figure 5.5 ^{13}C NMR spectra of unsubstituted mandelic acid. 142

Figure 5.6 ^{13}C NMR spectra of *o*-fluoromandelic acid.. 143

Figure 5.7 ^{13}C NMR spectra of *o*-chloromandelic acid and *o*-bromomandelic acid. 144

Figure 5.8 Vibrational spectra of the *ortho*-substituted mandelic acids. 145

Figure 5.9 DSC scans of partially resolved *o*-chloromandelic acid samples. 148

Figure 5.10 DSC scans of mandelic acid, *o*-fluoromandelic acid, *o*-chloromandelic acid and *o*-bromomandelic acid. 149

Figure 5.11 DSC heating scans of *Rac*-*o*-fluoromandelic acid for multiple melts. 151

Figure 5.12 ^{13}C NMR spectra of *Rac*-mandelic acid and *Rac*-*o*-fluoromandelic acid after holding the hermetically sealed melt at $T = 400$ K for 5 minutes. 153

Figure 5.13 Molecular structure, numbering scheme and representative packing diagram for *Rac*-mandelic acid. 156

Figure 5.14 Molecular structure and representative packing diagram for *R*-(-)-mandelic acid. 157

Figure 5.15 Hydrogen-bonding patterns of the mandelic acid crystals. 160

Figure 5.16 Molecular structure, numbering scheme and representative packing diagram for *Rac*-*o*-fluoromandelic acid. 164

Figure 5.17 Molecular structure and representative packing diagram for *R*-(-)-*o*-fluoromandelic acid. 165

Figure 5.18 Molecular structure and representative packing diagram for *R*-(-)-*o*-chloromandelic acid. 169

Figure 5.19 Crystallographic parameters at various temperatures for mandelic acid crystals. 173

Figure 5.20 Crystallographic parameters at various temperatures for *o*-fluoromandelic acid crystals.......... 174

Figure 5.21 Crystallographic parameters at three temperatures for *o*-chloromandelic acid crystals. 175

Figure 6.1 The 30 vibrational modes of *mono*-light substituted benzene.. 185

Figure 6.2 Raman spectra of racemic deuterated mandelic acid and *o*-fluoromandelic acid. 191

Figure 7.1 A schematic of a power compensation DSC.......... 205

Figure 7.2 A typical DSC heat capacity scan using the enthalpic method.......... 207

Figure 7.3 Schematic of the small sample adiabatic calorimeter. 209

Figure 7.4 A typical adiabatic calorimeter heat pulse sequence.......... 211

Figure 7.5 Schematic of the PPMS relaxation calorimeter. 213

Figure 7.6 The modified heat capacity measurement method for volatile organic solids with the PPMS relaxation calorimeter and a Perkin-Elmer DSC pan.......... 216

Figure 7.7 DSC pans and aluminium heat capacities.......... 218

Figure 7.8 Apiezon grease heat capacities. 221

Figure 7.9 Sapphire standard heat capacities.......... 223

Figure 7.10 Copper standard heat capacities. 225

Figure 7.11 The relative difference between the measured heat capacity of benzoic acid using the adiabatic calorimeter and those reported in the literature.(159) 227

Figure 7.12 The relative contributions for the PPMS determination of the total heat capacity measurement of benzoic acid and Apiezon N grease in a hermetically sealed aluminium DSC pan.. 228

Figure 7.13 Benzoic acid standard heat capacities. 230

Figure 7.14 The relative DSC heat capacity differences from smoothed literature data(302) for indium. 231

Figure 7.15 Mandelic acid heat capacities. 244

Figure 7.16 Smoothed and best experimental heat capacities for *Rac*-mandelic acid and *R*-(-)-mandelic acid........ 245

Figure 7.17 *o*-Fluoromandelic acid heat capacities. 247

Figure 7.18 Smoothed and best experimental heat capacities for *Rac*-*o*-fluoromandelic acid and *R*-(-)-*o*-fluoromandelic acid. 248

Figure 7.19 *R*-(-)-*o*-Chloromandelic acid heat capacities. 250

Figure 7.20 Smoothed and best experimental heat capacities for *R*-(-)-*o*-chloromandelic acid. 251

Figure 7.21 The estimated external constant volume heat capacities for *Rac*-mandelic acid and *R*-(-)-mandelic acid, *Rac*-*o*-fluoromandelic acid and *R*-(-)-*o*-fluoromandelic acid. 257

Figure 7.22 The estimated external constant volume heat capacities for *R*-(-)-*o*-chloromandelic acid........ 258

Figure 7.23 The effective Debye temperatures for *Rac*-mandelic acid, *R*-(-)-mandelic acid, *Rac*-*o*-fluoromandelic acid, *R*-(-)-*o*-fluoromandelic acid and *R*-(-)-*o*-chloromandelic acid........ 262

Figure 7.24 The thermodynamic changes for forming *Rac*-mandelic acid from its corresponding conglomerate. 268

Figure 7.25 The thermodynamic changes for forming *Rac*-*o*-fluoromandelic acid from its corresponding conglomerate. 269

Abstract

Enantiomeric compounds can form crystals of two main types: conglomerates (1:1 mechanical mixture of optically pure crystals) or racemic crystals (1:1 enantiomers within the same crystal lattice). Conglomerates are less common than racemic crystals, and compounds which form conglomerate crystals generally are easier to resolve. Thermodynamic studies of the relative stability of conglomerate and racemic crystals could aid in the understanding and control of enantiomeric resolutions.

In this thesis, the thermodynamic changes on forming racemic crystals from the corresponding conglomerates have been investigated with emphasis on mandelic acids. Using a thermodynamic cycle and the fusion values, the thermodynamic changes for this process have been shown to be uncertain due to the common assumption that the solid-liquid heat capacity differences at the fusion temperature are zero. Semi-empirical investigations of the correlation between intermolecular rotational symmetry and flexibility with ideal gas, solid and liquid heat capacities, have shown that the solid and liquid heat capacity difference for various organic compounds can be estimated. This estimation has been applied to thermodynamic calculations involving enantiomeric crystals, to improve cycle calculation methods.

Furthermore, the experimental heat capacities of enantiomeric mandelic acid, *o*-fluoromandelic acid and *o*-chloromandelic acid crystals have been measured and used to independently calculate entropy and enthalpy changes from $T = 0$ K to above the fusion temperatures. *Rac*-mandelic acid was found to be entropically stabilised relative to its conglomerate, and this is linked to less hindered phenyl ring motion. *Rac*-*o*-fluoromandelic acid was found to the enthalpically stabilised and entropically destabilised relative to its conglomerate, and this is correlated with a stronger hydrogen bond network.

Overall, both enthalpic and entropic factors have been found to be potentially important for the relative stability of racemic and conglomerate enantiomeric crystals. However, the enthalpic differences were found to be more general than the entropic differences. Thus it would seem that if one wants to choose molecules which are more likely to form conglomerates, soft flexible molecules with sterically demanding groups would be favourable.

List of Abbreviations and Symbols Used

α	thermal expansion coefficient
$\alpha_{6\text{-exp}}$	parameter for the Buckingham 6-exp potential function
$\boldsymbol{a,b,c}$	crystallographic unit cell parameters
α,β,γ	crystallographic unit cell angles
β_T	isothermal expansion
$[\alpha]_D^{298}$	specific optical rotation at $\lambda = 589$ nm (sodium D line) and $T = 298$ K
c	speed of light in a vacuum
C_p	constant pressure heat capacity
C_V	constant volume heat capacity
e	elementary charge
E	potential energy (electronic)
$\Delta_{\text{rot}}E$	potential energy change for rotation of a dihedral angle
$\Delta_{\text{rot}}E^{\dagger}$	activation energy for rotation
ϵ_{LJ}	maximum well depth parameter for the (6-12) Lennard-Jones potential function
$\epsilon_{6\text{-exp}}$	maximum well depth parameter for the Buckingham 6-exp potential function
f	DSC heat calibration constant
F	X-ray diffraction intensity
G	Gibbs energy
$\Delta_{\text{Rac}}G$	Gibbs energy change for forming a racemic crystal from a conglomerate crystal system
h	Planck's constant
H	enthalpy
H_i	partial molar enthalpy of component i

H_0	partial molar enthalpy at $T = 0$ K
$\Delta_{\mathrm{fus}}H^R$	enthalpy of fusion of an optically pure *R* enantiomer crystal ($\Delta_{\mathrm{fus}}H^R = \Delta_{\mathrm{fus}}H^S$)
$\Delta_{\mathrm{fus}}H^{R/S}$	enthalpy of fusion of a conglomerate crystal system
$\Delta_{\mathrm{fus}}H^{Rac}$	enthalpy of fusion of a racemic crystal
$\Delta_{\mathrm{mix}}H$	enthalpy (excess) of mixing a two chemical species (e.g., liquid or solute enantiomers)
$\Delta_{\mathrm{Rac}}H$	enthalpy of forming a racemic crystal from a conglomerate crystal system
K	thermal conductivity
k	Boltzmann constant, $1.380658(12)\times10^{-23}$ J K^{-1}
κ_0	bulk modulus at $p = 0$ atm
μi	chemical potential (partial molar Gibbs energy) of component *i*
N	number of atoms (or particles)
N_A	Avogadro constant (Avogadro's number), $6.0221367(36)\times10^{23}$ mol^{-1}
P_{average}	average power supplied to DSC furnace heaters
ΔP	difference in power supplied to DSC furnace heaters
q	partition function or heat
Q	partition function for N_A indistinguishable molecules
R	rectus enantiomer configuration notation, or X-ray refinement agreement factor or the ideal gas constant, 8.314510(70) J K^{-1} mol^{-1}
Rac	true racemic crystal
ρ	specific density
S	sinister enantiomer configuration notation or entropy
S_i	partial molar entropy of component *i*
S_0	partial molar entropy at $T = 0$ K
$\Delta_{\mathrm{fus}}S^R$	entropy of fusion of an optically pure *R* enantiomer crystal ($\Delta_{\mathrm{fus}}S^R = \Delta_{\mathrm{fus}}S^S$)

$\Delta_{\text{fus}}S^{R/S}$	entropy of fusion of a conglomerate crystal system
$\Delta_{\text{fus}}S^{Rac}$	entropy of fusion of a racemic crystal
$\Delta_{\text{Rac}}S$	entropy of forming a racemic crystal from a conglomerate crystal system
$\Delta_{\text{rot}}S$	entropy change upon rotation
t	time
t_i	time of event i
T_{fus}	temperature of fusion
T_{fus}^{R}	temperature of fusion of an optically pure R enantiomer crystal ($T_{\text{fus}}^{R} = T_{\text{fus}}^{S}$)
T_{fus}^{Rac}	temperature of fusion of a racemic crystal
T_{fus}^{con}	temperature of fusion of a conglomerate crystal system
T_{sample}	temperature of DSC sample furnace
$T_{\text{reference}}$	temperature of DSC reference furnace
T_{initial}	initial temperature during DSC or adiabatic calorimetry heat capacity measurement
T_{final}	final temperature during DSC or adiabatic calorimetry heat capacity measurement
τ	time constant
U	internal energy
H_0	internal energy at $T = 0$ K
V	volume or voltage
$V_m(\text{cr})$	apparent molar volume of molecules in a molecular crystal
V_m^{R}	apparent molar volume of enantiomers in an optically pure crystal
V_m^{Rac}	apparent molar volume of enantiomers in a racemic crystal
$\Delta_{\text{mix}}V$	molar volume (excess) of mixing a two chemical species (e.g., liquid or solute enantiomers)
ν	vibrational frequency
θ	characteristic temperature for rotation, vibration or translation

$\Psi(r)$	interaction potential at distance r
σ	symmetry number
σ_{LJ}	parameter for the (6-12) Lennard-Jones potential function
x	mole ratio
Z	number of molecules in a crystal unit cell
AM1	a semi-empirical quantum mechanical model for *ab initio* molecular orbital calculations using the AM1 Hamiltonian
B3	Becke's 3-parameter hybrid functional for use with density functional methods
B	Becke's 1988 functional for use with density functional methods
CA	Chemical Abstract
CD	circular dichroism
CSD	Cambridge Structural Database
DSC	differential scanning calorimeter
DFT	density functional theory
GC	gas chromatography
HF	Hartree-Fock calculation
LYP	the correlation functional of Lee, Yang, and Parr for use with density functional methods
MP2-fc	Møller-Plesset correlation energy correction truncated at second-order with a specified frozen core for the electron correlation calculation
MP2-fu	Møller-Plesset correlation energy correction truncated at second-order with all electrons included in the electron correlation calculation
IR	infrared
NMR	nuclear magnetic resonance
NPT	constant number of particles, constant pressure and constant temperature
ORD	optical rotary dispersion

P86	the Perdew gradient corrections with the 1981 local correlation functional for use with density functional methods
PM3	a semi-empirical quantum mechanical model for *ab initio* molecular orbital calculations using the PM3 Hamiltonian
PW91	exchange component of Perdew and Wang's 1991 functional for use with density functional methods
PPMS	Physical Properties Measurement System
QCISD-fc	a Quadratic configuration interaction calculation of electron correlation restricted to single and double excitations
TGA	thermal gravimetric analysis
VCD	vibrational circular dichroism

Acknowledments

I am sincerely grateful for the guidance and support offered from my supervisor, Professor Mary Anne White. In addition, the members of Professor White's research group have been especially helpful and supportive throughout my time at Dalhousie: S. Fitzpatrick, M. Jakubinek, C. A. Kennedy, P. A. Laws, Dr. G. R. MacKay, Dr. D. C. MacLaren, J. Niema, Dr. L. Qiu, R. Sun and Dr. B.-Z. Zhan.

Prof. T. S. Cameron and Dr. K. N. Robertson have kindly performed multiple X-ray experiments over the course of this thesis work at the Dalhousie X-ray Diffraction Facility. The NMR spectra were obtained by Dr. B. Berno at the Atlantic Region Magnetic Resonance Centre. Prof. N. Burford, Prof. J. C. T. Kwak, Prof. R. L. White and Prof. J. W. Zwanziger have all generously allowed me access to their laboratory space.

Financial support and access to equipment for this thesis work was made possible through the Dalhousie Department of Chemistry, NSERC and the Institute for Research in Materials.

Finally, I will always be grateful for the most loving, understanding and supportive family a graduate student can have.

1 INTRODUCTION

> *When we study material things of whatever nature, as regards their forms and the repetition of their identical parts, we soon recognise that they fall into two large classes of which the following are the characters. …*
>
> Louis Pasteur, 1866[1]

1.1 Optical activity and molecular dissymmetry

Understanding the physical and chemical consequences of chirality or dissymmetry is fundamental to the current knowledge of any chemist. Stereochemical studies can be useful in further understanding reaction pathways, biological reaction activities and the efficiencies of resolution techniques.(1-3) Unfortunately many reaction pathways yield racemic mixtures after which the resolution of enantiomeric products is rarely trivial. Not only are reaction activities of enantiomers different with chiral reagents, some key physical properties also are different. These properties, such as optical activity, chromatographic mobility on chiral supports and spectroscopic properties in chiral environments, are important in the quantitative analysis of enantiomeric excess.(3-8) While knowledge of the enantiomeric excess is crucial to any stereochemical study, the physical properties representing enantiomer interactions also can offer clues towards the best possible resolution technique to be applied.(9-12) Indeed, the discovery and observation of these properties have led to the current understanding of stereochemistry and the physical importance of symmetry.

Generally chemists are familiar with most molecular stereochemical terms and descriptions; however some ambiguity is possible when describing solid-state enantiomeric mixtures and crystal types. To limit this ambiguity for the reader, some of the basic definitions and descriptions that have been used throughout this thesis are described here.

---

[1] At the beginning of every chapter in this thesis the reader will find a quote. Many of these belong to Louis Pasteur and have been taken from the translated memoirs of a young Pasteur (mid forties).(13) At one point, Pasteur apologises for emotional digressions and suggests that *in our day, and with our habits, they would offend in a scientific memoir.*

During the early 1800's Malus,(14) Arago(15) and Biot(16) all contributed to the characterisation of materials by first describing optical activity or rotation of plane polarised light. Yet, at that time the fundamentals and origins of optical activity and the nature of atoms and molecules were unknown.(17) Jean Baptist Biot had coined the term 'molecular rotary power' while studying the optical rotary differences between quartz crystals.(18) During the 1840's, the young Louis Pasteur obtained sodium ammonium tartaric tetrahydrate crystals and identified two mirror image crystal morphologies of equal and opposite molecular rotary power.(19) Remarkably, these crystals were obtained from a recrystallisation of the sodium ammonium paratartaric acid which exhibited no rotary power. The latter experiment was significant in showing that optical rotation is a property of the asymmetry or dissymmetry of the building blocks of a crystal, rather than simply a different organisation of identical units. The physical chemical experiments to follow would eventually lead to the understanding that optical rotary power is a consequence of both molecular dissymmetry and crystal dissymmetry. Kelvin later described this dissymmetry as chirality.(20) Objects which contain no improper symmetry elements are chiral.

In modern studies, still one of the most commonly described physical properties of enantiomers is their ability to rotate plane polarised light. In solution this property is a result of the symmetry of exciting and relaxing energy levels. These energy level differences also are dependent on environmental properties such as temperature, solvent and wavelength of incidental light. The utility of this property arises from the ability of enantiomeric molecules to rotate light in equal but opposite direction to that of their mirror image molecules or **optical antipodes**. As a result of this property, enantiomeric excess or enantiomeric purity is often measured by solution polarimetry.

In this thesis, the term **optical activity** will be used to describe the purity of an enantiomeric mixture, where it is understood an **optically active** mixture implies that there is an excess of one enantiomer, *i.e.*, a partially resolved mixture. Similarly, the term **optically pure** is used when describing a system containing only one enantiomer. This distinction is important, as these terms can imply the optical rotary power of a crystal. While enantiomorphic crystals have optical rotary power, an enantiomorphic crystal does not require molecular enantiomers as building blocks. Some achiral molecules also are known to form enantiomorphic crystals (*e.g.*, glycine, quartz and *o*-quinone).(21)

The distinction of enantiomers by the *dextro* and *levorotary*, *d* or *l*, system has not been used in this thesis as the symbolism does not convey information with respect to the absolute configuration of the molecules in question.(22) The thesis primarily will be concerned with molecular crystals, where the configurational differences of many of the molecules are known: therefore, the *rectus* and *sinister* notation of Cahn, Igold and Prelog,(23) *R* and *S*, has been chosen to distinguish between the absolute configurations of two different enantiomers using Fisher projection diagrams. However, the utility of assigning stereospecific nomenclature describing the molecular rotation direction of plane polarised light has not been totally ignored. The thesis will use the addition of bracketed positive and negative symbols, (+) and (-), to indicate the directions of polarised light rotation in solution and not in the crystal.

The word *racemic* was derived from the once common name for the paratartarate or racemic acid.(24) Chemists now describe paratartarate as a racemic mixture of tartaric acid enantiomers. In this thesis, equal mixtures of *R* and *S* enantiomers will always be described as a **racemic mixture** or a **racemate**, but the terms **racemic crystal** and **racemic compound** are reserved for describing a specific type of packing of enantiomers in a crystal lattice structure. In other words, the term racemate is not limited to a single physical state of the mixture, but rather describes the concentration of the bulk enantiomeric mixture. Upon crystallisation of a racemic mixture there are three possible types of crystals which are known to form: **conglomerate crystals**, **racemic crystals**, and the least common, **pseudoracemic crystals.**(3,25) Of these, only the first two will be discussed in detail.

1.2 Conglomerate crystals

A conglomerate crystal system is a heterogeneous racemic mixture of optically pure crystals, where the optically pure crystals are immiscible at all concentrations. As Pasteur discovered, given the right conditions, conglomerate crystals can naturally form upon crystallisation and mirror image crystals can be identified by morphology (allowing spontaneous resolution).(13) Through Pasteur's pioneering work, investigating spontaneous resolution by comparison of morphological differences was, for a time, the major method of characterising and resolving enantiomers. Indeed, publishing early stereochemical work often involved a drawing of the crystal morphologies to classify the type of enantiomer or crystal.(3) Characterising crystals by their morphology is now a scientific art of the past as chemists have turned to other more rapid and reliable methods to obtain crystal structures.

Aside from the visual-spatial challenges of observing crystal morphology differences, many crystals, especially conglomerate crystals, are too small to be separated by means of a human hand and/or small tweezers. However, the formation of a conglomerate crystal implies that other simple resolution techniques can be applied.(3,12,26-28) In some cases, if a racemic liquid mixture containing a seed crystal of one or more enantiomer were to be slowly cooled, the resulting crystals would be spontaneously resolved and separable by either crystal size or location.(19,29,30) Even when spontaneous resolution is not a viable alternative, a conglomerate has the potential to be resolved by several simple and inexpensive preferential crystallisation techniques.(3,31-34) It is often advantageous to investigate crystal formation with different solvents, temperatures and pressures, in order to find conditions where a conglomerate is favoured over other crystal types.(19,35,36) Those molecules which do not form conglomerate crystals under accessible conditions are generally more difficult to resolve and often require asymmetric reaction pathways, biological expression type synthesis or expensive and often impractical chiral chromatography techniques.(32,37) Therefore, the identification and causes of the equimolar enantiomeric crystal type, as a conglomerate or otherwise, provides very useful information.(3,26-28,38,39)

The previous discussion implies that the identification of conglomerate crystals by means other than crystal morphology is important prior to choosing a suitable resolution. In 1899, Roozeboom(25) introduced the use of characteristic binary phase diagrams as analytical fingerprints for enantiomeric crystals. Through these phase diagrams, Roozeboom was able to point out three categories of enantiomeric crystals.(25) Until the common use of X-ray crystallography, the measurement of melting points eliminated the need to publish drawings of the crystal morphology and it became routine to publish phase diagrams. Figure 1.1 shows a typical conglomerate melting point phase diagram.

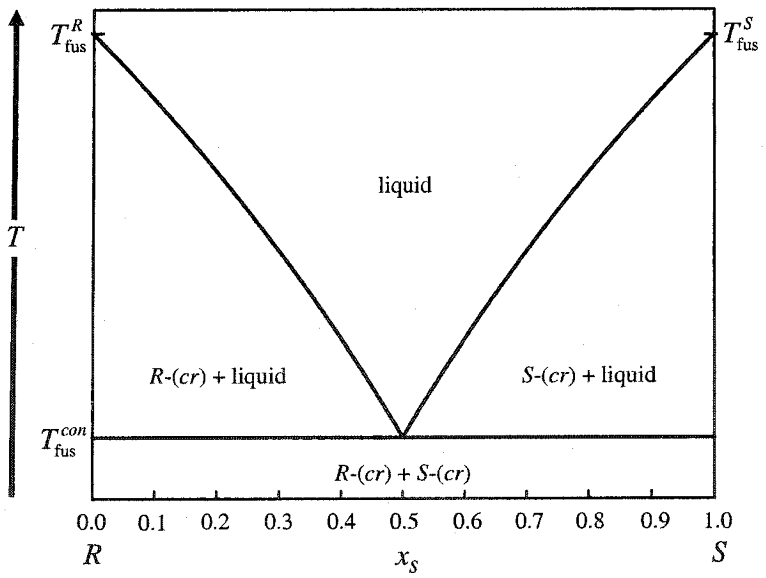

Figure 1.1 A typical melting point phase diagram for a conglomerate enantiomeric mixture.

By measuring the melting point of an optically pure crystal, $T_{\text{fus}}{}^{R}$ or $T_{\text{fus}}{}^{S}$, and that of the racemic mixture, $T_{\text{fus}}{}^{con}$, one can determine with good accuracy whether a conglomerate crystal type has formed. The liquidus in figure 1.1 can be calculated using a simplified freezing point depression equation (simplified Schröder-van Laar equation):(40,41)

$$\ln x = \frac{\Delta_{\text{fus}} H^{R}}{R}\left(\frac{1}{T_{\text{fus}}^{R}} - \frac{1}{T_{\text{fus}}}\right), \tag{1.1}$$

where x is the mole fraction of the more abundant enantiomer, $\Delta_{\text{fus}}H^{R}$ is the enthalpy of fusion for the optically pure enantiomer ($\Delta_{\text{fus}}H^{R} = \Delta_{\text{fus}}H^{S}$) and R is the ideal gas constant. The notation $T_{\text{fus}}{}^{con}$ is used to denote the depressed melting point at $x = 0.5$. The assumptions made in deriving equation 1.1 and the apparent success of the equation for conglomerate racemic mixtures have important thermodynamic implications which will be discussed further in Section 2.2.1. It should be noted that equation 1.1 is sometimes referred to as the van't Hoff freezing point depression equation.

Spectroscopy also can aid in the detection of a conglomerate crystals. Spectroscopic solid-state characterisation techniques include comparing infrared and Raman spectra of the racemic mixture to that of the optically pure crystal.(42,43) The vibrational spectrum of an optically pure crystal is equivalent to the opposite enantiomeric crystal; therefore, if the spectrum of a crystalline racemic mixture is superposable on the spectrum of the optically pure species, the mixture is likely a conglomerate. Unfortunately, the latter methods are not always conclusive because the vibrational modes often do not show a large change when the lattice symmetry and arrangement is different. Many solid-state NMR studies have had good success in determining if an enantiomeric molecule's crystal environment has changed.(3,44) In many cases spectroscopic methods are not convenient for studying crystals; however, with enantiomers in solution they are very useful.

Because the ultimate goal of many stereochemical studies is a successful optical resolution, trial and error is often the approach.(3) For example, if a preferential crystallisation is shown to resolve enantiomers, then the component is forming a conglomerate under the conditions of the crystallisation. Determining the optical resolution of the resulting crystals by redissolving the crystals in an appropriate solvent or determining the optical resolution of the mother liquor is where many of the spectroscopic techniques have most of their utility. Here circular dichroism (CD), optical rotatory dispersion (ORD), ultraviolet/visible absorption and NMR are all useful.(45,46) Hence, indirectly spectroscopic methods can be important for determining what type of crystal has been formed.

Finally, knowing the crystal structure on a molecular basis through X-ray crystallography has allowed chemists to catalogue many conglomerate crystals. In addition, determining the structures often indicates which intermolecular forces are more important to the packing nature of the molecules. With this inventory of conglomerate crystals, chemists also are able to investigate the frequency of conglomerate crystals with respect to other known enantiomeric mixtures. A commonly discussed problem is that conglomerate crystals are rare and much less common than racemic crystals, the former accounting for approximately 10% or less of the known solid-state racemic mixtures.(3,47,48) Because conglomerate crystals are formed from enantiomers which are generally easier to resolve, it would be an asset to know why conglomerate crystals appear to be less favoured than racemic crystals.

1.3 Racemic crystals

A racemic crystal is one where a 1:1 ratio of enantiomers is distributed in an ordered fashion within the same crystal lattice. It is the most common type of solid-state enantiomeric mixture.(3) Prior to using measured melting points, Pasteur and others were able to distinguish racemic crystals by determining if the crystals morphology contained inversion symmetry elements. Thus, during the very early years of stereochemistry, achiral crystal morphology was thought to indicate a racemic compound and enantiomorphic or chiral crystals were identified as crystals containing only one enantiomer. Therefore, if a system produced chiral crystals, the system was thought to be a conglomerate. These definitions have changed because some racemic compounds such as *Rac-o*-tyrosine and *Rac-α*-methylsuccinic acid are now known to form enantiomorphic crystals.(3) Enantiomorphic crystals rotate plane polarised light; therefore, neither crystal morphology nor lack of optical rotary power alone can distinguish a crystal as a racemic compound. A typical racemic crystal phase diagram is shown in figure 1.2.

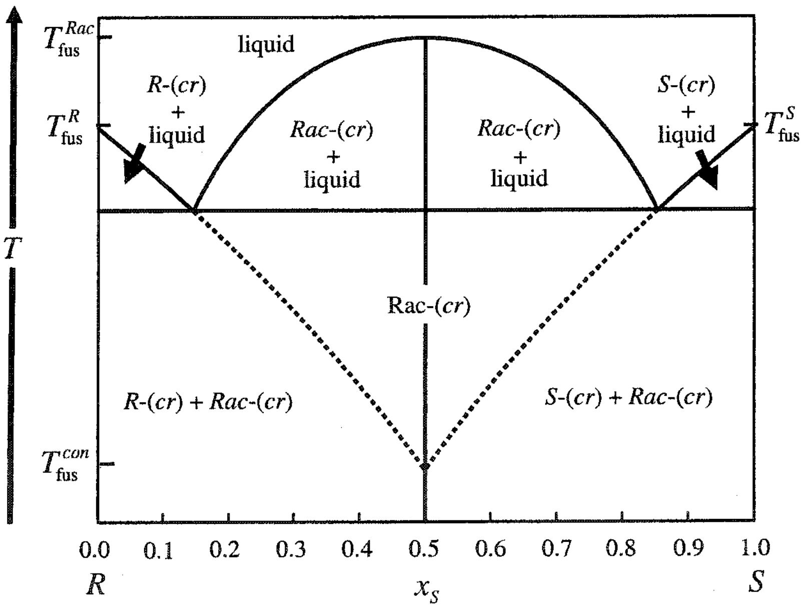
T_{fus}^{Rac}
T_{fus}^{R}
T
T_{fus}^{con}
liquid
R-(cr) + liquid
Rac-(cr) + liquid
Rac-(cr) + liquid
S-(cr) + liquid
T_{fus}^{S}
Rac-(cr)
R-(cr) + Rac-(cr)
S-(cr) + Rac-(cr)
0.0
0.1
0.2
0.3
0.4
0.5
0.6
0.7
0.8
0.9
1.0
R
x_S
S

Figure 1.2 A typical melting point phase diagram for an enantiomeric mixture which forms a racemic crystal. ——— typical liquidus and solidus for the racemic crystal; ▪▪▪▪▪▪▪ liquidus for the hypothetical conglomerate crystal.

Once again, one of the simplest methods to identify racemic crystals is by utilising the melting point phase diagram. The melting point test for a racemic crystal is similar to the test described for the conglomerate. If the melting point and enthalpy of fusion of the optically pure enantiomers are known, then the trademark eutectic melting point corresponding with the conglomerate can be calculated using equation 1.1. This value can then be compared to the actual melting point of the racemic mixture. If the melting point of the racemic mixture is higher than the calculated conglomerate eutectic, then the mixture is probably a racemic crystal.

A more thorough test for a racemic crystal is to measure the melting points at various resolutions and then compare to the calculated liquidus of a racemic compound. The liquidus curves between a eutectic point and the pure enantiomer can be calculated using the Schröder-van Laar equation, equation 1.1, and the liquidus curve between the two eutectic points can be calculated using the Prigogine-Defay equation:(49)

$$\ln 4x(1-x) = \frac{2\Delta_{\text{fus}}H^{Rac}}{R}\left(\frac{1}{T_{\text{fus}}^{Rac}} - \frac{1}{T_{\text{fus}}}\right), \qquad (1.2)$$

where x is the mole fraction of one of the enantiomers, $\Delta_{\text{fus}}H^{Rac}$ is the enthalpy of fusion for the racemic crystal ($x = 0.5$), and $T_{\text{fus}}{}^{Rac}$ is the melting point of the racemic crystal. The importance of the assumptions made in deriving equation 1.2 and the apparent success of the equation for racemic crystal mixtures will be discussed further in Section 2.2.2.

The small possibility of a third crystal type, the pseudoracemic crystal, can complicate the identification of racemic and conglomerate crystals by phase diagrams.(3,25) The phase diagrams shown in figures 1.1 and 1.2 all rely on the thermodynamic assumption that optically pure and racemic crystals are immiscible at all concentrations. There have been reported cases of solid solutions of enantiomers (ideal and non-ideal) which fall under the category of pseudoracemic crystals.(3,25) These cases are rare and will not be a focus of this thesis, thereby allowing the more common crystal types to be discussed in greater detail.

In summary, the majority of crystalline enantiomer mixtures are racemic crystals and enantiomers which form racemic crystals are generally more difficult to resolve than enantiomers which form conglomerate crystals. Although a variety of techniques can be used to identify a racemic or conglomerate crystal, identifying preferential crystallisation techniques remains a matter of trial and error, because the physical factors governing the formation of these types are poorly understood. Ultimately, predicting the class of enantiomeric crystal from an accumulated knowledge of symmetry and crystal stability relationships would be of great industrial and academic value. As history indicates, understanding the physical chemistry of racemic and conglomerate crystals is indirectly very important to many aspects of stereochemistry.

1.4 Thesis objectives

So far, the first chapter has outlined the historical usefulness of discovering some physical stereochemical properties.

The second chapter continues by reviewing some recent studies and addressing the current theoretical and experimental limitations. The chapter concludes with some calculations, which reveal a need for heat capacity measurements and estimations which can be used to for quick thermodynamic calculations. The differences between liquid and solid heat capacities at the fusion temperature will be shown to be larger for chiral molecules compared to achiral molecules.

Throughout the investigation of condensed phase heat capacities for chiral molecules, molecular properties of molecular symmetry, flexibility and vibration will be considered several times. Many of these properties affect the solid, liquid and ideal gas thermodynamic properties in similar ways. Empirical and semi-empirical models have used indicators of these effects in estimating ideal gas properties; therefore, this area is important to studies reported in subsequent chapters. Some schemes for estimating ideal gas heat capacities were investigated and these are discussed in Chapter three. This chapter concludes with a semi-empirical equation which takes advantage of rotational symmetry numbers to estimate ideal gas heat capacities for molecular organic molecules. The investigations in this chapter have helped in understanding the thermodynamic properties of condensed phase molecular organics.

The fourth chapter discusses condensed phase heat capacities. Common empirical values were investigated for solid and liquid heat capacities. The differences between solid and liquid heat capacities at the fusion temperatures for molecules of different rotational symmetries are pressented. A symmetry relationship, similar to that shown in Chapter three for ideal gases and empirical correlations with fusion properties, has been found for molecular organic solid and liquid heat capacity differences. This relationship has been used to empirically estimate the differences between the liquid and solid heat capacity at the fusion temperature for a large list of chiral molecules. These estimations are used to compare thermodynamic calculations for enantiomeric crystals to those originally discussed in Chapter two.

The fifth chapter is used to introduce the mandelic acid systems, including their synthesis and characterisation. This chapter also reports estimations of thermal expansion and isothermal compressibility, where these properties are used to calculate constant volume heat capacities from experimental constant pressure heat capacities, later in the thesis.

The sixth chapter describes the assignment of solid state vibrational modes for enantiomeric mandelic acid, *o*-fluoromandelic acid and *o*-chloromandelic acid. These vibrational mode assignments are used to calculate intramolecular vibrational heat capacity contributions, with the equations discussed in Chapters three and four.

The experimental heat capacities of enantiomeric mandelic acid, *o*-fluoromandelic acid and *o*-chloromandelic acid are reported and discussed in Chapter seven. Thermodynamic calculations utilising these heat capacities are compared to the quick calculation methods discussed in Chapters two and four. The calculations reveal the importance of the entropic and enthalpic differences between the crystals. These differences are related to molecular flexibility and hydrogen-bonding pattern differences for difference crystal types.

Finally the eighth chapter summarises the research presented in the thesis and suggests possible future directions.

The overall objective of the thesis is to calculate and compare the Gibbs energy, enthalpy and entropy changes for forming racemic crystals from their corresponding conglomerate crystals using experimental fusion temperatures, entropies of fusion and heat capacities.

2 CURRENT UNDERSTANDING OF THE RELATIVE STABILITY OF CONGLOMERATE AND RACEMIC CRYSTALS

> *...the dissolved tartarate deviates the plane of polarisation, while the paratartarate is indifferent.... Yet, here the nature and number of the atoms, their arrangement and distances, are the same in the two substances compared.*
>
> Mitscherlich, 1844(50)

2.1 Packing enantiomers into crystal structures

2.1.1 Crystallographic and volumetric considerations

The number of known enantiomers which form racemic crystals is much larger than the number of known conglomerates.(3,47,48) This implies that enantiomers preferentially pack in racemic crystals rather than conglomerate crystals. Knowledge of the crystal structures and other physical properties of the crystal types has enabled researchers to postulate why this preference occurs. Most experimental properties have been confined to investigations at the melting point or within the limited temperature range where solution experiments are practical. Most crystal structures have been determined only at one temperature.(3) In addition, volumetric and thermodynamic calculations and generalisations which rely on literature values have been the source of some debate.(3,51) In this chapter, some of these generalisations and calculations will be discussed in detail with reference to the relative stability of the following equilibrium system,

$$0.5\ R\text{-crystal} + 0.5\ S\text{-crystal} \rightleftharpoons \text{racemic crystal.} \qquad (2.1)$$

The concept that molecular symmetry was related to crystal morphology was discussed by chemists well before Pasteur's studies. In 1819, the famous crystallographer Eilhardt Mitscherlich had introduced what was to become 'Mitscherlich's law of isomorphism.'(17,52) Mitscherlich had reported that tartaric and paratartaric acid formed the same crystals and were the same molecules, a report which Thomas Graham suggested *defeated every attempt at explanation* for optical isomerism.(24,50,53) Pasteur later wrote that *the celebrated crystallographer, in spite of the most minute and severe study possible, was not able to recognise the smallest difference.*(13) Application of Mitscherlich's law of isomorphism implied that because paratartaric acid crystals included mirror image crystals, the molecules of paratartaric acid also must be optical enantiomers. The crystallography of enantiomeric crystals has now been well studied for over 150 years and much better understood. However, like Pasteur, researchers periodically return to the subject to lend further insight.

The extensive availability of X-ray crystallographic information has prompted many investigators to consider the possible packing arrangements of enantiomers and the statistical probability of these arrangements. Of the 230 possible crystal space groups, 66 (29%) have chirality, *i.e.*, no inversion symmetry elements. These 66 space groups fall into 11 of the 32 crystal classes. Thus an optically pure enantiomer can only crystallise in one of the 66 chiral space groups whereas a racemic mixture can, in principle, form crystals in any of the 230 space groups. This statistic would seem to indicate, to some extent, why racemic crystals are more common than conglomerate crystals; however, the experimental probability of finding particular space groups also is different from one space group to another. By examining several compiled inventories, Jacques *et al.*(3) found that 70 to 90% of optically pure enantiomers, for which crystal structures are known, crystallise in the $P2_12_12_1$ and $P2_1$ space groups, whereas 60 to 80% of racemic crystals belong to the $P2_1/c$, $C2/c$, and $P\bar{1}$ space groups.(3) Brock and Dunitz(48) have compiled a more recent (1994) list to obtain space group distributions using the Cambridge Structural Database (CSD). These authors have suggested that, because only a limited number of the 66 chiral space groups are common, the probability of racemic crystal formation is even higher. For example, it was found that the centrosymmetric space groups $P2_1/c$ and $P\bar{1}$ together account for 60% of known organic crystal structures and the third most common, $P2_12_12_1$, which is chiral, accounts for approximately 11%.(48) It was noted that the high probability of the $P2_1/c$ and $P\bar{1}$ space groups includes crystals which are formed from achiral molecules; therefore, the probability of obtaining a racemic crystal type would significantly decrease if these were removed from the statistics.

One reason why these types of statistical inference studies can be invalid for this argument was outlined in a previous study by Brock *et al.*,(51) where it was pointed out that some of these statistical studies are biased. They have suggested that compiled lists of enantiomer crystal structures predominantly exclude non-resolvable or rapidly interconverting enantiomers and compiled lists do not include those crystal pairs where the racemic crystal is less stable. This prompted the authors to partition a large list of racemic and conglomerate crystal structures into two sample populations; the first included non-resolvable systems (achiral molecules and those that rapidly interconvert in solution) and the second included resolvable enantiomers. In particular, those authors were investigating the validity of the packing rule proposed by Wallach,(54) that high packing density is favourable for racemic crystals. Wallach's rule was found to be statistically valid at the 95% confidence level for the group of molecules which included resolvable enantiomers but invalid for the first group. Most stereochemical studies are concerned with those molecules which are resolvable; however, the study by Brock *et al.*(51) has shown one reason why statistical comparisons of crystallographic data can be misleading.

Wallach's rule is a good example of the type of controversial generalisations alluded to in the introduction. In 1895 Wallach(54) studied the densities of eight pairs of enantiomers and found that seven of eight racemic crystals were denser than their corresponding optically pure crystals. The study has been used to justify why racemic crystals are more stable, *i.e.*, racemic crystals are generally denser; therefore, heterochiral packing would be more efficient and favourable than homochiral packing of the same species. Although many textbooks(55,56) reiterate Wallach's rule, several crystallographic studies have found that the densities of racemic crystals can be either higher or lower than their corresponding optically pure crystals.(3,51)

For comparison of packing, an apparent molar volume, $V_m(cr)$, for any crystal can be calculated:

$$V_m(cr) = \frac{VN_A}{Z}, \tag{2.2}$$

where, V is the volume of the unit cell, Z is the number of molecules in the unit cell, and N_A is the Avogadro constant. Equation 2.2 yields an apparent molar volume since empty crystal space has been included. Alternatively, packing coefficients can be considered, but for two crystal pairs of the same molecule this would be equivalent, assuming that configurational intra-molecular volume changes are negligible.

Of the 65 enantiomeric structure pairs reported in table 1 of Brock *et al.*(51) (Group II: Enantiomers that can be resolved), 22 were found to violate Wallach's rule. Their study shows that for these 65 pairs, there is a small but significant difference in the molar volumes of the two different crystal types. A histogram of the volume ratio for the 65 enantiomers is shown in figure 2.1. The overall average molar volume was found to be 0.92 ± 0.29% smaller for molecules in group II; however, the authors also indicated that the distribution was not symmetric.

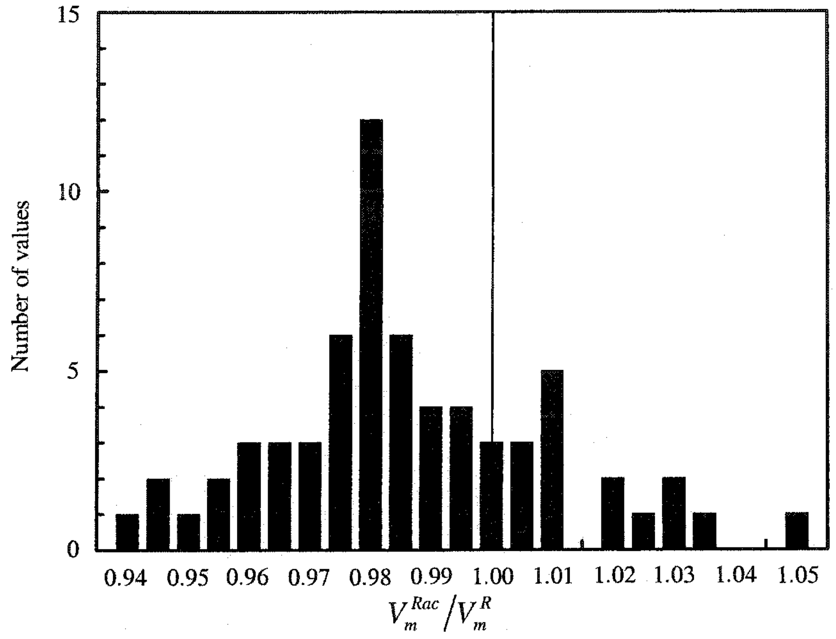

Figure 2.1 Histogram of relative molar volumes from table 1 of Brock *et al.*(51) Relative molar volumes of $V_m^{Rac}/V_m^R < 1.00$ are in agreement with Wallach's rule.

There have been other compilations of racemic crystal and conglomerate crystal pairs. Those which have been discussed here represent the smallest and oldest compilation (Wallach)(54) and the most recent and comprehensive compilation (Brock *et al.*).(51) While both these studies show a small statistical validity for Wallach's rule, it should be noted that other authors have disagreed.(3) In addition, several exceptions are expected as Wallach's rule is a generalisation.

The apparently higher probability of racemic crystals cannot be entirely attributed to denser packing, as the orientational dependence of homochiral and heterochiral interactions must be considered. Strong intermolecular interactions can change molecular geometry, such that the close packing is compromised. While the differences in volume do offer pressure-dependent thermodynamic stability information, the pressure derivative of the Gibbs energy difference, *i.e.*, the volume difference, is usually much smaller than the total Gibbs energy difference between two condensed phases.(57) In addition, although rare, the volumetric difference need not have the same sign as the entropic difference, *e.g.*, fusion of water. Moreover, most crystallographic structures are only available at one temperature.

Aside from space group distributions and volumetric information, X-ray structures also offer information about molecular interactions. Structures of enantiomeric crystals can be partitioned into categories describing the similarities between different racemic and conglomerate crystal pairs. Several authors have described similarities and preferences of packing modes for racemic and conglomerate crystals.(3,51,58) By examining the list from Brock *et al.*(51) of separable enantiomers from the CSD, Marthi *et al.*(59) were able to identify 14 crystals with 'identical packing' (similar packing modes) and they summarised some of the similarities by describing three types of similar packing modes. The 14 chiral molecules showing the three types of similar packing modes are shown in table 2.1 along with their respective relative molar volumes.

The first category defined by Marthi *et al.*(59) is where the racemic and the optically pure crystal have the same number of molecules in the respective unit cell, $Z^{Rac}=Z^{R}$, and the dimensions of the unit cells are very similar. In this case the enantiomers are arranged in a similar way in both the optically pure crystal and the racemic crystal; however, the racemic crystal has a pseudoinversion centre which relates the two different enantiomers, *e.g.*, $P1 \xrightarrow{i} P\bar{1}$. The first six crystal pairs in table 2.1 belong to this group. The second case is where the unit cell dimensions are similar and the unit cells contain the same number of molecules; however, the pseudoinversion centre is absent. Here the crystals differ in layers, where both crystals are composed of homochiral layers. The third group contains only optically pure crystals belonging to the $P2_1$ space group. Here the relative positions of one optical enantiomer are the same for both crystal types; however, the volume of the unit cell of the racemic crystal is twice that of the optically pure crystal and contains both enantiomers. Conceptually, one can think of expanding and overlapping two optically pure structures.

Table 2.1 The 14 structural pairs studied by Marthi *et al.*(59) showing similar packing modes.

CSD REFCODE	Crystal system	Space group	Z	a / Å	b / Å	c / Å	α / °	β / °	γ / °	V / Å^3	V_m^{Rac} / V_m^{R}
ZEGGIB[e]	Triclinic	$P\bar{1}$	2	9.300(2)	15.283(3)	7.808(1)	96.61(1)	101.25(1)	111.12(1)	994	
ZEGGEX	Triclinic	$P1$	2	9.313(3)	15.564(5)	7.764(2)	96.76(2)	102.03(3)	111.80(3)	998	0.9960
BAGMUR[f]	Monoclinic	$P2_1/n$	4	15.824(3)	12.704(1)	9.559(1)		92.78(2)		1919	
BAGMOL	Monoclinic	$P2_1$	4	16.036(3)	12.606(1)	9.634(1)		94.44(2)		1941	0.9887
COBDEC[g]	Monoclinic	$P2_1/a$	4	8.691(10)	28.05(2)	8.864(7)		114.49(7)		1966	
COBDEC	Monoclinic	$P2_1$	4	8.875(7)	28.525(10)	8.694(5)		115.59(6)		1985	0.9904
BZPPBA[h]	Monoclinic	$P2_1/c$	4	9.206(3)	10.530(4)	17.223(5)		111.89(6)		1949	
EBPVPO	Monoclinic	$P2_1$	4	9.147(3)	10.294(3)	16.911(4)		98.08(4)		1577	0.9822
CARVOX[i]	Monoclinic	$P2_1/c$	4	9.856(3)	11.848(3)	8.480(3)		98.95(5)		978	
LCARVX	Monoclinic	$P2_1$	4	10.24(1)	11.67(1)	8.54(2)		103.1(1)		994	0.9839
PRCOUM[j]	Monoclinic	$P2_1/n$	4	11.407(3)	18.005(4)	7.177(2)		95.30(10)		1468	
PPRHCM	Monoclinic	$P2_1$	4	11.752(2)	17.751(5)	7.171(1)		95.58(2)		1494	0.9826
KUHLAA[k]	Monoclinic	$P2_1/c$	4	7.349(1)	7.203(2)	24.729(4)		91.27(1)		1309	
KUHLEE	Orthorhombic	$P2_12_12_1$	4	7.3342(8)	7.3587(4)	24.613(6)				1326	0.9872
DLALNI[l]	Orthorhombic	$Pna2_1$	4	12.06(1)	6.05(1)	5.82(1)				425	
LALNIN	Orthorhombic	$P2_12_12_1$	4	12.343(1)	6.032(1)	5.784(1)				430	0.9884
DLTYRS[m]	Orthorhombic	$Pna2_1$	4	20.8360(8)	6.810(2)	5.905(1)				838	
LTYROS	Orthorhombic	$P2_12_12_1$	4	21.116(3)	6.913(5)	5.829(4)				851	0.9847
MBABIQ[n]	Orthorhombic	$Pna2_1$	4	8.571(4)	30.754(2)	5.957(2)				1570	
MBABIQ	Orthorhombic	$P2_12_12_1$	4	8.730(5)	30.094(4)	5.950(2)				1563	1.0045
FBPACR[o]	Orthorhombic	$Pna2_1$	4	5.95(1)	7.661(1)	19.25(3)				877	
DFBPAC	Monoclinic	$P2_1$	2	5.963(3)	7.411(6)	10.019(9)		102.9(1)		432	1.0150
APALAM[p]	Monoclinic	$P2_1/n$	4	19.45(4)	4.98(1)	12.29(2)		91.92(7)		1190	
APHAMA	Monoclinic	$P2_1$	2	11.531(1)	4.966(1)	11.695(1)		116.6(1)		599	0.9933
CDBMPI[q]	Monoclinic	$P2_1/a$	4	11.220(6)	14.571(6)	10.688(7)		99.38(8)		1724	
BZMPIZ	Monoclinic	$P2_1$	2	5.889(5)	14.25(1)	10.789(7)		102.59(6)		884	0.9751
DLVALC[r]	Monoclinic	$P2_1/c$	4	11.722(4)	7.007(3)	11.143(4)		120.53		788	
VALEHC	Monoclinic	$P2_1$	2	10.382(2)	7.066(1)	5.4407(9)		91.40(2)		399	0.9875

Structures contain the following molecules : [e](1-cyanoethyl)-bis(dimethylglyoximato)-(4-pyridinecarbonitrile)-cobalt(III); [f](1-cyanoethyl)-pyridine- bis(dimethylglyoximato-cobalt(III); [g](1-cyanoethyl)-bis(dimethylglyoximato)-(4-methylpyridine)-cobalt(II); [h]3-(benzyl(phenyl)phosphinyl)-2-butanoic acid; [i]carvoxime; [j]3-(1-phenylpropyl)-4-hydroxycoumarin; [k](7aS)-2,3,7,7a-tetrahydro-7a-phenylthio-1H-indene-1,5(6H)-dione; [l]alanine; [m]tyrosine; [n]1β-(p-methoxybenzyl)-9a,10β-dihydroxydecahydroisoquinoline; [o]β-(p-fluorophenyl)-β-hydroxypropionic acid; [p]N-acetylphenylalanine-N-methylamide; [q]1,4-dibenzoyl-cis-2,5-dimethylpiperazine; [r]valine hydrochloride. The structures immediately below all labelled structures are the corresponding optically pure crystals of the same molecule.

Other authors also describe the first two categories of Marthi *et al.*(59) by considering the packing arrangements of homochiral columns.(60,61) A homochiral column related by a binary axis would form a homochiral layer as described by their second group.(59) This homochiral layer can subsequently be related by another binary axis or by an inverse symmetry element. The latter operation results in a racemic crystal while the former results in an optically pure crystal.

As Marthi *et al.*(59) have noted, these types of comparative studies show a diverse range of relationships between racemic and enantiomeric crystals and also show that the incidence of similar packing modes cannot be considered rare among enantiomeric crystal types. Although not shown in the study by Marthi *et al.*,(59) table 2.1 also shows the ratio of the molar volume of the racemic to that of the optically active crystal. It is interesting that even after further partitioning the list from Brock *et al.*(51) into 14 species of even greater similarity, the sample group shows no strong statistical validity for Wallach's rule.

Although only a few examples and concepts have been discussed here, many statistical studies using the CSD have been presented in the literature;(3,51) however, structural information offers little quantitative thermodynamic stability information. The structural studies do show that no one concept can predict all crystal structures and those that differ only slightly require that many interactions be considered. In addition, the relationships between symmetry and close packing are not well understood.(28,48,62,63) However, similarities and differences between known structures can be used empirically to describe what forces dictate the homochiral or heterochiral preference.

2.1.2 Interaction potentials and computational insights

Many theoretical calculations used to investigate possible and energetically favourable packing arrangements require empirical potentials which can be calibrated using known structures and thermodynamic quantities.(64) Unfortunately, most enantiomeric mixtures involve organics which exhibit many contributing interactions including the π-π interactions of planar aromatic rings, hydrogen-bonding interactions, and Coulombic interactions. For example, it is well established that hydrogen-bonding influences racemic crystal formation; however, sometimes the X-ray structure reveals that racemic crystal stability can only be rationalised by considering various other weak molecular interactions.(65,66) Furthermore, some interactions are very directional; therefore, additional empirical terms are required to describe the potential. Thus, the total chiral discriminating interaction potentials are often complex.

Many studies have attempted to obtain simple empirical atom-atom interaction potentials by collecting information concerning a large sample of crystals involving similar molecular interactions. The distances and orientations between atoms obtained from the crystallographic data are then used to fit empirical potential functions, $\Psi(r)$. Two common potential functions used for these types of studies are the (6-12) Lennard Jones potential and the modified Buckingham 6-exp potential. These functions were developed for investigating the interaction of semipermeable spheres. The functions are mathematically convenient and relatively adjustable with few parameters.(67) Both will be introduced briefly as both have had advantages and successes in modelling different types of interactions.

The first interaction potential to be discussed is the (6-12) Lennard-Jones potential, figure 2.2, which has had success in modelling induced dipole-dipole interactions:

$$\Psi(r) = 4\in_{\mathrm{LJ}}\left[\left(\frac{\sigma_{\mathrm{LJ}}}{r}\right)^{12} - \left(\frac{\sigma_{\mathrm{LJ}}}{r}\right)^{6}\right], \qquad (2.3)$$

where r is the distance between two interacting spheres, σ_{LJ} defines the value of r where the potential is zero, and $4\epsilon_{\mathrm{LJ}}$ is the maximum depth of the potential well located at $r = 2^{1/6}\sigma_{\mathrm{LJ}}$. It is often computationally convenient to modify the Lennard-Jones potential by adding an additional function which defines boundary regions, whereby the potential is zero beyond some selected value of r. Conceptually, the Lennard-Jones potential models the interaction of two molecules or groups which can be represented as near rigid spheres, where ϵ_{LJ} defines the strength of the interaction and σ_{LJ} defines the minimum equilibrium distance of the interaction.

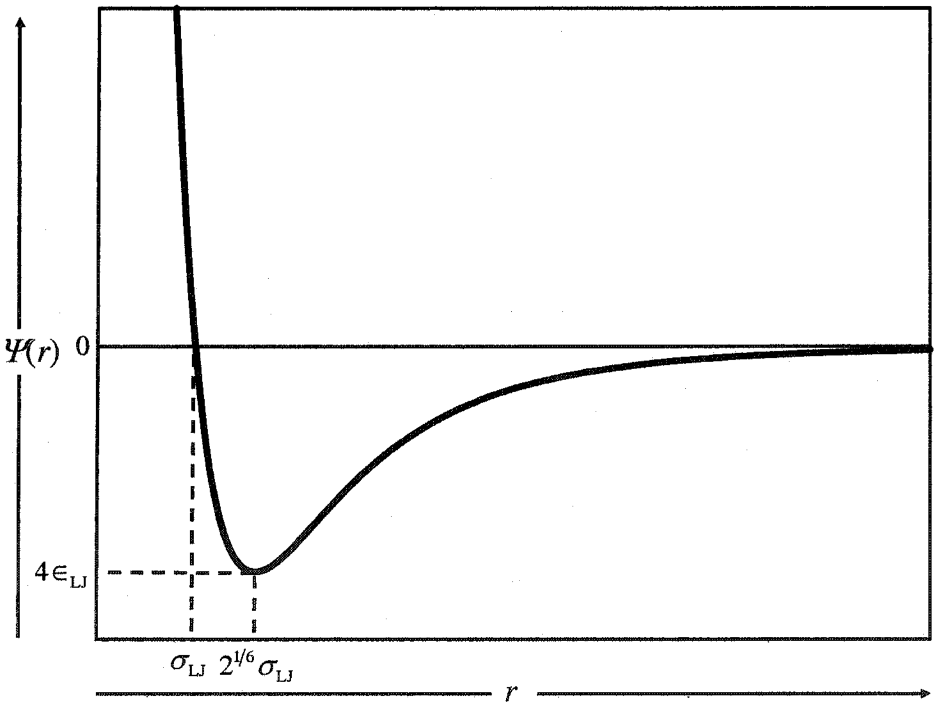

Figure 2.2 The (6-12) Lennard-Jones potential function.

The second commonly used potential is the modified Buckingham 6-exp potential, figure 2.3. The 6-exp potential is somewhat more flexible than the (6-12) Lennard-Jones potential and can be used to model several different types of interaction. The 6-exp potential is given by:

$$\Psi(r) = \begin{cases} \dfrac{\epsilon_{6-\exp}}{1-\frac{6}{\alpha}}\left[\dfrac{6}{\alpha_{6-\exp}} e^{\alpha_{6-\exp}\left(1-\frac{r}{r_{\mathrm{m}}}\right)} - \left(\dfrac{r_{\mathrm{m}}}{r}\right)^{6}\right] & \text{for } r \geq r_{\max} \\ \infty & \text{for } r < r_{\max} \end{cases} . \qquad (2.4)$$

In equation 2.4, $\alpha_{6\text{-exp}}$ defines the steepness of the repulsive portion of the potential well and $\epsilon_{6\text{-}exp}$ defines the minimum depth of the potential well at $r = r_{\mathrm{m}}$. The potential function exhibits an unrealistic maximum at $r = r_{\max}$. In order to avoid the danger of falling into the region of close-range interaction distances where the 6-exp potential is unrealistic (attractive), the function is modified by setting $\Psi(r) = \infty$ at $r < r_{\max}$. Although the 6-exp potential is designed to account for dipole-dipole interactions, with the r^{-6} dependence,(68) the high flexibility of the function allows for reasonable modelling of other types of interactions. For example, it has been shown by Gavezzotti and Filippini(69) that the 6-exp function can partially model the interaction differences associated with various donating/accepting atoms involving weak- to medium-strength hydrogen bonding.

The two potentials briefly introduced here are for spherical interactions; however, it is possible to modify the functions to contain some directional dependence. For example, r_m in the 6-exp potential can be represented by a function in a polar coordinate system; thus, the separation distance at the minimum would have a directional component. Alternatively, the interaction strength can be represented as a tensor property. The addition of a Lennard-Jones potential to a permanent dipole-dipole interaction potential function (Stockmayer potential) has been successful in modelling interactions between small diatomic molecules.(67)

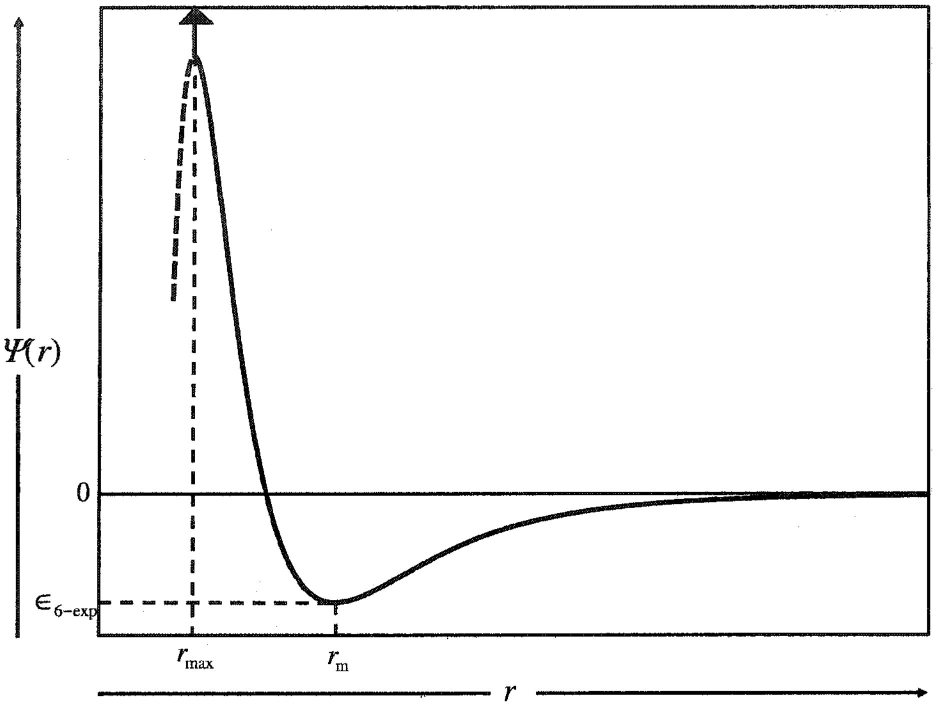

Figure 2.3 The Buckingham 6-exp potential function.

Two ways in which these empirical potentials have helped to explain crystal interaction energies will be discussed: (1) attempts at crystal structure prediction (and exploration) and, (2) the exploratory calculations of enantiomeric phase diagrams using simplified molecules. Two interacting enantiomers can be used to illustrate how empirical potentials can be obtained for predictive type programs, where the total affinity for the homochiral versus the heterochiral interaction can be considered the sum of all the intermolecular interactions in a group of optically pure and racemic mixtures. If an atom-atom approximation (additivity) is assumed valid, then the interactions can be summed to compare the homochiral and heterochiral interactions. However, crystals have many molecules interacting and require the sampling of a large phase space; therefore, computational simplifications are usually made. Using the same atom-atom approximation and neglecting the vibrational energy, the cohesive energy of the crystal as $T \rightarrow 0$ K can be calculated by adding the intermolecular potentials.(58) With crystals containing many molecules, the molecular equilibrium distances can be obtained from measured crystal structures. The experimental distances can be used to obtain a realistic form for the potential function and experimental heats of sublimation can be used to establish the energy scale for the interaction.

Calibrated potential functions have been incorporated in many different available crystal prediction programs discussed in the literature, *e.g.*, UNPACK(70) and the several packages used by CERIUS$^{2\text{TM}}$ (Molecular Simulations Inc., San Diego, CA).(62,71) Through the calibration process, some general knowledge of the forms of particular interactions can be obtained. Most models claim internal validity by being able to reproduce crystal structures, enthalpies of sublimation (within 10%), and vibrational lattice frequencies. The external validity, with respect to *a priori* knowledge of a crystal structure, is debatable.(62) Partitioning interactions is a problem; therefore, most potentials are calibrated by considering a select group of molecules exhibiting limited types of interactions.(62) Adding to the complexity of partitioning the several types of contributing interactions is the lack of confidence in many structures used to obtain the empirical coefficients and multiple intramolecular configurations. For example, although the CSD supplies a large amount of structural information, screening structural data for acceptable *R*-factors often limits the useful data. Presumably a large portion of the error also comes from the lack of total entropic correction, as the enthalpies of sublimation and unit cell volumes are all determined above $T = 0$ K.(72) The calibration process also is difficult because, while there are many available crystal structures, there are few materials for which the enthalpies of sublimation also are reported. The advantage to having these types of modelling programs is that crystal structures which would otherwise be kinetically difficult to obtain experimentally can be investigated. Organic crystals are particularly prone to crystallisation problems.

Being able to predict crystal lattice energies to within *ca.* 10% might not be sufficient to explore the small relative differences in the stability of racemic versus conglomerate crystals. However, Li *et al.*(72) have investigated several enantiomeric crystal pairs using the program CERIUS$^{2\text{TM}}$ to calculate lattice energy differences for racemic and optically pure crystals. It was found that all racemic crystal lattice energies were greater than those of their respective optically pure crystals at $T = 0$ K. The study notes that the lattice energies were all calculated for species where the racemic crystal is more stable at room temperature; therefore, the prediction of stability at $T = 0$ K has less significance, *i.e.*, the potential function calibration data have been determined at room temperature. Li *et al.*(72) also have found a small correlation between the difference in the melting point of the two crystal types and the difference in the lattice energies. The latter finding implies a residual enthalpic stabilisation for the racemic crystal.

Using uncalibrated potentials for exploratory calculations also can offer insight. Vlot *et al.*(73,74) have investigated racemic mixtures using Monte Carlo simulation studies. Here a modified (6-12) Lennard-Jones potential was used to model the interaction differences between two types of spheres, as shown in figure 2.4. The two spheres form binary mixtures and can be considered to be an approximation of two enantiomers by fixing the interaction parameters.

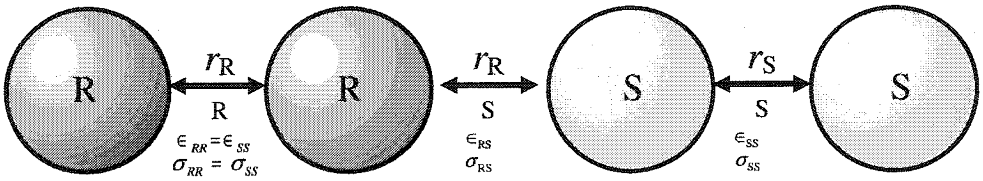

Figure 2.4 A binary mixture model using homochiral and heterochiral Lennard-Jones interaction potentials. The heterochiral interactions are quantified by $e = \epsilon_{RS}/\epsilon_{SS}$ and $s = \sigma_{RS}/\sigma_{SS}$.

Symmetry was ensured by setting the homochiral interaction parameters equal; $\epsilon_{RR} = \epsilon_{SS}$ and $\sigma_{RR} = \sigma_{SS}$. Scaling factors were used to adjust heterochiral interactions; $e = \epsilon_{RS} / \epsilon_{RR}$ and $s = \sigma_{RS} / \sigma_{RR}$. Monte Carlo NPT (constant number of particles, constant pressure and constant temperature) simulations were performed with 500 particles resulting in ensemble averages at several different temperatures. Enthalpies, H, were then calculated using an additive assumption:

$$H = \sum_{i<j} \Psi_{ij} + \tfrac{3}{2} NkT + pV , \tag{2.5}$$

where N is the number of spheres and k is the Boltzmann constant. The enthalpies were then fit to a temperature polynomial to obtain $H(T)$. By using several models corresponding to the phase and the Gibbs-Helmholtz relation,

$$\left(\frac{\partial G/T}{\partial T} \right) = -\frac{H}{T^2} , \tag{2.6}$$

a Gibbs energy function, $G(T,x)$, for each phase was calculated. Thus, the transition temperatures were investigated by observing the intersection points of $G(T,x)$ for several phases. The authors went on to further develop relationships describing the excess properties and investigated the mixing interactions over a range of temperatures and concentrations. This enabled the calculation of several binary phase diagrams of racemic mixtures using several different values for the relative heterochiral interaction parameters, e and s.

The study found that weak heterochiral interactions, $e<1$, stabilised conglomerate crystals or phase separation. Mixtures of both shorter and longer heterochiral distances, $s \neq 1$, were found to stabilise racemic crystals. While the shorter distances agree with Wallach's rule, the stabilisation of the racemic crystal at large s was coupled to a decrease in the entropy of the racemic crystal. This is a direct result of the simplicity of the model and the neglect of the orientational and internal (intramolecular) entropy.(73) In addition, the majority of the binary mixtures produced phase diagrams where solid solutions were formed, corresponding to the experimentally rare pseudoracemic enantiomeric mixtures. More complicated potentials with orientational dependence might lead to more realistic results. The novelty of this study was that a simple microscopic potential was used to investigate several different phase diagrams in an approach similar to that which an experimental physical chemist would take.

While there are many more computational techniques, those discussed here have all alluded to a lack of entropic stability information. In many cases, assumptions about temperature dependent properties must be made due to the lack of information in the literature. Experimental fusion enthalpies are readily available and easily obtained at the normal melting point ($p = 0.10$ MPa) of the respective crystals. Experimental combustion enthalpies are available at or above ambient temperatures and pressures. However, the temperature dependence of the racemic crystal stability is an important piece of the puzzle. Indeed, Pasteur's discovery of spontaneous resolution occurred only because he placed his solution in the cool window.(36,53) In a more recent paper by Dunitz,(75) Wallach's rule and the racemic crystal stability questions have been discussed again. Here Dunitz comments on the lack of thermodynamic stability studies in this area and on the prevalence of room temperature data. Entropic and enthalpic arguments are debated at room temperature, where the entropic stability is very difficult to measure.(75) Brock *et al.*(51) had suggested that if there is entropic stabilisation of racemic crystals, it is very small and difficult to measure. In order to discuss how a more thorough thermodynamic study might be pursued, the thermodynamic assumptions and definitions must be considered.

2.2 Thermodynamic mixtures and their phase diagrams

2.2.1 Thermodynamic definitions required to discuss phase stability

In understanding how the current literature helps lend insight towards racemic crystal stability, the simplifications made throughout thermodynamic derivations must be considered. These simplifications also indicate how the enantiomeric systems behave as very fundamental thermodynamic systems. In fact, many textbooks derive solid and liquid mixing properties by considering phase diagrams which look identical to the racemic and conglomerate melting point phase diagrams presented in the first chapter.(49,67,76) Therefore, studying and understanding these types of systems using thermodynamics is not only of interest to the stereochemist, but also to the thermodynamicist at a very fundamental level.

Beginning at a basic level, some of the simplest thermodynamic relationships can be derived. Through the laws of thermodynamics the existence of some equation of state for G can be established, where temperature, pressure, and composition in number of moles, n_i, are considered independent variables:

$$G = G(T,V;n_1 \cdots n_i)\,. \tag{2.8}$$

The total differentiation of equation 2.8 yields an equation describing the change in G for the increment of any independent variable. Choosing S, V, and $n_1 \ldots n_i$, yields the equation proposed by Gibbs:(49)

$$\mathrm{d}G = T\mathrm{d}S - p\mathrm{d}V + \sum_i \left(\frac{\partial G}{\partial n_i}\right)_{T,p,n_{j\neq i}} \mathrm{d}n_i\,. \tag{2.9}$$

Equation 2.9 shows one way in which the energy of the system can be regarded as a sum of extensive and intensive properties. More generally the extensive forms of the internal energy, Gibbs energy, Helmholtz free energy, and enthalpy can all be considered weighted sum quantities of intensive partial molar quantities (all are homogeneous in n_i). Here, intensive properties can be denoted with the addition of a subscript *i*, *e.g.*, partial molar enthalpy is H_i. The intensive partial molar property of the Gibbs energy is the chemical potential, μ_i. Here the extensive Gibbs energy of the system is a weighted sum of the chemical potentials:

$$G = \sum_i n_i \mu_i \,, \tag{2.10}$$

where

$$G = U - TS + pV \tag{2.11}$$

and U is the internal energy of the system.

Therefore,

$$\mu_i = U_i - TS_i + pV_i = H_i - TS_i \,. \tag{2.12}$$

Furthermore, because the chemical potential is a derivative of the Gibbs energy, differentiating the function further yields the following relationship for the partial molar enthalpy and partial molar volume:

$$\left(\frac{\partial \mu_i^{\circ}/T}{\partial T}\right)_{p,n_{j\neq i}} = -\frac{H_i}{T^2} \tag{2.13}$$

and

$$\left(\frac{\partial \mu_i^{\circ}/T}{\partial p}\right)_{T,n_{j\neq i}} = \frac{V_i}{T} \,, \tag{2.14}$$

where μ_i° is the chemical potential for pure component *i*. Equation 2.13 is the partial molar form of the Gibbs-Helmholtz relationship given previously as equation 2.6. It follows that other thermodynamic independent variables can be defined through chemical potentials of the individual species involved in the system.(67) The latter derivatives are important for the derivation of the binary phase diagrams for enantiomeric mixtures.

When investigating mixtures of molecules, an important consideration is how the mixtures are defined. The important thermodynamic definitions for enantiomeric mixtures involve the concepts of ideal solutions and mechanical mixtures. A solution is considered ideal if the chemical potentials of all components are well described by

$$\mu_i = \mu_i^{\circ}(T, p) + RT \ln x_i . \tag{2.15}$$

In equation 2.15, the activity coefficients are all unity and the last term is derived through the Boltzmann relationship for entropy. Therefore, there is no interaction difference between the individual components and the system obeys the Lewis fugacity rule. For example, chiral molecules in an ideal solution would have the same homochiral and heterochiral interactions.

The ideal solution is different from a mechanical mixture or a phase-separated mixture in that it is entropically more favourable. Equation 2.10 can be recast to represent the molar Gibbs energy of these two different mixtures:

$$G_{\text{Mech. Mix.}} = \sum_i x_i \mu_i^{\circ} \tag{2.16}$$

and

$$G_{\text{Ideal Sol'n}} = \sum_i x_i \mu_i^{\circ} + RT \sum_i x_i \ln x_i . \tag{2.17}$$

Here the phases of a mechanical mixture are defined by the number of pure constituents where the ideal solution forms only one phase with zero excess enthalpy and zero excess volume. Thus, in the mechanical mixture, the phases only contain pure constituents and the second term required for the ideal solution is absent.

The thermodynamic relationships as defined above can be used to show how a system's components pass from one phase to another. Consider two phases, *A* (mechanical mixture) and *B* (solution phase), with a fixed number of components in equilibrium. If component *j* can exist in both phases and all other components only exist in one of the two phases, then using equations 2.16 and 2.17, one can relate the chemical potentials of *j* in the two phases at equilibrium, *i.e.*, $G_{j,\text{A}} = G_{j,\text{B}}$; therefore, $\mu_{j,\text{A}} = \mu_{j,\text{B}}$:

$$\mu_{j,\text{A}}^{\circ} = \mu_{j,\text{B}}^{\circ} + RT \ln x_{j,\text{B}} . \tag{2.18}$$

Dividing equation 2.18 by T and using the derivative relationships of equations 2.13 and 2.14 one can write the full derivative,

$$-\frac{H^{\circ}_{j,\mathrm{A}}}{T^2}\mathrm{d}T+\frac{V^{\circ}_{j,\mathrm{A}}}{T}\mathrm{d}p=-\frac{H^{\circ}_{j,\mathrm{B}}}{T^2}\mathrm{d}T+\frac{V^{\circ}_{j,\mathrm{B}}}{T}\mathrm{d}p+R\mathrm{d}\ln x_{j,\mathrm{B}}. \qquad (2.19)$$

Furthermore, if the phase change of A to B is fusion, then by definition $\Delta_{\mathrm{fus}}H^j = H^{\circ}_{j,\mathrm{B}} - H^{\circ}_{j,\mathrm{A}}$ and $\Delta_{\mathrm{fus}}V^j = V^{\circ}_{j,\mathrm{B}} - V^{\circ}_{j,\mathrm{A}}$. Thus equation 2.19 can be solved for the fusion of component j into phase B for any change in temperature or pressure by integrating from $x = 0$ to x,

$$\ln x_{j,\mathrm{B}}=\int_{T_{\mathrm{fus}}}^{T}\frac{\Delta_{\mathrm{fus}}H^{j}}{RT^2}\mathrm{d}T-\frac{1}{RT}\int_{p_{\mathrm{fus}}}^{p}\Delta_{\mathrm{fus}}V^{j}\mathrm{d}p, \qquad (2.20)$$

where $\Delta_{\mathrm{fus}}H^j$ and $\Delta_{\mathrm{fus}}V^j$ are the changes in enthalpy and volume on fusion for the pure j. Equation 2.20 is derived in many introductory textbooks in many different ways.(49,76) While the derivation up to now is very fundamental in classical thermodynamics, depending on the assumptions made during the solution of the integrals, the final solution can take several forms.

2.2.2 Melting point phase diagrams of conglomerate crystals

In the case of enantiomeric mixtures, one can first consider constant pressure; therefore, the second integral of equation 2.20 is zero. The second common simplification is that the difference in the heat capacity of the solid and liquid component is constant over the temperature range of the liquidus. If component j is an enantiomer in an enantiomeric mixture, equation 2.20 is then substantially simplified because the temperatures and enthalpies of fusion for both enantiomers are equivalent:

$$\ln x=\frac{\Delta_{\mathrm{fus}}H^{R}}{R}\left(\frac{1}{T^{R}_{\mathrm{fus}}}-\frac{1}{T_{\mathrm{fus}}}\right)+\frac{\Delta_{\mathrm{fus}}C_{p}}{R}\left(\ln\frac{T^{R}_{\mathrm{fus}}}{T_{\mathrm{fus}}}+1-\frac{T^{R}_{\mathrm{fus}}}{T_{\mathrm{fus}}}\right). \qquad (2.21)$$

Here $\Delta_{\text{fus}}C_p = C_p(l) - C_p(s)$ and the standard enthalpy of fusion is defined at $T = T_{\text{fus}}{}^R = T_{\text{fus}}{}^S$ and pressure is constant at $p = 0.10$ MPa. The derivation of the full Schröder-van Laar equation with the volume difference is given in Appendix A. If the heat capacity difference in equation 2.21 is deemed to be negligible, then equation 2.21 corresponds to the common simplified Schröder-van Laar equation given previously as equation 1.1.

Several questions arise when considering enantiomeric mixtures and the assumptions that have been made to arrive at equation 2.21 or equation 1.1: (1) Does the solid behave like a mechanical mixture? (2) Does the liquid behave as an ideal solution? (3) Is the heat capacity difference negligible? Several methods can be used to test these assumptions.

As discussed already, conglomerate mixtures are composed of immiscible enantiomer crystals; therefore, by definition the conglomerate is a solid state mechanical mixture. However, the assumptions for the liquid are not as definitive. One of the most compelling reasons to accept the assumption that the liquid behaves ideally is the success of the Schröder-van Laar equation with modelling conglomerate crystal systems. Experimental enthalpies of fusion tend to agree with those derived from experimental temperatures of fusion at different mole ratios.(3)

If the enantiomeric mixture in the liquid is assumed to be an ideal solution, then the enthalpy of mixing of 1:1 enantiomers should be zero. Takagi *et al.*(77) in 1968 were the first to show that, although very small, the enthalpy of mixing of enantiomers can be measured by solution microcalorimetry. Due to the precision and limited temperature range required for these types of measurements, very few experimental studies have been done in this area.(3,78) Table 2.2 shows experimental data for some reported enthalpies of mixing in the liquid and in solution.(3,77,78-82) All the studies were carried out at $p = 0.10$ MPa.

Table 2.2 Some reported enthalpies of enantiomer mixing at $x_R = 0.50 \pm 0.01$.

Formula	Name	$\Delta_{mix}H$ / J mol^{-1}	Solvent	T / K	Ref.
$C_3H_8O_2$	1,2-propanediol	-5.7 ± 0.2	—	298.15	78
$C_4H_6O_6$	tartaric acid	1.9 ± 0.2	H_2O	298.8	77
$C_4H_8O_3$	methyllactate	14.2 ± 0.3	—	298.15	78
$C_4H_9NO_3$	threonine	-5.5	H_2O	298.8	77
$C_6H_{12}O_3$	glycerol acetonide	6.8 ± 0.2	—	298.15	79
$C_7H_8O_4$	α-methyl-α-ethylsuccinic acid	-140 ± 10	$CHCl_3$	298.2	81
$C_8H_{11}N$	α-methylbenzylamine	9.6 ± 0.8	—	298.2	80
$C_8H_{11}N$	α-methylbenzylamine	7.3 ± 0.3	—	303.11	82
$C_8H_{11}N$	α-methylbenzylamine	5.3 ± 0.3	—	313.11	82
$C_8H_{14}O_4$	α-methyl-α-isopropylsuccinic acid	-210 ± 20	$CHCl_3$	298.2	81
$C_8H_{18}O$	2-octanol	13 ± 1	—	298.2	80
$C_{10}H_{13}NO_2$	2-*p*-nitrophenylbutane	1.9 ± 2	—	298.2	80
$C_{10}H_{14}O$	carvone	-2.1 ± 0.2	—	298.15	79
$C_{10}H_{16}$	limonene	1.1 ± 0.1	—	298.15	79
$C_{10}H_{16}$	α-pinene	7.2 ± 0.2	—	298.15	79
$C_{10}H_{16}O$	fenchone	-4.5 ± 0.1	—	303.11	82

Molecular names are those given in the literature cited. These names have been cross-referenced to Chemical Abstract names, CA, in Appendix B.

Table 2.2 shows that the enthalpies of mixing are indeed small, ranging from $\Delta_{mix}H = -210$ to 14.2 J mol^{-1}. Leaving out the results obtained from mixing in chloroform, which are extraordinarily high, the average enthalpy of mixing is $\Delta_{mix}H = 5 \pm 14$ J mol^{-1}. This range of enthalpies of mixing is much smaller in magnitude than the common error in enthalpies of fusion for enantiomers reported in the literature ($\delta\Delta_{fus}H \approx 500$ J mol^{-1}). Therefore, it would seem that the assumption of an ideal liquid solution is robust for most systems.

For any ideal solution the volume change on mixing also should be zero. Therefore, it is worth noting that measurements of the excess volume of mixing enantiomers by solution vibrating tube densimetry and dilatometry also have been reported.$^{(83,84)}$ These studies have shown that liquid homochiral and heterochiral packing differences also are very small. The data of Lepori *et al.*$^{(83)}$ and Atik *et al.*$^{(84)}$ are shown in table 2.3. The small number of values in table 2.3 shows no apparent generalisation similar to Wallach's rule, with an average excess volume of mixing of $\Delta_{mix}V = -0.001 \pm 0.008$ cm^3 mol^{-1}.

Table 2.3 Some reported excess volumes of enantiomer mixing at $x_R = 0.50 \pm 0.01$.

Formula	Name	$\Delta_{mix}V$ / cm^3 mol^{-1}	T / K	Ref.
$C_8H_{11}N$	α-methylbenzylamine	-0.0047 ± 0.0006	298.15	83
$C_8H_{11}N$	α-methylbenzylamine	-0.0018 ± 0.0004	303.11	84
$C_8H_{18}O$	2-octanol	0.0076 ± 0.0005	298.15	83
$C_{10}H_{14}O$	carvone	-0.0050 ± 0.0005	298.15	83
$C_{10}H_{16}$	limonene	-0.0014 ± 0.0004	298.12	84
$C_{10}H_{16}$	limonene	-0.0027 ± 0.0011	298.15	83
$C_{10}H_{16}$	limonene	-0.0027 ± 0.0008	303.11	84
$C_{10}H_{16}$	α-pinene	0.0020 ± 0.0004	298.15	83
$C_{10}H_{16}O$	fenchone	-0.0041 ± 0.0005	298.15	84

Chemical names are those given in the literature cited. These names have been cross-referenced to Chemical Abstract names, CA, in Appendix B.

A sample calculation also is helpful in looking the consequences of the ideal solution assumption. If the heat capacity difference is assumed to be negligible, the enthalpy of fusion is assumed to be approximately $\Delta_{fus}H^R = 30$ kJ mol^{-1} at $T = 373$ K, and the error in the fusion enthalpy at $x = 0.5$ is assumed to be $\delta\Delta_{fus}H^R = 300$ J mol^{-1} (*i.e.*, only from the enthalpy of mixing), then equation 1.1 gives an estimated error for the depressed fusion temperature for a racemic mixture. This turns out to be $\delta T_{fus}^{con} = 0.23$ K at $T_{fus}^{con} = 349$ K. This is acceptable considering the accuracy of most experimentally determined melting temperatures, therefore supporting the previous assumption that the liquid is an ideal solution.

Finally, there have been some limited measurements of liquid and solid heat capacities of enantiomeric mixtures near the melting point.(3,85) These measurements show no difference to within 99% confidence for the heat capacities of the optically pure and racemic liquid. The systems included those which form racemic crystals and conglomerates, therefore, showing that all these enantiomeric mixtures can be assumed to form ideal solutions in the liquid phase.

Leclercq *et al.*(85) have reported that the difference in heat capacities of enantiomeric crystals and enantiomeric liquids is in the range of $\Delta_{fus}C_p = 100 \pm 20$ J K^{-1} mol^{-1} (20 to 30 cal K^{-1} mol^{-1})(3) and constant. Using equation 2.21 one can calculate the worst case scenario for the error in the temperature depression associated with the assumption that the difference in heat capacity does not contribute. Using the same enthalpy and temperature of fusion as before, the melting point error changes from $\delta T_{\mathrm{fus}}{}^{con} = -0.9$ to -1.4 K at $x_R = 0.5$. Although this error seems large it is usually small enough to show the existence of an alternate crystal, such as a racemic crystal. Racemic crystals usually have much higher temperatures of fusion than the calculated conglomerate eutectic temperature, $T_{\mathrm{fus}}{}^{Rac} - T_{\mathrm{fus}}{}^{con} > 5$ K. Where temperatures of fusion are near the calculated conglomerate eutectic temperature, further complementary techniques are required to rule out or confirm the existence of conglomerate crystals.

Although the heat capacity correction often is ignored in equation 2.21, it should be noted that assuming the heat capacity difference at the fusion temperature is zero is experimentally unrealistic. The heat capacities of molecular liquids are found to be larger than the corresponding heat capacities of ordered molecular solids. Therefore the uncorrected depressed melting point will be greater than the heat capacity-corrected depressed melting point. In addition, the larger the melting points of the pure species, the lower the expected error because the terms $(1-T_{\mathrm{fus}}{}^{R}/T_{\mathrm{fus}})$ and $\ln(T_{\mathrm{fus}}{}^{R}/T_{\mathrm{fus}})$ both become small when $T_{\mathrm{fus}}{}^{R} \approx T_{\mathrm{fus}}$. This error is discussed further in Section 2.3.

2.2.3 Melting point phase diagrams of racemic crystals

The system with an additional solid phase composed of equimolar quantities of enantiomers, the racemic crystal, is now considered. The liquid is still an ideal mixture, therefore, when equilibrium shifts, the components of the racemic crystal phase must pass to an ideal solution phase composed of x_S of one enantiomer and $x_R = 1 - x_S$ of the other enantiomer. Once again using equations 2.16 and 2.17, the racemic phase equilibrium is given by

$$\begin{aligned}2\mu^{\circ}_{Rac}(cr) &= \mu^{\circ}_{R}(l) + \mu^{\circ}_{S}(l) + RT\ln x_R(1-x_R) \\ &= 2\mu^{\circ}_{R}(l) + RT\ln x_R(1-x_R)\end{aligned} \quad . \tag{2.22}$$

As before, the full derivative can be obtained with the substituted identities for the enthalpy and volume change associated with melting the racemic crystal,

$$\Delta_{\text{fus}}H^{Rac} = H^{Rac}(cr) - 0.5\, H^{R}(l) - 0.5\, H^{S}(l) \tag{2.23}$$

$$\Delta_{\text{fus}}V^{Rac} = V^{Rac}(cr) - 0.5\, V^{R}(l) - 0.5\, V^{S}(l) \tag{2.24}$$

$$\mathrm{d}\ln x_R(1-x_R) = -\frac{2\Delta_{\text{fus}}H^{Rac}}{RT^2}\mathrm{d}T + \frac{2\Delta_{\text{fus}}V^{Rac}}{RT}\mathrm{d}p\,. \tag{2.25}$$

Because the concentration of the liquid at $x_R = 0.5$ is known from the composition of the racemic crystal melt, one can integrate from ln(0.5(1-0.5)) to ln(x_R(1- x_R)):

$$\ln 4x_R(1-x_R) = \int_{T^{Rac}_{\text{fus}}}^{T_{\text{fus}}} \frac{2\Delta_{\text{fus}}H^{Rac}}{RT^2}\mathrm{d}T - \frac{2}{RT}\int_{p^{Rac}_{\text{fus}}}^{p_{\text{fus}}} \Delta_{\text{fus}}V^{Rac}\mathrm{d}p\,. \tag{2.26}$$

Equation 2.26 is an extended version of the Prigogine and Defay$^{(49)}$ equation, where the solution is given in Appendix A. If the pressure is held constant, as with equation 2.21, then equation 2.26 yields

$$\ln 4x_R(1-x_R) = \frac{2\Delta_{\text{fus}}H^{Rac}}{R}\left(\frac{1}{T^{Rac}_{\text{fus}}} - \frac{1}{T_{\text{fus}}}\right) + \frac{2\Delta_{\text{fus}}C^{Rac}_{p}}{R}\left(\ln\frac{T^{Rac}_{\text{fus}}}{T_{\text{fus}}} + 1 - \frac{T^{Rac}_{\text{fus}}}{T_{\text{fus}}}\right). \tag{2.27}$$

If the pressure is held constant and the difference in the heat capacity of the liquid and solid is considered negligible, equation 2.26 becomes the Prigogine and Defay$^{(49)}$ equation, equation 1.2. The Prigogine and Defay$^{(49)}$ equation is the most common equation used to model the liquidus of the racemic crystal melt, or the liquidus between the two eutectic points shown in figure 1.2.

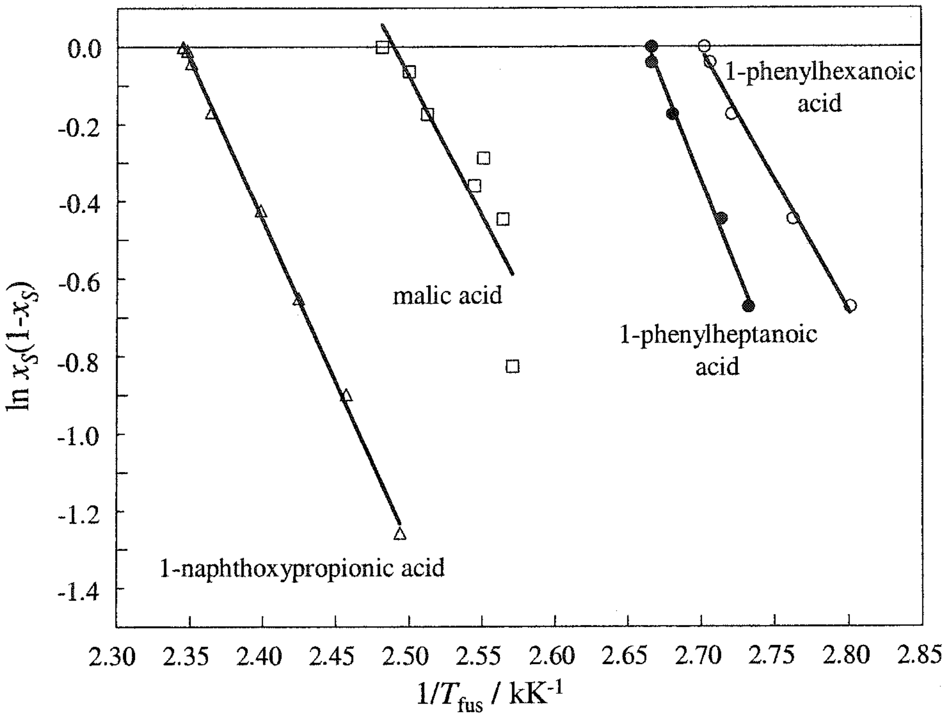

Figure 2.5 A test of the Prigogine and Defay equation for racemic crystals. 1-phenylhexanoic acid;(86) 1-phenylheptanoic acid;(86) malic acid;(87) 1-(napthoxy)propionic acid.(88) A straight line indicates that the Prigogine and Defay equation models the system well.

Many of the assumptions about liquid enantiomeric mixtures already have been discussed. The only additional assumption in deriving the Prigogine and Defay(49) equation has been that the racemic crystal phase and the optically pure phases are completely immiscible in the solid state. The Prigogine and Defay(49) equation can be tested by plotting $\ln(4x_R(1-x_R))$ versus $1/T_{\mathrm{fus}}$. The plot should be linear with a slope of $2\Delta_{\mathrm{fus}}H^{Rac}/R$. Four examples are shown in figure 2.5 for some racemic crystal cases.(86,87,88) All of these plots are linear, indicating that the assumptions made in deriving the Prigogine and Defay(49) equation are valid. Furthermore, the enthalpy of fusion for malic acid has been reported in the literature(85) as $\Delta_{\mathrm{fus}}H^{Rac} = 27$ kJ mol^{-1}. This agrees well with that calculated from the slope in figure 2.5, $\Delta_{\mathrm{fus}}H^{Rac} = 29 \pm 7$ kJ mol^{-1}.

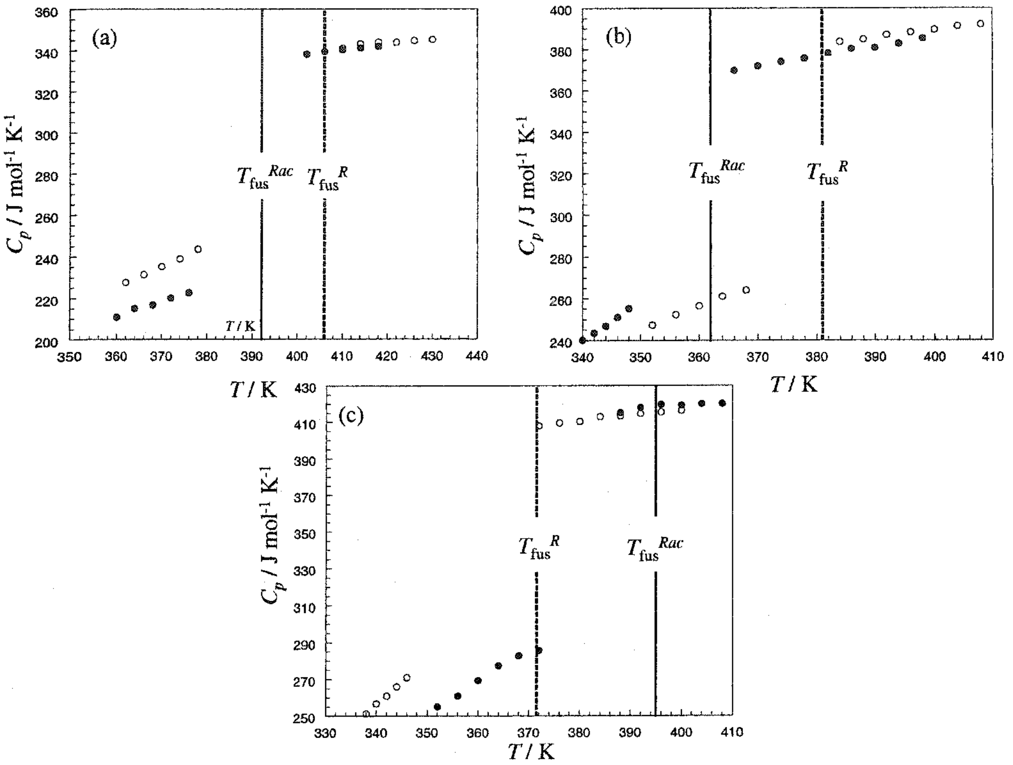

Figure 2.6 Experimental heat capacities of three racemic crystal forming systems.(85) (a) mandelic acid; (b) 3-(*p*-fluorophenyl)hydracrylic acid; (c) *erythro*-phenylglyceric acid; ● racemic crystal and its liquid; ○ optically pure crystal and its liquid.

Leclercq *et al.*(85) have measured the heat capacities of some racemic and optically pure crystal pairs at temperatures within *ca.* 40 K of the corresponding fusion temperature, figure 2.6. The measurements were made using a Perkin Elmer DSC 1 and the authors claim to be able to reproduce heat capacities within *ca.* 2%. The results show that the difference in heat capacities, $\Delta_{\text{fus}}C_p$, for the optically pure and racemic crystals versus their liquids range from $\Delta_{\text{fus}}C_p = 84$ to 117 J mol^{-1} K^{-1}. The heat capacities for three of these systems are shown in figure 2.6. The study shows that the differences in the liquid heat capacities (racemic versus optically pure) are less than the 2% precision of the measurements. The authors also have concluded that the heat capacity difference over the temperature range of $T = T_{\text{fus}}^{R}$ to

T_{fus}^{Rac} can be considered constant. It has been shown that the Prigogine and Defay$^{(49)}$ equation is fairly robust for calculating temperatures of fusion; however, these heat capacity results suggest that the difference between the liquid and solid heat capacities can be measured and used to better define the thermodynamic stability of a racemic crystal versus the conglomerate.

The data also show that there is an even smaller difference between the crystal heat capacities in the relatively small temperature range where the melting point depression equations are used. However, if the thermodynamic stability over a larger temperature range is considered, the difference in the heat capacities of different crystal types could be significant. This leads to discussion of the transition from a conglomerate to a racemic crystal.

2.3 Thermodynamic cycles for investigating the formation of a racemic crystal from a conglomerate

Apart from understanding and modelling the melting phase changes of conglomerate and racemic crystals, the experimental thermodynamic parameters required to calculate the melting point phase diagrams provide some basic information for other calculations. In particular, the enthalpy changes and temperatures of fusion can be used to calculate the phase of a conglomerate to a racemic crystal, equation 2.1. In this manner these accessible values can provide important information about possible resolution conditions. From the entropy and enthalpy changes for forming a racemic crystal from a conglomerate, one can identify if any temperature condition might lead to spontaneous resolution or conglomerate stability, table 2.4. Similarly, a volumetric change obtained from X-ray analyses can be used to obtain possible pressure conditions for spontaneous resolution.$^{(89)}$

Table 2.4 Speculations of possible conditions where conglomerate crystal formation would be spontaneous relative to spontaneous racemic crystal formation.

$\Delta_{\text{Rac}}H$	$\Delta_{\text{Rac}}S$	$\Delta_{\text{Rac}}V$	Spontaneity of conglomerate crystal formation	Speculative experimental condition for spontaneous resolution
+	+		spontaneous at lower temperatures[a]	try a lower temperature
+	-		spontaneous at all temperatures	
-	+		non-spontaneous at all temperatures	try other conditions such as solvent change, etc.
-	-		spontaneous at higher temperatures[a]	try a higher temperature
		-	spontaneous at lower pressures[a]	try a low pressure
		+	spontaneous at higher pressures[a]	try a high pressure

[a] Speculation also would require that the magnitudes of $\Delta_{\text{Rac}}S$ and $\Delta_{\text{Rac}}V$ are large enough to cause a positive $\Delta_{\text{Rac}}G$ under some accessible condition, *i.e.*, the table is not meant to provide rigid rules rather only examples of what might be possible given the experimental information and other assumptions.

Aside from the above application, a list of thermodynamic information for a significant number of crystal pairs provides for fundamental interpretations of nature's preference for racemic crystals. The largest of these published lists was completed by Leclercq *et al.*,(85) 36 experimental fusion temperatures and enthalpies for racemic crystals and their respective optically pure crystals. Using this list, both Brock *et al.*(51) and Leclercq *et al.*(85) have given thermodynamic arguments justifying why racemic crystals are more stable than conglomerate crystals; however, Brock *et al.*(51) have stated that the argument of Leclercq *et al.*(85) is fallacious. In this section, their thermodynamic arguments and derivations are reviewed with the addition of a discussion of error associated with some heat capacity assumptions.

Using the 36 pairs of experimental fusion temperatures and enthalpies, Leclercq *et al.*(85) have calculated the Gibbs energy change for forming a racemic crystal from its respective optically pure crystals at the highest temperature where both crystals exist. Here, $\Delta_{\text{Rac}}G$ refers to reaction 2.1 at the lower temperature of $T = T_{\text{fus}}{}^{R}$ or $T_{\text{fus}}{}^{Rac}$. The authors have assumed the differences between the respective racemic and optically pure liquid and crystal heat capacities are negligible. They supported this assumption by showing a linear correlation between the Gibbs energy changes for reaction 2.1 and the difference in the temperatures of fusion, $T_{\text{fus}}{}^{Rac}$ - $T_{\text{fus}}{}^{R}$:

$$\Delta_{\text{Rac}}G \approx \Delta_{\text{fus}}S^{avg}\,(T_{\text{fus}}^{Rac} - T_{\text{fus}}^{R}) - T_{\text{fus}}^{avg} R\ln 2, \tag{2.28}$$

where, $\Delta_{\text{fus}}S^{avg}$ is the average entropy of fusion for all the racemic and optically pure crystals in the list (71 J mol^{-1} K^{-1}) and $T_{\text{fus}}{}^{avg}$ is the approximate average fusion temperature (400 K).(3) They also have shown that the calculation error is larger as the difference between the fusion temperature of the racemic crystals and the optically pure crystal becomes larger. This error was attributed to the differences in the heat capacities of the racemic and optically pure crystals. The list, equations, and the derivations are presented in English in the book by Jacques *et al.*,(3) where the authors point out that equation 2.28 agrees with another correlation study by Pettersson.(90)

Brock *et al.*(51) have argued that the *R*ln2 term in equation 2.28 is incorrectly attributed to separation of enantiomers on solidification. They also have argued that while Leclercq *et al.*(85) have calculated the thermodynamic stability at either $T_{\text{fus}}{}^{Rac}$ or $T_{\text{fus}}{}^{R}$, depending on which is lower, the more correct derivation would be at the predicted conglomerate fusion temperature of $T_{\text{fus}}{}^{con}$. Here Brock *et al.*(51) have commented that in order to characterise this stability correctly, one must consider that the two crystals are in equilibrium with the same liquid. The liquid is a racemic mixture; therefore, the stability comparison of interest is really for the conglomerate versus the racemic crystal.

Brock *et al.*(51) have shown a linear correlation between entropy differences and the differences in measured racemic and predicted conglomerate fusion temperatures:

$$\Delta S_{\text{fus}}^{Rac} - \Delta S_{\text{fus}}^{R} \approx R\ln 2 + \Delta_{\text{fus}}C_p \frac{T_{\text{fus}}^{Rac} - T_{\text{fus}}^{con}}{T_{\text{fus}}^{R}}. \tag{2.29}$$

They suggest that the correlation is fair ($R^2 = 0.77$) and the slope corresponds to an acceptable liquid-solid heat capacity difference of 125 ± 13 J mol^{-1} K^{-1} at $T = 295$ K. This is comparable to the range given by Leclercq *et al.*$^{(85)}$ (as discussed earlier) of $\Delta_{\text{fus}}C_p = 84$ to 117 J mol^{-1} K^{-1}. The imperfect correlation factor of $R^2 = 0.77$ was attributed to the assumption that the heat capacities of the two different crystal types were equal and to the experimental errors for the entropies of fusion. Brock *et al.*$^{(51)}$ also show a linear correlation between ($\Delta_{\text{fus}}H^{Rac}$ - $\Delta_{\text{fus}}H^{R}$) and the same difference in fusion temperature, $T_{\text{fus}}{}^{Rac}$ - $T_{\text{fus}}{}^{con}$. Thus, Brock *et al.*$^{(51)}$ concluded that stability of a racemic crystal is governed by an enthalpic difference and there is no appreciable entropic difference relative to the conglomerate.

In summarising the arguments, Brock *et al.*$^{(51)}$ have argued that by the third law of thermodynamics, the entropy difference between two ordered crystals (racemic or separate enantiomers) is zero at $T = 0$ K. There is no appreciable entropy of mixing until a temperature where the liquid is formed and there is no appreciable entropy difference between the conglomerate and racemic crystals at any temperature from $T = 0$ to $T_{\text{fus}}{}^{Rac}$. However, Leclercq *et al.*$^{(85)}$ argue that the racemic crystal is entropically stabilised because of a linear correlation of the Gibbs energy change with the difference in temperature, equation 2.28. So which authors are correct?

Both ideas are similar, as both groups agree that the temperature of interest should be where both crystals exist. In my opinion, the suggestion offered by the Brock *et al.*$^{(51)}$ that the Gibbs energy differences should be calculated at the conglomerate's melting temperature of $T_{\text{fus}}{}^{con}$ makes sense. A comparison of the conglomerate and the racemic crystal versus the racemic liquid seems to be clearer. If the reference point is the racemic liquid, then the differences in the crystallisation enthalpies and entropies comply better with the stability being considered.

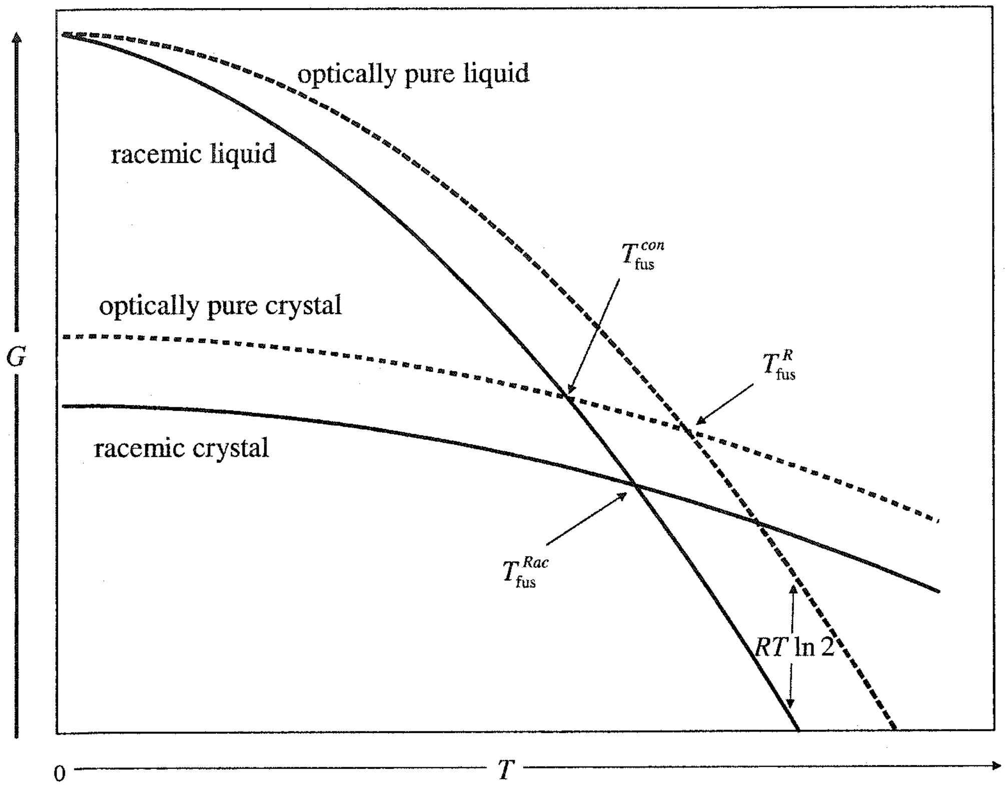
optically pure liquid
racemic liquid
optically pure crystal
racemic crystal
T_{fus}^{con}
T_{fus}^{R}
T_{fus}^{Rac}
$RT \ln 2$
G
0
T

Figure 2.7 A Gibbs energy schematic of solid and liquid enantiomers and enantiomer mixtures. Styled after Brock *et al.*(51)

Brock *et al.*(51) also show a very convenient schematic diagram of the Gibbs energy versus temperature for enantiomeric mixtures. Figure 2.7 shows how the entropy change associated with the mixing of liquid enantiomers lowers the fusion temperature of the 1:1 enantiomer crystal mixture, the conglomerate. In addition, they have assumed a residual enthalpy difference at $T = 0$ K. The diagram shows how a small enthalpy difference can raise the fusion temperature of a racemic crystal well above the conglomerate fusion temperature and often above the optically pure melting point. Figure 2.7 is helpful because the fusion entropy difference is shown pictorially by the first derivative difference and the solid-liquid heat capacity difference is shown pictorially by the second derivative difference. In this way, one can see how these thermodynamic parameters serve to drastically change the melting points.

Note that figure 2.7 shows the entropy difference between the conglomerate crystals and the racemic crystals is zero at all temperatures. However, this seems unlikely. While the entropic difference for two ordered crystals is zero at $T = 0$ K and there is no appreciable entropy of mixing for the conglomerate and racemic crystal, there is very little evidence that there is no absolute entropic difference at $T = T_{\mathrm{fus}}^{con}$. In fact, as shown in figure 2.6, Leclercq *et al.*(85) have measured a non-zero heat capacity difference between some optically active crystals and their corresponding racemic crystals. In addition, Brock *et al.*(51) have partially attributed an imperfect correlation of their entropy equation to the assumption that the heat capacities of the two different crystal types were equal. Since both studies agree that there is a small heat capacity difference between the two crystal types at $T = T_{\mathrm{fus}}^{con}$, the enthalpy difference most likely changes with temperature, *i.e.*, $\Delta C_p = (\partial \Delta H/\partial T)_p \neq 0$. As Brock *et al.*(51) have pointed out using a diagram similar to figure 2.7, a small enthalpic stability can elevate the temperature of fusion of the racemic crystal above the fusion temperature of the conglomerate. However, entropic stability also can provide the same increase in fusion temperature. This does not mean that there is an entropic difference at $T = 0$ K or that there is no residual enthalpic stabilisation, rather there can be both enthalpic and entropic differences between the two crystal types. The only way to know the thermodynamic entropic and enthalpic stability down to $T = 0$ K is through the knowledge of low-temperature heat capacities.

Finally, considering the assumptions made by both studies, if one develops the concepts for crystallising the conglomerate and racemic crystals from the racemic liquid, as suggested by Brock *et al.*,(51) the equations developed agree with those of Leclercq *et al.*(85) The derivations at the lower of T_{fus}^{Rac} or T_{fus}^{R} (Leclercq *et al.*'s(85) method) are the same as those at T_{fus}^{con} (Brock *et al.*'s(51) method), because both groups have assumed that the heat capacities of the solids are the same. The point here is subtle; therefore, a more thorough examination of the derivation in question will be helpful in concluding this chapter.

Thermodynamic cycles for calculating the Gibbs energy change for forming a racemic crystal from conglomerate crystals, $\Delta_{\mathrm{Rac}}G = \Delta_{\mathrm{Rac}}H - T\Delta_{\mathrm{Rac}}S$, are shown in figure 2.8. In figure 2.8, a liquid temperature above all fusion temperatures has been defined, T_l, because the racemic and optically pure fusion temperatures can be either higher or lower than the other. This removes the confusion of having to derive two different sets of equations, as in the derivations of Leclercq *et al.*(85)

As discussed, to be consistent with the suggestion of Brock *et al.*,(51) the thermodynamic stability of the racemic compound relative to the conglomerate can be derived by considering crystallisation from a racemic liquid. Figure 2.8 shows how this thermodynamic stability can be calculated via two different pathways, *i.e.*, figure 2.8 shows that there are two reference temperatures for the entropy change; $T = 0$ K or T_l.

The crystallisation of the racemic crystal from the racemic liquid via the right path in figure 2.8 is straightforward, because the thermodynamic quantities required for the calculation are within the list of Leclercq *et al.*,(85) *i.e.*, fusion enthalpy and temperature of the racemic crystal. The crystallisation of the conglomerate crystal from the racemic liquid can be calculated via the middle path in figure 2.8. However, the experimental enthalpy of fusion for the conglomerate system is rarely available. The temperature and enthalpies of fusion for the optically pure crystals, as they melt to optically pure liquids, are known and the Gibbs energy of a conglomerate crystal is the same as an equimolar mixture of optically pure crystals. As the left hand path in figure 2.8 shows, the entropy of separating the racemic liquid to obtain the optically pure liquids is $-R\ln 2$. This $R\ln 2$ entropy factor is included in the equations of Brock *et al.*,(51) Leclercq *et al.*(85) and the Schröder-van Laar equation.

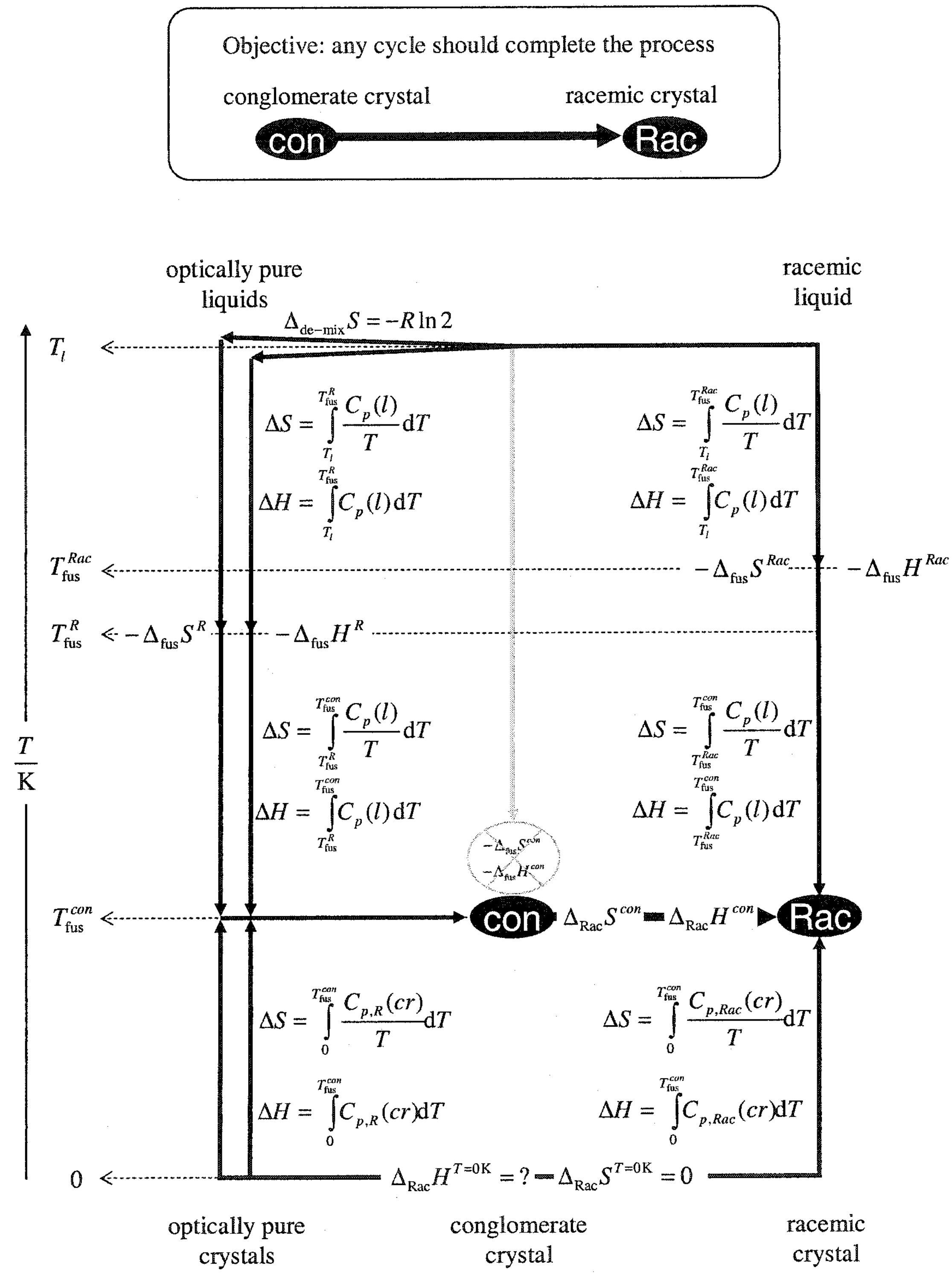
Objective: any cycle should complete the process
conglomerate crystal
racemic crystal
con
Rac
optically pure liquids
racemic liquid
$\Delta_{\text{de-mix}}S = -R\ln 2$
T_l
T_{fus}^{Rac}
T_{fus}^{R}
T_{fus}^{con}
T/K
0
$\Delta S = \int_{T_l}^{T_{\text{fus}}^{R}} \frac{C_p(l)}{T}\mathrm{d}T$
$\Delta H = \int_{T_l}^{T_{\text{fus}}^{R}} C_p(l)\mathrm{d}T$
$\Delta S = \int_{T_l}^{T_{\text{fus}}^{Rac}} \frac{C_p(l)}{T}\mathrm{d}T$
$\Delta H = \int_{T_l}^{T_{\text{fus}}^{Rac}} C_p(l)\mathrm{d}T$
$-\Delta_{\text{fus}}S^{Rac}$
$-\Delta_{\text{fus}}H^{Rac}$
$-\Delta_{\text{fus}}S^{R}$
$-\Delta_{\text{fus}}H^{R}$
$\Delta S = \int_{T_{\text{fus}}^{R}}^{T_{\text{fus}}^{con}} \frac{C_p(l)}{T}\mathrm{d}T$
$\Delta H = \int_{T_{\text{fus}}^{R}}^{T_{\text{fus}}^{con}} C_p(l)\mathrm{d}T$
$\Delta S = \int_{T_{\text{fus}}^{Rac}}^{T_{\text{fus}}^{con}} \frac{C_p(l)}{T}\mathrm{d}T$
$\Delta H = \int_{T_{\text{fus}}^{Rac}}^{T_{\text{fus}}^{con}} C_p(l)\mathrm{d}T$
$-\Delta_{\text{fus}}S^{con}$
$-\Delta_{\text{fus}}H^{con}$
$\Delta_{\text{Rac}}S^{con}$ $\Delta_{\text{Rac}}H^{con}$
$\Delta S = \int_{0}^{T_{\text{fus}}^{con}} \frac{C_{p,R}(cr)}{T}\mathrm{d}T$
$\Delta H = \int_{0}^{T_{\text{fus}}^{con}} C_{p,R}(cr)\mathrm{d}T$
$\Delta S = \int_{0}^{T_{\text{fus}}^{con}} \frac{C_{p,Rac}(cr)}{T}\mathrm{d}T$
$\Delta H = \int_{0}^{T_{\text{fus}}^{con}} C_{p,Rac}(cr)\mathrm{d}T$
$\Delta_{\text{Rac}}H^{T=0\text{K}} = ?$ $\Delta_{\text{Rac}}S^{T=0\text{K}} = 0$
optically pure crystals
conglomerate crystal
racemic crystal

Figure 2.8 Thermodynamic cycles for calculating the Gibbs energy change for forming a racemic crystal from a conglomerate. $\Delta_{\text{fus}}S^{con}$ and $\Delta_{\text{fus}}H^{con}$ are rarely available, because obtaining these values requires having pure and metastable conglomerate crystals. T_{fus}^{Rac} can be greater or less than T_{fus}^{R}.

Using figure 2.8 the enthalpy and entropy change for crystallisation at the conglomerate temperature are given as follows:

$$\begin{aligned}\Delta_{\mathrm{cr}} H^{Rac}_{T^{con}_{\mathrm{fus}}} &= -\Delta_{\mathrm{fus}} H^{Rac}_{T^{con}_{\mathrm{fus}}} \\ &= -\Delta_{\mathrm{fus}} H^{Rac} + \int_{T^{Rac}_{\mathrm{fus}}}^{T^{con}_{\mathrm{fus}}} C_{p,Rac}(cr)\mathrm{d}T + \int_{T_l}^{T^{Rac}_{\mathrm{fus}}} C_p(l)\mathrm{d}T,\end{aligned} \tag{2.30}$$

$$\begin{aligned}\Delta_{\mathrm{cr}} H^{R}_{T^{con}_{\mathrm{fus}}} &= -\Delta_{\mathrm{fus}} H^{R}_{T^{con}_{\mathrm{fus}}} \\ &= -\Delta_{\mathrm{fus}} H^{R} + \int_{T^{R}_{\mathrm{fus}}}^{T^{con}_{\mathrm{fus}}} C_{p,R}(cr)\mathrm{d}T + \int_{T_l}^{T^{R}_{\mathrm{fus}}} C_p(l)\mathrm{d}T,\end{aligned} \tag{2.31}$$

$$\begin{aligned}\Delta_{\mathrm{cr}} S^{Rac}_{T^{con}_{\mathrm{fus}}} &= -\Delta_{\mathrm{fus}} S^{Rac}_{T^{con}_{\mathrm{fus}}} \\ &= \frac{-\Delta_{\mathrm{fus}} H^{Rac}}{T^{Rac}_{\mathrm{fus}}} + \int_{T^{Rac}_{\mathrm{fus}}}^{T^{con}_{\mathrm{fus}}} \frac{C_{p,Rac}(cr)}{T}\mathrm{d}T + \int_{T_l}^{T^{Rac}_{\mathrm{fus}}} \frac{C_p(l)}{T}\mathrm{d}T\end{aligned} \tag{2.32}$$

and

$$\begin{aligned}\Delta_{\mathrm{cr}} S^{R}_{T^{con}_{\mathrm{fus}}} &= -\Delta_{\mathrm{fus}} S^{R}_{T^{con}_{\mathrm{fus}}} \\ &= \frac{-\Delta_{\mathrm{fus}} H^{R}}{T^{R}_{\mathrm{fus}}} + \int_{T^{R}_{\mathrm{fus}}}^{T^{con}_{\mathrm{fus}}} \frac{C_{p,R}(cr)}{T}\mathrm{d}T + \int_{T_l}^{T^{R}_{\mathrm{fus}}} \frac{C_p(l)}{T}\mathrm{d}T.\end{aligned} \tag{2.33}$$

If it is assumed that the heat capacities of the racemic crystal and conglomerate crystal are equal and that over the temperature range of $T = T_{\mathrm{fus}}{}^{Rac}$ to $T_{\mathrm{fus}}{}^{con}$ the heat capacities are constant, T_l and $T_{\mathrm{fus}}{}^{con}$ will drop out upon deriving the enthalpy and entropy of forming a racemic crystal from the conglomerate crystal:

$$\Delta_{\mathrm{Rac}} H = \Delta_{\mathrm{fus}} H^{R} - \Delta_{\mathrm{fus}} H^{Rac} + \Delta_{\mathrm{fus}} C_p (T^{Rac}_{\mathrm{fus}} - T^{R}_{\mathrm{fus}}) \tag{2.34}$$

and

$$\Delta_{\mathrm{Rac}} S = \frac{\Delta_{\mathrm{fus}} H^{R}}{T^{R}_{\mathrm{fus}}} - \frac{\Delta_{\mathrm{fus}} H^{Rac}}{T^{Rac}_{\mathrm{fus}}} + \Delta_{\mathrm{fus}} C_p \ln \frac{T^{Rac}_{\mathrm{fus}}}{T^{R}_{\mathrm{fus}}} + R\ln 2, \tag{2.35}$$

where $\Delta_{\mathrm{fus}}C_p = C_p(l) - C_p(cr)$. Equations 2.34 and 2.35 are consistent with the derivations of Leclercq *et al.*(85) and Jacques *et al.*(3)

Subsequently the Gibbs energy change for forming a racemic crystal from a conglomerate can now be calculated at the conglomerate fusion temperature,

$$\Delta_{\mathrm{Rac}}G = \Delta_{\mathrm{Rac}}H - T_{\mathrm{fus}}^{con}\Delta_{\mathrm{Rac}}S\,, \tag{2.36}$$

where $T_{\mathrm{fus}}{}^{con}$ can be calculated iteratively from the appropriate Schröder-van Laar equation for $x = 0.5$.

Figure 2.9 shows my results of this calculation for the 36 racemic crystals listed by Leclercq *et al.*(85) plotted against the difference between the fusion temperatures of the racemic crystal and the calculated theoretical conglomerate fusion temperatures, $T_{\mathrm{fus}}{}^{Rac}$ - $T_{\mathrm{fus}}{}^{con}$. The figure shows the validity of the calculations because as the Gibbs energy change for forming the racemic crystal becomes unfavourable, the racemic fusion temperature drops below that of the conglomerate. This type of plot underlies the straight line correlations of Leclercq *et al.*(85)

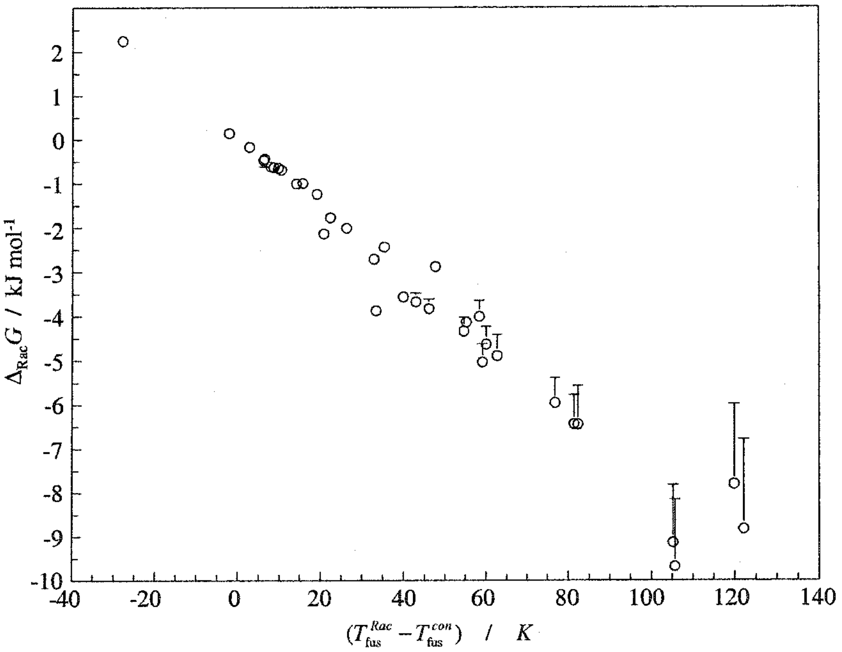

Figure 2.9 The Gibbs energy change for forming racemic crystals from conglomerate crystals versus their differences in fusion temperature. Calculated from the experimental data of Leclercq *et al.*(85) and with $\Delta_{\mathrm{fus}}C_p = 0$ J K^{-1} mol^{-1}. Error bars only show the propagated error using a positive solid-liquid heat capacity difference, $\delta\Delta_{\mathrm{fus}}C_p > 0$ J K^{-1} mol^{-1}.

In observing that $\Delta_{\text{fus}}C_p$ made little difference on the Gibbs energy change for forming a racemic crystal and that the Gibbs energy change was linear with $T_{\text{fus}}{}^{Rac} - T_{\text{fus}}{}^{con}$ for $\Delta_{\text{fus}}C_p = 0$ J K^{-1} mol^{-1}, Leclercq *et al.*$^{(85)}$ assumed that $\Delta_{\text{fus}}C_p = 0$ J K^{-1} mol^{-1} was a fair assumption. Note that this is a similar conclusion drawn from the discussion of the Schröder-van Laar equation and the Prigogine and Defay equation. Therefore, the final Gibbs energy, enthalpy and entropy changes for forming a racemic crystal from a conglomerate reported by Leclercq *et al.*$^{(85)}$ assumed that $\Delta_{\text{fus}}C_p$ was negligible. The error bars in figure 2.9 also show the effect of the propagation of error associated with the approximation of the difference in the heat capacities. This error has been estimated as follows:

For $X = G$, H or S,

$$\delta\Delta_{\text{Rac}}X = \sqrt{\left[\left(\frac{\partial\Delta_{\text{Rac}}X}{\partial\Delta_{\text{fus}}H^{R}}\right)^2 + \left(\frac{\partial\Delta_{\text{Rac}}X}{\partial\Delta_{\text{fus}}H^{Rac}}\right)^2\right]\delta\Delta_{\text{fus}}H^2 + \left(\frac{\partial\Delta_{\text{Rac}}X}{\partial\Delta_{\text{fus}}C_p}\right)^2 \delta\Delta_{\text{fus}}Cp^2}\ . \tag{2.37}$$

Because $T_{\text{fus}}{}^{Y} / T_{\text{fus}}{}^{Y'} \approx 1$ ($Y, Y' = Rac$, con or R) the enthalpy derivatives of $\Delta_{\text{Rac}}G$ are small,

$$\left(\frac{\partial\Delta_{\text{Rac}}G}{\partial\Delta_{\text{fus}}H^{R}}\right) = 1 - \frac{T_{\text{fus}}^{con}}{T_{\text{fus}}^{R}} \approx 0 \tag{2.38}$$

and

$$\left(\frac{\partial\Delta_{\text{Rac}}G}{\partial\Delta_{\text{fus}}H^{Rac}}\right) = \frac{T_{\text{fus}}^{con}}{T_{\text{fus}}^{Rac}} - 1 \approx 0 \quad , \tag{2.39}$$

but the heat capacity derivative is not,

$$\left(\frac{\partial\Delta_{\text{Rac}}G}{\partial\Delta_{\text{fus}}C_p}\right) = T_{\text{fus}}^{Rac} - T_{\text{fus}}^{R} - T_{\text{fus}}^{con}\ln\frac{T_{\text{fus}}^{Rac}}{T_{\text{fus}}^{R}}\ . \tag{2.40}$$

Thus the error in the Gibbs energy change is

$$\delta\Delta_{\text{Rac}}G = (T_{\text{fus}}^{Rac} - T_{\text{fus}}^{R} - T_{\text{fus}}^{con}\ln\frac{T_{\text{fus}}^{Rac}}{T_{\text{fus}}^{R}})\delta\Delta_{\text{fus}}C_p\ . \tag{2.41}$$

In figure 2.9, $\delta\Delta_{\text{fus}}C_p = +120$ J K^{-1} mol^{-1}, which is the large limit of the heat capacity range reported by Leclercq *et al.*(85) The error in fusion temperatures is small (including T_{fus}^{con}).

As expected, the errors in the calculation become larger as the temperature difference becomes larger, *i.e.*, the error in the heat capacity difference assumption becomes more significant. This error also was addressed by Leclercq *et al.*(85) However, while this error is small for the Gibbs energy changes, it is not small for the enthalpy and entropy changes for forming a racemic crystal from a conglomerate. In fact, this error is correlated with T_{fus}^{Rac} - T_{fus}^{con} for both calculations, as shown in figure 2.10.

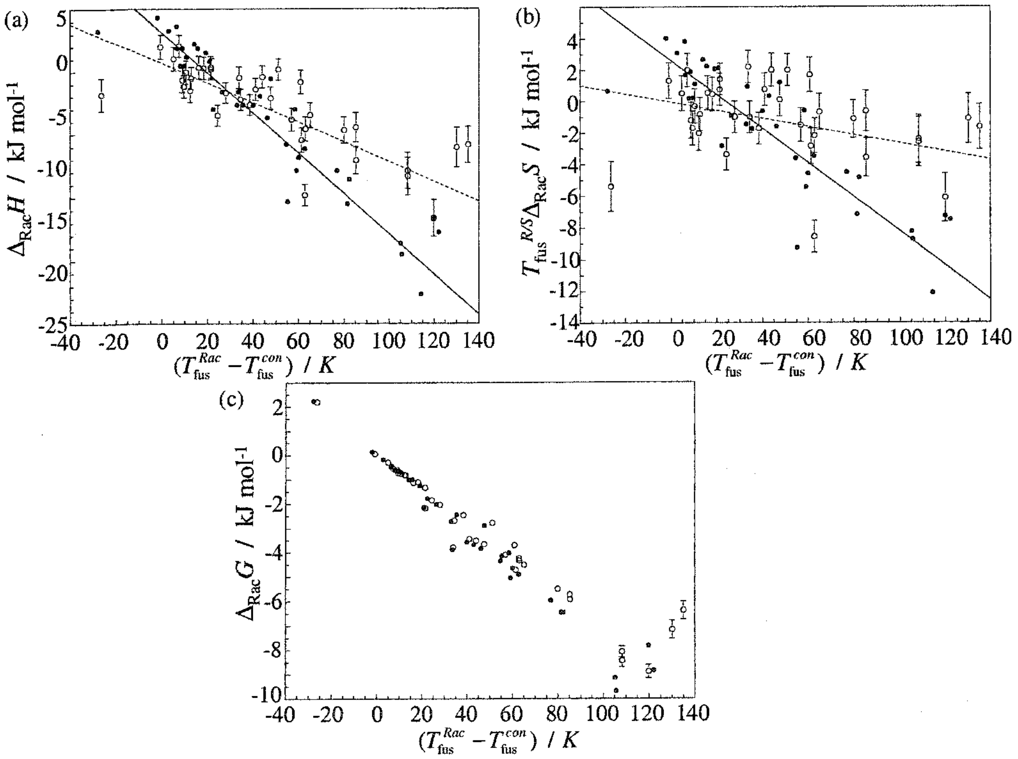

Figure 2.10 The calculated enthalpy, entropy and Gibbs energy changes for forming racemic crystals from conglomerate crystals versus their differences in fusion temperature. (a) enthalpy changes calculated using equation 2.34; (b) entropy changes calculated using 2.35; (c) Gibbs energy changes at the conglomerate fusion temperature calculated using 2.36. Two calculations using the compiled literature data from Leclercq *et al.*(85) are shown: -----, ○ $\Delta_{\text{fus}}C_p$ estimated as $\Delta_{\text{fus}}C_p = 100 \pm 20$ J K^{-1} mol^{-1} ——,● $\Delta_{\text{fus}}C_p = 0$ J K^{-1} mol^{-1}.

Figure 2.10 shows the calculated enthalpy, entropy and Gibbs energy changes (equations 2.34, 2.35 and 2.36) for the 36 racemic crystals listed by Leclercq *et al.*(85) now with $\Delta_{\text{fus}}C_p = 0$ J K^{-1} mol^{-1} and with $\Delta_{\text{fus}}C_p = 100 \pm 20$ J K^{-1} mol^{-1}. Note that as discussed previously, Leclercq *et al.*(85) have found that the heat capacity differences between the liquids and crystals range from $\Delta_{\text{fus}}C_p = 84$ to 117 J mol^{-1} K^{-1}. For thermodynamic values with $\Delta_{\text{fus}}C_p = 100 \pm 20$ J K^{-1} mol^{-1} in figure 2.10, the error bars for Gibbs energy changes have been calculated using equation 2.41 and the error bars for enthalpy and entropy changes have been calculated as follows. Using the same simplification as before, $T_{\text{fus}}{}^{Y} / T_{\text{fus}}{}^{Y'} \approx 1$ ($Y, Y' = Rac$, con or R), the fusion enthalpy change derivative of $T_{\text{fus}}{}^{con}\Delta_{\text{Rac}}S$ can be approximated by

$$\left(T_{\text{fus}}^{con}\frac{\partial\Delta_{\text{Rac}}S}{\partial\Delta_{\text{fus}}H^{R}}\right)^2+\left(T_{\text{fus}}^{con}\frac{\partial\Delta_{\text{Rac}}S}{\partial\Delta_{\text{fus}}H^{Rac}}\right)^2=\left(\frac{T_{\text{fus}}^{con}}{T_{\text{fus}}^{R}}\right)^2+\left(\frac{T_{\text{fus}}^{con}}{T_{\text{fus}}^{Rac}}\right)^2\approx 2. \qquad (2.42)$$

The fusion enthalpy change derivative of $\Delta_{Rac}H$ also is two,

$$\left(\frac{\partial\Delta_{\text{Rac}}H}{\partial\Delta_{\text{fus}}H^{R}}\right)^2+\left(\frac{\partial\Delta_{\text{Rac}}H}{\partial\Delta_{\text{fus}}H^{Rac}}\right)^2=2. \qquad (2.43)$$

The $\Delta_{\text{fus}}C_p$ derivatives are

$$T_{\text{fus}}^{con}\left(\frac{\partial\Delta_{\text{Rac}}S}{\partial\Delta_{\text{fus}}C_p}\right)=\ln\frac{T_{\text{fus}}^{Rac}}{T_{\text{fus}}^{R}} \qquad (2.44)$$

and

$$\left(\frac{\partial\Delta_{\text{Rac}}H}{\partial\Delta_{\text{fus}}C_p}\right)=T_{\text{fus}}^{Rac}-T_{\text{fus}}^{R}. \qquad (2.45)$$

Substituting these derivatives into equation 2.37, the errors can be calculated by

$$\delta T_{\text{fus}}^{con}\Delta_{\text{Rac}}S=\sqrt{4\delta\Delta_{\text{fus}}H^2+\left(T_{\text{fus}}^{con}\ln\frac{T_{\text{fus}}^{Rac}}{T_{\text{fus}}^{R}}\right)^2\delta\Delta_{\text{fus}}C_p{}^2} \qquad (2.46)$$

and

$$\delta\Delta_{\mathrm{Rac}}H = \sqrt{4\delta\Delta_{\mathrm{fus}}H^2 + \left(T_{\mathrm{fus}}^{Rac} - T_{\mathrm{fus}}^{R}\right)^2 \delta\Delta_{\mathrm{fus}}C_p^{\ 2}}\ . \tag{2.47}$$

In figure 2.10 the constant error for the heat capacity and fusion enthalpy change is estimated to be $\delta\Delta_{\mathrm{fus}}C_p = \pm 20$ J K^{-1} mol^{-1} and $\delta\Delta_{\mathrm{fus}}H = \pm 500$ J mol^{-1}. Note that the error propagation for the $\Delta_{\mathrm{fus}}C_p = 0$ J K^{-1} mol^{-1} case was more complicated, because the error is not symmetric about the calculated point, *i.e.*, $\delta\Delta_{\mathrm{fus}}C_p > 0$ for $\Delta_{\mathrm{fus}}C_p = 0$ J K^{-1} mol^{-1}. Also the error from the fusion enthalpy change and much of the heat capacity error cancels for the Gibbs energy change calculation because the entropy and enthalpy changes are derived from the condition that $\Delta_{\mathrm{fus}}H = T_{\mathrm{fus}}\ \Delta_{\mathrm{fus}}S$ at the melting point.

These equations and figure 2.10 show how the correlations of entropy or enthalpy changes are in error (large error) if the liquid and solid heat capacity difference is neglected. They also show why Leclercq *et al.*(85) have found $\Delta_{\mathrm{Rac}}S$ to be significant correlated with (T_{fus}^{Rac} - T_{fus}^{con}) when assuming that $\Delta_{\mathrm{fus}}C_p = 0$ J K^{-1} mol^{-1}. The correlation of $\Delta_{\mathrm{Rac}}S$ values is greatly reduced for $\Delta_{\mathrm{fus}}C_p = 100 \pm 20$ J K^{-1} mol^{-1} (such a complicated problem for such a simple equation, $\Delta G = \Delta H - T\Delta S$).

Recall the original objective of this thermodynamic derivation was to have an equation which can be used to determine if some temperature condition might lead to spontaneous resolution, *i.e.*, conglomerate crystal stability. For this purpose, it is the enthalpy and entropy changes that are just as important as the Gibbs energy change calculation. On a larger scale both Leclercq *et al.*(85) and Brock *et al.*(51) have discussed the importance of understanding why nature prefers racemic crystals over conglomerates and as shown here the liquid and solid heat capacity differences are not negligible in the overall calculations. Brock *et al.*(51) also have put together a large list for testing Wallace's rule and concluded that previous lists were somewhat small and biased. It is difficult to conclude from the small list of five $\Delta_{\mathrm{fus}}C_p$ values given by Leclercq *et al.*,(85) that the assumption of

$\Delta_{\text{fus}}C_p = 100 \pm 20$ J K^{-1} mol^{-1} is robust. In fact, the $\Delta_{\text{fus}}C_p$ values which have been collected for review in the literature(91) for achiral molecules show lower values. Figure 2.11 shows a histogram of these values with those measured by Leclercq *et al.*,(85) where it is apparent $\Delta_{\text{fus}}C_p = 100 \pm 20$ J K^{-1} mol^{-1} is possibly only internally valid for the systems measured by Leclercq *et al.*(85) These calculations are again performed for a larger compilation of fusion data and an empirical estimation of $\Delta_{\text{fus}}C_p$ in Chapter four.

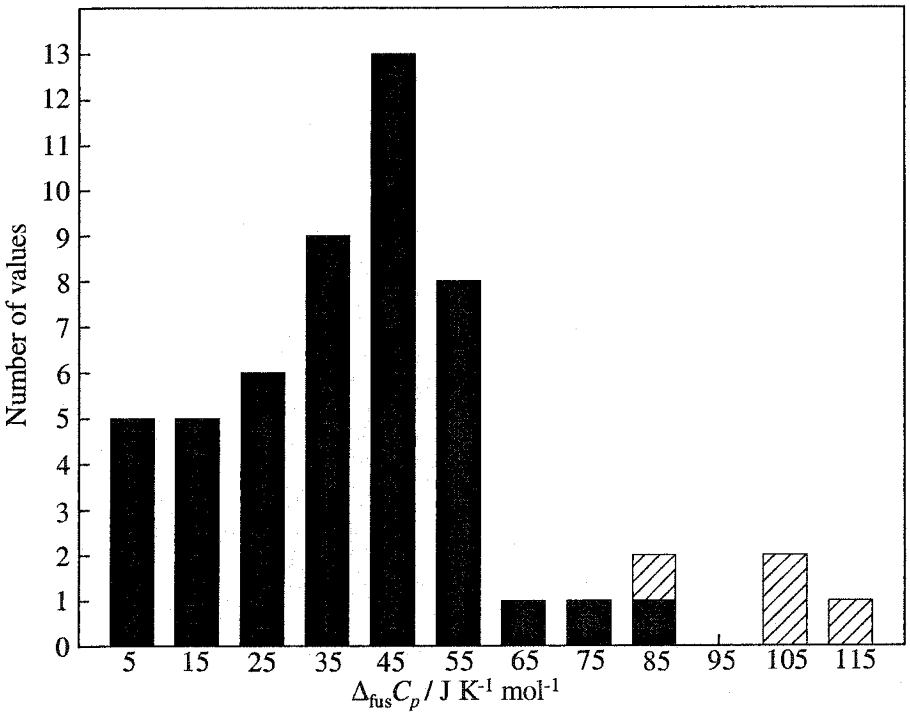

Figure 2.11 Histogram of $\Delta_{\text{fus}}C_p$ from the literature.(85, 91) ▨ are the data of Leclercq *et al.*(85) (chiral molecules) and ■ are from the compilation of Neau and Flynn(91) (achiral molecules).

It seems that Brock *et al.*(51) have referred to the derivations given in an early (1981) edition of in the book by Jacques *et al.*,(3) which they cite as originally given by Leclercq *et al.*(85) Leclercq *et al.*(85) have suggested that their calculations are only valid near the fusion temperatures of the compounds in their list. Leclercq *et al.*(85) also have discussed the cases in table 2.3 along with the temperature dependence of the error associated with the heat capacity assumptions. This error was stressed by Jacques *et al.*(3) in the final chapters of the 1994 edition of this book.(3)

Heat capacities and $\Delta_{\text{fus}}C_p$ values are less available in the literature than enthalpies and entropies of fusion. Heat capacity changes for solids and liquids also are difficult to predict well. Most authors assume $\Delta_{\text{fus}}C_p = 0$ J K^{-1} mol^{-1} while others have suggested that a better approximation is $\Delta_{\text{fus}}C_p \approx \Delta_{\text{fus}}S$.(92) The discussion here shows that predicting and/or estimating these differences is important to calculating the thermodynamics of enantiomeric crystals and to the subsequent work presented in this thesis. For this purpose, a semi-empirical estimation of $\Delta_{\text{fus}}C_p$, based in part on molecular symmetry, has been developed in Chapter four. However, before returning to this subject, it was useful to investigate the theoretical and empirical relationships for ideal gas molecules in the next chapter, as these relationships turn out to be applicable to estimations concerning $\Delta_{\text{fus}}C_p$.

In summary, there is a lack of temperature dependent thermodynamic information for racemic and optically pure crystals. It would seem that the speculations made by Leclercq *et al.*(85) and Brock *et al.*(51) can benefit from $\Delta_{\text{fus}}C_p$ values to extend entropic or enthalpic information to temperatures removed from the fusion temperatures. Either a large number of $\Delta_{\text{fus}}C_p$ values must be measured or a method of estimating the $\Delta_{\text{fus}}C_p$ values is required. In addition, low-temperature heat capacity experiments would assist in understanding entropic differences by choosing an alternative thermodynamic cycle for calculation (the lower cycle figure 2.8).

3 ESTIMATION OF IDEAL GAS THERMODYNAMIC PROPERTIES

> *Thermodynamics is a funny subject. The first time you go through it, you don't understand it at all. The second time you go through it, you think you understand it, except for one or two small points. The third time you go through it, you know you don't understand it, but by that time you are so used to it, it doesn't bother you any more.*
>
> Arnold Sommerfield

3.1 Introduction to classical and empirical estimation methods

Intramolecular molecular degrees of freedom are considered many times in this thesis. It proved necessary to consider ideal gas heat capacities and entropies by performing some exploratory calculations. These exploratory calculations evolved into a study of semi-empirical estimations of molecular ideal gas properties. For this reason, it is convenient to discuss some thermodynamic properties of ideal gases, before returning to the subject of enantiomeric crystals and their stability relationships.

In condensed phases, *i.e.*, liquids and solids, the intermolecular and intramolecular contributions to thermodynamic properties are coupled. This coupling adds a significant mathematical complexity to any interaction model, *i.e.*, it is a many-body-problem. Therefore, additive or uncoupled contributions are often assumed. Many models assume a separation of internal (intramolecular) and external (intermolecular) contributions. If internal contributions are not coupled with external contributions then the internal contributions are the same for a molecular ideal gas, real gas, liquid and solid. In this way, a coupling in a liquid or solid can be treated as a perturbation to the ideal gas property.

This chapter will focus on the heat capacity of an ideal gas. Because heat capacities are second temperature derivatives of fundamental thermodynamic state functions, the values provide fundamental thermodynamic information, *e.g.*,

$$H = H_0 + \int_0^T C_p dT, \tag{3.1}$$

$$S = S_0 + \int_0^T \frac{C_p}{T} dT, \tag{3.2}$$

and

$$U = U_0 + \int_0^T \frac{C_V}{T} dT. \tag{3.3}$$

Here U, S, and H are the internal energy, entropy and enthalpy of a system and U_0, S_0 and H_0 are these values at $T = 0$ K.

Experimentally, ideal gas heat capacities can be evaluated by extrapolating real gas heat capacity data to $p = 0$ atm (infinite dilution) by using various theoretically and empirically based equations of state. One of the simplest of these is the van der Waals equation. From the experiment ideal gas heat capacities, both correlation type and theoretical equations of state can be tested. One common aim of a robust equation of state is the prediction of thermodynamic quantities at other temperatures and pressures, either by extrapolation or interpolation. Given a good equation of state, another aim is to predict how the properties of other molecules (not studied experimentally) would behave. Two useful methods will be discussed here: the group additivity method and the theoretical statistical mechanics method. These methods are useful for modelling molecules which have not or cannot be measured in the gas form, *e.g.*, amino acids are important molecules which decompose before their melting point; therefore, gas properties are difficult to measure.

3.2 Additivity

Additivity is an empirical correlation method. Molecules of known structure and properties can be grouped into categories having particular molecular groups, bonds or atoms. For example, piperidine contains five $-CH_2-$ groups and one -NH- group. Through statistical correlations of properties for many molecules containing these same groups, the property contribution for each group can be found and used to estimate the property for piperidine. Property X for piperidine can be calculated by $X = 5 \cdot X(-CH_2-) + X(-NH-)$, provided that the molecules used to parameterise the additivity scheme contained both these groups. Non-additive contributions are often used with additivity schemes to account for molecular properties which are understood theoretically; thus, many molecular additivity schemes are semi-empirical.

Benson and Buss(93) have discussed the hierarchy of additivity approximation methods. From the simplest to the most robust, Benson and Buss(93) define these approximations as; (1) zero-order: additivity of atomic properties, (2) first-order: additivity of bond properties, (3) second-order: additivity of group properties. Higher orders can be devised where nearest neighbour contributions are taken into account. It should be noted that the additivity schemes of Benson and Buss(93) and Benson *et al.*(94) (referred to as the Benson and Buss method)(95) also account for isomerisation and rotational symmetry semi-empirically. Additivity parameters have been described for constant pressure heat capacities, formation entropies and formation enthalpies. To improve the estimations, in addition to additive parameters, symmetry numbers must be included to calculate the formation entropy of an ideal gas by the Benson and Buss method.

Through statistical mechanics, the entropy of a molecule requires knowing something about the indistinguishability of complete or internal molecular rotations, discussed further in Section 3.3. When using the Benson and Buss method, non-additive molecular symmetry contributions are applied to estimated entropies by a factor of $-R\ln\sigma$, where σ is the number of indistinguishable permutations that can be derived by rotating either end groups or the entire molecule.(95) Here inversion is not allowed. The σ value also is split into two contributions, σ_{int} and σ_{ext}, where σ_{ext} is the molecular rotational symmetry number and σ_{int} is number of indistinguishable possible internal rotations or permutations. The total number of indistinguishable permutations is then given by,

$$\sigma = \sigma_{\text{ext}}\sigma_{\text{int}} \,. \tag{3.4}$$

How one arrives at these permutations or symmetry numbers is outlined by Benson(96) and others(94,97) who have regularly reviewed and evaluated the method. Some examples are given in table 3.1. Note that all methyl groups are considered rotating when obtaining σ_{ext}.

Table 3.1 Examples of the symmetry numbers used in the additivity scheme of Benson and Buss.(93)

Formula	Name	σ_{ext}	σ_{int}	σ
CH_4	methane	4	3	12
C_3H_9N	trimethylamine	3	3^3	81
$C_5H_{11}N$	piperidine	1	1	1
C_6H_6	benzene	(6)(2)	1	12
C_7H_8	toluene	2	3	6
C_9H_{12}	1,3,5-trimethylbenzene	2	3^4	162
C_9H_{12}	1,2,3-trimethylbenzene	2	3^3	54
$C_9H_{12}O$	1,2,4-trimethylbenzene	1	3^3	27

All molecular names have been cross-referenced to Chemical Abstract names, CA, in Appendix B.

The Benson and Buss method also uses several ring contribution terms depending on the class of molecule and a mixing entropy factor of $R\ln\eta$ to predict the contribution to estimate entropy for the presence of η different optical isomers.(95) The latter prediction also has a statistical mechanical origin. Provided that all conformers are treated as though they were of the same energy, one can use Boltzmann's famous equation,

$$S = R\ln\Omega\,, \tag{3.5}$$

where Ω is the number of distinguishable conformations of equal probability. A more rigorous calculation would reveal different potential energies for individual permutations, which would lead to conformational heat capacity contributions. Note that equation 3.5 already has been used in Section 2.2.1 for defining the entropy of mixing.

Of course there are many other group additivity schemes(96,97,98,99,100,101) which also aim to make reasonable predictions of ideal gas properties. However, like any other empirical correlation model,(102) they all suffer from external validity problems. The input data or calibration values must be composed of molecules similar to those that the user has an interest in predicting. Users must take care to choose the appropriate method or scheme which would best predict the property for the molecule of interest. Furthermore, some methods are more complicated than others. Statistical mechanics is another method to predict ideal gas properties and this method partially justifies why additivity schemes work.

3.3 Statistical mechanical methods

3.3.1 Rotation and translation

Additivity is predominantly concerned with empirical estimations of thermodynamic properties; however, one can explain the overall success of additivity schemes with vibrational temperatures and statistical mechanics. The symmetry numbers given in equation 3.4 also have a statistical mechanical origin.

The rotational partition function for a nonlinear polyatomic ideal gas molecule (assumed a rigid rotator) is given by(103)

$$Q_{\mathrm{rot}} = \frac{8\pi^2(8\pi^3 I_A I_B I_C)^{1/2}(kT)^{3/2}}{\sigma h^3}, \tag{3.6}$$

where I_A, I_B, and I_C are the three principal moments of inertia, k is the Boltzmann constant, h is Planck's constant, and σ is the external rotational symmetry number described previously. Using the three moments of inertia one can define three rotational temperatures by

$$\theta_i = \frac{h^2}{8\pi^2 I_i k} \text{ for } i = A, B, C, \tag{3.7}$$

which gives

$$Q_{\mathrm{rot}} = \frac{\pi^{1/2}}{\sigma}\left(\frac{T^3}{\theta_A\theta_B\theta_C}\right)^{1/2}. \tag{3.8}$$

The symmetry number accounts for allowable rotational quantum numbers due to the symmetry of the rigid rotor. The entropy and heat capacity are given by

$$\frac{S_{\mathrm{rot}}}{R} = \frac{3}{2}\ln T - \frac{1}{2}\ln\theta_A\theta_B\theta_C - \ln\sigma + \frac{3}{2} + \frac{1}{2}\ln\pi \tag{3.9}$$

and

$$C_{V,\mathrm{rot}} = \frac{3}{2}R. \tag{3.10}$$

Note that equations 3.6 through to 3.10 are approximations which are not good at low temperature and 3.10 is the equipartition rotational heat capacity.

The translational heat capacity is $C_{V,\mathrm{trans}} = 3/2\ R$. The constant pressure heat capacity can be derived from the constant volume heat capacity using

$$C_p - C_V = \frac{\alpha^2 VT}{\beta_T}, \tag{3.11}$$

where α is the thermal expansion coefficient,

$$\alpha = \frac{1}{V}\left(\frac{\partial V}{\partial T}\right)_P, \tag{3.12}$$

and β_T is the isothermal compressibility,

$$\beta_T = -\frac{1}{V}\left(\frac{\partial V}{\partial P}\right)_T. \tag{3.13}$$

For an ideal gas, C_p-$C_V = R$. Thus the total external, *i.e.*, non-internal vibrational, contributions to the heat capacity of an ideal gas give $C_{V,ext} = 3\,R$ and $C_{p,ext} = 4\,R$.

The translational entropy is given by the Sackur-Tetrode equation:(103)

$$\frac{S_{\text{trans}}}{R} = \frac{5}{2} + \frac{3}{2}\ln\frac{2\pi k}{h^2} - \frac{5}{2}\ln N_A + \ln V + \frac{3}{2}\ln T + \frac{3}{2}\ln M\,, \tag{3.14}$$

where V is the volume of a cubic box containing the ideal gas (free volume) and M is molar mass.

3.3.2 Internal vibration and the harmonic oscillator approximation

A full description of internal contributions contains both the rotational and vibrational partition function. However, if the coupling contribution is ignored, the two are separable, leading to equation 3.8 and a partition function for internal vibrations. The first estimation is often calculation through the statistical mechanical partition function for a one-dimensional harmonic oscillator:

$$Q_{\text{vib}} = \frac{1}{1 - e^{h\nu/kT}}, \tag{3.15}$$

where ν is the vibrational frequency. Further corrections for interactions such as vibrational anharmonicity and rotational stretching also can be applied as perturbations to equation 3.15.

The vibrational heat capacity for an ideal gas with n harmonic oscillators is given by

$$C_{V,\mathrm{vib}} = R\sum_{i=1}^{n} \frac{x_i^2 e^{x_i}}{(e^{x_i}-1)^2}, \tag{3.16}$$

where x_i is defined by

$$x_i = \frac{h\nu_i}{kT}. \tag{3.17}$$

The quantity $h\nu/k$ is commonly called the vibrational temperature.

3.3.3 An example of an anharmonic effect: internal rotation

Internal rotation is an example of an effect which causes the harmonic oscillator approximation to fail at high temperatures. Pitzer(104-107) has made an approximation to the restricted internal rotation by considering the potential function

$$\Psi(\phi) = \frac{1}{2}\Psi_0(1-\cos n\phi), \tag{3.18}$$

where Ψ_0 is the potential barrier to rotation, ϕ is the relative rotation angle and n is the reduced symmetry number of the rotating group. Both the quantum mechanical and classical expressions can be numerically solved for this potential using a reduced moment of inertia.(103,108)

Briefly, there are three temperature regions of interest, as shown in figure 3.1. The first region is for $kT \ll \Psi_0$ where a functional group is vibrating as a harmonic oscillator, *i.e.*, the normal torsional mode, equation 3.15. The second region is where $kT \approx \Psi_0$ and the motion is neither fully vibrational nor rotational. The third region is where $kT \gg \Psi_0$ and the group is freely rotating (equation 3.10 for one degree of freedom). As the temperature rises from $T = 0$ K, the heat capacity behaves as a harmonic oscillator vibrational mode, $C_V(\max) = R$, then goes through a transition and then becomes freely rotating, $C_V = \frac{1}{2}R$. Thus, if a molecule contains an internal rotator and the harmonic oscillator approximation is applied, the predicted heat capacity can be expected to poor in region 2 and overestimated in region 3.

Note that the Pitzer model is only one example of internal molecular flexibility and it only describes a molecule with one rotor or two symmetric tops, such as ethane. Molecules with more possible internal rotations or non-symmetrical internal rotations, such as longer chain *n*-alkanes, require more complicated models.(103,109,110) The study of rotational contributions to ideal gas properties is an extensive field and very few models are both simple and applicable to a large number of molecules. However, all these models contain internal symmetry numbers. In addition, some internal conformational contributions also seem to be additive or modelled well empirically.(102,111)

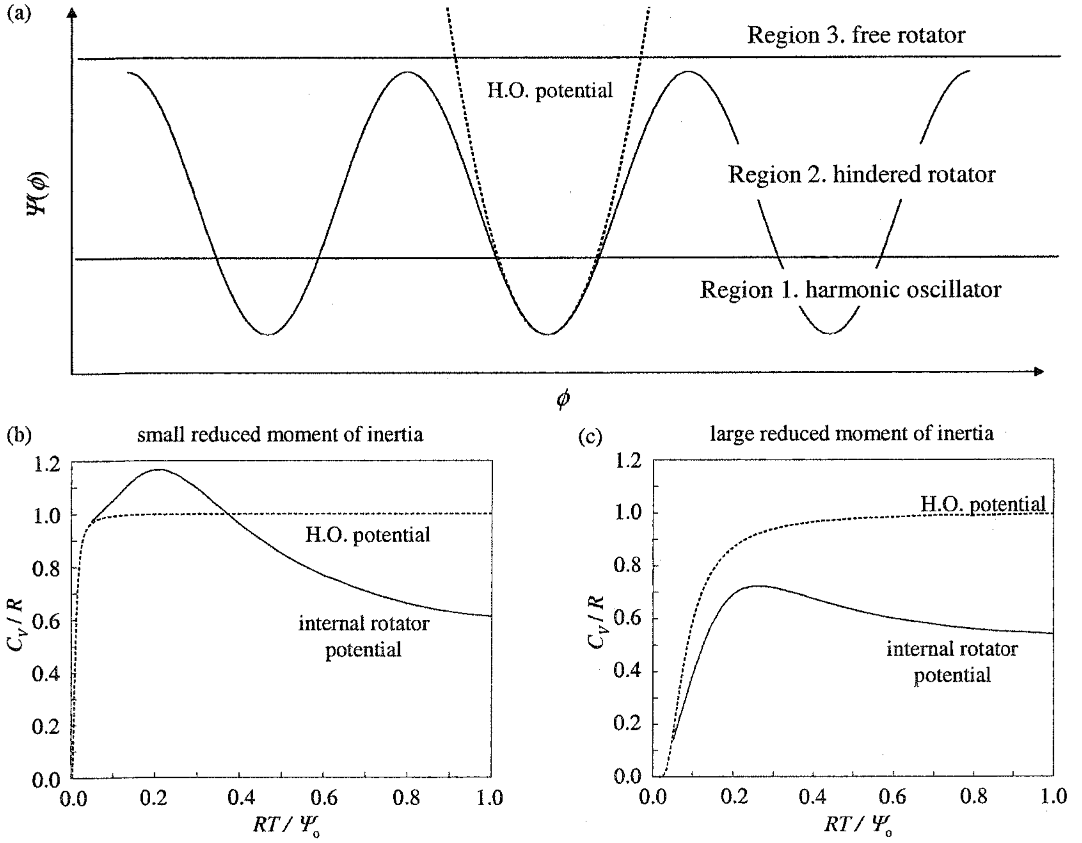

Figure 3.1 A schematic of the (a) Pitzer internal rotator potential and the ((b) & (c)) calculated constant volume heat capacities of two internal rotators.(103)

3.3.4 An example of computation using fundamental vibrational frequencies

With the rotational, translational and vibrational heat capacity contributions known, the heat capacity for any one configuration of an ideal gas can be calculated. This provides yet another method to predict the heat capacity of an ideal gas. As an example one can calculate the constant pressure heat capacity of piperidine, $C_5H_{10}NH$, which has no internal rotations, but does have two conformations. The hydrogen on the nitrogen can be in either the axial and equatorial orientations for the chair conformation of piperidine.

The ideal gas constant pressure heat capacity has been calculated here by $C_p = C_{V,\mathrm{vib}} + 4R$, where $C_{V,\mathrm{vib}}$ was calculated using the experimental vibrations of Vedal *et al.*(112) and equation 3.16. Hossenlopp and Archer(113) have measured the isobaric heat capacities of gaseous piperidine at $T = 368.2$, 389.2, 427.2, 463.2 and 500.2 K and at $p = 25.33$, 50.67 and 101.3 kPa. The real gas heat capacities were then used to obtain the ideal gas quantities via a least squares fitting of a virial equation. These experimentally derived ideal gas values, $C_{p,\mathrm{exp}}$, are shown in figure 3.2 along with the calculated ideal gas heat capacity.

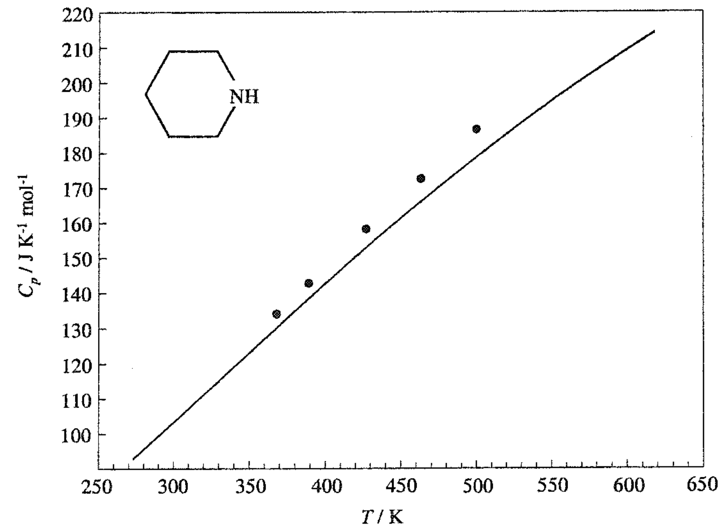

Figure 3.2 The ideal heat capacity of piperidine. —— has been calculated using the vibrational frequencies of Vedal *et al.*(112) and ● are the limiting pressure values, $p \rightarrow 0$ atm, reported by Hossenlopp and Archer.(113)

The calculated heat capacity differences between the equatorial and axial piperidine conformations are very small, $C_{V,\mathrm{calc}}$(equatorial)-$C_{V,\mathrm{calc}}$(axial) < 0.15 J K^{-1} mol^{-1} for $T = 273$ to 618 K. As shown by figure 3.2, the experimental heat capacities values are above the calculated heat capacity ($C_{p,\mathrm{exp}} - C_{p,\mathrm{calc}} = 5.6 \pm 3.3$ J K^{-1} mol^{-1}). This positive deviation is expected, because the vibrations have been assumed to be harmonic and there is a conformational heat capacity contribution, *i.e.*, there is a small change in equatorial-axial equilibrium with temperature. Even with this discrepancy, figure 3.2 shows the largest contribution to the heat capacity can be estimated using vibrational frequencies ($C_{p,\mathrm{calc}} / C_{p,\mathrm{exp}} > 95$ %). In addition, the vibrational contribution is more than *ca.* 70% of the total experimental heat capacity for a relatively small molecule over a large temperature range. Even at $T = 650$ K, the vibrational heat capacity has not exceeded 40% of the theoretical maximum value of $C_p = 45\,R$. At higher temperatures the vibrational heat capacity would be even more dominant. The dominance of the vibrational heat capacity contributions would only become larger for molecules containing more atoms.

The data of Vedal *et al.*(112) also show only small differences between the vibrational frequencies of vapour, liquid and crystalline piperidine. This is not uncommon as fundamental frequencies do not change a large amount when transferring from phase to phase. Note that this generalisation is in agreement with the uncoupled intra- and intermolecular contribution assumption and the separation of the rotational and vibrational partition functions. The frequencies known to change significantly, either by splitting or shifting, are those perturbed by hydrogen bonding and low internal torsional frequencies. The point here is that the error in the vibrational heat capacity is not large and some cancellation of error can be expected.

If the average error for the fundamental vibrational frequencies, $\delta\nu$, is known, then the error in the calculated heat capacity can be estimated by

$$\delta C_{V,\text{vib}} = \frac{100Rhc}{kT}\sqrt{\delta \nu^2\left[\sum_{i=1}^{n}\frac{x_i^{\,2}e^{2x_i}(x_i e^{x_i}+x_i-2e^{x_i}+2)^2}{(e^{x_i}-1)^6}\right]}, \tag{3.19}$$

where x_i is defined by equation 3.17. The estimated error for the calculated vibrational heat capacity of piperidine (equatorial) is shown in figure 3.3 for $\delta\nu = \pm 50\ \text{cm}^{-1}$. Note that $\delta\nu = \pm 50\ \text{cm}^{-1}$ is grossly overestimating the change in frequencies for a piperidine molecule going from a vapour to a crystal.

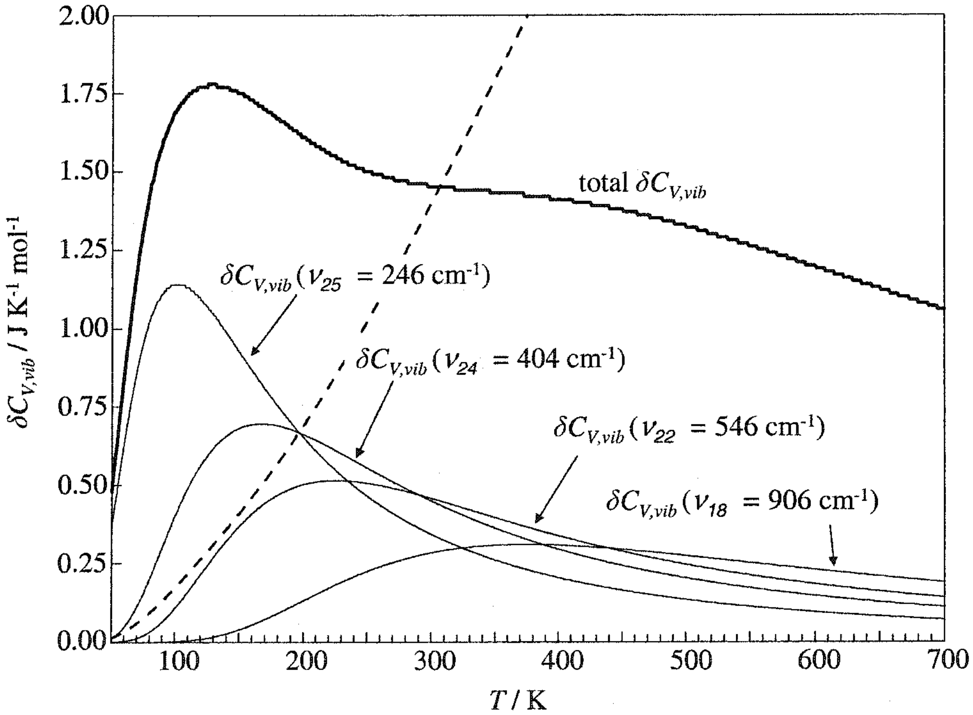

Figure 3.3 The effect of frequency uncertainty of $\delta\nu = 50\ \text{cm}^{-1}$ on the error in vibrational heat capacity, $\delta C_{V,\text{vib}}$, for various modes of piperidine. Vibrational frequencies are those of Vedal *et al.*(112) and ------ is 2% of the total vibrational heat capacity.

Figure 3.3 shows the estimated error from four fundamental frequencies corresponding to vibrational temperatures of 354, 581, 786 and 1304 K. Most of the error occurs at $T < 300$ K, because the low-frequency vibrations within equation 3.13 are approaching the maximum value of $C_{V,\mathrm{vib}} = R$, *i.e.*, $\partial C_{V,\mathrm{vib}}/\partial v$ goes through a maximum well below $T = 300$ K. Thus, error in low frequencies is dominant below room temperature. The relative error for higher vibrational temperatures is broad and subsequently small for higher frequencies. With the large low-temperature error, one can expect a significant error in formation entropies and enthalpies. In addition, all frequencies are significant in calculation of a zero point energy. However, frequency estimations within *ca.* 50 cm^{-1} are good for estimating internal heat capacities at higher temperatures. Using $\delta v = \pm 50\ \mathrm{cm}^{-1}$, the error in vibrational heat capacity is estimated to be $\delta C_{V,\mathrm{vib}} / C_{V,\mathrm{exp}} = 1.1$ to 1.8 % for the temperature range shown in figure 3.2.

This example calculation for piperidine shows that apart from additivity schemes, vibrational frequencies can be used to estimate the ideal gas heat capacities of single isomer molecules without considering conformational effects, which are often a small fraction of the total heat capacity. However, just as experimental heat capacities are not available for many molecules, complete molecular vibration assignments also are rare. In many cases, one must choose to use methods to estimate fundamental vibrational frequencies, such as molecular mechanics or *ab initio* calculations.(114,115) To extend the calibration data, some newer additivity schemes are parameterised using high level *ab initio* calculations.(116) Provided that the same level of theory is employed throughout, *ab initio* calculations can yield qualitatively more consistent predictions.(115) Curiosities about the quantitative estimation of heat capacities lead to some exploratory calculations in this area. Note that one question raised for subsequent work in this thesis was 'can internal heat capacities for condensed phases be estimated by *ab initio* methods?'

3.4 Introduction to exploratory *ab initio* calculations

Since 1958, when Benson and Buss(93) first proposed their additivity scheme, computers have become faster and *ab initio* calculations are better and more readily available. Therefore, provided that the frequencies are sufficiently accurate, one can use the *ab initio* frequencies for a single minimised structure. From the piperidine example, frequencies above *ca.* 250 cm^{-1} and within $\delta\nu = \pm 50\ \mathrm{cm}^{-1}$ of the real values would be sufficient for estimating internal heat capacities used within semi-empirical equations of state. Error in lower-frequencies would have little impact on the heat capacity above room temperature. Indeed, many current molecular spectroscopy studies utilise *ab initio* frequencies to help with frequency assignments. Some exploratory calculations and comparisons were performed to evaluate the quantitative value of ideal gas heat capacities using simple *ab initio* methods and the harmonic oscillator approximation.

Three types of comparisons were made: (1) a comparison of calculated heat capacities using *ab initio* predicted zero point vibrations versus the experimental fundamental vibrations of piperidine was made; (2) the heat capacities using low-level *ab initio* vibrational frequencies, compared to those of a recent evaluation of additivity methods;(97) (3) the heat capacities of some small to medium *n*-alkanes using low-level *ab initio* vibrational frequencies, compared to experimental and *ab initio* calculations using uncoupled rotational corrections.(117)

All *ab initio* calculations were performed using the Gaussian98® package(118) for Windows on an Intel® Pentium® IV 2.4 GHz processor. Abbreviations for the level of theory have been defined in the list of symbols and abbreviations, page xix. Vibrational calculations were performed assuming only the harmonic oscillator approximation and taking the zero point vibrations as the fundamental frequencies. All frequencies have been scaled using the factors of Scott and Radom.(119)

3.5 *Ab initio* results and discussion

3.5.1 Piperidine

In 1991, Scott and Radom(119) evaluated and reported a set of scaling factors for zero point vibrational frequencies for 19 levels of theory.(120-128) The data set of Scott and Radom included 1066 vibrational frequencies (excluding degeneracies). These scaling factors are shown in table 3.2 with the respective root-mean-square deviations reported by Scott and Radom(119) and the root-mean-square deviations for the 45 experimental frequencies of axial piperidine.(112)

Table 3.2 Frequency scaling factors and root-mean-square deviations of Scott and Radom.(119)

Method	Scale factor	rms_{ov} / cm^{-1}	rms_{pip} / cm^{-1}
AM1	0.9532	126	54
PM3	0.9761	159	68
HF/3-21G	0.9085	87	34
HF/6-31G(d)	0.8953	50	20
HF/6-31+G(d)	0.8970	49	20
HF/6-31G(d,p)	0.8992	53	21
HF/6-311G(d,p)	0.9051	54	22
HF/6-311G(df,p)	0.9054	56	22
MP2-fu/6-31G(d)	0.9427	61	27
MP2-fc/6-31G(d)	0.9434	63	28
MP2-fc/6-31G(d,p)	0.9370	61	-----
MP2-fc/6-311G(d,p)	0.9496	60	-----
QCISD-fc/6-31G(d)	0.9537	37	25
BLYP/6-31G(d)	0.9945	45	31
BLYP/6-311G(df,p)	0.9986	42	34
BP86/6-31G(d)	0.9914	41	29
B3LYP/6-31G(d)	0.9614	34	25
B3P86/6-31G(d)	0.9558	38	26
B3PW91/6-31G(d)	0.9573	34	26

rms_{ov} is the overall root-mean-square deviation for the 1066 fundamental vibrations of Scott and Radom(119) and rms_{pip} is the root-mean-square deviation from the 45 experimental fundamental frequencies of Vedal *et al.*(112) Two Møller-Plesset theory levels were not available due to limited hard-disk scratch space.

Table 3.2 shows that at a Hartree-Fock theory level and basis sets of 6-31G(d) and 6-31+G(d), the root-mean-square vibrational error is within 50 cm^{-1}. In addition, the many variations of density functional theory, DFT, also are within the *ca.* 50 cm^{-1} level discussed previously. Scott and Radom also have reported scaling factors for internal vibrational enthalpies and entropies, which unlike higher temperature heat capacities, are susceptible to errors in the lower frequency region. They also have determined different scaling factors for lower frequencies, to bring lower frequencies closer to real values. This is necessary for entropies and enthalpies of formation, but as discussed before, the error in the higher temperature heat capacity is less significant. From Scott and Radom's analysis and considering accuracy and computational cost, the best theory level seems to be B3LYP/6-31G(dp).

Selected heat capacity differences, $C_p - C_{p,\mathrm{calc}}$(exp. frequencies), for piperidine are shown in figure 3.4. As expected, from the discussion of vibrational errors, figure 3.4 shows that the *ab initio* heat capacity predictions are very close to those predicted from experimental frequencies.

Alternatively one can use the Benson and Buss additivity scheme, however, this method requires temperature-dependent contributions for ring compounds. In earlier compilations of group and ring contributions, the ring contributions for piperidine were not available. The 1998 release of CHETAH™ Version 7.2(129) uses piperidine ring factors of -24.7 to 17.58 J K^{-1} mol^{-1} over the temperature range of $T = 298$ to 1000 K (the correction is -3.77 J K^{-1} mol^{-1} at $T = 600$ K). These contributions are much larger than the error in the *ab initio* predictions made here. Thus at an earlier date, when the ring contributions were not available, the error in the estimated heat capacities would have been much larger than the uncorrected *ab initio* predictions.

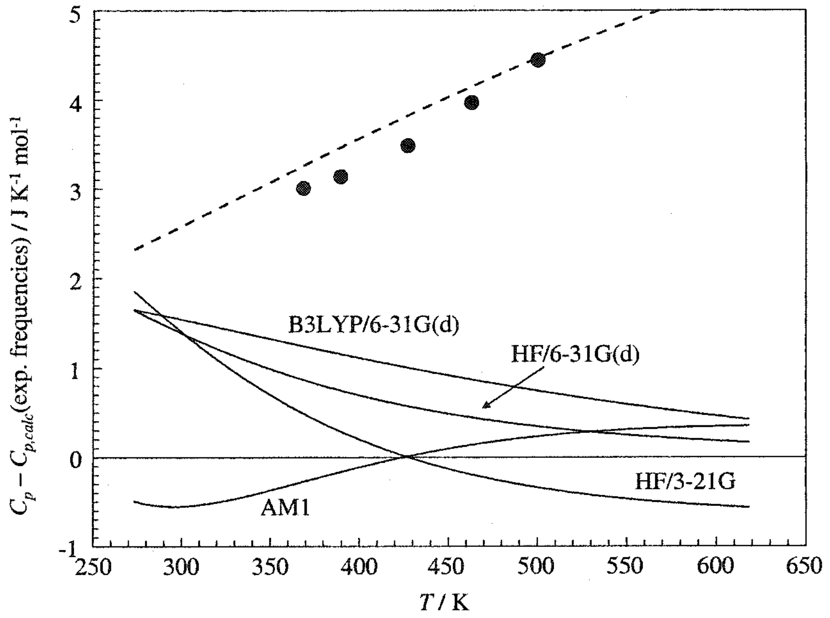

Figure 3.4 Results for piperidine heat capacity as a function of temperature.
●, the difference between the experimental ideal gas heat capacity(113) and the heat capacity calculated from experimental vibrational frequencies;(112) — values marked with different levels of *ab initio* theory corresponds to the difference between the heat capacity calculated from vibrational frequencies at that level of theory, and the heat capacity calculated using experimental vibrational frequencies;(112) -----, 2.5% of the total heat capacity.

3.5.2 A comparison to various estimated and literature ideal gas heat capacities

In the 5th edition of *The properties of gases and liquids* (2001), Poling and Prausnitz(97) evaluated the additivity schemes of Benson and Buss,(93,129) Joback,(98,130) and Constantinou and Gani.(101) Based on 27 molecules of various connectivity, they were able to make recommendations for predicting ideal gas heat capacities.(97) All three methods were found to be adequate at estimating heat capacities (*ca.* 10% accuracy) at $T = 298.15$ and 700 K. Benson's method was recommended as the highest accuracy method; however, the methods of Joback(98,130) and Constantinou and Gani(101) are less complicated.

The experimental heat capacities and relative errors, $((C_{p,\text{calc}}\text{-}C_{p,\text{exp}})/C_{p,\text{exp}})$, given by the evaluation of Poling and Prausnitz(97) are shown in table 3.3. In addition table 3.2 shows the relative errors for the heat capacities of these molecules, as calculated using zero-point vibrations at the AM1, HF/3-21G and B3LYP/6-31G(d) theory levels. All conformational contributions have been neglected; therefore the vibrations are applicable to only one minimised structure.

Figure 3.5 shows a box-and-whisker plot of the relative error values reported in table 3.3. The average deviations of heat capacities at all three *ab initio* theory levels are comparable to those of the additivity schemes. At the lower temperature of $T = 298$ K, the *ab initio* methods are slightly better than the methods of Joback(98,130) and Constantinou and Gani(101) and slightly poorer than the Benson and Buss method.(93,129) The *ab initio* methods show fewer outliers than the additivity methods. This is likely due to the internal consistency of the theory levels as compared to the empirical additivity methods. At $T = 700$ K, the deviations of *ab initio* methods and Benson and Buss method are similar.

The *ab initio* results are better than those from additivity methods for propanenitrile, octafluorocyclobutane, 3-methylthiophene and 2-methyl-2-butanethiol. The average absolute deviation from the experimental heat capacity is 1.7% from *ab initio* methods, and 7.0% from additivity approaches for those four compounds. Indeed, within the 27 benchmark compounds, where additivity methods show an average deviation of more than about 2%, *ab initio* methods show a marked improvement.

Some of the extreme data in figure 3 can be explained by neglect of conformational effects. For example, *n*-heptane has internal rotation which would be expected to cause significant deviation from the harmonic oscillator assumption in the *ab initio* methods; the relative error in the heat capacity at T = 298 K is *ca.* 1% using the additivity methods and *ca.* -7% using the *ab initio* methods.

Table 3.3 Relative error in % of some estimated ideal gas heat capacities.

Formula	Name	$C_{p,\mathrm{exp}}$ / J K^{-1} mol^{-1}		Benson		Joback		C/G		AM1		HF/3-21G		B3LYP/6-31G(d)	
	T / K	298	700	298	700	298	700	298	700	298	700	298	700	298	700
C_2HCl_3	trichloroethene	80.25	109.30	0.9	-0.3	-4.0	-4.7	-1.5	0.0	-1.6	-0.7	1.3	-0.1	1.2	0.4
$C_2H_4F_2$	1,1-difluoroethane	68.49	117.53	-2.2	-0.5	-1.1	-1.2	0.3	2.0	-2.3	0.2	-2.3	-1.0	-1.5	0.2
C_3H_5N	propanenitrile	73.92	126.62	-1.2	-0.5	8.7	12.8	-0.4	-0.6	-4.1	0.8	-4.8	-1.0	-1.9	0.5
C_3H_8	propane	73.76	143.11	0.3	-0.1	1.1	-0.5	-0.9	-0.7	-2.3	2.2	-3.9	-0.4	-2.5	0.8
C_3H_9N	trimethylamine	91.77	177.08	0.3	-0.1	0.0	-0.7	0.1	0.1	-1.5	0.5	-3.1	-2.0	-3.0	-1.0
C_4F_8	octafluorocyclobutane	156.08	236.99	-12.9	-0.8	-13.8	0.7	3.1	13.0	3.2	-1.0	3.8	0.2	-0.5	-2.3
C_4H_8	*trans*-2-butene	80.3	160.5	0.9	-1.6	3.4	0.0	8.7	2.0	8.5	3.7	6.0	1.6	8.2	3.1
C_4H_8O	butanone	103.40	177.66	-2.3	0.2	-5.4	0.8	-2.2	0.9	-3.7	4.8	-4.1	3.4	-2.2	4.6
$C_4H_8O_2$	1,4-dioxane	92.35	200.12	-0.4	-0.6	1.7	0.9	9.1	0.6	-1.3	-0.7	2.9	-0.8	2.3	-0.1
$C_4H_8O_2$	ethylacetate	113.58	200.00	-4.0	-0.5	-0.1	-0.3	-7.7	-0.5	-0.9	2.7	-1.5	1.5	-0.5	2.6
$C_4H_9NO_2$	2-nitrobutane	123.6	232.8	0.3	-0.8	-3.9	-9.0	0.7	-0.8	1.6	1.5	3.6	1.7	3.5	1.8
C_5H_6S	3-methylthiophene	95.71	181.04	1.4	1.1	-18.6	-13.8	---	---	1.5	0.7	1.5	0.3	4.6	1.8
C_5H_8	2-methyl-1,3-butadiene	102.64	187.53	2.3	0.3	-3.3	-2.0	-1.5	-2.5	-3.2	-0.7	-6.2	-2.2	-3.1	-0.5
C_5H_8	2-pentyne	98.70	178.86	-0.7	0.1	2.2	0.2	1.2	0.2	2.4	3.8	-0.1	1.5	4.1	3.2
$C_5H_{12}S$	1-thiahexane	140.84	254.60	0.1	0.2	-0.3	0.3	0.2	-0.2	-3.9	2.3	-3.6	0.4	-3.4	1.2
$C_5H_{12}S$	2-methyl-2-butanethiol	143.50	259.49	0.4	-0.6	-5.5	-5.2	16.3	18.0	-1.4	1.4	-2.4	-0.3	-0.6	0.8
C_6H_5Br	bromobenzene	100.71	190.04	-0.7	-1.1	-2.7	-1.0	-2.4	-0.9	-0.9	-1.7	-5.5	-2.6	0.3	-0.6
C_6H_7N	3-methylpyridine	99.88	206.07	2.1	-0.5	3.3	0.2	0.3	0.4	3.6	0.9	0.4	-0.1	4.9	1.4
C_6H_{12}	3,3-dimethyl-1-butene	126.40	245.71	0.5	3.4	4.9	3.7	7.2	5.1	4.2	4.5	2.4	2.7	5.2	4.2
$C_6H_{14}O$	di-(methylethyl)ether	158.27	288.65	-0.8	2.2	-0.8	-1.5	-1.1	-2.1	-3.3	4.2	-3.1	2.6	-2.3	3.7
$C_6H_{14}S_2$	4,5-dithiaoctane	187.09	322.66	-0.6	0.7	-2.0	0.7	-0.7	1.2	-5.7	1.9	-4.7	0.2	-4.1	1.1
C_7H_8O	4-methylphenol	124.86	240.91	0.1	-1.2	-0.3	-1.2	2.9	0.3	1.3	0.2	-0.2	0.2	3.6	1.6
C_7H_{14}	*cis*-1,3-dimethylcyclopentane	134.60	292.64	-2.7	-1.2	0.0	1.6	-3.1	1.2	-1.1	0.5	0.6	-0.5	2.1	0.6
C_7H_{16}	*n*-heptane	165.80	318.38	-1.1	0.1	0.3	-1.0	-1.3	-0.9	-6.9	1.3	-7.3	-0.6	-6.2	0.5
C_7H_{16}	2,2,3-trimethylbutane	163.39	326.73	1.6	-1.1	1.1	-3.0	1.1	-0.8	-1.5	-0.5	-1.2	-2.2	0.6	-0.9
C_9H_{12}	1-methyl-4-ethylbenzene	148.60	303.30	1.6	-1.8	4.1	0.2	5.4	0.5	3.0	1.9	1.2	1.0	4.6	2.3
$C_{11}H_{10}$	2-methylnaphthalene	159.79	319.32	-2.4	-1.4	-1.1	-0.6	-0.7	0.4	-1.9	-0.1	-4.1	-0.3	0.3	1.3
Average				-0.7	-0.2	-1.2	-0.9	1.3	1.4	-0.7	1.3	-1.3	0.1	0.5	1.2
Sample standard deviation				2.9	1.1	5.4	4.4	4.8	4.5	3.4	1.8	3.4	1.5	3.5	1.7

All experimental and additive calculations from Poling and Prausnitz.(97)

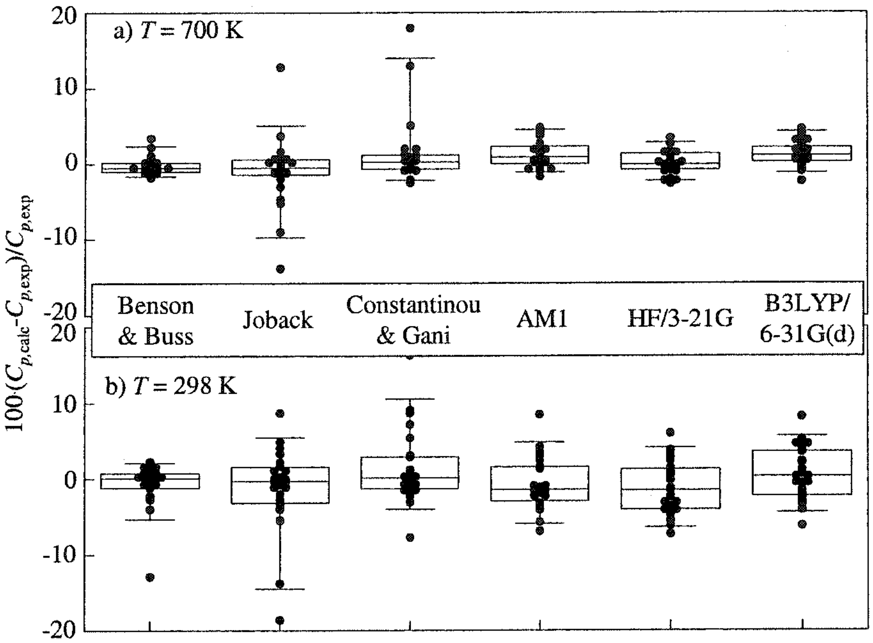

Figure 3.5 Relative error of heat capacities for 27 organic compounds calculated by three additivity schemes(97) and from present *ab initio* results. • are individual points (data given in table 3.3); box shows 25th to 75th percentile; box centre line is the mean; bars are the 5th and 95th percentile.

Overall, this limited data set shows that *ab initio* frequencies, determined with very little computational cost, can predict ideal gas heat capacities for organic compounds with similar accuracy to predictions from recently updated additivity schemes. Furthermore, the temperature dependence of the *ab initio* heat capacities arises directly from statistical thermodynamics and therefore does not require correlation type equations or additional fitting parameters, as for additivity schemes. The additivity methods and the *ab initio* methods are both good at higher temperatures. As this assessment does not include conformational effects, this matter seemed to be worth a separate investigation.

3.5.3 The *n*-alkanes from ethane to decane

3.5.3.1 An uncoupled internal rotator model

As discussed previously, the study of rotational contributions to ideal gas properties is an extensive field and very few models are both simple and applicable to a large number of molecules. Recently, Vansteenkiste *et al.*(117) have tested the estimation of heat capacities and entropies of some gas phase *n*-alkanes by replacing torsional modes with uncoupled hindered internal rotators. The study has utilised both the quantum mechanical and the classical solution to equation 3.18. Zero point frequencies and transition energies were calculated at the B3LYP/6-311G(d,p) level of theory. They have pointed out that consideration of rotator coupling or the full multi-dimensional potential energy surface leads to a very large increase in computational cost.

In this section, heat capacities calculated using *ab initio* frequencies at the B3LYP/6-31G(d) level of theory are compared to the results of Vansteenkiste *et al.*(117) The discrepancies are discussed with reference to partially fixed and relaxed potential energy surface scans of dihedral angle rotation. Both -CH_2CH_2-CH_2CH_2- dihedral angle rotation and terminal methyl group rotation, -CH_3, have been considered in a plausible explanation of results.

The entropy and heat capacity predictions made by Vansteenkiste *et al.*(117) for ethane through decane and those predicted here have be compared to the experimental heat capacities(131) at $T = 298.15$, 500, 700 and 1000 K in figure 3.6. Overall the agreement between the experimental and theoretical heat capacities is good. However, the improvement of error (agreement with experimental) using the hindered rotator model over those of the uncorrected harmonic oscillator model is better for entropies than for heat capacities, 6-12 % improvement for entropies and 0-4 % improvement for heat capacities.

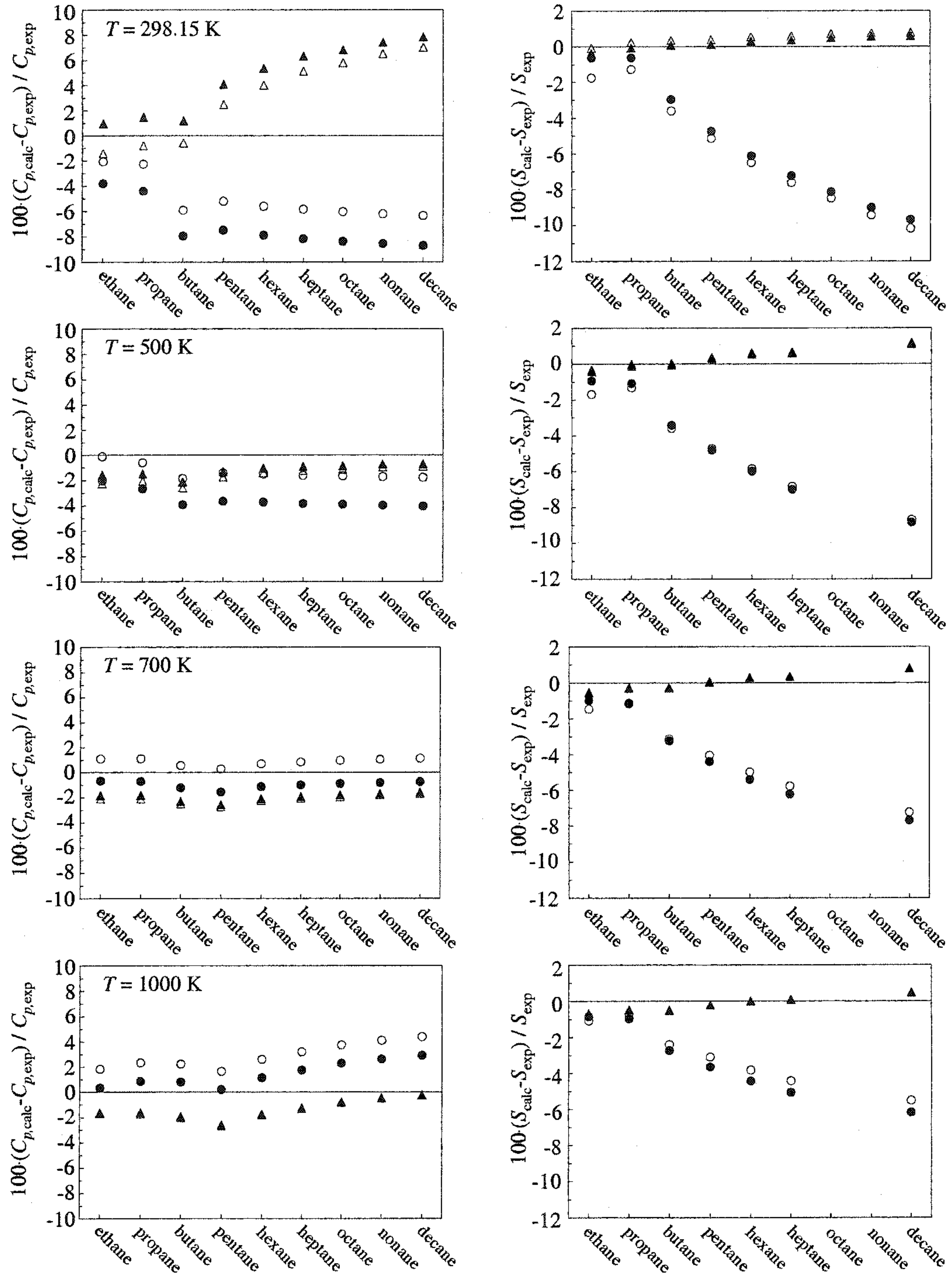

Figure 3.6 The relative error of calculated heat capacities and entropies for some *n*-alkanes at $T = 298.15$, 500, 700 and 1000 K. ●, harmonic oscillator (staggered configuration) B3LYP/6-311G(d,p);(117) ○, harmonic oscillator (staggered configuration) B3LYP/6-31G(d); ▲, quantum mechanical uncoupled internal rotation;(117) Δ, is the classical uncoupled internal rotation;(117) all y-axis are fixed at the same range for easier comparison between errors at different temperatures.

Vansteenkiste *et al.*(117) have used relaxed potential energy surfaces to identify the transition energy, $\Delta_{\mathrm{rot}}E^{\dagger}$, for rotation of methyl, ethyl, propyl, butyl and pentyl groups. For ethane this is a common method and is properly treated by the Pitzer model.(103,104) The symmetry number for ethane is $\sigma = 6$ and the rotational barrier is $\Delta_{\mathrm{rot}}E^{\dagger} = 11.8$ kJ mol^{-1}. This is an example of methyl rotation which is presented in many introductory organic text books. Transition energies for methyl rotation, calculated here using the B3LYP/6-31G(d) theory level, are shown in figure 3.7. These transition energies are in good agreement with those of Vansteenkiste *et al.*(117) The transition energies represent the lowest saddle point between two rotamer conformations.

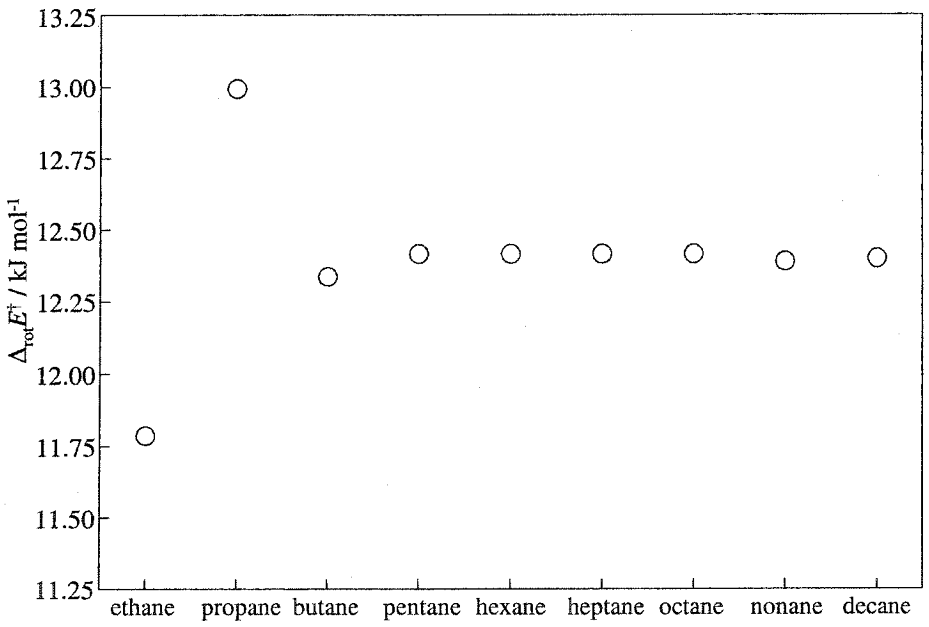

Figure 3.7 Calculated activation energies for methyl rotation for ethane through decane.

Figure 3.7 shows that the methyl rotation barrier converges to a value of $\Delta_{\mathrm{rot}}E^{\dagger} \approx 12.4$ kJ mol^{-1} for pentane and larger chains. At room temperature and this rotational barrier the rotamers will rotate in a hindered fashion; however, free rotation does not occure until $T > 2400$ K. The heat capacity of an internal rotor is not reduced to ½R until the rotor is free; therefore, the estimation of heat capacities by the harmonic oscillator approximation is expected be in error, figure 3.1. For $T < 2400$ K, the anti conformation is favoured. Vansteenkiste *et al.*(117) have used a figure similar to figure 3.7 to show that the two terminal methyl groups interact more in molecules of lower chain lengths than higher chain lengths, *i.e.*, these two terminal methyl rotamers are decoupled because they are further apart. This decoupling is necessary for the model, which considers methyl rotation to be independent of conformation. If coupling is considered, free rotation of internal rotors does not occure until even higher temperatures.

By investigating the relaxed energy surface scans, Vansteenkiste *et al.*(117) have effectively considered some coupling interactions, *i.e.*, rotations are path dependent and limited to the lowest saddle point (transition state). However, only a small amount of phase space was sampled in this way; therefore, the total coupling was not considered and the barriers for free rotation are underestimated. The internal rotations of propane and butane are examples of this underestimation.

Pitzer(132) has estimated, by interpolation from experimental data, a rotational barrier of $\Delta_{\mathrm{rot}}E^{\dagger} = 14.2$ kJ mol^{-1} for propane and Kemp and Egan(133) have measured $\Delta_{\mathrm{rot}}E^{\dagger} = 13.8$ kJ mol^{-1}. Both these values are greater than the average calculated value of $\Delta_{\mathrm{rot}}E^{\dagger} = 12.4$ kJ mol^{-1} for the longer chain *n*-alkanes and the value calculated for propane, $\Delta_{\mathrm{rot}}E^{\dagger} = 13.0$ kJ mol^{-1}. Wesenberg and Weinhold(134) have investigated the coupling of the two terminal rotors and found that non-vicinal CH bond interactions cause the barrier to be larger for propane, *i.e.*, the terminal rotors are coupled. In terms of calculating heat capacities, a similar steric interaction is the cause of the lack of free rotation. This is discussed briefly here by examining the calculated potential energy surface of propane.

There are two dihedral angles required to specify the conformation of propane and there are two torsional vibrational modes; one mode/rotation where the methyl groups librate in the same direction and one where the methyl groups librate in opposite directions. Figure 3.8 shows the potential energy surface of propane with respect to both of these dihedral angles. An uncoupled model assumes that each can rotate in either direction, independently of the other. However, as shown by figure 3.8 the direction of rotation is affected by the potential energy surface. The largest potential energy barrier on this surface is $\Delta_{\mathrm{rot}}E^{\dagger} = 27.9\ \mathrm{kJ\ mol^{-1}}$, which is much greater than the saddle point at $\Delta_{\mathrm{rot}}E^{\dagger} = 13.0\ \mathrm{kJ\ mol^{-1}}$ as shown in figure 3.7. This larger free rotation barrier can cause the harmonic oscillator model to be better than expected for heat capacities.

The ethyl rotation energy barrier also was discussed in detail by Vansteenkiste *et al.*,(117) with respect to butane and hexane. By a relaxed energy surface scan, the *trans* → *gauche* → *cis* → *gauche* → *trans* conformation energies can be examined. This potential energy surface is shown in one dimension in figure 3.9. Figure 3.9 also contains the same rotational energy surface scan with the methyl groups in the eclipsed conformation. The difference in maxima shows that the positions of other rotators (conformations) are relevant to the transition energy (path dependence). When the methyl groups are in the eclipsed conformation, the terminal hydrogens pass closer together upon ethyl rotation. In other words, the ethyl rotations are coupled to the methyl rotations and, like propane, free uncoupled rotation does not exist until much higher temperatures.

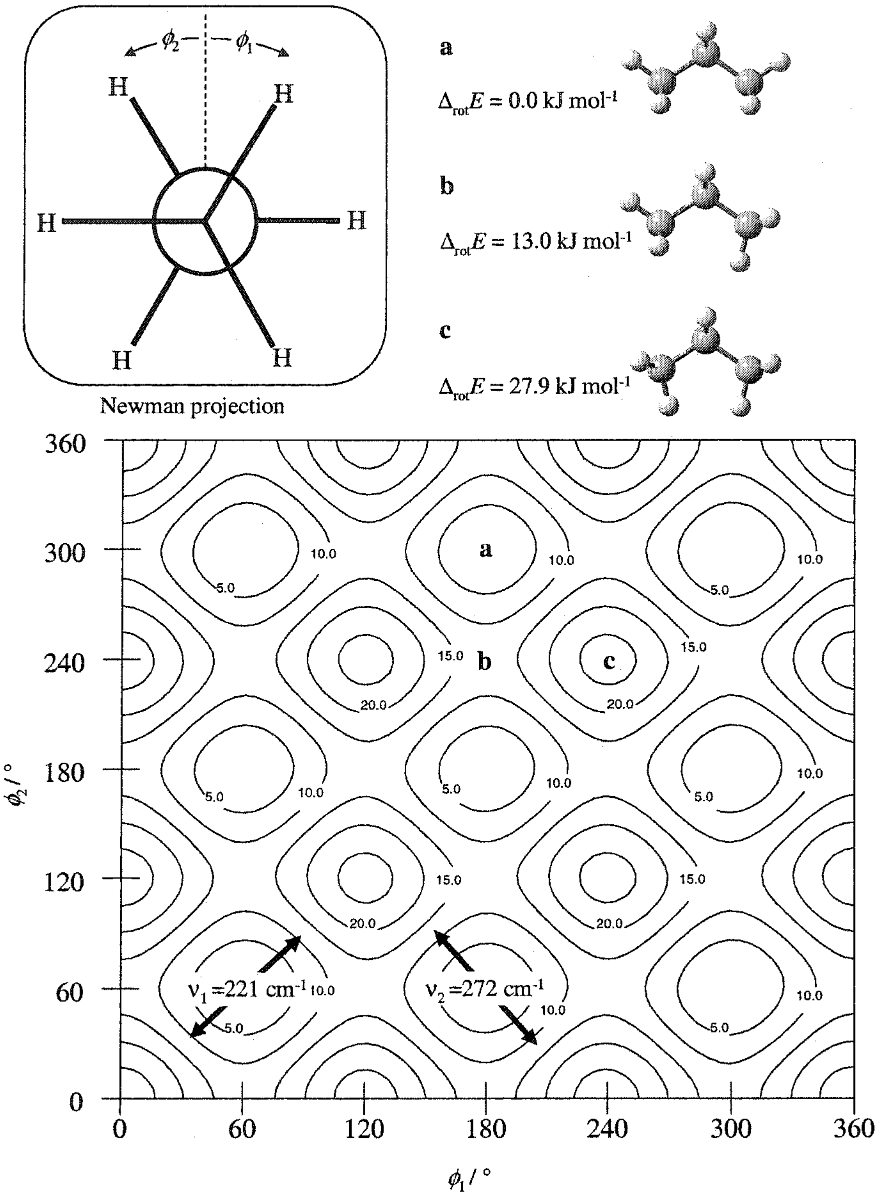

Figure 3.8 The calculated potential energy surface for the methyl rotations of propane. All potential energies are given relative to the lowest energy, configuration **a**, and in units of kJ mol^{-1}.

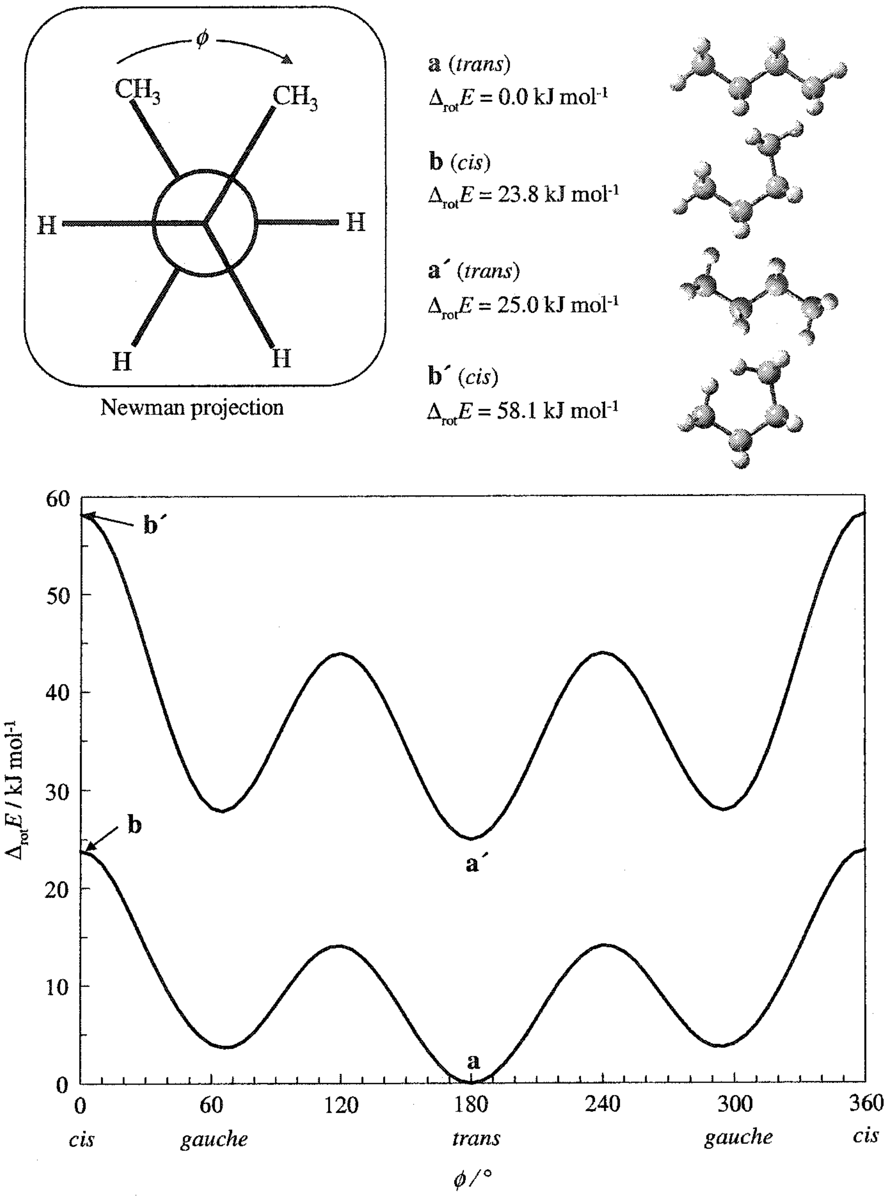

Figure 3.9 Two calculated paths across the calculated potential energy surface of *n*-butane. Potential energies are given relative to the lowest energy, configuration **a**.

Examination of the uncoupled model of Vansteenkiste *et al.*(117) shows the complications in predicting thermodynamic properties affected by conformation. Rotational conformation is considered a basic effect; however, the treatment and the prediction of the density of rotamer states is still debated in the literature.(135) The good estimation of entropies is the result of accessible conformation energies and symmetry. Two conformers of close energy will contribute to the entropy through conformer mixing and the symmetry determines if these energies are equivalent.

Guthrie(136) tested the prediction of entropies for 128 organic compounds by only considering the entropy of mixing conformers. Thus free rotation was ignored. Guthrie's test shows that entropies are predicted within an overall standard deviation of $\delta S \pm 5.4$ J K mol^{-1} (~2%). In Guthrie's model, all conformations within *ca.* 8 kJ mol^{-1} were considered equally possible; therefore, the temperature dependence of the conformation equilibrium was ignored and the heat capacities would be nearly equal to the harmonic oscillator model. Thus, in terms of entropy estimation, Guthrie's model works just as well as the uncoupled hindered rotator model and is possibly just as valid.

More recently, Katzer and Sax(137) have proposed an extensive, but closed form partition function for partially asymmetric internal rotations such as the two shown in figure 3.9. Using three adjustable parameters they were able to investigate the affect of difference in minima, difference in rotation barriers and minimum rotation barriers on internal energy, entropy and heat capacity. The most important parameter was found to be the difference in the energy minima, while barrier height differences were found to be less important. They concluded that asymmetric corrections to the rotational potential have a larger affect on the heat capacity than on the entropy.(137) This result agrees with the findings here.

3.5.3.2 Semi-empirical equations for estimating ideal gas heat capacities

There is an emphasis on predictions of heat capacities in this thesis. The exploratory calculations within this chapter have shown that a large portion of the heat capacity can be estimated (with temperature dependence) using the harmonic oscillator model and the *ab initio* frequencies for one conformer. With the frequencies, angular momentum, molecular mass and molecular symmetry number, the entropy at any given temperature also can be estimated by the harmonic oscillator model. Both these estimations will be in error depending on the conformation equilibrium and the shape of the potentials which influence that equilibrium. Thus first-principles calculations have not completely replaced empirical estimations.

Hypothetically, if one had experimentally determined entropies at some temperature, one could calculate the difference between the disordered and ordered entropy for any given molecule. In other words, $S_{\mathrm{exp}} - S_{\mathrm{calc}}$(lowest energy conformer), yields information about the conformational populations. If there is a simple relationship between the similar heat capacity difference and the entropy difference, this information can be utilised for the estimation of the heat capacity. In a plausible semi-empirical model, one can use the correlation between the differences to estimate the correction to the heat capacity. After all, both statistical mechanics and classical thermodynamics suggest such a relationship. However, without a robust and computationally expensive model, the exact mathematical relationship is unknown.

Several linear correlations between the entropy differences and the heat capacity differences for the *n*-alkanes were tested here by best-subset-regression. The best equation for estimating the heat capacity was found to be:

$$C_p \approx C_{p,\mathrm{calc,HO}} + (a_1 + a_2 T)(S_{\mathrm{exp}} - S_{\mathrm{calc,HO}}) \tag{3.20}$$

where $C_{p,\mathrm{calc,HO}}$ and $S_{\mathrm{calc,HO}}$ are the entropy and heat capacity calculated using the harmonic oscillator approximation (B3LYP/6-31G(d)) and a_1 and a_2 are empirical fitting coefficients. The equation was fit to 30 entropy differences for *n*-ethane through *n*-decane at temperatures of $T = 298.15$ to 1000 K. Coefficients of $a_1 = 0.580 \pm 0.018$ and $a_2 = -0.000959 \pm 0.000028\ \mathrm{K}^{-1}$ were found to reproduce heat capacities with a standard error of $\delta C_p = 0.14\,R$ ($R^2 = 0.976$).

The relative error of the estimated heat capacities is shown in figure 3.10, which can be compared to the plots within figure 3.6. The differences are somewhat systematic; however, they are within 3%. If the scaling factor of Scott and Radom(119) is considered, equation 3.20 has only 3 fitting parameters.

The applicability of such an equation is rather limited, because experimental entropies are often calculated from experimental heat capacities. However, the knowledge that there exists an apparently robust empirical correlation between an order-disorder entropy difference and an order-disorder heat capacity difference is useful. Note that this empirical correlation model assumes nothing about the nature of the disorder.

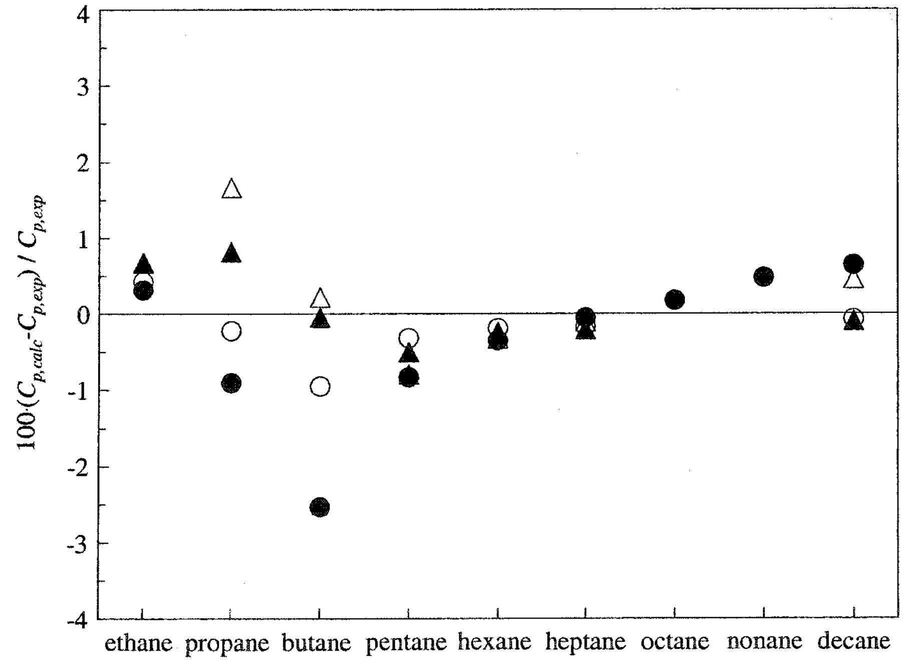

Figure 3.10 The relative heat capacity errors from equation 3.20 for some *n*-alkanes at $T = 298.15$, 500, 700 and 1000 K. ● $T = 298.15$ K, ○ $T = 500$ K, ▲ $T = 700$ K and △ $T = 1000$ K.

With the knowledge that the heat capacity for several different types of molecules can be estimated well by *ab initio* harmonic frequencies and that for particular types of molecules there is a correlation between order-disorder entropy and heat capacity differences, one can choose to find correlation indicators based upon well known contributions to the entropy. Note that the Benson and Buss method used this approach to correct for isomerisation and symmetry. The potential energy surfaces of two simple alkanes, although computationally intensive, showed the number of minimum and the symmetry of the potential energy surface. If all minima are estimated to be of similar energy, these observations could have been estimated by simply examining the structure. For example, the rotation of a methyl group provides three indistinguishable dihedral angles; therefore, there are three minima and the internal symmetry number also is three. Rotation of an ethyl group of a simple *n*-alkane provides 3 minima (two equivalent) and a rotational symmetry of two (two equivalent *gauche* conformers). These values are in the statistical mechanics equation for entropy by a factor of $R\ln(\phi/\sigma_{\text{int}})$, where $\phi = \prod \phi_i$ and ϕ_i is the estimated number of minima for rotation of bond *i*. Using this factor instead of the known entropy difference for the *n*-alkanes provides:

$$C_p \approx C_{p,\text{calc,HO}} + (a_3 + a_4 T) R \ln(\frac{\phi}{\sigma_{\text{int}}}) . \tag{3.21}$$

Equation 3.21 is an example of a semi-empirical equation to estimate heat capacities using only three fitting parameters, simple *ab initio* calculations and knowledge of the molecular connectivity. Because the equation is no longer dependent on knowing the experimental entropies, equation 3.21 was fit to 36 heat capacity values for ethane through to *n*-decane at temperatures of $T = 298.15$ to 1000 K.(131) Coefficients of $a_3 = 1.417 \pm 0.047$ and $a_4 = -0.00235 \pm 0.00007$ K^{-1} reproduce heat capacities with a standard error of $\delta C_p = 0.17\ R$ ($R^2 = 0.972$). It is an improvement over additive methods with little complication.

As shown in figure 3.11, the errors are very similar to those in figure 3.10. This comes as little surprise given that the entropic differences are known to be modelled well by simplified potential energy models.(117,136) Of course this type of correlation still suffers from an external validity problem. As shown previously, if a calibration set is not available, only the harmonic frequencies are required for good quality estimates. Based on the case studies here, one would expect the external validity errors to be less significant than with other empirical models.

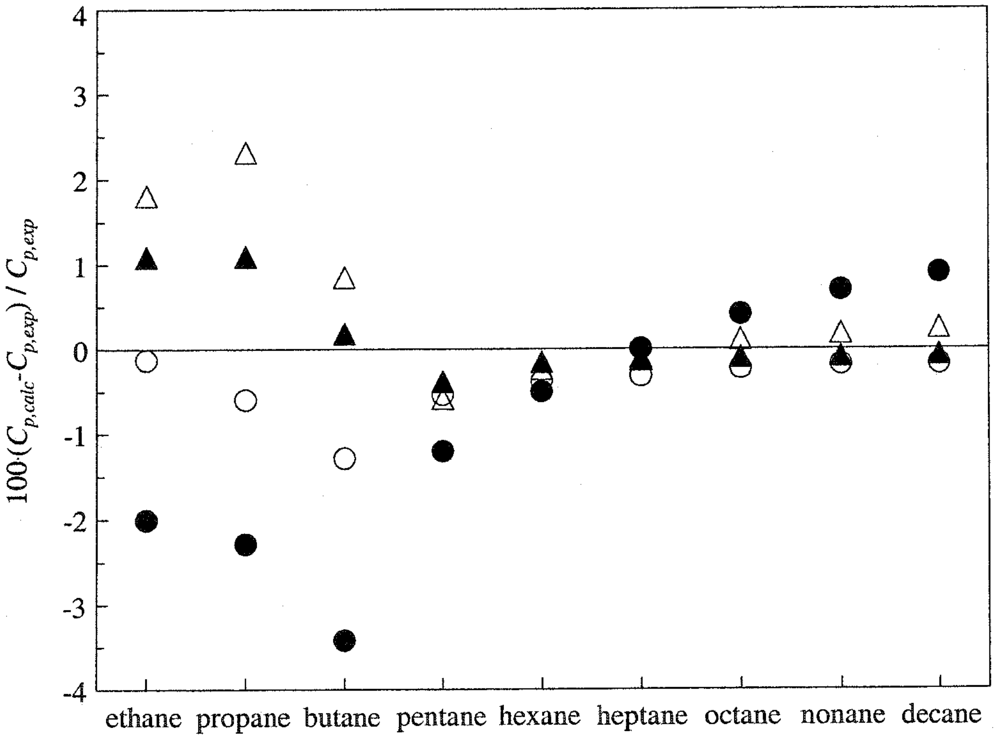

Figure 3.11 The relative heat capacity errors from equation 3.21 for some alkanes at $T = 298.15$, 500, 700 and 1000 K. ● $T = 298.15$ K, ○ $T = 500$ K, ▲ $T = 700$ K and △ $T = 1000$ K.

3.6 Conclusions

With respect to understanding thermodynamic cycles and developing equations of state, approximations and estimations of ideal gas properties are useful. Recently updated and common empirical additivity methods have been compared to statistical mechanical methods using vibrational frequencies. With the example of piperidine, it was observed that a simple harmonic oscillator model and experimental vibrational frequencies can estimate the ideal gas heat capacity well over a small, but relevant, temperature range. Large errors in vibrational frequencies were found to have little impact on the heat capacity of piperidine. Some low level *ab initio* frequencies were found to estimate the heat capacity of piperidine in good agreement with experimental frequencies.

Exploratory calculations with *ab initio* frequencies for 34 additional molecules, showed that low levels of theory can be used to estimate ideal gas heat capacities in reasonable agreement with experimental values. The *ab initio* calculated heat capacities were found to perform as well as recently updated and common additivity methods.

The multiple conformation and internal rotation effects on the heat capacity of some *n*-alkanes were investigated further, and it was shown that the potential energy surfaces are complicated, but simple attributes can still be utilised. Even for small *n*-alkanes it was shown the free rotation of internal groups does not take place until high temperatures. Without a robust and computationally intensive model, two semi-empirical relationships were shown to provide reasonable methods for estimating heat capacities.

As a final note to this chapter, it is worthwhile to reiterate that the harmonic oscillator approach worked surprisingly well. If the rotational and translational equipartition heat capacities were unknown or never introduced here, the calculations would have revealed $(C_{p,\text{exp}} - C_{p,\text{vib}})/R = 3.8 \pm 0.6$ (68 heat capacities), as shown in figure 3.12.(97,131) This is in good agreement with the equipartition value of $C_p - C_{V,\text{vib}} = C_{V,\text{rot}} + C_{V,\text{trans}} + R = 4\,R$.

These conclusions imply that *ab initio* frequencies can be used to investigate external and disorder properties in condensed phases, such as liquids and solids. In addition it is worthwhile to investigate the heat capacities differences and the correlation with properly corrected entropy differences. Note that equations such as the Schröder-van Laar equation and the thermodynamic cycle given in Chapter two, contain known entropy differences, but unknown heat capacity differences. As discussed previously, these unknown heat capacity differences are required to clarify thermodynamic generalisations regarding enantiomers.

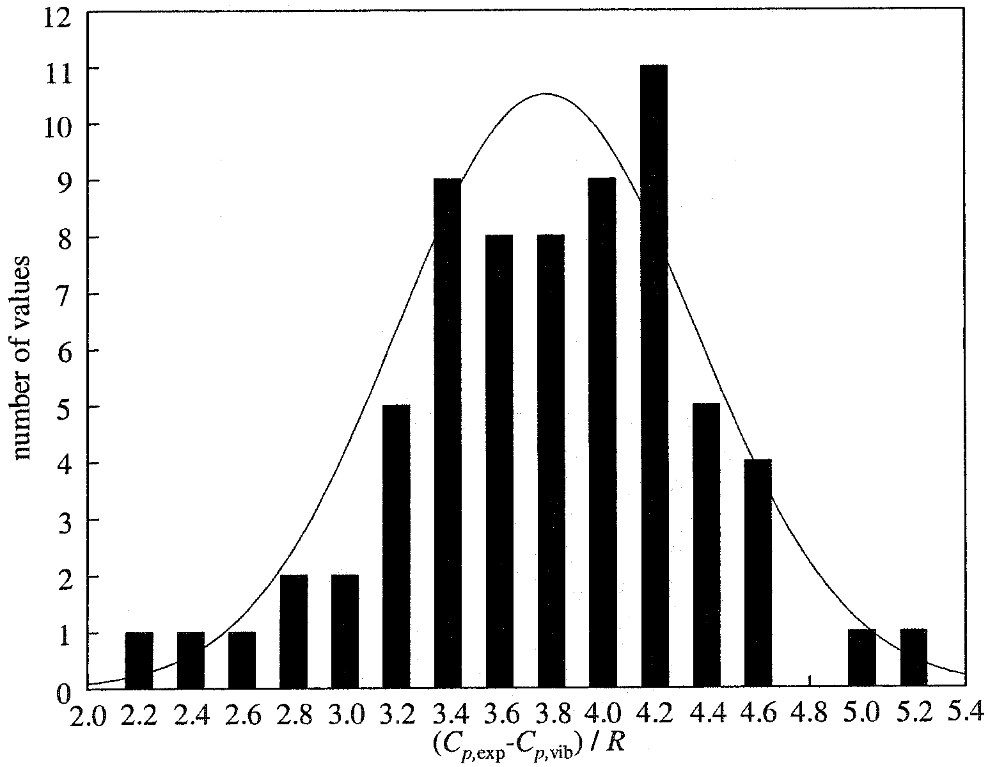

Figure 3.12 A histogram of 68 $C_{p,\text{exp}} - C_{V,\text{vib}}$ values for the harmonic oscillator approximation at the B3LYP/6-31G(d) theory level.(97,131)

4 CONDENSED PHASE HEAT CAPACITIES

> *A very old rule of thumb says that symmetric molecules pack in a three-dimensional periodic lattice more easily than less symmetrical ones, and hence form more stable, higher melting and less soluble crystals. No strict definition of symmetry in this context has ever been given, nor has any theoretical justification ever been found...*
>
> Angelo Gavezzotti, 1995(63)

4.1 Introduction

In Chapter two the calculation of the thermodynamics for forming a racemic crystal from a conglomerate crystal using the thermodynamic cycle in figure 2.8 was shown to be affected by the assumption that the difference between the solid and liquid heat capacity was zero at the fusion temperature, $\Delta_{\text{fus}}C_p \approx 0 \text{ J K}^{-1} \text{ mol}^{-1}$. It also was shown that $\Delta_{\text{fus}}C_p$ was apparently larger for chiral molecules. The goal of the studies within this chapter was to find some empirical or semi-empirical way to estimate $\Delta_{\text{fus}}C_p$ to improve the calculations.

Estimations for $\Delta_{\text{fus}}C_p$ are useful for thermodynamic calculations other than those used to calculate the Gibbs energy, enthalpy and entropy change for forming racemic crystals. Many thermodynamic cycles for investigating stability are derived by using the fusion temperature as a reference point,(85, 138,139) since the thermodynamic relationships at that temperature are commonly measured and reported. If the heat capacity difference between the two phases can be estimated, the utility of available fusion temperatures and entropies is increased considerably.

A common application of estimated liquid-solid heat capacity differences is freezing point depression. The simplified Schröder-van Laar equation,(49) equation 2.21, can be rewritten in another commonly used form for ideal solubility,(140)

$$\ln x = \frac{\Delta_{\text{fus}} S^i}{R}\left(\frac{T_{\text{fus}} - T^i_{\text{fus}}}{T_{\text{fus}}}\right) + \frac{\Delta_{\text{fus}} C_p}{R}\left(\ln\frac{T^i_{\text{fus}}}{T_{\text{fus}}} + 1 - \frac{T^i_{\text{fus}}}{T_{\text{fus}}}\right). \tag{4.1}$$

In equation 4.1 the optically pure species R is now replace with i, where i can be any pure compound. Since values for $\Delta_{\text{fus}}C_p$ are rarely available, there are two assumptions which have been commonly used: $\Delta_{\text{fus}}C_p \approx 0\ \text{J K}^{-1}\ \text{mol}^{-1}$ and $\Delta_{\text{fus}}C_p \approx \Delta_{\text{fus}}S$.(141) The second assumption leads to another simplified version of the freezing point depression equation,

$$\ln x = \frac{\Delta_{\text{fus}} S^i}{R}\ln\frac{T_{\text{fus}}}{T^i_{\text{fus}}}. \tag{4.2}$$

In addition to the second chapter of this thesis, which focused on enantiomeric melting point phase diagrams, there have been several recent papers discussing the error associated with these $\Delta_{\text{fus}}C_p$ assumptions.(91,141-143) Mishra and Yalkowsky suggest that assuming $\Delta_{\text{fus}}C_p \approx 0\ \text{J K}^{-1}\ \text{mol}^{-1}$ is suitable for polycyclic aromatic compounds.(142) Neau and Flynn(91) have shown that $\Delta_{\text{fus}}C_p \approx 0\ \text{J K}^{-1}\ \text{mol}^{-1}$ is reasonable for rigid molecules whereas equation 4.2 is suitable for non-rigid molecules. Later, Mishra and Yalkowsky point out that either equation is suitable and that there is very little difference in ideal solubility.(143) The latter conclusion also was presented in Section 2.2.1, when discussing the conglomerate melting temperature error associated with the $\Delta_{\text{fus}}C_p \approx 0\ \text{J K}^{-1}\ \text{mol}^{-1}$ assumption.

Both the subjects of freezing point depression and the cycle for calculating the Gibbs energy of forming a racemic crystal from its corresponding conglomerate require understanding some aspects of melting (solid-liquid equilibrium) of pure organic molecular crystals of various symmetries. When a crystal melts, its molecules are going from a high degree of order to high degree of disorder. Hence, fusion is a primary order-disorder transition, not totally unlike a gas molecule going from an ordered single conformation to a disordered state with several conformations. Discussing melting by first considering crystalline properties also is a reasonable way to begin the discussion and introduce some models used later in the thesis.

4.2 Crystal heat capacities

4.2.1 Simple crystals and harmonic centre-of-mass modes

For a brief introduction to crystalline heat capacities, simple crystals are first considered, *i.e.*, lattices containing one or two spherically symmetric rigid particles (atoms). A simple crystal can be considered a super-molecule, where each atom is held at a lattice site by intermolecular forces. Displacement of the atoms from their respective potential well minima takes place through oscillation or vibration. Normal vibrational modes can be defined for 3Z modes, where Z is the number of atoms in the primitive unit cell. The modes are described by wave vectors or phonons, which can be related to the unit cell parameters. The spectrum of frequencies is dense and can be approximated by a vibrational density of states function, $P(\nu)$, where

$$\int_0^\infty P(\nu)d\nu = 1\,. \tag{4.3}$$

From the partition function and equation 4.3, the constant volume heat capacity is defined as

$$C_{V,\mathrm{vib}} = 3R\int_0^\infty P(\nu)\frac{x^2e^x}{(e^x-1)^2}\mathrm{d}\nu\,, \tag{4.4}$$

where x is defined by

$$x = \frac{h\nu}{kT}\,. \tag{4.5}$$

The heat capacity was presented in this way, to point out that equation 4.4 is equivalent to equation 3.16, with the replacement of the summation by an integral.

The vibrational density of states for a crystal usually is very complicated. Therefore, mathematically convenient functions for $P(\nu)$ can be chosen. Einstein$^{(144)}$ proposed that $P(\nu)$ be approximated by the Dirac-delta function:

$$P(\nu) = \delta(\nu) = \frac{1}{\pi}\lim_{\gamma\to 0}\frac{\gamma}{(\nu-\nu_{\mathrm{E}})^2+\gamma^2}\,. \tag{4.6}$$

Therefore, all vibrational frequencies are approximated by a single frequency, ν_{E}. The vibrational temperature given by this single frequency is generally referred to as the Einstein temperature, $\theta_{\mathrm{E}} = h\nu_{\mathrm{E}}/k$. The Einstein heat capacity is given by

$$C_{V,\mathrm{Einstein}} = 3R\left(\frac{\theta_{\mathrm{E}}}{T}\right)^2\frac{e^{\theta_{\mathrm{E}}/T}}{(e^{\theta_{\mathrm{E}}/T}-1)^2}\,. \tag{4.7}$$

Equation 4.7 is simply 3 times the 1-D vibrational heat capacity given previously as equation 3.16. The heat capacity given by equation 4.7 approaches $C_V = 3R$ as the temperature is increased above θ_{E} and $C_V \to 0\ \mathrm{J\ K^{-1}\ mol^{-1}}$ as $\mathrm{T} \to 0$ K.

The Einstein heat capacity function agrees with the empirical relationship given by the Dulong-Petit law. Dulong and Petit$^{(145)}$ found that the high temperature constant volume molar heat capacities of several crystalline elements were constant, where $C_V \approx 3R$. The Dulong-Petit value of $3R$ is approached for many simple monatomic crystals as the temperature is increased.$^{(146)}$ The Einstein heat capacity function also agrees with the observation that crystalline $C_V = \to 0\ \mathrm{J\ K^{-1}\ mol^{-1}}$ as $T \to 0$ K.$^{(146,147)}$

Experimental heat capacities for insulators suggest that the heat capacity approaches $C_V = 0\ \mathrm{J\ K^{-1}\ mol^{-1}}$ with a limiting value proportional to T^3.$^{(146,147)}$ The Einstein heat capacity function does not correctly predict this limiting behaviour. To rectify this, Debye$^{(148)}$ suggested that $P(\nu)$, be approximated by $P(\nu) = a\nu^2$ up to a cut-off frequency of $\nu = \nu_{\mathrm{D}}$ ($P(\nu)=0$ for $\nu > \nu_{\mathrm{D}}$). Here a is a proportionality constant which is set by the normalisation condition of equation 4.3 and the Debye cut-off frequency, $a = 9N / \nu_D^3$. The Debye heat capacity is given by

$$C_{V,\text{Debye}} = 9Nk\left(\frac{kT}{h\nu_D}\right)^3 \int_0^{h\nu_D/kT} \left(\frac{h\nu}{kT}\right)^4 \frac{e^{h\nu/kT}}{(e^{h\nu/kT}-1)^2}\, d\left(\frac{h\nu}{kT}\right). \tag{4.8}$$

The integral in equation 4.8 cannot be evaluated in closed form and must be evaluated numerically.

Because the vibrational density of states differs for different crystals, the Debye model is not exact. However, it shares the same characteristics as many crystalline solids and approaches $T = 0$ K as a function of T^3, in agreement with experimental heat capacities. A comparison between the Einstein heat capacity and the Debye heat capacity is shown in figure 4.1. The schematic comparison of the vibrational density of states is given for $\nu_E \approx$ ¾ ν_D in the inset of figure 4.1.

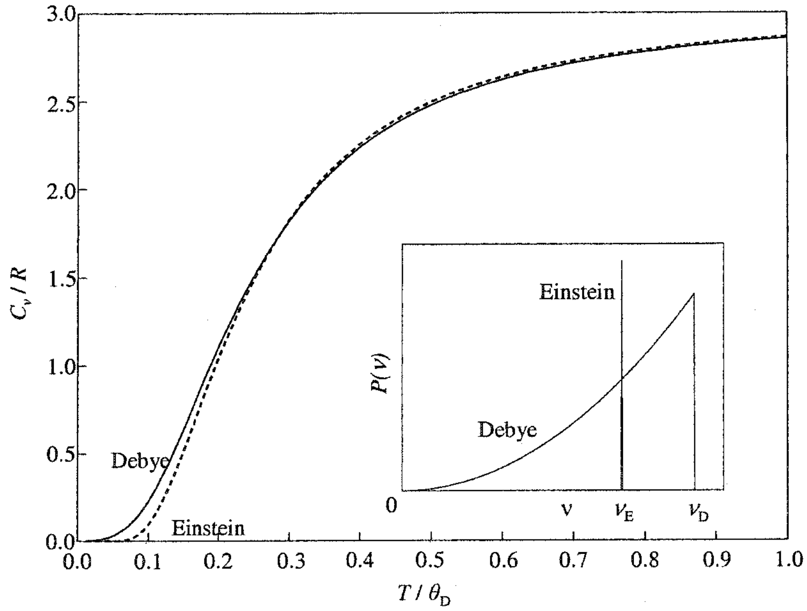

Figure 4.1 The Debye and Einstein heat capacity functions, $\nu_E = 3/4\,\nu_D$. The inset figure shows the vibrational density of states for these functions, where $\nu_E = 3/4\,\nu_D$.

Although the vibrational density of states is much more complicated for most solids, Debye theory has become the bench-mark for calculating and comparing anharmonic contributions.(147) For example, non-constant effective Debye temperatures are commonly reported to show anharmonic effects and changes in the hardness of modes with temperature.(147)

Thus far the discussion has been concerned with one particle or atom per lattice site or unit cell. Many unit cells have more than one atom; therefore, two types of wave vectors for each lattice direction can be described. The two types of transverse wave vector modes are shown in figure 4.2. The wave showing in-phase motion is called the acoustic mode. Acoustic modes have a strong dispersion and large frequency range from $\nu = 0$ to some cut-off frequency. The other mode, shown in figure 4.2, shows a motion for the two different types of atoms, with an oscillating dipole. This mode is referred to as an optic mode, since it can interact with light, and has a smaller dispersion of frequencies. Acoustic modes are generally modelled by the Debye heat capacity equation (equation 4.8) and optical modes are modelled well by the Einstein heat capacity equation.(147) For Z atoms per primitive unit cell, there are three acoustic modes and 3Z-3 optic modes.

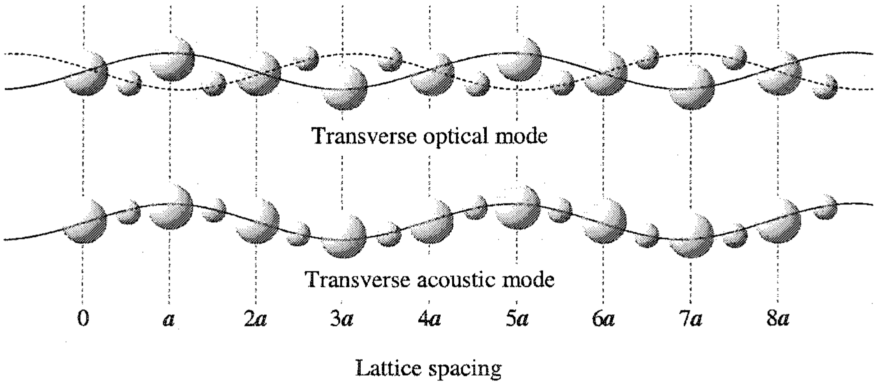

Figure 4.2 A schematic of transverse vibrational modes along one lattice direction for a crystal with two atoms per unit cell.

For solids, constant pressure heat capacities are much more practical to measure than C_V, which are more accessible theoretically. To calculate C_p, the harmonic models of experimental properties must include an additional contribution for C_p-C_V, see equations 3.11 to 3.13. Temperature-dependent thermal expansion coefficients and isothermal compressibilities are sparse in the literature. However, at low temperatures this correction term is very small. At higher temperatures approximations can be made or simple empirical equations can be used, *i.e.*, the utility of the Debye and Einstein models is the extrapolation to $T = 0$ K[(149)] and not necessarily to higher temperatures.

4.2.2 Molecular crystals

Molecular crystals are more complex than simple crystals. In addition to centre of mass modes involving the motion of complete molecules, there are torsional modes and internal or intramolecular modes. For Z molecules in a primitive unit cell, each having n atoms, there are three acoustic modes, $3Z$-3 external optical modes, $3Z$ external torsional modes and $Z(3n$-$6)$ internal modes. There is a total of $3(nZ) = 3N$ vibrational modes which is agreement with the total number of modes given previously for the simple crystal. Thus, assuming no coupling, the lattice dynamic model would give an overall constant pressure molar heat capacity of

$$C_p = \frac{1}{Z}\left(\sum_i^3 3C_{V,i,\mathrm{aco.}} + \sum_i^{3Z-3} C_{V,i,\mathrm{opt.}} + \sum_i^{3Z} C_{V,i,\mathrm{tor.}} + \sum_i^{Z(3n-6)} C_{V,i,\mathrm{vib}}\right) + (C_p - C_V), \quad (4.9)$$

where $C_{V,i,\mathrm{aco.}}$, $C_{V,i,\mathrm{opt.}}$, $C_{V,i,\mathrm{tor.}}$ and $C_{V,i,\mathrm{vib.}}$ are the i^{th} acoustic, optical, torsional and internal vibrational heat capacities, respectively. Equation 4.9 can be used to extrapolate to $T = 0$ K in a semi-empirical fashion if some vibrational modes are known. If vibrational modes are unknown, modes can be truncated to a single weighted apparent Debye temperature and a single weighted apparent Einstein temperature.

Extrapolation to higher temperatures is not as easily done, because of anharmonicity and the larger C_p-C_V term. Here heat capacities are usually modelled by a smoothing function such as temperature polynomials or splines. Assuming that all external modes are active at the fusion temperature, equation 4.9 shows that the constant volume heat capacity of a molecular crystal at the high temperature is given by

$$C_{V,\mathrm{min}}^{\mathrm{high\ T}} = 6R + \sum_{i}^{3n-6} C_{V,i,\mathrm{vib}} \,. \tag{4.10}$$

In arriving at equation 4.10, all internal vibrational modes are considered uncoupled with the lattice site. To obtain the constant pressure heat capacity, the C_p-C_V term is added onto equation 4.10; therefore, thermal expansion and isothermal compressibility (anharmonic effects) become important. A softening of the crystal lattice due to imperfections and the onset of conformational disorders can cause the external heat capacities to rise well above $6R$. This rise is referred to as a premelting and is often attributed to crystal imperfections.(103,140) Since no real crystal is absolutely perfect there is always some premelting.

With the discussion in the previous chapter, heat capacities were split into internal, $C_{V,\mathrm{int}}$ (intramolecular), and external contributions, $C_{p,\mathrm{ext}}$ or $C_{V,\mathrm{ext}}$ (intermolecular). The first term in equation 4.10 is the external constant volume contribution and the second term is the internal constant volume contribution. In the subsequent sections of this chapter, external constant pressure heat capacities were investigated for many organic compounds. Here the internal vibrations were calculated by assuming that the constant volume internal contribution to a condensed phase molecule can be approximated by the constant volume vibrational heat capacity of an ideal gas, $C_{V,\mathrm{int}}\,(cr \text{ or } l) \approx C_{V,\mathrm{vib}}(g)$. Note that all internal and external contributions in a crystal are vibrational. Figure 4.3 shows how *ab initio* frequencies can be used to compare thermal properties of molecular crystals by the same method used in Section 3.6, $C_{p,\mathrm{ext}} \approx C_{p,\mathrm{exp}} - C_{V,\mathrm{int}}$.

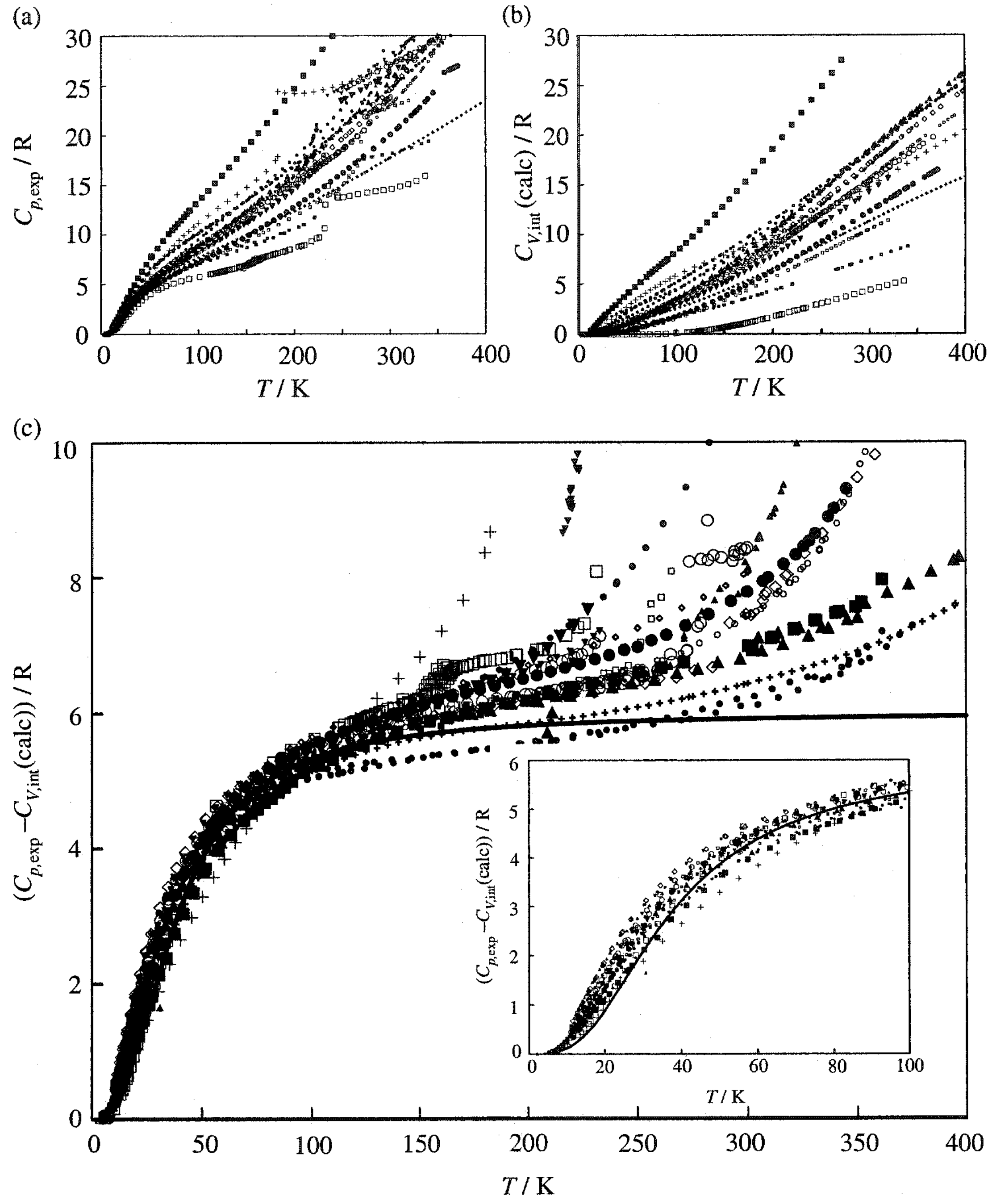

Figure 4.3 (a) Experimental constant pressure, (b) internal constant volume and (c) external constant pressure heat capacities for 20 molecular organic crystals over a large temperature range. Internal molecular vibrations have been calculated at the B3LYP/6-31G(d) theory level; • naphthalene;(156) ○ 1-methylnaphthalene,(156) 2-methylnaphthalene;(156) ● 1,8-dimethylnaphthalene,(158) 2,6-dimethylnaphthalene,(158) 2,7-dimethylnaphthalene;(158) ○ acenaphthalene;(158) ■ 1,2'-dinaphthylmethane;(158) □ thiazole;(150) ▪ 1-methylthiazole;(151) ▫ benzothiazole;(152) ▼ 1,2,3,4-tetrahydronaphthalene;(156) ▼ *trans*-decahydronaphthalene,(156) *cis*-decahydronaphthalene;(156) ▲ anthracene;(160) ▲ phenanthrene;(158) ◊ fluorene;(158) ◊ diphenylether;(159) + heptane;(159) + benzoic acid;(159) —— 6*N* Debye C_V for θ_D = 155 K.

Figure 4.3 shows a plateau at *ca.* 6R, in a similar way that many text books show the Dulong and Petit value for simple crystals; here this value is quite approximate, since these are external constant pressure heat capacities and not external constant volume heat capacities. By estimating external heat capacities using calculated *ab initio* frequencies at the fusion temperature, the general distribution of external constant pressure heat capacities for organic molecular solids and liquids has been investigated.

Neau and Flynn(91) have collected constant pressure heat capacities at the fusion temperature for 48 different molecular organic species. These 48 experimental heat capacities have been used here to estimate the external heat capacity at the fusion temperature, table 4.1. The internal vibrational heat capacities were calculated using the Gaussian98® package(118) for Windows. Optimisations and vibrational calculations were performed at the B3LYP/6-31G(d) theory level assuming only the harmonic oscillator approximation and the zero point vibrations as the fundamental frequencies. All frequencies have been scaled using the factors of Scott and Radom.(119)

Figure 4.4 shows histograms of the apparent external heat capacities at the fusion temperature for the liquids and solids of the compounds compiled by Neau and Flynn.(91) Given that this sample set contains a wide variety of molecules and many contributions have been neglected (β_T, α and V), the distribution is not expected to be narrow. Neglecting molecular and lattice symmetry, $C_{p,\text{ext}}$ for the solids is expected to be *ca.* 6 R or greater, which is in agreement with this apparently asymmetric distribution. The average value of the solid external heat capacity is $C_{p,\text{ext}} = 9 \pm 5\ R$.

Table 4.1 Experimental and internal vibrational heat capacities for the 48 compounds compiled by Neau and Flynn.(91)

Formula	Name	T_{fus} / K	$C_p(cr)^a$	$C_p(l)^a$	$C_{V,\mathrm{int}}(\mathrm{calc})^{a,b}$	Ref.
CH_3NO_3	methylnitrate	190.2	97.9	131.5	25.6 ± 1.7	153
CH_5N	methylamine	179.8	59.8	98.2	5.9 ± 1.1	154
C_2H_7N	dimethylamine	181.0	77.8	121.0	17.9 ± 1.8	154
$C_2H_8N_2$	1,1-dimethylhydrazine	216.0	93.4	152.1	37.6 ± 2.1	153
C_2ClF_3	chlorotrifluoroethene	115.0	73.1	111.5	18.3 ± 2.8	153
C_3H_8S	isopropylmercaptan	142.6	104.9	131.1	28.2 ± 3.0	153
C_3H_9N	trimethylamine	156.1	94.5	114.6	26.1 ± 2.7	154
C_4H_4O	furan	187.5	82.2	99.5	9.0 ± 1.0	153
$C_4H_8O_2$	ethylacetate	189.6	115.4	156.6	52.4 ± 2.2	154
$C_4H_{10}S$	*t*-butylmercaptan	274.3	152.2	170.1	81.1 ± 2.1	153
$C_5H_{12}S$	amylmercaptan	197.5	139.0	186.3	68.8 ± 2.4	153
C_6H_6	benzene	278.7	126.6	131.6	44.2 ± 1.9	155
C_6H_{14}	hexane	177.9	123.0	169.0	60.8 ± 2.6	155
C_7H_8	toluene	178.2	89.7	134.5	35.1 ± 2.2	155
$C_7H_8O_4S_2$	benzyl alcohol	257.9	141.5	187.1	74.1 ± 2.3	155
C_7H_{16}	heptane	182.6	143.9	198.4	76.4 ± 2.8	155
C_7H_{16}	2-methylhexane	154.9	133.4	178.2	67.4 ± 3.5	155
C_7H_{16}	2-ethylpentane	154.6	127.0	171.7	66.9 ± 3.5	155
C_7H_{16}	2,2-dimethylpentane	149.3	134.6	163.1	64.4 ± 3.9	155
$C_8H_9NO_2$	methyl-p-aminobenzoate	385.2	255	304	181.4 ± 2.3	91
C_8H_{10}	ethylbenzene	178.2	106.6	156.0	47.6 ± 2.5	155
C_8H_{10}	*o*-xylene	247.8	144.7	172.9	79.8 ± 2.4	155
C_8H_{10}	*m*-xylene	255.3	124.6	161.5	84.4 ± 2.3	155
C_8H_{10}	*p*-xylene	286.4	157.4	177.4	97.3 ± 2.2	155
$C_8H_{17}Br$	1-bromo-octane	218.2	185.0	260.8	116.6 ± 2.6	153
C_8H_{18}	octane	216.4	174.0	230.0	104.2 ± 2.6	155
$C_9H_{11}NO_2$	ethyl-*p*-aminobenzoate	362.9	282	331	197.4 ± 2.5	91
C_9H_{12}	propylbenzene	173.6	120.8	180.0	60.3 ± 2.8	155
C_9H_{12}	1,2,3-trimethylbenzene	247.8	181.3	199.4	102.3 ± 2.6	155
C_9H_{12}	1,2,4-trimethylbenzene	229.3	152.5	192.8	95.0 ± 2.7	155
C_9H_{12}	1,3,5-trimethylbenzene	228.4	147.3	184.2	96.4 ± 2.6	155
$C_{10}H_8$	naphthalene	353.4	208.1	217.8	128.5 ± 2.4	156
$C_{10}H_{13}NO_2$	propyl-*p*-aminobenzoate	346.6	333	362	213.2 ± 2.6	91
$C_{11}H_{10}$	1-methylnaphthalene	242.7	155.1	202.3	95.6 ± 2.8	156
$C_{11}H_{10}$	2-methylnaphthalene	307.7	205.1	227.5	132.4 ± 2.6	156
$C_{11}H_{15}NO_2$	butyl-*p*-aminobenzoate	331.1	344	381	227.1 ± 2.8	91
$C_{12}H_8S$	dibenzothiophene	371.0	243.4	280.0	183.6 ± 2.6	157
$C_{12}H_{10}$	acenaphthene	366.6	258.5	262.9	169.6 ± 2.6	158
$C_{12}H_{10}$	biphenyl	342.2	229.0	268.5	160.3 ± 2.6	157
$C_{12}H_{10}O$	diphenyl ether	300.0	217.6	268.2	151.0 ± 2.8	159
$C_{12}H_{16}$	cyclohexylbenzene	280.5	217.6	252.3	143.9 ± 2.9	157
$C_{12}H_{17}NO_2$	pentyl-*p*-aminobenzoate	325.5	349	407	246.2 ± 2.9	91
$C_{13}H_{10}$	fluorene	387.9	294.3	294.4	196.7 ± 2.6	158
$C_{13}H_{19}NO_2$	hexyl-*p*-aminobenzoate	334.2	399	461	275.8 ± 3.0	91
$C_{14}H_{10}$	anthracene	488.9	356.2	362.4	266.3 ± 2.4	160
$C_{14}H_{10}$	phenanthrene	372.4	283.8	299.6	201.3 ± 2.7	158
$C_{16}H_{25}NO_2$	nonyl-*p*-aminobenzoate	343.4	505	557	355.2 ± 3.3	91
$C_{19}H_{16}$	triphenylmethane	365.3	392.8	445.6	301.1 ± 3.2	153

^{a} / J K^{-1} mol^{-1}; ^{b} calculated using B3LYP/6-31G(d) and the scaling factor of Scott and Radom(119). Errors have been estimated using equation 3.19 and $\delta\nu = \pm$ 68 cm^{-1} , which is twice the sum squared error given by Scott and Radom(119) for this theory level.

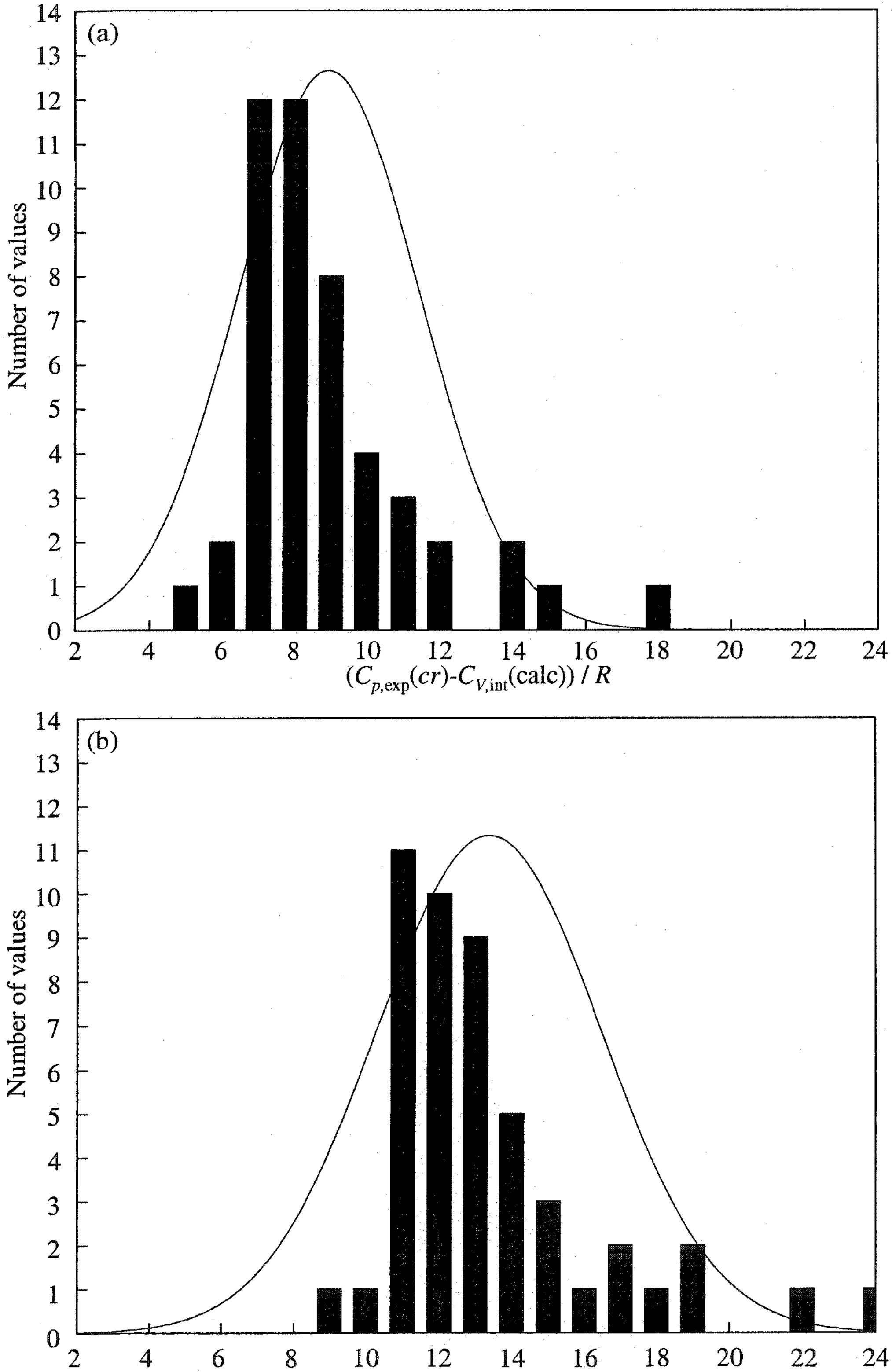

Figure 4.4 Histograms of the external constant pressure heat capacities at the fusion temperature for molecular organic compounds. (a) solids and (b) liquids. Internal vibrational heat capacities have been estimated using B3LYP/6-31G(d) and the scaling factor of Scott and Radom.(119)

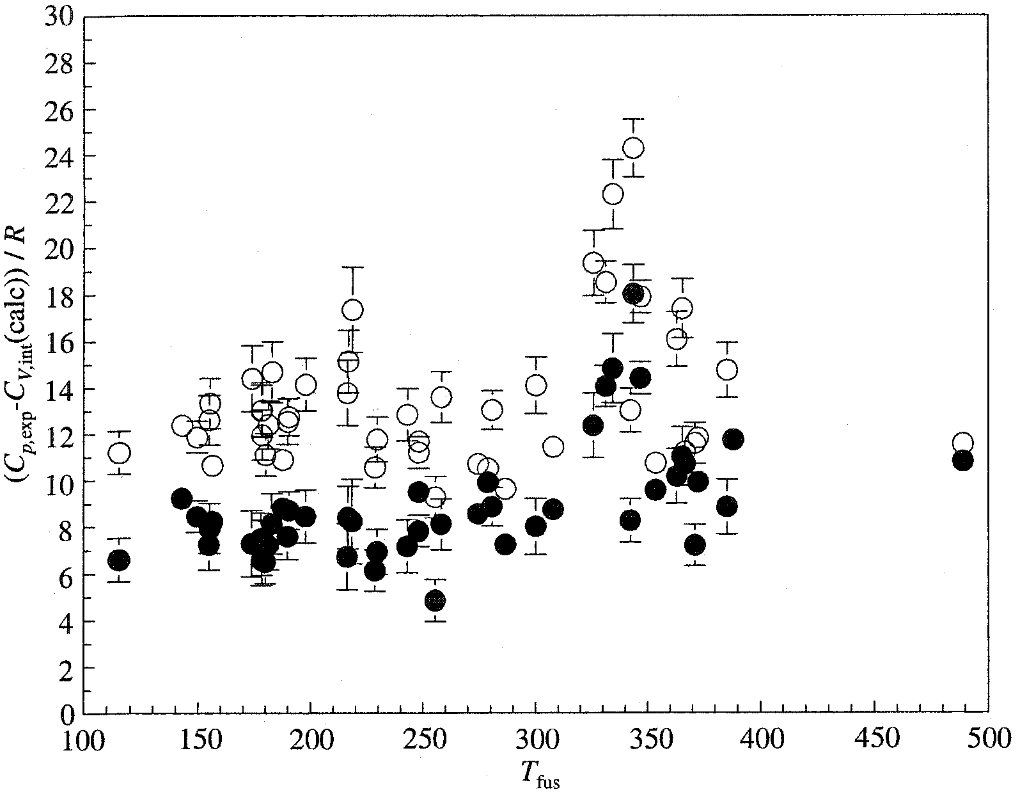

Figure 4.5 External constant pressure heat capacities at the fusion temperature for 48 molecular organic compounds plotted against the fusion temperatures. ○ liquids and ● solids. Internal vibrational heat capacities have been estimated using B3LYP/6-31G(d) and the scaling factor of Scott and Radom.(119) Error bars are calculated as 10% of the experimental heat capacity.

Figure 4.5 shows the external constant pressure heat capacities at the fusion temperature plotted against the fusion temperatures. There is no appreciable correlation with fusion temperature and the external constant volume heat capacities.

4.3 Liquid heat capacities

Compared to solids and gases, describing the thermodynamics of liquids is complicated, because liquids are only partially ordered. Simulations of liquids can provide for fundamental interpretations of thermodynamic properties;(57,161) however, simple models analogous to Debye and Einstein models for solids have not been very successful.(162-164) This lack of success is due to the complicated nature of liquids, since liquids are neither as well ordered as crystals nor as fully disordered as gases.(165) Some theories attempt to model this intermediate state by distinguishing between local structure and long range disorder.(164,166) While neither of these effects is simple, some studies have found success by treating liquids as ideal mixtures of solid phases.(167) As for the internal rotator discussion, molecules in a liquid are not freely rotating or translating, thus the theoretical and experimental description of hindered rotation has received a great deal of attention.(103,168) Liquids are further complicated from intermolecular conformations, which are less constrained than within the crystal, but more constrained than in the gas.

In some cases, liquid heat capacities can be estimated through simple correlation-type empirical schemes, such as group additivity(169,170) or molecular connectivity mapping schemes.(170-172) Since intramolecular vibrations are expected to contribute a major fraction of the total heat capacity, it is unknown how much of the correlation is due to the intermolecular forces which define many properties of the liquid. In fact, correcting empirically estimated thermodynamic properties for internal vibrational components is rare.

Figures 2.11, 4.4 and 4.5 show that external heat capacities for molecular organic liquids are, on average, larger than the solid ($C_{p,\text{ext}} > 9\ R$) and that there is a wider variance in the heat capacities from compound to compound. Other commonly observed positive heat capacity changes are premelting for solids and prefreezing for liquids as the fusion temperature is approached.(140,162) This suggests that the difference between the two heat capacities at the fusion temperatures, $\Delta_{\text{fus}}C_p$, is better estimated by some value greater than zero and that free rotation or translation is not achieved in the liquid state. Here free rotation would result in a lower liquid heat capacity than that of the solid.

The investigation of ideal gas heat capacities showed that heat capacities for molecules, which have not achieved free internal rotation, were semi-empirically estimated using statistical mechanical descriptors of flexibility and symmetry. This same approach was used here to find an empirical correlation model for estimating the heat capacity change at the fusion temperature. This approach has been widely used in estimation equations for entropies of fusion and can be used to explain observed correlations with fusion temperatures. A brief description of these empirical relationships for fusion entropies is given before returning to subject of estimating $\Delta_{\text{fus}}C_p$, because they also were investigated for correlation with $\Delta_{\text{fus}}C_p$.

4.4 Fusion entropies and empirical relationships

The goal of many studies has been to find empirical rules for entropies of fusion.(162,173-178) Some of the motivation to find the average entropy of fusion comes from considering the entropy of vapourisation *via* Trouton's rule.(179) Trouton(179) pointed out that entropies of vapourisation are approximately $\Delta_{\text{vap}}S \approx 88$ J K^{-1} mol^{-1}. The consistency of Trouton's rule is mainly due to the contribution from the expansion of a small volume liquid to a large volume gas.(162,173) The volume change, $\Delta_{\text{fus}}S$(vol), is not the only contributor to entropies of fusion. In addition, entropies of fusion are smaller than those for vapourisation have a much larger variance from compound to compound, *ca.* 50 J K^{-1} mol^{-1}.(173) Other examples of major contributions to fusion are rotational, positional and conformational disorder changes. In addition, molecular symmetry(63,180-182) and structural group contributions(183,184) (group additivity) are common methods for estimating fusion entropies.

The melting enthalpies and temperatures for 428 molecular organic solids listed in the 2000-2001 CRC Handbook of Chemistry and Physics(185) have been used to calculate the fusion entropies which are shown in figure 4.6. The values have a wide range, $\Delta_{fus}S = 3$ to $226\ J\ K^{-1}\ mol^{-1}$, and an average value of $\Delta_{fus}S = 51 \pm 57\ J\ K^{-1}\ mol^{-1}$. Gilson(173) has compiled and presented a similar figure and has discussed several generalities. As discussed by Gilson,(173) the distribution of fusion entropies is not symmetric and shows more than one statistical population. The distribution includes three groups; $\Delta_{fus}S \lesssim 21$, $25 \lesssim \Delta_{fus}S \lesssim 90$ and $\Delta_{fus}S \gtrsim 90\ J\ K^{-1}\ mol^{-1}$.

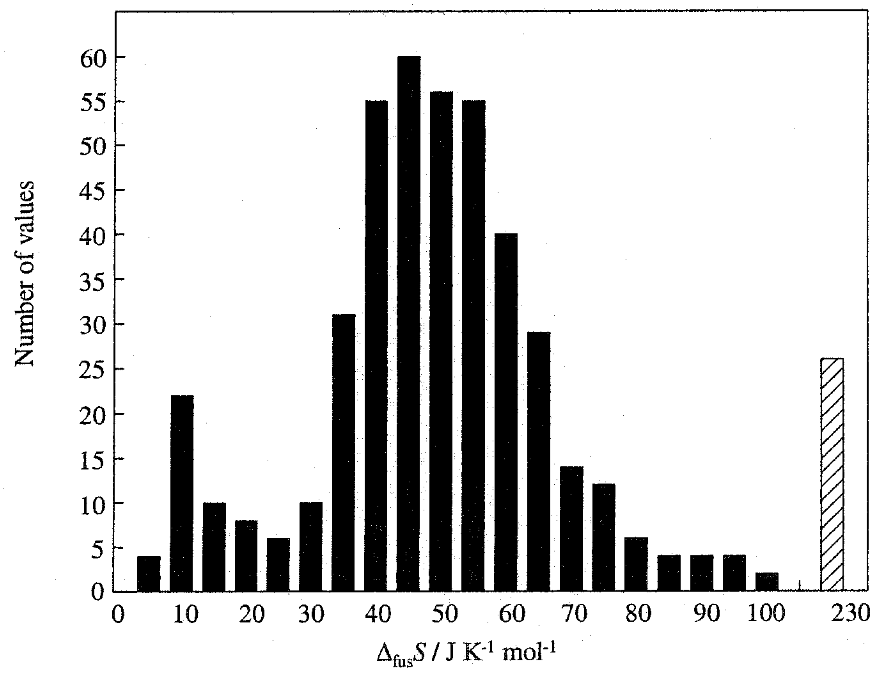

Figure 4.6 Histogram of $\Delta_{fus}S$ for 428 organic molecular solids. Data from ref.(185) ▨ is the number of values from $\Delta_{fus}S = 107.5$ to $230\ J\ K^{-1}\ mol^{-1}$.

Fusion entropies in the range of $\Delta_{\text{fus}}S = 50$ to 60 J K^{-1} mol^{-1} are normal for rigid molecules with no special properties associated with disorder in the solid or the liquid phase. As Timmermans(186) suggested, those with $\Delta_{\text{fus}}S \lesssim 21$ J K^{-1} mol^{-1} ($\Delta_{\text{fus}}S \lesssim 2.5R$) are generally rigid spherically shaped molecules (globular) where there is dynamic rotational or translational disorder in the solid. Thus, much of the order-disorder melting entropy has been accounted for prior to melting. The fusion entropies where $\Delta_{\text{fus}}S \gtrsim 90$ J K^{-1} mol^{-1} generally belong to molecules with long chains or additional intramolecular degrees of freedom. These degrees of freedom are confined in the crystal lattice but not in the liquid. The breadth of the distribution also is complicated by liquid association.

Although Gilson's explanation is simple and understandable, his observations about fusion entropies are not new. Walden(177) observed that rigid organic molecules generally have a fusion entropy of $\Delta_{\text{fus}}S \approx 54$ J K^{-1} mol^{-1} (Walden's rule) and several studies have described the correlation of fusion entropies with chain length.(162,175-178) A simple equation for *n*-alkanes, given by Yalkowsky(178), is one example of these types of empirical correlations:

$$\Delta_{\text{fus}}S = 56.5 + 10(n-5)\,, \tag{4.11}$$

where n is the number of carbon atoms. This internal or intramolecular contribution is consistent with the observation that the fusion entropy does not increase for *n*-alkanes less that 5 carbons in chain length.(140,173) The first coefficient in equation 4.11 is a value close to Walden's rule.(177)

Others have suggested that hydrogen-bonding groups, such as -OH and -NH$_2$, cause association within the liquid, which lowers the fusion entropy.(162,173,180) Yalkowsky(178) has discussed association in the liquid and observed that, at least for some substituted benzenes, the presence of these groups does not appreciably change the fusion entropy. Yalkowsky(178) also discussed the possibility of a correlation of fusion entropies with symmetry.

Carnelley$^{(181,182)}$ observed that higher molecular symmetry increases the melting point of a chemical (Carnelley's rule). This was the subject of Gavezzotti's 1995 study,$^{(63)}$ from which the quote at the beginning of this chapter was taken. Gavezzotti,$^{(63)}$ as many others,$^{(180,187,188)}$ concluded that symmetric molecules melt higher with an increase in molecular symmetry. Gavezzotti$^{(63)}$ also has searched the CSD for packing properties and concluded that the fusion temperature is poorly correlated with close packing or point group symmetry. Rockwell *et al.*$^{(189)}$ have pointed out the importance of considering the stability of the liquid phase, which solid molecular packing arguments ignore. In other words, fusion temperature is affected through an enthalpy-entropy compensation, $T_{\text{fus}}=\Delta_{\text{fus}}H \,/\, \Delta_{\text{fus}}S$.

Lack of rotational distinguishability for higher molecules of higher symmetry can reduce the relative entropy of the liquid and the fusion entropy. In this case, the fusion entropy is lowered by symmetry, thus the fusion temperature rises if the fusion enthalpy has not changed appreciably. Dannenfelser and Yalkowsky in 1996 proposed another empirical equation for predicting fusion entropies for organic molecules,$^{(188)}$

$$\Delta_{\text{fus}}S = 50 - R\ln\sigma + \tau R\ln 2.85\,, \tag{4.12}$$

where σ is the rigid molecular rotational symmetry number and τ is the number of torsional angles. The constant, 2.85, was given by Temperley$^{(190)}$ to reflect the degrees of freedom for an *n*-alkane *trans-gauch* conformation. Dannenfelser and Yalkowsky$^{(188)}$ have chosen to refer to $\phi = 2.85^{\tau}$ as a molecular flexibility number. Equation 4.12 addresses both intramolecular entropic contributions and symmetrical rigid rotator considerations. In addition, the correlation is conveniently simple.

Centre of mass type arguments also have been discussed in the literature. Specifically, in some cases, fusion has been explained by considering a solid-solid transition. Therefore, the entropy is related to differences between the intermolecular vibrational temperature of the solid and liquid. Ultimately this amounts to differences in intermolecular force constants, since the mass of the molecules is the same in both solid and liquid.(103) In addition, the volumetric differences can be attributed to the different force constants.(162,191) While a vibrational temperature change and a volume change will cause a change in entropy, this model fails to account for appreciable heat capacity differences.

Chickos *et al.*(183,184) have reported a slightly more complicated group contribution method for predicting fusion entropies. Interestingly enough, Chickos *et al.*(183) have justified choosing a group additivity scheme based on the distribution of entropies reported in the same paper by Leclercq *et al.*,(85) *i.e.*, the same paper which prompted the writing of this chapter. Group additivity schemes are common and have had success in predicting fusion enthalpies(192) and other thermodynamic properties of gases,(94,95) liquids, solids(193) and solutions.(194,195) Tesconi and Yalkowsky(192) have reviewed both the Dannenfelser and Yalkowsky(188) and the Chickos *et al.*(183,184) methods and determined that both methods are able to predict fusion entropies to within *ca.* 11 J K^{-1} mol^{-1} for 934 organic compounds. Both methods rely on empirical correlations which can include volumetric, symmetric and structural information.

Walden's rule, Carnelley's rule and the above methods lend insight into solid-liquid entropy differences. In addition there are many advantages to being able to estimate fusion entropies: (1) With the prediction of fusion enthalpies, the melting temperatures of materials can be estimated. (2) With the fusion temperature (predicted or measured) the ideal solubility of a crystalline compound can be estimated. (3) Measured fusion entropies can be compared to expected values. (4) The success of some correlations can contribute to an understanding of both solid and liquid thermodynamics. If experimental fusion entropies are used in thermodynamic cycles over a significant temperature range,(51,138) a good estimation of the heat capacity change at the fusion temperature also is important; see conclusions of Section 2.3.

4.5 An empirical equation for estimating the heat capacity of fusion

4.5.1 Objective

Apart from showing the success of *ab initio* estimations of vibrational heat capacities, Chapter three also showed a correlation between order-disorder heat capacity changes and order-disorder entropy changes. The $\Delta_{\text{fus}}C_p$ values of Neau and Flynn(91) and Leclercq *et al.*(85) do not correlate well with $\Delta_{\text{fus}}S$, figure 4.7. Figure 4.7 also suggests that molecular symmetry has a stronger affect on $\Delta_{\text{fus}}C_p$ than $\Delta_{\text{fus}}S$, because the chiral molecules are high outliers for $\Delta_{\text{fus}}C_p$ but not for $\Delta_{\text{fus}}S$. As shown previously, correlations between molecular symmetry and heat capacity changes are not unprecedented.

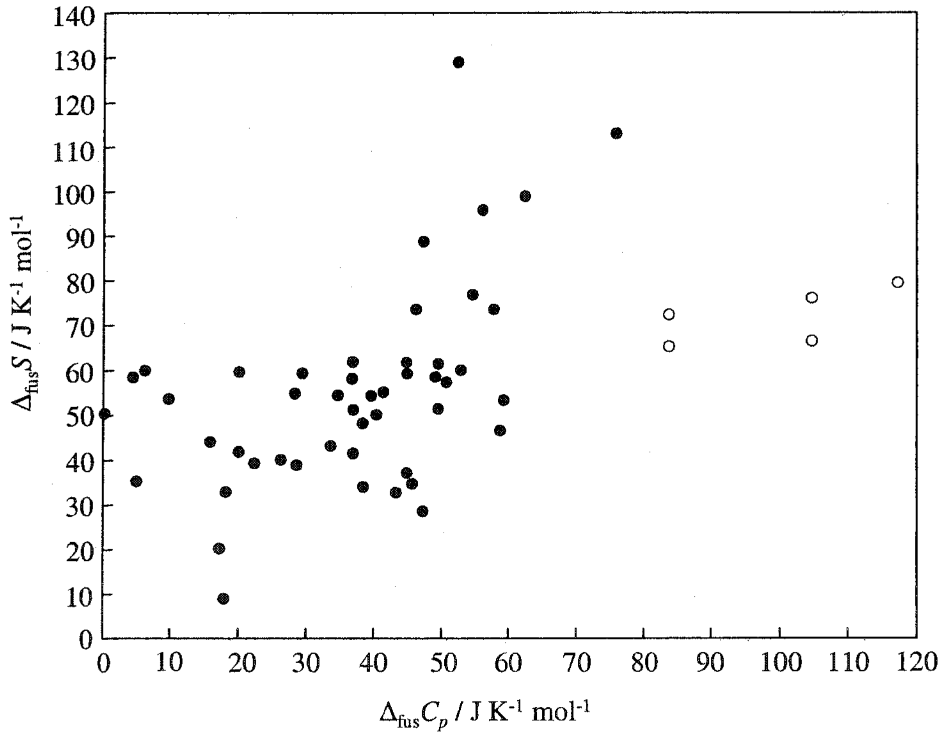

Figure 4.7 Fusion entropies versus solid-liquid heat capacity differences at the fusion temperature. ○ chiral molecules, data from Leclercq *et al.*;(85) ● achiral molecules, data from Neau and Flynn.(91)

The simplest estimation of $\Delta_{\text{fus}}S$ is given by Walden's rule ($\Delta_{\text{fus}}S \approx 54$ J K^{-1} mol^{-1}). A similar type of estimate for heat capacity differences at the fusion temperature include using the common assumptions of $\Delta_{\text{fus}}C_p \approx 0$ J K^{-1} mol^{-1} and $\Delta_{\text{fus}}C_p \approx \Delta_{fus}S$ J K^{-1} mol^{-1}(91,143) or, based on the data in figure 4.7, the average value of $\Delta_{\text{fus}}C_p \approx 49 \pm 58$ J K^{-1} mol^{-1}.

The objective of the present study was to improve the estimation of the fusion heat capacity difference by finding some empirical relationship based on a reasonable and simple structural scheme, like those discussed with fusion entropies. Many values and empirical indices are available for testing correlations; however, very few include symmetry numbers. Like other structure-property studies, the aim was to ensure that the scheme is practical, by being simple and general.

Schemes that were tested for good correlation included various additivity schemes, the molecular flexibility number of Dannenfelser and Yalkowsky,(188) various molecular connectivity indices(171) and *ab initio* derived indicators. In addition, these were combined with experimental fusion temperatures, enthalpies and entropies. While these schemes were not particularly successful, a theoretical graph descriptor was found based on limited knowledge of general internal rotation potentials and a combination of ideas discussed previously for ideal gases and fusion entropy correlation schemes.

4.5.2 Correlation scheme

In Chapter three, the potential energy surfaces of some simple alkanes were discussed in terms of rotating dihedral angles. Without examining these computationally expensive potential energy surfaces, the number of minima and the symmetry of the potential energy surfaces were estimated by simply examining the structures. For example, the rotation of a methyl group provides three indistinguishable dihedral angles; therefore, there are three minima and the internal symmetry number also is three. Rotation of an ethyl group of a simple *n*-alkane provides three minima (two equivalents) and a rotational symmetry of two. In fact the symmetry numbers are almost easier to predict by visual examination than the number of minima or the number of conformations. In this scheme all, as with the correlation equation for ideal gas *n*-alkanes, conformations are considered to be of equivalent energy and distinguishability is determined using rotational symmetry numbers.

The experimental heat capacity differences compiled by Neau and Flynn(91) and Leclercq *et al.*(85) were represented by

$$\Delta_{\text{fus}} C_p = 35.3 \pm 1.8 + (1.558 \pm 0.094) R \ln \frac{\phi}{\sigma_{\text{ext}} \sigma_{\text{int}}}, \tag{4.13}$$

where ϕ is the estimated number of conformations and σ_{int} and σ_{ext} are the internal and external rotational symmetry numbers, respectively, as given in table 4.2.

For simplicity the number of conformations is estimated by

$$\phi = 3^{n_{sp^3-X}} 2^{n_{sp^2-sp^2}}, \tag{4.14}$$

where $n_{sp^3\text{-}X}$ is the number of dihedral angles involving a bond with at least one non-terminal sp^3 hybridized atomic orbital and $n_{sp^2\text{-}sp^2}$ is the number of dihedral angles involving a bond between two non-terminal sp^2 hybridized atomic orbitals. Only those bonds that can be rotated without breaking any other bonds are considered. Therefore bonds within a ring were not considered.

Table 4.2 Experimental fusion entropies and heat capacities differences for the 53 compounds used for testing correlation equations.

Formula	Name	$\Delta_{fus}S$ [a]	$\Delta_{fus}C_p$ [a]	σ_{ext}	σ_{int}	ϕ	Ref.
CH_3NO_3	methylnitrate	43.3	33.6	1	$2\cdot3$	3^2	153
CH_5N	methylamine	34.1	38.4	1	3	3	154
C_2H_7N	dimethylamine	32.8	43.2	1	3^2	3^2	154
$C_2H_8N_2$	1,1-dimethylhydrazine	46.7	58.7	1	$2\cdot3^2$	3^3	153
C_2ClF_3	chlorotrifluoroethene	48.3	38.4	1	2	2	153
C_3H_8S	isopropylmercaptan	40.2	26.2	1	$2\cdot3^2$	3^3	153
C_3H_9N	trimethylamine	42.0	20.1	3	3^3	3^3	154
C_4H_4O	furan	20.3	17.3	2	1	1	153
$C_4H_8O_2$	ethylacetate	55.2	41.2	1	$2^2\cdot3^2$	3^4	154
$C_4H_{10}S$	*t*-butylmercaptan	9.0	17.9	3	3^4	3^4	153
$C_5H_{12}S$	amylmercaptan	88.8	47.3	1	$2^4\cdot3$	3^5	153
C_6H_6	benzene	35.4	5.0	12	1	1	155
C_6H_{14}	hexane	73.6	46.0	2	$2^3\cdot3^2$	3^5	155
C_7H_8	toluene	37.2	44.8	2	3	3	155
$C_7H_8O_4S_2$	benzyl alcohol	34.8	45.6	1	2^2	3^2	155
C_7H_{16}	heptane	76.9	54.5	2	$2^4\cdot3^2$	3^6	155
C_7H_{16}	2-methylhexane	59.3	44.8	1	$2^3\cdot3^3$	3^6	155
C_7H_{16}	2-ethylpentane	61.8	44.7	1	$2^3\cdot3^3$	3^6	155
C_7H_{16}	2,2-dimethylpentane	39.0	28.5	1	$3^4\cdot2^2$	3^6	155
$C_8H_7O_3F$	*m*-fluoromandelic acid	66.5[b]	104.6	1	1	3^4	85
$C_8H_7O_3F$	*o*-fluoromandelic acid	76.4[b]	86	1	1	3^4	c
$C_8H_8O_3$	mandelic acid	65.3[b]	83.7	1	2	3^4	85
$C_8H_9NO_2$	methyl-p-aminobenzoate	58.6	49.0	1	$2^3\cdot3$	$2\cdot3^3$	91
C_8H_{10}	ethylbenzene	51.5	49.4	1	$3\cdot2$	3^2	155
C_8H_{10}	*o*-xylene	54.9	28.2	2	3^2	3^2	155
C_8H_{10}	*m*-xylene	51.3	36.9	2	3^2	3^2	155
C_8H_{10}	*p*-xylene	59.7	20.0	4	3^2	3^2	155
$C_8H_{17}Br$	1-bromo-octane	113.1	75.8	1	$2^6\cdot3$	3^7	153
C_8H_{18}	octane	95.9	56.0	2	$2^5\cdot3^2$	3^7	155
$C_9H_9O_3F$	3-(*p*-fluorophenyl)hydracrylic acid	76.1[b]	104.6	1	2	3^5	85
$C_9H_{10}O_4$	erthyrophenylglyceric acid	79.5[b]	117.2	1	2	3^6	85
$C_9H_{11}NO_2$	ethyl-*p*-aminobenzoate	61.5	49.0	1	$2^4\cdot3$	$2\cdot3^4$	91
C_9H_{12}	propylbenzene	53.4	59.2	1	$3\cdot2^2$	3^3	155
C_9H_{12}	1,2,3-trimethylbenzene	33.0	18.1	2	3^3	3^3	155
C_9H_{12}	1,2,4-trimethylbenzene	50.2	40.3	1	3^3	3^3	155
C_9H_{12}	1,3,5-trimethylbenzene	41.6	36.9	6	3^3	3^3	155
$C_{10}H_8$	naphthalene	53.7	9.7	4	1	1	156
$C_{10}H_{13}NO_2$	propyl-*p*-aminobenzoate	59.4	29.0	1	$2^5\cdot3$	$2\cdot3^5$	91
$C_{11}H_{10}$	1-methylnaphthalene	28.6	47.2	1	3	3	156
$C_{11}H_{10}$	2-methylnaphthalene	39.4	22.4	1	3	3	156
$C_{11}H_{15}NO_2$	butyl-*p*-aminobenzoate	61.9	37.0	1	$2^6\cdot3$	$2\cdot3^6$	91
$C_{12}H_8S$	dibenzothiophene	58.2	36.6	2	1	1	157
$C_{12}H_{10}$	acenaphthene	58.5	4.4	2	1	1	158
$C_{12}H_{10}$	biphenyl	54.4	39.5	4	2	2	157
$C_{12}H_{10}O$	diphenyl ether	57.4	50.6	2	2^2	3^2	159
$C_{12}H_{16}$	cyclohexylbenzene	54.5	34.7	1	2	3	157
$C_{12}H_{17}NO_2$	pentyl-*p*-aminobenzoate	73.6	58.0	1	$2^7\cdot3$	$2\cdot3^7$	91
$C_{13}H_{10}$	fluorene	50.5	0.1	2	1	1	158
$C_{13}H_{12}O_2$	2-(1-naphthyl)propionic acid	72.4[b]	83.7	1	3	3^4	85
$C_{13}H_{19}NO_2$	hexyl-*p*-aminobenzoate	99.0	62.0	1	$2^8\cdot3$	$2\cdot3^8$	91
$C_{14}H_{10}$	anthracene	60.0	6.2	4	1	1	160
$C_{14}H_{10}$	phenanthrene	44.2	15.8	2	1	1	158
$C_{16}H_{25}NO_2$	nonyl-*p*-aminobenzoate	129.0	52.0	1	$2^{11}\cdot3$	$2\cdot3^{11}$	91
$C_{19}H_{16}$	triphenylmethane	60.1	52.8	3	2^3	3^3	153

[a] / $J\ K^{-1}\ mol^{-1}$; [b] $\Delta_{fus}S = \Delta_{fus}S^{Rac}$; [c] Experimental heat capacity to be reported in Chapter eight.

External symmetry numbers were estimated by considering terminal -CH_3, -NH_2 and -OH groups as rapidly rotating. Thus, these groups are considered spherically symmetric on a rigid molecule of the highest symmetry. Choosing molecular symmetry numbers in this way has been outlined by Benson and Buss.(93) Internal symmetry numbers can be estimated by rotating the groups on one side of the bond through 360°, while keeping all other bonds in the original and most symmetrical position (rigid).

4.5.3 Discussion

Equation 4.13 reproduced experimental heat capacity differences, within 3*R* at a 95% confidence level ($R^2 = 0.82$, *S.E.* = 12.5 J K^{-1} mol^{-1}); see figure 4.8. This accuracy is comparable with the reproducibility of the Dannenfelser and Yalkowsky(188) equation for estimating fusion entropies. The 95% confidence interval is a significant improvement over the mean value of $\Delta_{fus}C_p \approx 6 \pm 7\ R$ as calculated from these same data.

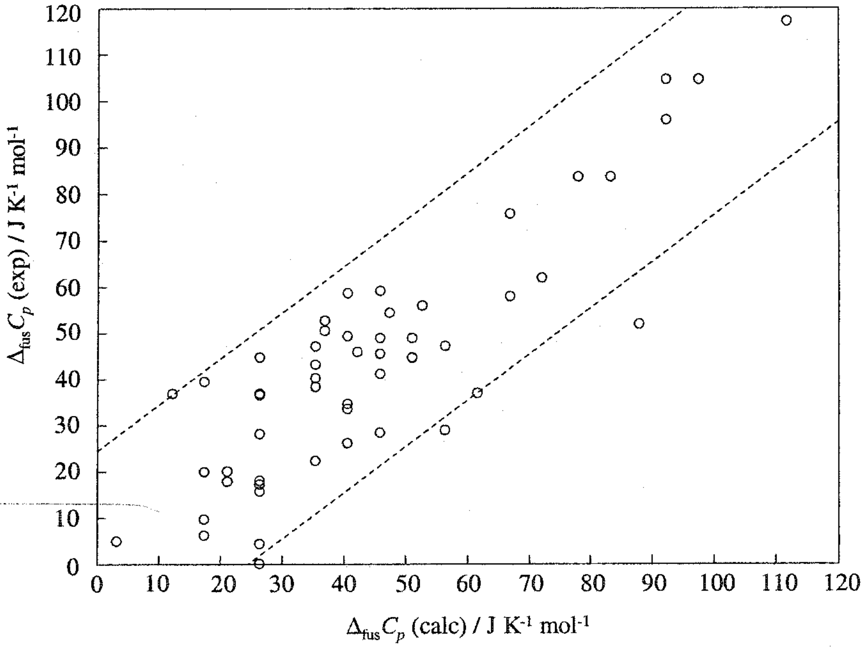

Figure 4.8 Experimental solid-liquid heat capacity differences at the fusion temperature versus the estimated values. Experimental data from Leclercq *et al.*(85) and Neau and Flynn.(91) Estimated values calculated using equation 4.13.

The counting of three configurations for every bond involving *sp*^{3} hybridized orbitals is an estimate which is expected to over count the number of conformations. Some molecules will have conformations which are of much higher energy and some can have only two minima or even one minimum. Two examples are the H_2N-C_6H_4- bond of the aminobenzoates and the OC-OH bond of carboxylic acids. Despite this over counting, the overall molecular flexibility seems to be well represented by equation 4.14, based on the success of the correlation.

Molecular connectivity mapping schemes apparently fail to represent this flexibility and additivity ignores the effects of symmetry. While Dannenfelser and Yalkowsky's(188) flexibility indicator is similar, it was found to poorly represent the heat capacity differences. This is in agreement with the poor correlation between the heat capacity differences and fusion entropies shown in figure 4.7.

The inclusion of the internal rotational symmetry numbers seems to be a major reason why equation 4.13 performs better than other correlation type equations. With the inclusion of internal rotational symmetry, the distinguishability of conformations is increased for molecules with atomic chiral centres, *i.e.*, rotation about a bond where one side of the bond is chiral often amounts to a symmetry number of one for all bonds. In addition, all the chiral molecules in this list contain *sp*^{3} chiral carbons; therefore this lack of symmetry affects at least four dihedral angles. This is not to say that there is no symmetry in a chiral molecule. For example, the potential energy surfaces of mandelic acid and *o*-fluoromandelic acid are shown in figure 4.9 for the rotation of the phenyl and hydroxyl groups, XH_4C_6-C and C-OH_{al} bonds. The figure shows that rotation of the phenyl ring has an internal symmetry of two for mandelic acid; however, this symmetry is lost for the *ortho*- or *meta*-substituted mandelic acids, *e.g.* *o*-fluoromandelic acid.

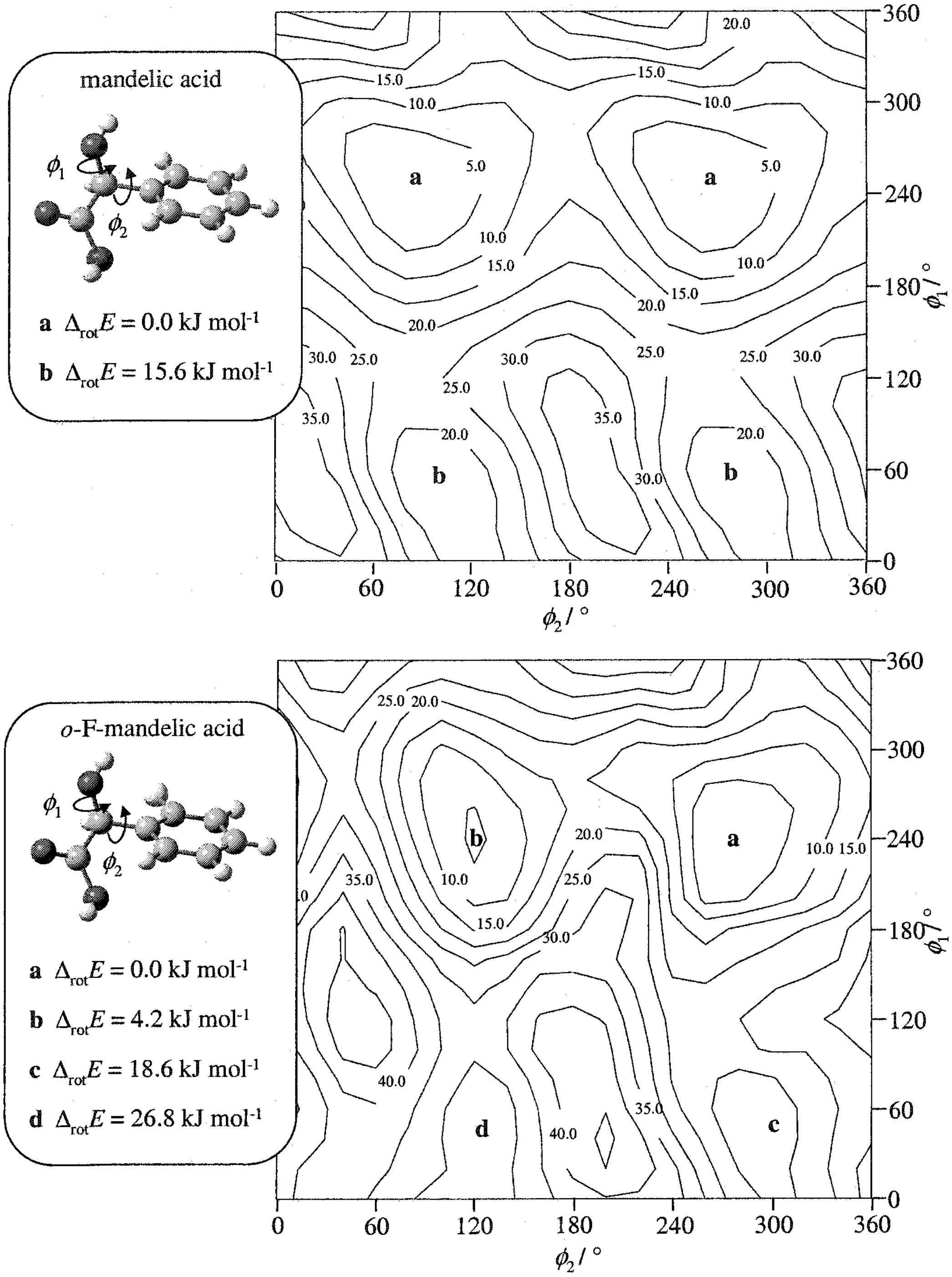

Figure 4.9 The *ab initio* calculated potential energy surfaces of mandelic acid and *o*-fluoromandelic acid. All potential energies are given relative to the lowest energy, configuration **a**, and in units of kJ mol^{-1}. Surface scans have been performed at the B3LYP/6-311G(d,p) theory level.

The flexibility and symmetry relationship shown here can provide the heuristics for predicting other properties where symmetry is expected to be a dominant factor. In the future it would be convenient to test the utility of equation 4.13 for molecules not included in the input set. In terms of an immediate application, the prediction of the fusion heat capacity differences at the fusion temperature has already been identified as being important towards the calculation of racemic and conglomerate crystal stability.(51,85)

4.6 Returning to racemic and conglomerate crystal stability

As discussed in the second chapter, a list of thermodynamic information for a significant number of crystal pairs provides fundamental interpretations of nature's preference for racemic crystals. Several research groups have systematically determined melting point phase diagrams or X-ray structures for related groups of enantiomeric molecules.(66,196-201)

During the early 1970's the research groups headed by Professor Jean Jacques and the late Professor André Collet(202) focussed on the resolution and measurement of the physical properties of many enantiomers. Among of these studies were related molecules such as derivatives of mandelic acid and 3-phenylhydracrylic acid (3-hydroxy-3-phenylpropionic acid), where halogens were substituted onto the phenyl rings in the *ortho*, *meta*, and *para* positions.(196,197) Larsen and Marthi have been reviewing and completing the X-ray structures for some of these molecules.(66,200,201) Through these types of studies, where chiral molecules are related as much as possible, the first large list of thermodynamic values was compiled and reported by Leclercq *et al.*(85) The list contained 36 experimental fusion temperatures and enthalpies for racemic crystals and their respective optically pure crystals. Brock *et al.*(51) and Leclercq *et al.*(85) have given thermodynamic arguments using this list.

In another example, Nemák *et al.*(199) have determined the melting point phase diagrams for 2',6'-pipecoloxylidide and four 1-alkyl-2',6'-pipecoloxylidides, where the alkyl chains varied in length. Using the fusion temperatures and enthalpies reported by Nemák *et al.*,(199) equations 1.1 and 1.2 have been used here to calculate the phase diagrams shown in figure 4.10. The study shows a small variance with respect to racemic crystal stability and the length of the alkyl chain. The phase diagrams calculated from the data of Nemák *et al.,*(199) figure 4.10, show that 1-*n*-butyl-2',6'-pipecoloxylidide forms a conglomerate.

Nemák *et al.*(199) have noted that 1-methyl-2',6'-pipecoloxylidide and 1-*n*-butyl-2',6'-pipecoloxylidide are active ingredients in the local anaesthetics Mepivacaine and Bupivacaine, respectively.(203) In spite of the different enantiomers of these drugs having different pharmacological activities, they were still on the market as racemates.(199,204) If 1-*n*-butyl-2',6'-pipecoloxylidide is a conglomerate, as the phase diagram suggests, an industrial scale resolution by selective precipitation of the active ingredient in the Bupivacaine anaesthetic might be feasible.

Li *et al.*(198) have discussed and performed calculations using 19 racemic and conglomerate crystal pairs of pharmaceutically active molecules. Their calculations have followed the same method and assumptions as Leclercq *et al.*(85) Li *et al.*(198) have concluded "The free energy calculations show that the entropy of mixing is the driving force for the formation of racemic compounds."

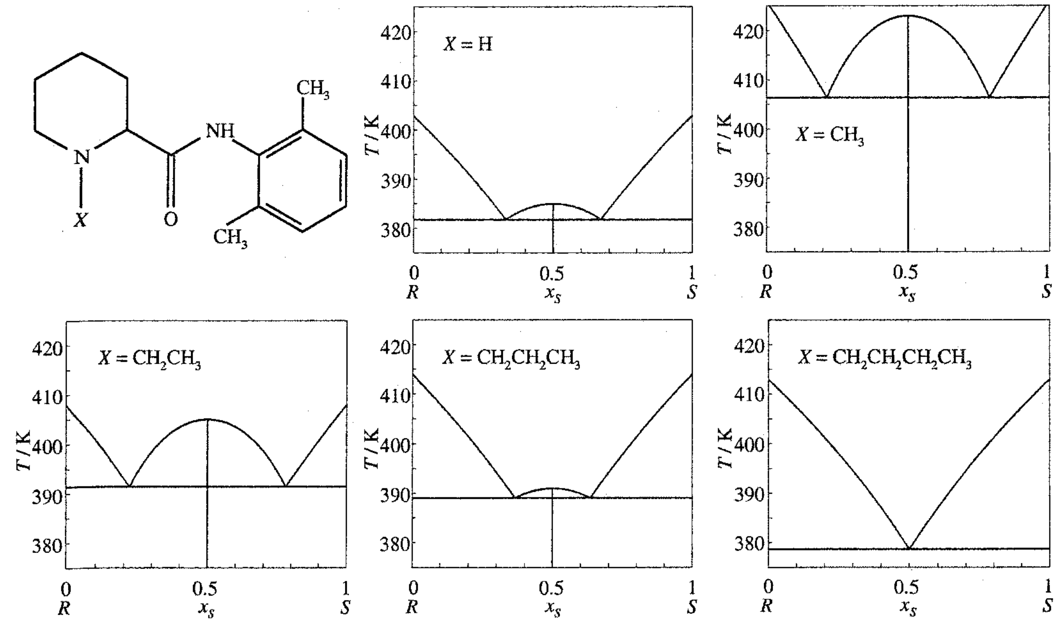

Figure 4.10 The calculated melting point phase diagrams of the 1-*X*-2',6'-pipecoloxylidides. Calculated from the fusion data from Nemák *et al.*(199)

For the calculations performed here, the lists of Leclercq *et al.*,(85) Li *et al.*(198) and Nemák *et al.*(199) have been combined to provide the basis of a larger list with 67 racemic and conglomerate crystal pairs. Fusion temperatures, entropies, internal symmetry numbers, flexibility numbers and estimated heat capacity changes for these species are given in Table 4.3.

Many of the molecules listed in table 4.3 are structurally related. Of particular note are the various mandelic acids, 2-phenoxypropionic acids and 3-phenylhydracrylic acids. As shown in figure 4.9, the phenyl substituent position either destroys or preserves the limited potential energy surface symmetry, *i.e.*, through the phenyl ring rotation.

Table 4.3 The thermodynamic fusion and racemic crystal formation data for some racemic and conglomerate crystal pairs.

Formula	Name	T_{fus}^{Rac}	T_{fus}^{R}	$\Delta_{fus}S^{Rac}$	$\Delta_{fus}S^{R}$	σ_{int}	ϕ	$\Delta_{fus}C_p$	T_{fus}^{con}	$\Delta_{Rac}H$	$\Delta_{Rac}S$	$\Delta_{Rac}G$	Ref.
		a		b				b	a	c	b	c	
$C_4H_6O_5$	malic acid	402	376	68.6	61.1	1	3^6	121	340	-1.46	6.35	-3.62	85
$C_8H_7O_3F$	*o*-fluoromandelic acid	390	363	77.4	57.7	1	3^4	92	327	-6.76	-7.34	-4.35	85
$C_8H_7O_3F$	*m*-fluoromandelic acid	370	394	66.5	61.5	1	3^4	92	358	-2.58	-5.02	-0.79	85
$C_8H_7O_3F$	*p*-fluoromandelic acid	403	426	72.8	71.5	2	3^4	83	393	-0.79	-0.14	-0.73	85
$C_8H_7O_3Cl$	*m*-chloromandelic acid	388	380	69.6	65.8	1	3^4	92	348	-1.26	3.88	-2.61	196
$C_8H_7O_3Cl$	*p*-chloromandelic acid	394	394	69.2	58.4	2	3^4	83	356	-4.26	-5.04	-2.46	85
$C_8H_7O_3Br$	*m*-bromomandelic acid	394	378	76.1	66.1	1	3^4	92	346	-3.53	-0.42	-3.38	196
$C_8H_7O_3Br$	*p*-bromomandelic acid	392	404.	61.2	59.3	2	3^4	83	366	-1.05	1.22	-1.49	196
$C_8H_8O_3$	mandelic acid	392	406	65.3	64.9	2	3^4	83	371	-0.41	2.45	-1.32	85
$C_9H_9NO_5$	2-(*p*-nitrophenoxy)propionic acid	411.5	362	78.2	57.7	$2^2\cdot3$	$2\cdot3^4$	83	327	-7.18	-4.10	-5.84	85
$C_9H_9O_3F$	3-(*o*-fluorophenyl)hydracrylic acid	342	348	79.5	64.9	1	3^5	106	318	-5.24	-10.7	-1.85	85
$C_9H_9O_3F$	3-(*p*-fluorophenyl)hydracrylic acid	362	381	76.1	82.4	2	3^5	97	355	2.00	7.10	-0.52	85
$C_9H_9O_3Cl$	3-(*o*-chlorophenyl)hydracrylic acid	364	357	74.2	61.6	1	3^5	106	324	-4.28	-4.78	-2.73	197
$C_9H_9O_3Cl$	3-(*m*-chlorophenyl)hydracrylic acid	340	368	70.3	76.1	1	3^5	106	341	1.13	3.17	-0.05	85
$C_9H_9O_3Cl$	2-(*o*-chlorophenoxy)propionic acid	388	369	82.8	72.4	3	3^5	92	340	-3.66	-0.02	-3.66	85
$C_9H_9O_3Cl$	2-(*m*-chlorophenoxy)propionic acid	386	367.	85.8	80.8	3	3^5	92	342	-1.72	5.28	-3.53	85
$C_9H_9O_3Br$	3-(*o*-bromophenyl)hydracrylic acid	370	360	73.0	50.0	1	3^5	106	318	-7.95	-14.3	-3.39	197
$C_9H_9O_3Br$	3-(*m*-bromophenyl)hydracrylic acid	349	350	76.6	68.2	1	3^5	106	321	-2.97	-2.94	-2.03	85
$C_9H_9O_3Br$	2-(*p*-bromophenoxy)propionic acid	385	380	82.4	72.8	$2\cdot3$	3^5	83	351	-3.65	-2.75	-2.68	85
$C_9H_{10}O$	1-indanol	324.3	345.	50.9	56.4	1	3	50	312	1.92	8.07	-0.60	4
$C_9H_{10}O_3$	2-phenoxypropionic acid	388	359	85.4	62.8	$2\cdot3$	3^5	83	321	-11.8	-20.4	-5.23	85
$C_9H_{10}O_4$	erthyrophenylglyceric acid	395	371.	79.5	62.8	2	3^6	112	330	-9.16	-14.1	-4.51	85
$C_9H_{13}NO$	norephedrine	374.3	324.	69.76	48.91	$2\cdot3$	3^5	83	287	-6.10	-3.19	-5.19	198
$C_9H_{13}NO\cdot HCl$	norephedrine•HCl	469.1	446.	61.74	45.38	$2\cdot3$	3^5	83	390	-6.81	-6.41	-4.31	198
$C_{10}H_{11}O_3Cl$	2-(2-chloro-3-methylphenoxy)propionic acid	391.5	359.	77.8	61.5	3^2	3^6	92	327	-5.41	-2.69	-4.53	85
$C_{10}H_{12}O_3$	3-hydroxy-3-phenylbutyric acid	330	357	59.4	63.2	$2\cdot3$	3^6	97	325	-0.34	1.93	-0.29	85

continued ...

Table 4.3 continued.

Formula	Name	T_{fus}^{Rac}	T_{fus}^{R}	$\Delta_{fus}S^{Rac}$	$\Delta_{fus}S^{R}$	σ_{int}	ϕ	$\Delta_{fus}C_p$	T_{fus}^{con}	$\Delta_{Rac}H$	$\Delta_{Rac}S$	$\Delta_{Rac}G$	Ref.
		a		b				b	a	c	b	c	
$C_{10}H_{14}O_8$	dimethyl-O,O'-diacetyltartarate	357.5	377.	77.4	72.0	3^4	3^{13}	163	347	-3.75	-8.51	-0.80	85
$C_{10}H_{15}NO$	Ephedrine	350.7	312.	82.92	55.35	$2•3^2$	3^6	83	281	-8.62	-12.3	-5.15	198
$C_{10}H_{15}NO$	pseudoephedrine	391.1	392.	87.16	81.40	$2•3^2$	3^6	83	366	-2.25	-0.27	-2.16	198
$C_{10}H_{15}NO•HCl$	ephedrine•HCl	464.0	492.	75.26	64.37	$2•3^2$	3^6	83	450	-5.58	-10.0	-1.07	198
$C_{10}H_{15}NO•HCl$	pseudoephedrine•HCl	439.2	456.	64.18	61.26	$2•3^2$	3^6	83	414	-1.65	-0.29	-1.53	198
$C_{10}H_{18}O_2$	*trans*-sobrerol	404.9	423.	85.0	81.9	3^3	3^6	78	395	-1.18	-0.86	-0.84	205
$C_{10}H_{18}O_2$	*cis*-sobrerol	378.9	382.	68.4	60.6	3^3	3^6	78	348	-3.03	-2.86	-2.03	205
$C_{11}H_{12}I_3NO_2$	iopanoic acid	427.0	438.	27.7	26.0	3	3^7	121	396	-3.12	-3.14	-1.88	206
$C_{11}H_{14}O_4$	3-hydroxy-3-phenylvaleric acid	394	379	89.1	81.6	2•3	3^7	112	353	-2.50	2.61	-3.42	85
$C_{11}H_{16}N_4O_4$	Razoxane	507.4	467.	88.63	80.8	3	3^4	78	435	-4.08	4.30	-5.96	207
$C_{12}H_8Br_2$	*trans*-1,2-dibromoacenaphthene	397	416	63.2	63.2	1	1	35.3	380	0.53	4.11	-1.03	85
$C_{13}H_{12}N_2O_4$	2-(1-nitro-2-naphthoxy)propionamide	431	461.	67.8	66.1	2•3	$2•3^6$	92	422	-1.52	-2.23	-0.58	85
$C_{13}H_{12}O_2$	2-(1-naphthyl)propionic acid	422.5	342	72.4	41.4	3	3^4	78	294	-10.2	-8.75	-7.57	85
$C_{13}H_{18}O_2$	Ibuprofen	349.7	326.	73.6	56.2	$2•3^5$	3^8	69	294	-5.79	-6.86	-3.77	198,208
$C_{14}H_{20}N_2O$	2'6'-pipecoloxylidide	385	403	60.1	60.0	$2•3^2$	3^5	69	366	-0.20	2.51	-1.12	199
$C_{14}H_{20}N_2O$	Pindolol	442.9	365.	130.7	70.3	3	3^9	149	335	-20.7	-26.1	-11.9	209
$C_{14}H_{22}N_2O_3$	Atenolol	423.4	420.	84.20	87.44	$2•3^2$	3^{12}	169	393	-1.62	10.2	-2.39	198
$C_{15}H_{22}NO_2$	Alprenolol	331.2	298.	107.5	79.66	3^2	3^{11}	163	277	-6.50	-5.13	-5.07	210
$C_{15}H_{22}N_2O$	1-methyl-2'6'-pipecoloxylidide (mepivicaine)	423	426	40.0	41.7	$2•3^3$	3^6	69	368	0.64	6.98	-1.93	199
$C_{15}H_{23}N_3O_4S$	Sulpiride	451.0	459.	102.3	91.40	3^2	$2•3^9$	144	431	-5.36	-7.83	-1.99	211
$C_{16}H_{12}Cl_2$	1,5-dichloro-9,10-ethanoanthracene	424	353.	65.3	70.7	1	1	35.3	326	-0.21	17.6	-5.94	85
$C_9H_{13}NO•C_7H_6O_3$	norephedrine salicylate	390.5	374.	76.26	62.07	$2^3•3$	$2•3^7$	103	340	-4.89	-4.15	-3.48	198
$C_{16}H_{21}NO_2$	propranolol	365.5	344.	118.9	105.2	3^2	3^9	135	326	-4.39	-0.03	-4.38	198
$C_{16}H_{21}NO_2•HCl$	propranolol•HCl	436.6	467.	89.30	76.93	3^2	3^9	135	433	-7.21	-15.9	-0.32	198
$C_{16}H_{24}N_2O$	1-ethyl-2'6'-pipecoloxylidide (ethycaine)	405	408	44.7	48.8	$2•3^3$	3^7	83	361	1.56	9.25	-1.78	

continued …

Table 4.3 continued.

Formula	Name	T_{fus}^{Rac}	T_{fus}^{R}	$\Delta_{fus}S^{Ra}$	$\Delta_{fus}S^{R}$	σ_{int}	ϕ	$\Delta_{fus}C_p$	T_{fus}^{con}	$\Delta_{Rac}H$	$\Delta_{Rac}S$	$\Delta_{Rac}G$	Ref.
		a		b				b	a	c	b	c	
$C_{17}H_{20}N_2S$	N,N'-*bis*-α-methylbenzylthiourea	410.5	471.	75.3	75.7	$2^2\cdot3^2$	3^8	103	436	-1.50	-8.11	2.04	85
$C_{17}H_{20}O$	benzylidenecamphor	350.3	371	64.9	63.6	$2\cdot3^3$	$2\cdot3^3$	35.3	339	-0.12	2.46	-0.71	85
$C_{17}H_{26}N_2O$	1-propyl-2'6'-pipecoloxylidide (ropivicane)	391	414	60.9	59.2	$2\cdot3^3$	3^8	97	374	-1.53	-1.48	-0.98	199
$C_{18}H_{16}O_2Cl_2$	1,5-dichloro-11,12-di(hydroxymethyl)-9,10-dihydro-9,10-ethanoanthracene *trans* (*exo*)	519.5	527	105	102	1	3^4	92	498	-1.48	1.44	-2.20	85
$C_{18}H_{16}O_2Cl_2$	1,5-dichloro-11,12-di(hydroxymethyl)-9,10-dihydro-9,10-ethanoanthracene *trans* (*endo*)	441	435	74.9	45.2	1	3^4	92	379	-12.8	-22.7	-4.22	85
$C_{18}H_{16}I_2$	11,12-di(iodomethyl)-9,10-dihydro-9,10-ethanoanthracene	468.5	491	71.5	71.5	1	3^2	92	453	-0.46	1.45	-1.12	85
$C_{18}H_{18}O_2$	11,12-di(hydroxymethyl)-9,10-dihydro-9,10-ethanoanthracene	474.5	405.	86.6	59.0	1	3^4	92	367	-10.8	-7.38	-8.11	85
$C_{18}H_{27}NO_2S$	tazofelone	428.9	423.	89.8	57.8	$2\cdot3^4$	3^{11}	126	381	-13.4	-24.7	-3.96	212
$C_{20}H_{16}O_4Cl_2$	1,5-dichloro-9,10-dihydro-9,10-ethano-11,12-dicarbomethoxyanthracene (*exo*)	465	424	79.1	54.4	3^2	3^6	92	380	-9.94	-10.5	-5.98	85
$C_{20}H_{16}O_4Cl_2$	1,5-dichloro-9,10-dihydro-9,10-ethano-11,12-dicarbomethoxyanthracene (*endo*)	436	427	60.2	57.7	3^2	3^6	92	385	-0.78	5.18	-2.78	85
$C_{20}H_{18}O_4$	9,10-dihydro-9,10-ethano-11,12-dicarbomethoxyanthracene (*exo*)	380	363	61.5	46.0	3^2	3^6	92	317	-5.11	-5.53	-3.35	85
$C_{20}H_{18}O_8$	dimethyl-O,O'-dibenzoyltartarate	422.5	409	115	113	$2^2\cdot3^2$	$2^2\cdot3^{11}$	163	388	-0.17	9.06	-3.69	85
$C_{10}H_{15}NO\cdot C_{10}H_8O_3S$	Ephendrine napsylate	443.6	443.	86.79	74.25	$2^3\cdot3^2$	3^8	94	410	-5.57	-6.82	-2.77	198
$C_{20}H_{27}NO_4$	bevantolol	360.6	348.	127.3	124.1	3^3	3^{14}	192	332	-0.32	9.23	-3.38	209
$C_{22}H_{22}O_4$	9,10-dimethyl-9,10-dihydro-9,10-ethano-11,12-dicarbomethoxyanthracene (*exo*)	465	393	88.3	47.3	3^4	3^8	92	345	-15.9	-19.8	-9.03	85
$C_{22}H_{22}O_4$	2,3,3-triphenylvaleric acid	480	441.	77.4	60.7	$2^3\cdot3$	3^7	94	400	-6.73	-3.08	-5.50	85

[a] K^{-1} mol^{-1}, [b] $J\ K^{-1}\ mol^{-1}$, [c] $kJ\ mol^{-1}$

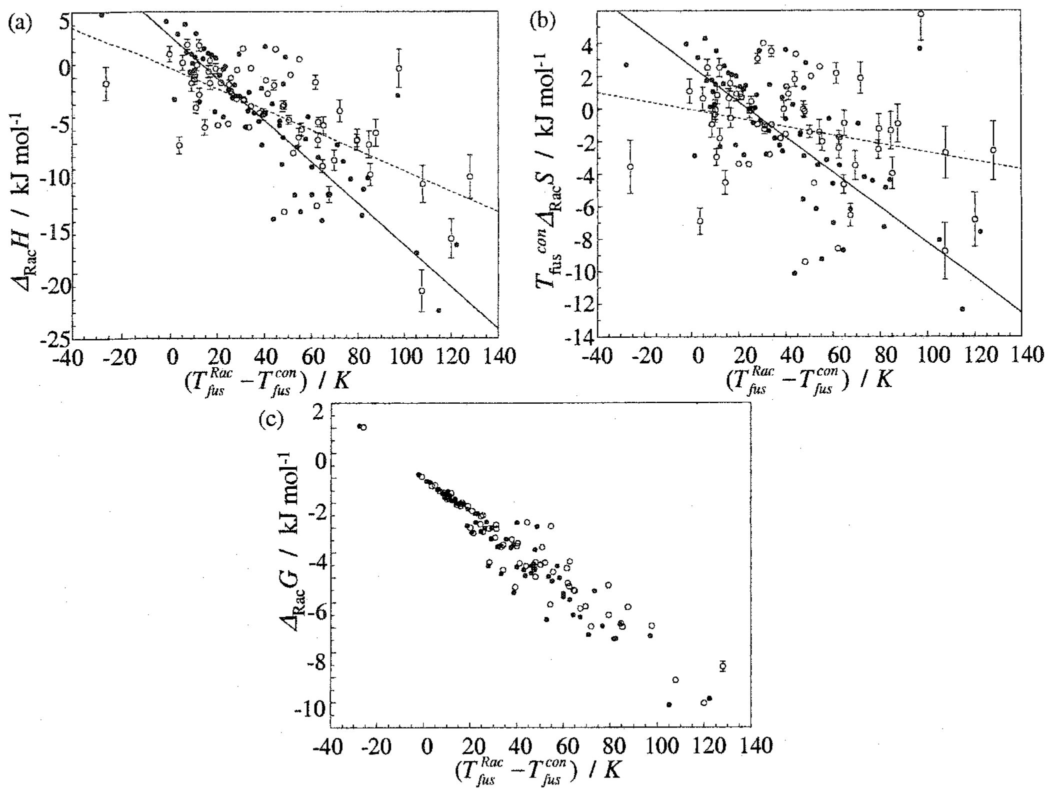

Figure 4.11 The calculated enthalpy, entropy and Gibbs energy changes for forming racemic crystals from conglomerate crystals versus their differences in fusion temperature. (a) enthalpy changes calculated using equation 2.34; (b) entropy changes calculated using 2.35; (c) Gibbs energy changes at the conglomerate fusion temperature calculated using 2.36. Two calculations using the compiled literature data from table 4.3 are shown; ----- , ○ $\Delta_{fus}C_p$ estimated with equation 4.13 and ——,● $\Delta_{fus}C_p = 0$ J K^{-1} mol^{-1}.

Using the estimated change in heat capacities at the fusion temperature from equation 4.13, the Gibbs energy, enthalpy and entropy changes for forming a racemic crystal from a conglomerate were calculated using equations 2.34, 2.35 and 2.36. These results are shown in figure 4.11 where the errors have been estimated using equations 2.41, 2.46 and 2.37. Figure 4.11 also shows the same calculations with the assumption that $\Delta_{fus}C_p = 0$ J K^{-1} mol^{-1}. As was shown by Brock *et al.*$^{(51)}$ and in Chapter two, the estimation of the heat capacity changes at the fusion temperature has as significant affect on the enthalpy and entropy changes associated with this process. A similar figure using only the data of Leclercq *et al.*$^{(85)}$ was shown as figure 2.10.

In figure 4.11 the error in the Gibbs energy, enthalpy and entropy changes have been calculated using equations 2.41, 2.46 and 2.47 with $\delta\Delta_{fus}C_p = \pm 25$ J K^{-1} mol^{-1} and $\delta\Delta_{fus}H = \pm 500$ J mol^{-1}. As expected, the errors in the calculation become larger as the temperature difference becomes larger, *i.e.*, the error in the heat capacity difference estimation becomes more significant.

The average $\Delta_{\text{fus}}C_p$ from equation 4.13, *ca.* 97 ± 26 J K^{-1} mol^{-1}, is in very good agreement with Brock *et al.*(51) and Leclercq *et al.*(85), 96 and 100 ± 20 J K^{-1} mol^{-1} respectively.

Overall the relative stability seems to be predominantly enthalpic in nature, but the entropic differences are significant for some individual crystal pairs. A more accurate method for obtaining and confirming these entropic differences is through experimental heat capacities from near $T = 0$ K up to the liquidus temperature; see the lower cycle in figure 2.8. In this way the reference temperature becomes $T = 0$ K rather than the lower of two different fusion temperatures. These types of data can be used to further provide an independent test of equation 4.13 for the estimation of fusion heat capacity differences. Currently, there are no available low-temperature heat capacities for true racemic and optically pure crystal pairs.

In conclusion, a flexibility and symmetry relationship has been shown to estimate $\Delta_{fus}C_p$. Perhaps the form of this equation can provide the heuristics for predicting other properties where symmetry is expected to be a dominant factor. The correlation equation suggests that the $\Delta_{fus}C_p$ of chiral chemicals are expected to be greater than those of achiral chemicals. Using the heat capacity predictions for a large list of chiral compounds, the large $\Delta_{fus}C_p$ is shown to be important for calculating the relative stability of common enantiomeric crystal types. In addition, the enthalpy of forming a racemic crystal from a conglomerate was found to be correlated with the fusion temperature differences, while the entropy difference is not. The conclusion that stability of a racemic crystal is correlated with an enthalpic difference is in agreement with Brock *et al.*(51) While not general, some entropic changes for forming racemic crystals from the conglomerate are significant for some compounds. The conclusion that racemic and conglomerate crystals are not entropically different is neither supported nor disproved by this lack of correlation. Low-temperature heat capacities could assist with testing the latter hypothesis and investigating the thermodynamic stability differences for individual crystal pairs.

5 THE MANDELIC ACIDS

> *...very visibly affected, the illustrious old man took me by the arm and said: "My dear child, I have loved science so much throughout my life that this makes my heart throb."*
>
> Louis Pasteur, 1860[1]

5.1 Introduction

In Chapters two and four, the calculation of the Gibbs energy change for forming a racemic crystal from the corresponding conglomerate showed that most racemic crystals are enthalpically favoured. Some compounds showed significant entropy changes; however, not all of these entropy changes were in favour of the more stable racemic crystal. Another method outlined in those Chapters was the use of low-temperature heat capacities and the lower temperature thermodynamic cycle shown in figure 2.8.

During the course of this thesis work, an adiabatic calorimeter, a relaxation calorimeter and a differential scanning calorimeter, DSC, were available to measure heat capacities from $T = 0.4$ K up to and beyond the fusion temperature of most racemic and optically pure crystals; see the cycles in figure 2.8. In addition, an X-ray facility was available for obtaining structures at different temperatures. The question became, which racemic and conglomerate enantiomeric systems should be studied? In this chapter, the mandelic acids are proposed and evaluated for calorimetric studies.

Compounds considered for these calorimetric techniques must be available in gram quantities, in high purity and at a reasonable cost. Samples up to *ca.* 2.5 g will yield better heat capacities with the adiabatic calorimeter, by increasing the relative heat capacity of the sample versus the addenda. It also was more convenient to choose compounds which have already received some attention in the literature, *e.g.,* known X-ray structures, known fusion temperatures, known crystal types and known specific optical rotation.

---

[1] Pasteur is quoting Jean Baptist Biot, who tried to replicate Pasteur's experiment but could not. This is Biot's reaction after traveling to Pasteur's lab to witness the experiment. Pasteur's lab was at a different temperature than Biot's lab.

Ideally, compounds which appear to be related as much as possible also were considered. In this way, chemical modification can lead to a better understanding of the interactions which are governing the thermodynamic stability. For example, studies have focussed on controlling crystallisation of chiral molecules by altering counter ions, changing resolving agents, and developing molecules which mimic the shape of other conglomerate-forming species.(3,38) The experiments conducted throughout this thesis will not be extensive enough to complete an entire group of compounds; however, beginning within such a group can direct future studies.

In Chapter four, the various derivatives of mandelic acids (α-hydroxyphenylacetic acids) and 3-phenylhydracrylic acids (3-hydroxy-3-phenylpropionic acids) were introduced as two well-studied families. Some physical properties of the mandelic acids and 3-phenylhydracrylic acids from the literature are shown in table 5.1 with the results of Gibbs energy change calculations using the method outlined in Chapter four, Subsection 4.6. The phase diagrams calculated from the thermodynamic data in table 5.1 are shown in figures 5.1 and 5.2. Figures 5.1 and 5.2 show a large range in racemic crystal stability with different halogen-substitution positions. All but one of the substituted mandelic acids form a racemic crystal as do six of the ten studied 3-phenylhydracrylic acids.

Table 5.1 Some physical properties of the halogen-substituted mandelic acids and 3-phenylhydracrylic acids.

X	T_{fus}^{Rac}	T_{fus}^{R}	$\Delta_{\text{fus}}H^{Rac}$	$\Delta_{\text{fus}}H^{R}$	T_{fus}^{con}	$\Delta_{\text{Rac}}H$	$\Delta_{\text{Rac}}S$	$\Delta_{\text{Rac}}G$	V_m^{Rac}/V_m^{R}	*Rac*-space group	Z_{Rac}	*R*-space group	Z_R	$[\alpha]_{578}$	Ref.
	/ K		/ kJ mol^{-1}		/ K	a	b	a							
									Mandelic acids						
H	392	406	26	26	371.1	-0.41	2.45	-1.32	1.052	Pbca	8	$P2_1$	4	163	196,213,214
o-F	390	363	30	21	327.4	-6.76	-7.34	-4.35	0.948	$P2_1/c$	4	$P2_1$	4	145.5	196,200,215
m-F	370	394	25	24	357.9	-2.58	-5.02	-0.79	1.004	$P2_1/a$	8	$P2_1$	4	129	196,200,215
p-F	403	426	29	31	392.8	-0.78	-0.14	-0.73	1.018	Pbca	8	C2	4	140	196,200,215
o-Cl	358.7	392.7	20	25	*358.0*	Conglomerate		*-0.04*	----	----		----		160.4	196
m-Cl	388	380	27	25	347.6	-1.26	3.88	-2.61	----	----		----		122	196
p-Cl	394	394	27	23	356.2	-4.26	-5.04	-2.46	----	----		----		136	196
o-Br	362	395	21	25	359.5	0.50	1.79	-0.14	----	----		----		143	196
m-Br	394	378	30	25	345.9	-3.53	-0.42	-3.38	----	----		----		100	196
p-Br	392	404.7	24	24	366.5	-1.05	1.22	-1.49	----	----		----		115	196
									3-phenylhydracrylic acids						
H	366	391	30	33	*365.1*	Conglomerate		*-0.07*	----	----		$P2_1$	2	60	197,216
o-F	342	348	27	23	317.6	-5.24	-10.7	-1.85	----	----		----		67	197
m-F	290	311	21	24	*288.3*	Conglomerate		*-0.12*	----	----		----		48	197
p-F	362	381	28	31	355.1	2.00	-2.52	-0.52	1.016	$Pna2_1$	4	$P2_1$	4	52.7	197,217,218
o-Cl	364	357	27	22	324.0	-4.28	-4.78	-2.73	----	----		----		95	197
m-Cl	343	368	24	28	340.8	1.13	3.17	0.05	1.030	$P2_1/c$	4	$P2_12_121$	4	57.5	66,197,201
p-Cl	357	385	28	30	*357.3*	Conglomerate		*0.02*	----	----		$P2_1$	4	50	197,219
o-Br	370	360	27	18	317.9	-7.95	-14.3	-3.39	----	----		----		81	197
m-Br	349	350	27	24	321.0	-2.97	-2.94	-2.03	1.009	$P2_1/c$	4	$P2_12_12_1$	4	39.6	66,197,201
p-Br	371	398	29	33	*371.1*	Conglomerate		*0.01*	----	----		$P2_1$	4	42.5	197,220

a / kJ mol^{-1}; b / J mol^{-1} K^{-1}. $\Delta_{\text{Rac}}G$ calculated for T_{fus}^{con}. T_{fus}^{con} values shown in italics are experimental conglomerate fusion temperatures. Gibbs energy changes for these conglomerate-forming species were calculated for T_{fus}^{con} assuming the 1:1 mixtures were racemic crystals.

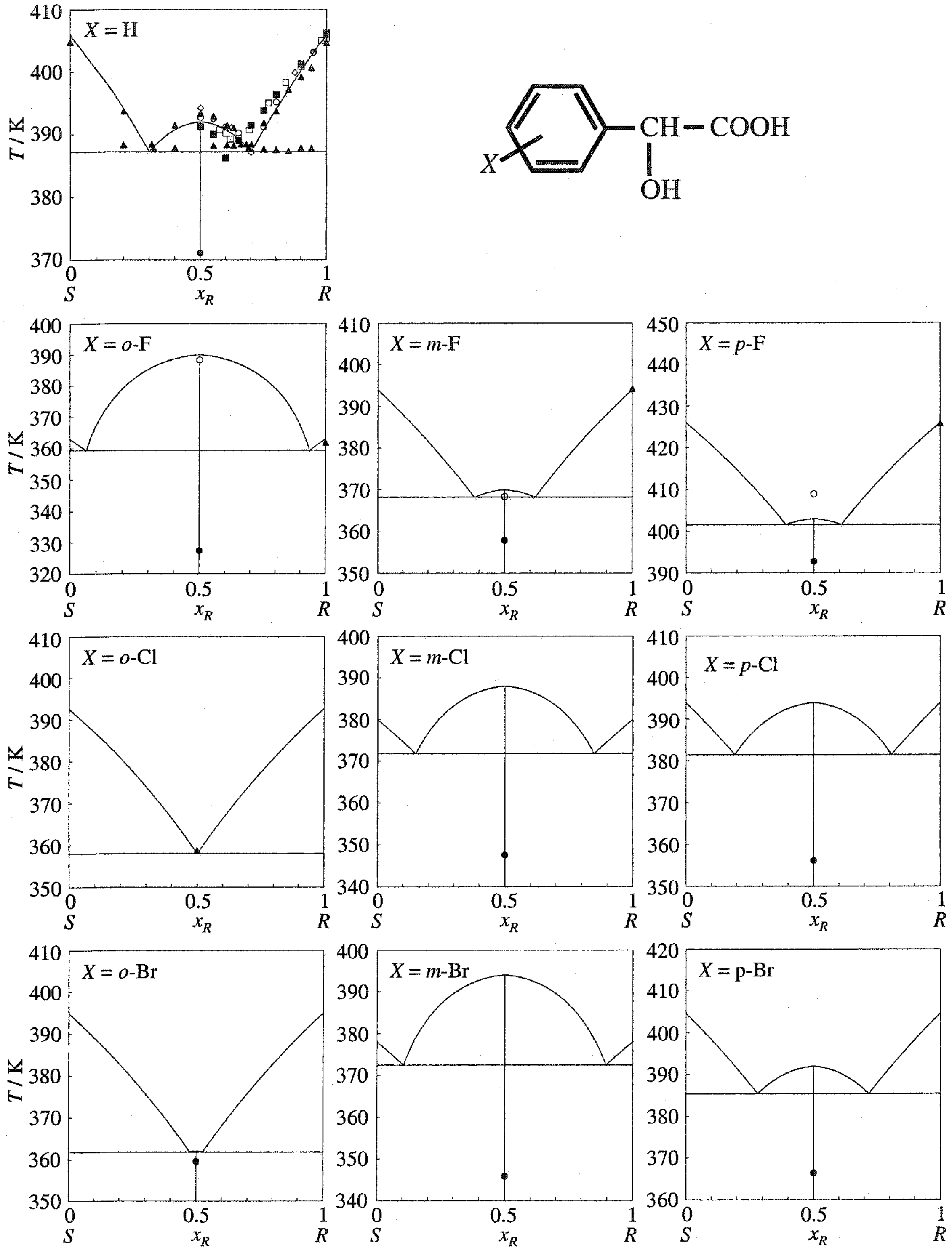

Figure 5.1 The calculated binary phase diagrams for selected halogen-substituted mandelic acids using the fusion data of Collet and Jacques.(196) ● are the hypothetical calculated T_{fus}^{con} for racemic-forming compounds. Other symbols show experimental fusion temperatures from the literature: for X = H, ▲Lorenz *et al.*,(221) □ Angus and Owen,(222) ◊ Centnerszwer,(223) ■ Adriani(224) and ○ Kuhnert-Brandstätter and Ulmer;(225) for X = *o*-F, *m*-F and *p*-F, ○ Larsen and Marthi(200) and ▲Larsen and Marthi;(215) for X = *o*-Cl, ▲is the experimental T_{fus}^{con} of Collet and Jacques.(196)

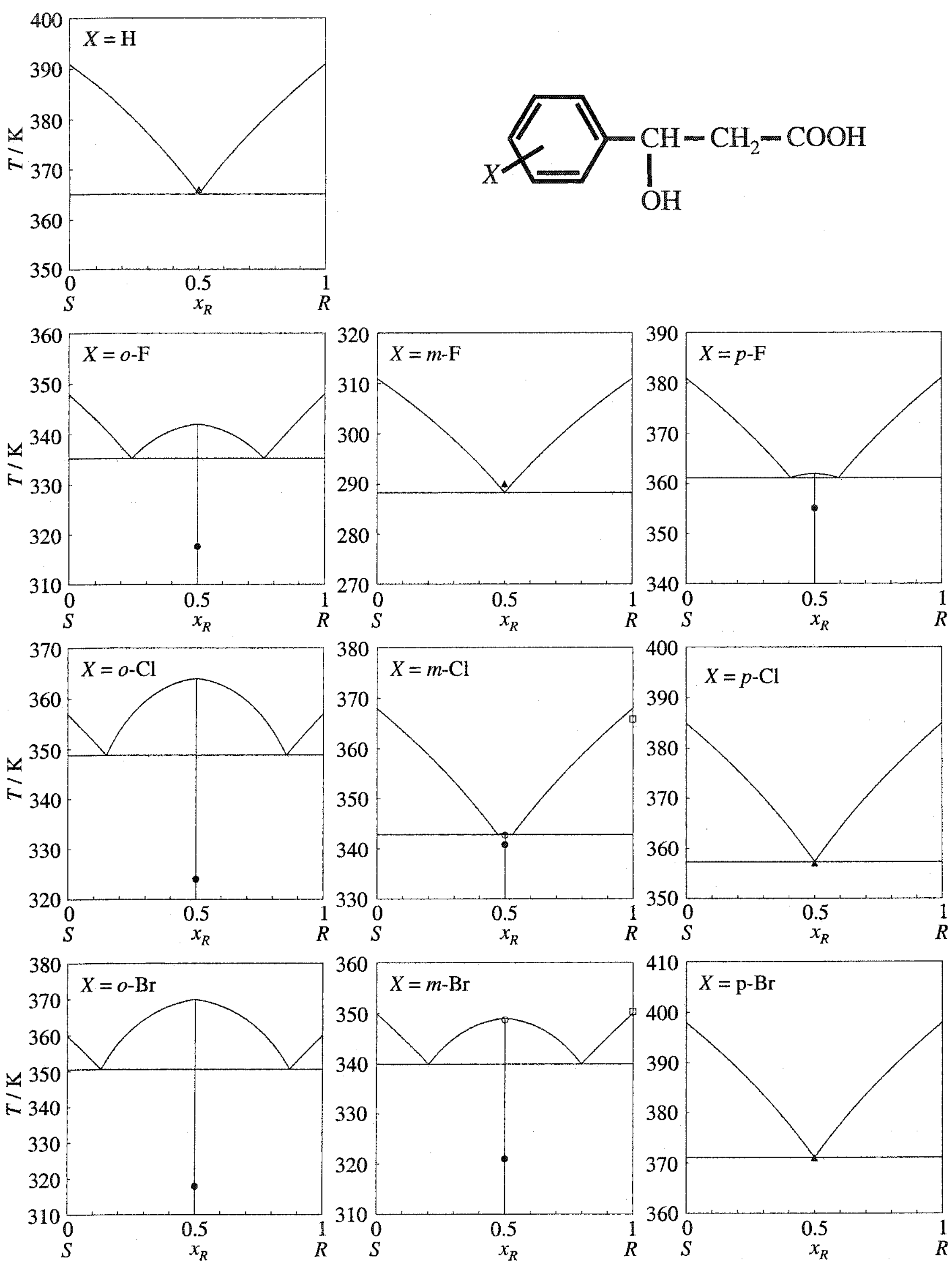

Figure 5.2 The calculated phase diagrams for selected halogen-substituted 3-phenylhydracrylic acids using the data of Collet and Jacques.(197) ● are the hypothetical calculated T_{fus}^{con} for racemic-forming compounds. Other symbols show experimental fusion temperatures from the literature: ○ Larsen and Marthi,(66) □ Larsen and Marthi(201) and ▲ is the experimental T_{fus}^{con} of Collet and Jacques(197) for conglomerate-forming compounds.

The fusion data for *o*-bromomandelic acid, *o*-chloromandelic acid and 3-(*m*-chlorophenyl)hydracrylic acid, show the usefulness of combining the techniques for conglomerate identification discussed previously in Chapter one. The experimental temperatures of fusion for the equimolar mixtures of these enantiomers are not very different from the calculated conglomerate fusion temperatures. Thus, other experimental techniques are required to determine if the equimolar solid is composed of racemic or conglomerate crystals. Larsen and Marthi(66) have confirmed the formation of the 3-(*m*-chlorophenyl)hydracrylic racemic crystal through X-ray crystallography. Collet and Jacques(196) have confirmed that *o*-chloromandelic acid forms a conglomerate, because the crystals can be physically separated, *i.e.*, *o*-chloromandelic acid spontaneously resolves. Using IR spectroscopy, Collet and Jacques(196,197) have argued that *o*-bromomandelic acid and 3-(*m*-chlorophenyl)hydracrylic acid form racemic crystals.

Both families of compounds can offer a reasonable selection of racemic crystal stability. Both have a rich history in circular dichroism and the unsubstituted mandelic acid phase diagram has been determined by several authors.(196,221-225) In addition, the mandelates are known to be good diastereomeric resolving agents(3,226,227) and many modified mandelic acids are readily available in large quantities. Therefore, the mandelic acid systems were selected for the current investigations.

According to the calculations described at the end of Chapter four, the unsubstituted mandelic acid and the *ortho*-substituted halogen mandelic acids provide five out of six possible cases listed in table 2.4 and a conglomerate case. The following signs for entropy and enthalpy changes resulted from these calculations: mandelic acid, $\Delta_{\mathrm{Rac}}S > 0$, $\Delta_{\mathrm{Rac}}H < 0$; *o*-fluoromandelic acid, $\Delta_{\mathrm{Rac}}S < 0$, $\Delta_{\mathrm{Rac}}H < 0$; *o*-chloromandelic acid, $\Delta_{\mathrm{Rac}}G > 0$; *o*-bromomandelic acid, $\Delta_{\mathrm{Rac}}S > 0$, $\Delta_{\mathrm{Rac}}H > 0$. Therefore, the *ortho*-substituted halogen mandelic acids provide a good group of compounds for thermodynamic measurements.

The main purpose of this chapter is to provide the details of synthesis, resolution and crystal growth of mandelic acid, *o*-fluoromandelic acid, *o*-chloromandelic acid and *o*-bromomandelic acid. The aim was to show both optical purity and crystalline samples. In addition, through X-ray structures at various temperatures, thermal expansion information and estimated isothermal compressibility are reported.

5.2 Experimental methods

5.2.1 Characterisation techniques

Microanalysis was carried out by Canadian Microanalytical Service Ltd, Delta, BC. ^{13}C NMR spectra were obtained at the Atlantic Region Magnetic Resonance Centre, using a Bruker AVANCE$^{\mathrm{TM}}$ 500 MHz Spectrometer. All NMR samples were prepared in dimethyl sulfoxide solvent, DMSO, *ca.* 200 g L^{-1}, and run at room temperature. The ^{13}C chemical shift of DMSO was fixed at 40.45 ppm.(228)

Raman spectra were obtained using a Bruker RFS 100$^{\mathrm{TM}}$ at room temperature (3000 scans observed at 180°, Nd:YAG laser set at 145 mW). IR spectra were obtained using a Bruker Vector 22$^{\mathrm{TM}}$ spectrometer under a dry nitrogen atmosphere (CsI plates). Multiple neat samples were measured with these spectrometers.

Optical rotation was determined at the sodium D line, $\lambda = 589$ nm, and room temperature using a DigiPol-series 781 polarimeter and a 10.00 cm cell (Rudolph Instruments, Inc.). These solutions were prepared in 5.00 mL volumetric flasks with HPLC grade acetone (Fisher, A949-1, Lot. 011277) and distilled water as solvent, *ca.* 4 mass % for acetone and *ca.* 2 mass % water.

Thermal analysis was carried out using a Perkin Elmer Pyris 1 power compensated DSC. All samples were contained in hermetically sealed aluminium pans, where the masses of the samples were in the range 8-20 mg.

Temperatures and fusion enthalpies for the DSC were calibrated using Calorimetry Conference standard benzoic acid (NBS-49, $T_{\text{fus}} = 395.52$ K, $\Delta_{\text{fus}}H = 147.91$ J g^{-1}) and 99.9999 % indium ($T_{\text{fus}} = 429.75$ K, $\Delta_{\text{fus}}H = 28.45$ J g^{-1}) at the beginning and end of each measurement day.(229) Several scanning rates were employed throughout the studies, from 20.00 to 320.00 mK s^{-1}. The low scanning rates were required to reduce thermal lag between the sample and heater during simultaneous heat capacity experiments and higher scanning rates were used for initial testing of chemical purity, including optically purity and crystallinity. Calibration factors for this instrument are dependent on temperature and scanning rate, figure 5.3. Based on multiple measurements of benzoic acid and mandelic acids, the error in fusion temperature and fusion enthalpy for molecular organics, *ca.* 10 mg, is estimated to be $\delta T_{\text{fus}} = \pm\ 0.3$ K and $\delta\Delta_{\text{fus}}H/\Delta_{\text{fus}}H = \pm\ 1\%$ respectively.

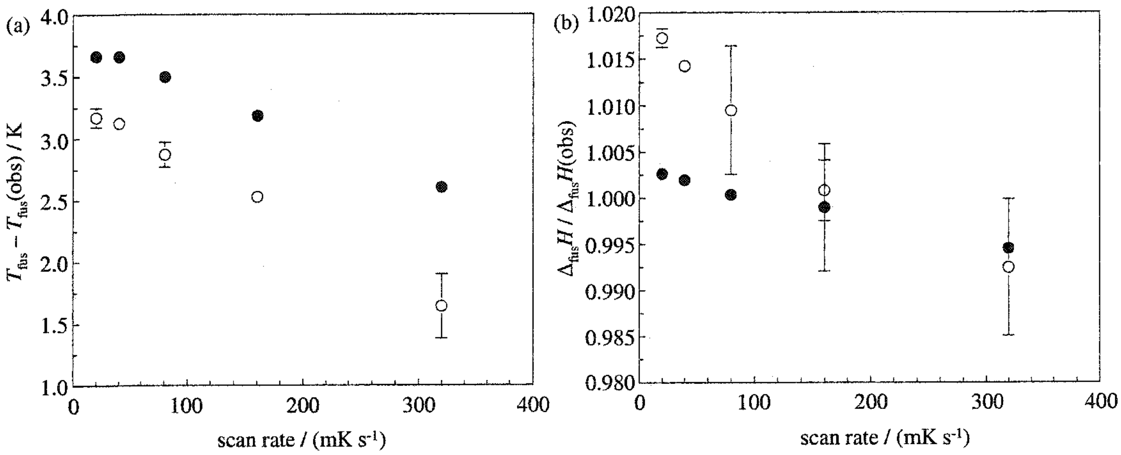

Figure 5.3 DSC calibration factors using benzoic acid and indium over three days of operation. (a) temperature calibrations and (b) fusion enthalpy calibrations. ● are for indium and ○ are for benzoic acid. Error bars are twice the standard deviation for six measurements and are not shown where the symbol is larger than the error.

Single crystal X-ray crystallography, solutions and refinements were carried out by Professor T. S. Cameron at DALX, The X-ray Crystallography Centre at Dalhousie University. X-ray measurements were made on a Rigaku AFC5R diffractometer with a rotating anode generator. Some independent measurements also were made on a Rigaku AFC8 diffractometer with a Mercury CCD area detector. Both these diffractometers used graphite monochromated Mo-Kα radiation. Data were collected for various temperatures from *ca.* 100 to *ca.* 300 K. For some of the intermediate temperatures only the unit cell parameters were obtained.

Structures were solved by direct methods and expanded using Fourier techniques (teXsan(230), CrystalStructure(231), SHELX97(232)). Where possible, hydrogen atoms were refined anisotropically, while others were fixed. Neutral atom scattering factors were taken from Cromer and Waber.(233) F_{calc} included anomalous dispersion effects. $\Delta f'$ and $\Delta f''$ were taken from Creagh and McAuley(234) and attenuation coefficients are those of Creagh and Hubbel.(235) Unweighted agreement factors, R, have been calculated as

$$R = \frac{\sum \left\| F_{\mathrm{o}} \right| - \left| F_{\mathrm{c}} \right\|}{\sum \left| F_{\mathrm{o}} \right|}, \qquad (5.1)$$

where F_{o} and F_{c} are observed and calculated intensities respectively.

5.2.2 Preparation

Mandelic acid

Unsubstituted racemic mandelic acid and *R*-(-)-mandelic acid were obtained from the Sigma-Aldrich Chemical Company, (99%+, Cat. No. 24,151-0, Lot TN 07114MT) and (99%+, Cat. No. 15,421-0, Lot LR 05707JR), respectively. Both chemicals, *ca.* 10 g, were recrystallised by dissolving in chloroform (Fisher Scientific, C298-4) at $T = 313$ K and allowing the solution to slowly cool to room temperature. After two days samples were filtered and washed with cold chloroform and benzene (Caledon Laboratories Ltd., 1600-1) before being stored under vacuum for 48 hours. These samples (4.8 g mandelic acid and 3.4 g *R*-(-)-mandelic acid) were then sealed in 15 mL vials and stored in darkness. Found (Racemic): C, 63.48 %; H, 5.45 %; O, 31.66 %. Found (*R*-(-)-): C, 63.57 %; H, 5.23 %; O, 31.44 %. Calculated: C, 63.15 %; H, 5.30 %; O, 31.55 %.

o-Fluoromandelic acid

Racemic compound

Racemic *o*-fluoromandelic acid was prepared by the standard method used by Collet and Jacques.(196) Figure 5.4 shows the general reaction steps for this method. A small control sample of racemic *o*-fluoromandelic acid was obtained from Oakridge Products, Inc, West Columbia, SC. (98+%, 009726).

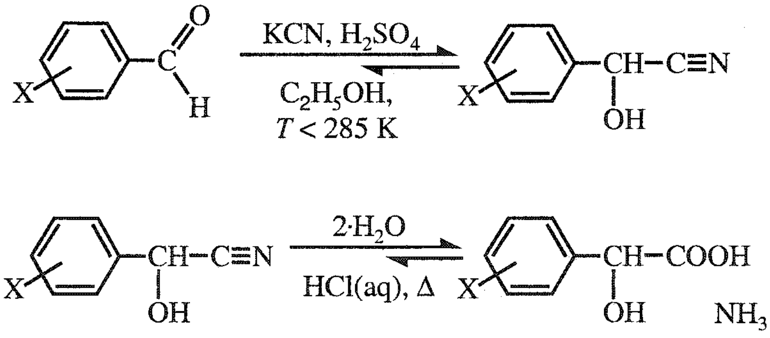

Figure 5.4 Standard mandelic acid preparation.(196)

47.57 g (731.1 mmol) of potassium cyanide (Baker Chemical Co., 1-3080, Lot. 525952) and 45.95 g (370.2 mmol) of *o*-fluorobenzaldehyde (Sigma-Aldrich Chemical Co., F480-7) were dissolved in 200.00 mL of 95% ethanol (Commercial Alcohols Inc., 1011) and stirred in a NaCl/ice bath. 190 mL of cold, *ca.* 278 K, 1.876 mol L^{-1} H_2SO_4 (Caledon Laboratories Ltd., 8825-1) in 95% ethanol were added drop wise to the solution for *ca.* six hours, where the temperature was never allowed to exceed $T = 284$ K. The product was filtered and the solid was washed with 150 mL of ether (Caledon Laboratories Ltd., 4700-1-25). The solution was extracted five times with 150 mL aliquots of ether and all ether solutions were combined, dried over $MgSO_4$ (Sigma-Aldrich Chemical Co., 24,697-2), filtered and left to evaporate. This resulted in 38.50 g of cyanohydrine (69 % yield).

The cyanohydrine was hydrolysed with 200 mL of concentrated HCl (aq) (Anachemia Canada Inc., AC-4955) for 24 hours at room temperature. 150 mL of distilled water were added to the suspension and the crude acid solution was steam distilled (100 mL). The resulting *o*-fluoromandelic acid was separated five times with 100 mL ether. The ether/*o*-fluoromandelic acid solution was dried over $MgSO_4$, filtered and left to evaporate. 35.28 g (56.2 % yield) of solid, slightly yellow, crude *o*-fluoromandelic acid was recovered.

The crude *o*-fluoromandelic acid was dissolved in 4.80 L of hot benzene and fractionally recrystallised. The first fraction resulted in 21.11 g of slightly yellow crystals and the second fraction resulted in 7.92 g of white crystals. The 7.92 g of white crystals were dissolved in 900 mL hot chloroform and allowed to slowly cool to room temperature. The solvent was allowed to evaporate until 500 mL remained, then sealed and refrigerated at $T = 278$ K for 12 hours. The solution was filtered and 5.68 g of pure *o*-fluoromandelic acid was recovered as white needles.

Resolution

To resolve a chiral acid, a chiral base is often the best choice; therefore, chiral phenylalkylamines are commonly used as resolving agents for mandelic acids, where ephedrine is the most common.(3,227) 21.11 g of crude *Rac*-o-fluoromandelic acid (124.1 mmol) from the first benzene recrystallisation were dissolved in 30 mL of 95% ethanol. This solution was added to a solution containing 18.32 g (1*R*,2*S*)-(-)-ephedrine (110.9 mmol) (99 %, Sigma-Aldrich Chemical Co., 13,491-0, Lot. 00610EO) in 25 mL ethanol. The theoretical yield was calculated to be 20.80 g of the diastereomer salt ((1*R*,2*S*)-(-)-ephedrine *o*-fluoromandelate). After two hours the solution was filtered and 21.19 g of solid salt was recovered. This salt was suspended in 50 mL of 95% ethanol. After 20 hours at room temperature, this suspension was filtered and washed three times with 15 mL of benzene to yield 14.85 g of diastereomer salt (71.4%).

(1*R*,2*S*)-(-)-ephedrine *o*-fluoromandelate was decomposed with 70 mL of 1 mol L^{-1} HCl (aq) and separated four times with 50 mL aliquots of ether. The ether solution was dried over $MgSO_4$, filtered and evaporated leaving an oil. The oil was recrystallised from 1 L benzene to yield 7.70 g of crude *R*-(-)-*o*-fluoromandelic acid. This solid was left under vacuum over phosphorous pentoxide for four days and recrystallised twice more from benzene to yield 4.14 g of soft white platelet-like *R*-(-)-*o*-fluoromandelic acid crystals (39.3 % overall resolution yield). Found (Racemic): C, 56.38 %; H, 4.04 %; F, 8.58 %. Found (*R*-(-)-): C, 56.21 %; H, 4.02 %; F, 10.47 %. Calculated: C, 56.48 %; H, 4.15 %; F, 11.17 %. Note: second analysis on the same samples found F, 9.26 % and 9.54 %, respectively. It appears that the confidence is low, *ca.* ± 2% based on twice the difference, for fluorine microanalyses.

o-Chloromandelic acid

Racemic mixture

The racemic mixtrure of *o*-chloromandelic acid was obtained from Acros Organics, (98%, Lot A014666401). Samples of the racemic mixture were recrystallised from chloroform, benzene, ethanol, acetonitrile, acetone and various *n*-heptane mixtures during several attempts to obtain good quality crystals. While some of these recrystallisations yielded what looked like good crystals, none was of crystallographic quality. Crystals used in calorimetric studies were from a recrystallised sample of resolved *R*-(-)-*o*-chloromandelic acid using a (1*R*,2*S*)-(-)-ephedrine resolving agent. These were compared to a small commercial sample of *R*-(-)-*o*-chloromandelic acid obtained from the Sigma-Aldrich Chemical Company (99%, Cat. No. 47,887-3, Lot 29702KI); see below for results.

Resolution

40.84 g (218.9 mmol) of the racemic *o*-chloromandelic acid mixture was dissolved in 100 mL of 95% ethanol and added to a solution containing 32.22 g (1*R*,2*S*)-(-)-ephedrine (195.0 mmol) in 25 mL ethanol. The theoretical yield was calculated to be 38.51 g of the least soluble diastereomer salt ((1*R*,2*S*)-(-)-ephedrine *R*-(-)-*o*-chloromandelate) or 20.42 g of *R*-(-)-*o*-chloromandelic acid. After 12 hours at room temperature the solution was refrigerated for 4 hours at $T = 278$ K and filtered (15.38 g, 39.9 % yield). A second fraction was recovered by allowing the ethanol to evaporate at room temperature to an overall volume of 75 mL. The solution was then cooled to $T = 278$ K for 60 hours and filtered. This further yielded 6.35 g, which when combined with the first sample of 15.38 g, accounted for 56.4 % of the theoretical diastereomer salt yield and a calculated optical purity of 70 % *S*-(+)-*o*-chloromandelic acid left in the mother liquor.

The first fraction of (1*R*,2*S*)-(-)-ephedrine *R*-(-)-*o*-chloromandelate was suspended in 50 mL distilled water, decomposed by addition of 50 mL of 1 mol L^{-1} HCl (aq) and separated five times with 25 mL aliquots of ether. The ether solution was dried over $MgSO_4$, filtered and evaporated, leaving 6.74 g of solid product (33.0 % yield). This was dissolved in 350 mL of hot benzene and allowed to slowly cool to room temperature (4.19 g yield).

The second fraction was treated by the same method (25 mL distilled water, 25 mL of 1 mol L^{-1} HCl (aq) and 20 mL aliquots of ether). 3.69 g of crude *R*-(-)-*o*-chloromandelic acid were dissolved in 200 mL of hot benzene and allowed to slowly cool to room temperature (1.97 mg yield). After DSC analyses showed the first two fractions to be the same optical purity, they were combined for a total yield of 6.13 g optically pure *R*-(-)-*o*-chloromandelic acid. The 6.13 g were again dissolved in 350 mL of hot benzene, allowed to slowly cool to room temperature and filtered (5.01 g, 24.5 % overall yield). These large soft platelet like crystals were crystallographic quality.

S-(+)-*o*-chloromandelic acid also was recovered from the ethanol solution by the following method. After the second fraction of diastereomer salt was removed, 100 mL of 1 mol L^{-1} HCL (aq) were added to the mother liquor and the *o*-chloromandelic acid was extracted five times with 50 mL aliquots of ether. The ether solution was dried over $MgSO_4$, filtered and evaporated, leaving 24.91 g of solid product. This brought the total of recovered *o*-chloromandelic acid to 35.34 g or 86.5 % of the original sample. This final fraction was recrystallised from hot benzene three times, 900 mL (12.07 g), 500 mL (6.07 g) and finally 250 mL (3.705 g or 18.1 %). Found (*R*-(-)-): C, 50.68 %; H, 3.87 %; O, 26.33 %; Cl, 19.81 %. Calculated: C, 51.50 %; H, 3.78 %; O, 25.72 %; Cl, 19.00 %.

o-Bromomandelic acid

Racemic mixtrure

35.05 g (538.2 mmol) of potassium cyanide and 50.08 g (270.7 mmol) of *o*-bromobenzaldehyde (Sigma-Aldrich Chemical Co., B5,700-1, Lot. 05718BI) were dissolved in 200.00 mL of 95% ethanol and stirred in a salted iced bath. 130 mL of cold, *ca.* 278 K, 1.99 mol L^{-1} H_2SO_4 in 95% ethanol were added drop wise to the solution for *ca.* six hours, where the temperature was never allowed to exceed $T = 284$ K. The product was filtered and the solid was washed with 100 mL of ether. The solution was extracted five times with 100 mL aliquots of ether, all ether solutions were combined, dried over $MgSO_4$, filtered and left to evaporate. This resulted in 54.38 g of the cyanohydrine (99.9 % yield).

The cyanohydrine was hydrolysed with 250 mL of concentrated HCl (aq) for 24 hours at room temperature. 150 mL of distilled water were added to the suspension and the crude acid solution was steam distilled (100 mL). The resulting *o*-bromomandelic acid was separated four times with 100 mL aliquots of ether. The ether/*o*-bromomandelic acid solution was dried over $MgSO_4$, filtered and left to evaporate. 34.80 g (58.2 % yield) of solid, white, crude *o*-bromomandelic acid were recovered.

29.24 g of the crude *o*-bromomandelic acid were dissolved in 400 mL of hot benzoic acid and recrystallised (25.13 g). 22.61 g of this product were dissolved in 400 mL chloroform and fractionally recrystallised, 2.44 g from cold 400 mL chloroform, an additional 3.87 at 100 mL and 6.44 after all solvent was evaporated (56.4 % recovered). All these crystals were white platelet-like crystals. Other solvents used to grow crystals were ethanol, acetonitrile, acetone, water, various *n*-heptane mixtures and chloroform under *n*-heptane vapour pressure. Only the crystals from benzene were of marginal crystallographic quality; crystals from the other solvents did not result in high-quality single crystal X-ray diffraction.

Resolution

Resolution of *o*-bromomandelic acid followed the same method as *o*-chloro and *o*-fluoromandelic acid resolution, 6.43 g racemic *o*-bromomandelic acid and 4.60 g (1*R*,2*S*)-(-)-ephedrine. This produced an oil after several days. The oil at the bottom of the beaker was separated from the mother liquor. After one week, both fractions were oil. These oils were placed under vacuum for 7 days, after which a white glass-like solid was formed. Each solid was decomposed with 30 mL of 1 mol L^{-1} HCl(aq) and extracted five times with 50 mL aliquots of ether. 3.43 g were recovered from the first fraction and 1.97 from the second fraction. Both of these fractions were recrystallised from 100 mL of hot benzene.

A second resolution attempt with 5.18 g of racemic *o*-bromomandelic acid produced crystals from the solvent at $T = 278$ K, *i.e.*, no oil. After decomposition, 1.39 g were recovered from the first fraction, 1.21 g from the second fraction and 1.81 from a third fraction.

5.3 Results and discussion

5.3.1 Spectroscopy

^{13}C NMR

NMR spectra for racemic mandelic acid, *R*-(-)-mandelic acid, racemic *o*-fluoromandelic acid, *R*-(-)-*o*-fluoromandelic acid, *R*-(-)-*o*-chloromandelic acid and racemic *o*-bromomandelic acid are shown in figures 5.5 to 5.7. Table 5.2 shows the NMR peaks and the chemical shifts found by Larsen and Marthi.(200) No abnormal peaks were found and the spectra show only one product. Racemic and optically pure spectra show no difference.

Table 5.2 ^{13}C chemical shifts for mandelic acid and the *ortho*-halogen-substituted mandelic acids.

Carbon	Chemical shifts / ppm							
	X = H racemic	*X* = H *R*	*X* = F racemic	*X* = F(200) racemic	*X* = F *R*	*X* = F(215) *R*	*X* = Cl *R*	*X* = Br Racemic
Conc.[a]	200.8	205.0	200.6	50	202.4	5	202.4	238.8
1	140.39	140.4	127.72 127.83	127.558 127.702	127.72 127.84	127.65 (14.5)[c]	132.41	132.55
2	128.36	128.37[b]	158.87 160.82	158.395 160.837	158.87 160.82	159.63 (245.7)[c]	138.13	139.73
3	126.87	126.88[b]	115.35 115.52	115.155 115.368	115.35 115.52	115.28 (21.3)[c]	127.38[b]	122.90
4	127.89	127.91[b]	129.06[b] 129.08[b]	128.848[b] 128.878[b]	129.06[b] 129.08[b]	128.88 (4.5)[c]	129.34[b]	128.95[b]
5	126.87	126.88[b]	124.56	124.364 124.395	124.56	124.40 (3.0)[c]	128.90[b]	127.93[b]
6	128.36	128.37[b]	129.93[b] 130.00[b]	129.735[b] 129.819[b]	129.94[b] 130.00[b]	129.80 (7.5)[c]	129.56[b]	129.84[b]
7	72.66	72.66	66.66	66.446	66.66	66.44	69.63	71.86
8	174.33	174.35	173.55	173.293	173.55	173.312	173.28	173.21

Labels are shown in figures 5.5 to 5.7. [a] / g L^{-1}; [b]unambiguous assignments; [c]reported as a doublet, *J* coupling in brackets (/ Hz).

It was not possible to unambiguously assign the peaks for phenyl carbons 3,4,5 and 6 for mandelic acid, *o*-chloro and *o*-bromomandelic acid; however, the phenyl carbons 3 and 5 have been assigned for *o*-fluoromandelic acid. These assignments for *o*-fluoromandelic acid are in agreement with Larsen and Marthi.(200)

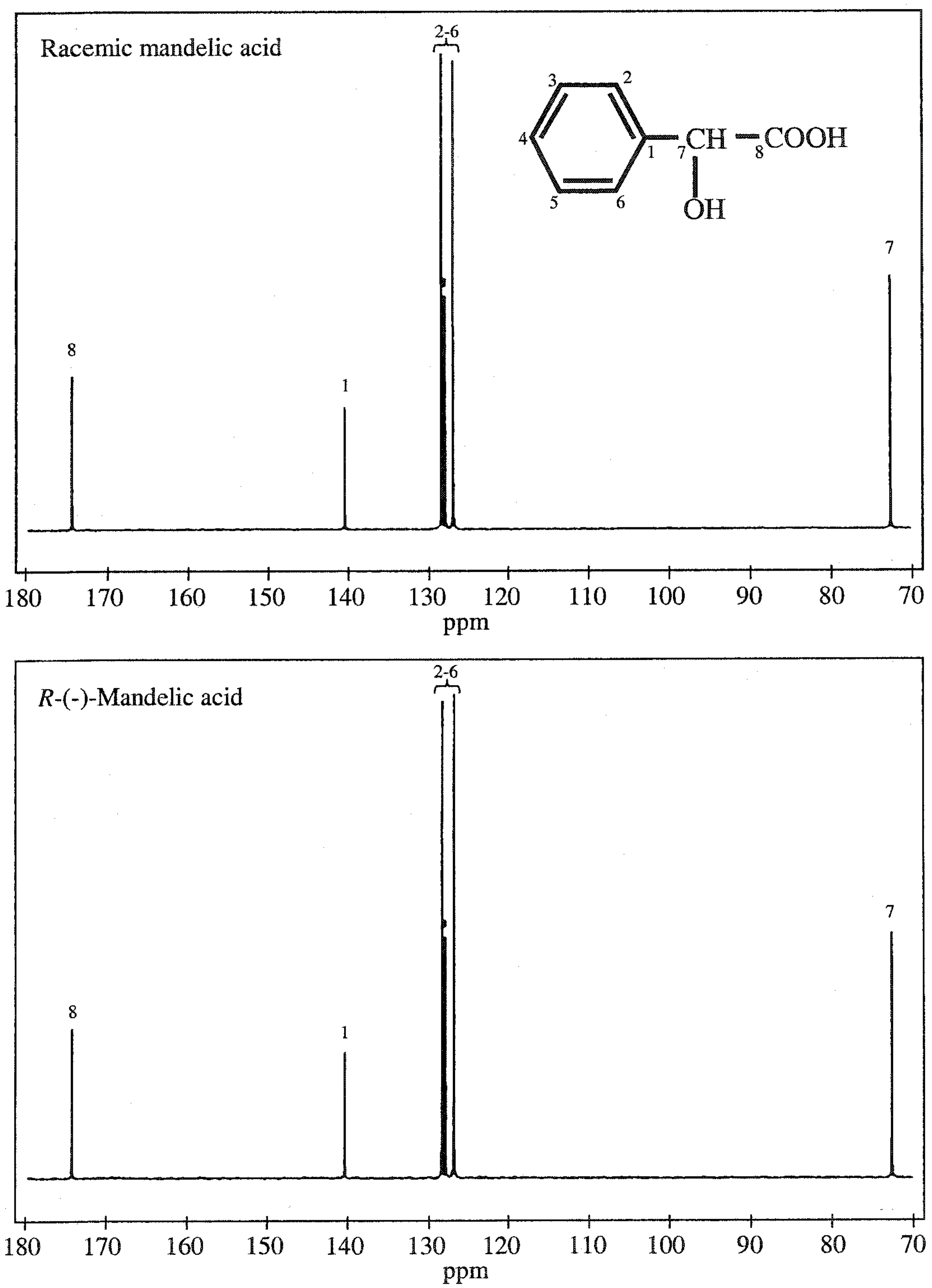

Figure 5.5 ^{13}C NMR spectra of unsubstituted mandelic acid. Chemical shifts are given in table 5.2.

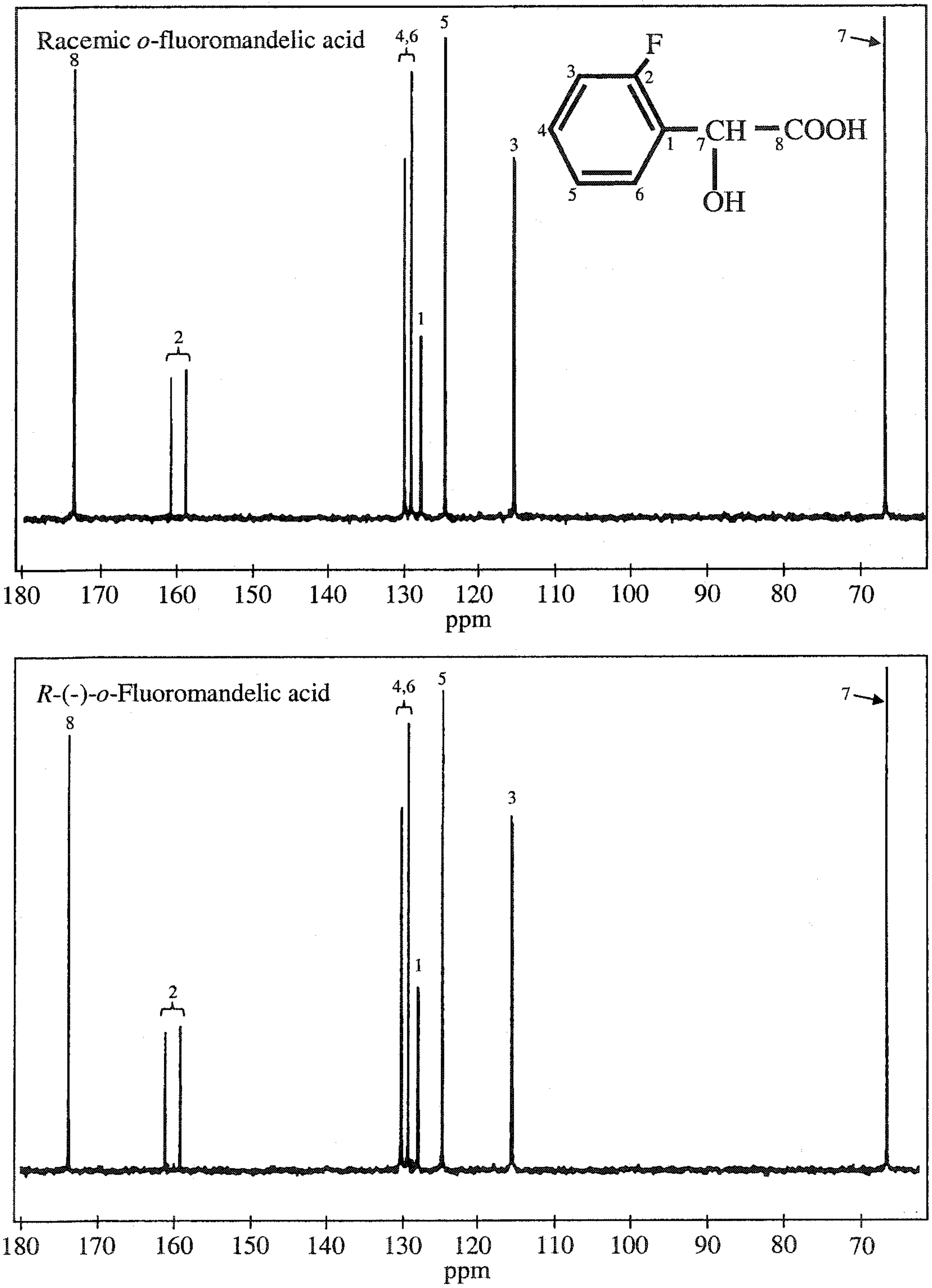

Figure 5.6 ^{13}C NMR spectra of *o*-fluoromandelic acid. Chemical shifts are given in table 5.2.

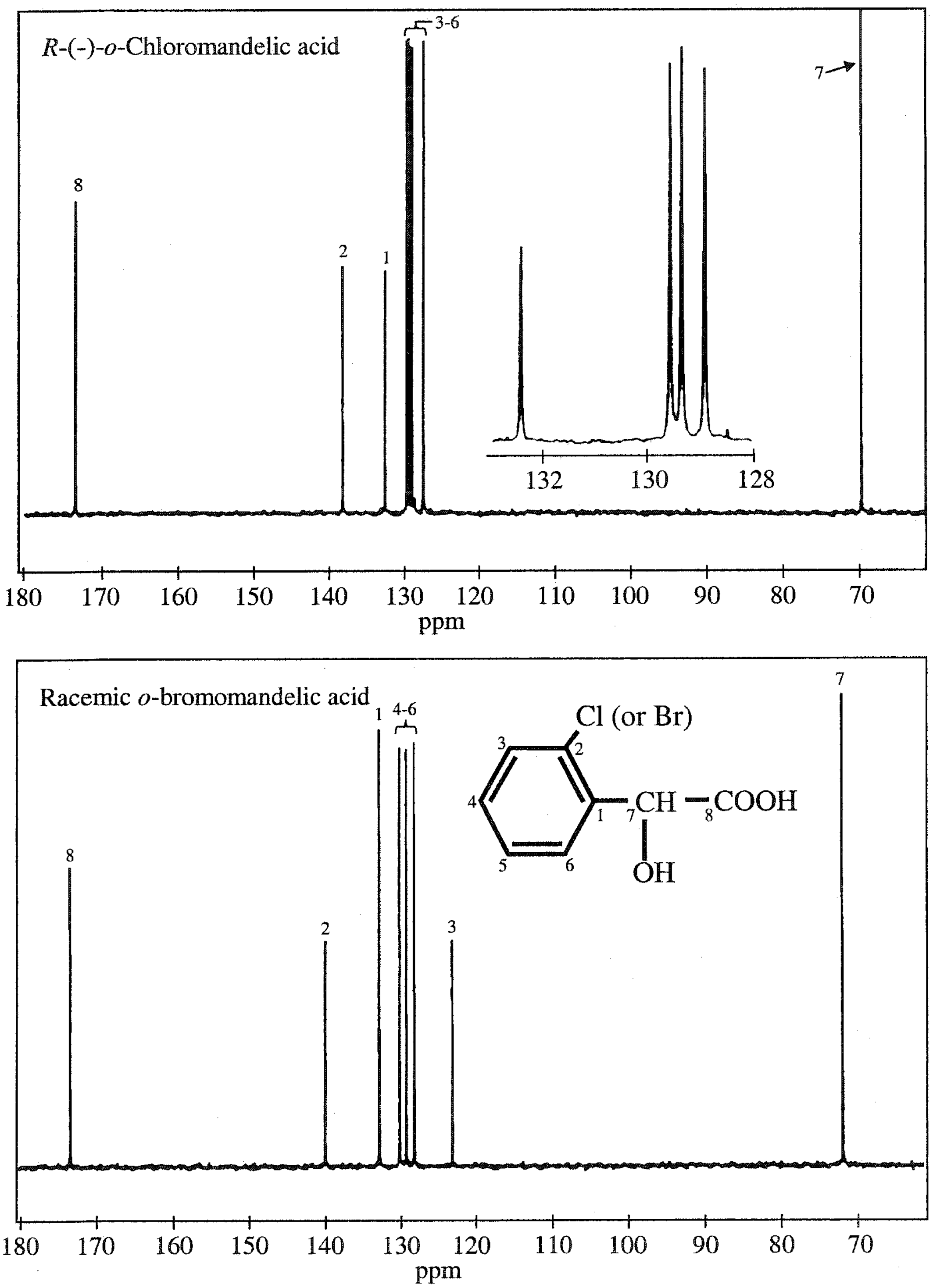

Figure 5.7 ^{13}C NMR spectra of *o*-chloromandelic acid and *o*-bromomandelic acid. Chemical shifts are given in table 5.2.

Vibrational spectroscopy

IR and Raman spectra are shown in figure 5.8. The spectra for optically pure mandelic acid and *o*-fluoromandelic acid are different from the spectra for the corresponding racemic crystals, which is in agreement with racemic crystal formation. The assignment of these vibrational modes is the subject of Chapter six.

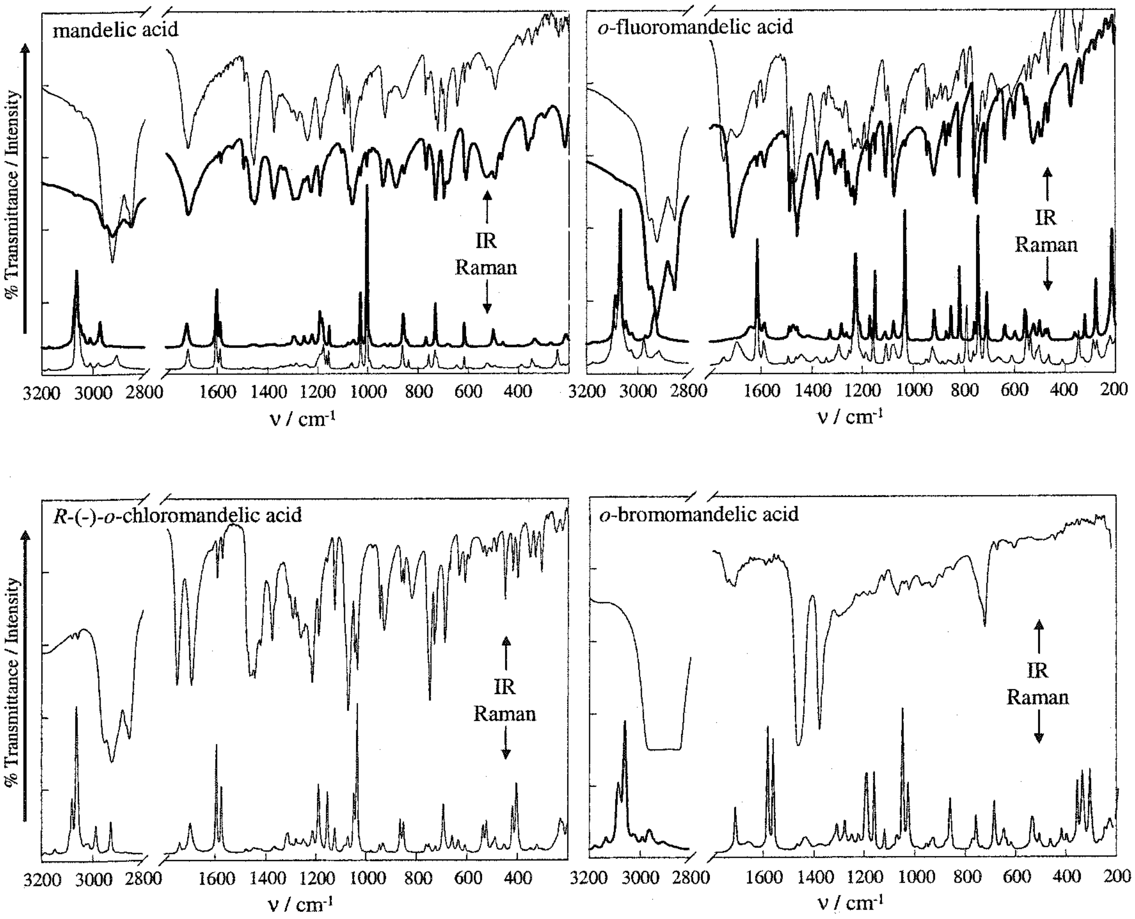

Figure 5.8 Vibrational spectra of the *ortho*-substituted mandelic acids. All Raman samples were neat and IR samples were in Nujol mul. For mandelic acid and *o*-fluoromandelic acid, the two spectra on the outside, ——, are for the racemic crystals and the two inside, ▬▬, are for the optically pure crystals.

Optical rotation

Low wavelength ($\lambda < 300$ nm) CD data have been reported in the literature, for investigations of the Cotton effects for the mandelic acids.(196,236,237) In addition, there are many specific optical rotations for mandelic acid and substituted mandelic acids reported at $\lambda = 578$ nm (Hg) in acetone; however, the polarimeter available in the Chemistry Department at Dalhousie University only has the option of one wavelength, $\lambda = 589$ nm (Sodium D line).

The specific optical activities of all racemic samples were found to be $[\alpha]^{297}{}_{D} = 0.0 \pm 0.1°$. Final specific optical acitivities and literature values reported at the sodium D line are reported in table 5.3.

Table 5.3 Specific optical rotations for *R*-(-)-mandelic acid, *R*-(-)-*o*-fluoromandelic acid and *R*-(-)-*o*-chloromandelic acid.

Present results				Literature values				
T / K	$[\alpha]_D$ / °	Conc. / (10 g L^{-1})	solvent	T / K	$[\alpha]_D$ / °	Conc. / (10 g L^{-1})	solvent	Ref.
R-(-)-Mandelic acid								
298	154 ± 1	4.12	acetone	300	154^a	2.047	water	238
298	153 ± 1	2.26	water	300	151	2.023	water	238
				293	154	0.5	water	226
					154^a		ethanol	227
					157		water	227
				295	156	2.12	water	239
				300	153^a	2.17	water	239
					154		water	SA
					153^a		water	SA
R-(-)-o-Fluoromandelic acid								
298	140 ± 1	4.36	acetone					
298	120 ± 1	1.80	water					
R-(-)-o-Chloromandelic acid								
298	153 ± 1	4.02	acetone	292	126^a	3	water	SA
298	126 ± 1	2.08	water					

[a] measurements made for the *S*-(+)- enantiomer; SA, reported by Sigma-Aldrich with their commercial supplies.

During the resolution, the first crude fraction of *R*-(-)-*o*-chloromandelic acid was $[\alpha]^{292}_{D} = -154 \pm 1°$ (6.02 g (100 mL)$^{-1}$, acetone) and the final fraction was $[\alpha]^{292}_{D} = 129 \pm 1°$ (4.40 g (100 mL)$^{-1}$, acetone) respectively. The Sigma-Aldrich reports a specific optical activity of $[\alpha]^{292}_{D} = -126°$ (3 g (100 mL)$^{-1}$, water). From these values, it would appear that the final fraction was 84 % optically pure S enantiomer, which is greater than the estimated optical purity from the mass calculation. In addition, the optical rotation of the first fraction agreed with measurements for the Sigma-Aldrich sample.

5.3.2 Thermal analysis

The calculated phase diagram for *o*-chloromandelic acid (conglomerate), figure 5.1, shows how optical purity can be measured using fusion information.(3,11) As any enantiomeric solid becomes optically purer, the solidus peak will become smaller and the liquidus peak will become larger and show a higher onset temperature. This also is the case for a racemic forming species, provided that the solution is more optically pure than the eutectic optical purity. In addition all other impurities, including polymorphism, crystal defects and glass formation, will lower the onset temperature and broaden the fusion peak.

The DSC results for partially resolved systems are shown in figure 5.9, with the DSC scans of the second fraction and final fraction of the *o*-chloromandelic acid resolution (final fraction is estimated at 84 % *S*-(+) from optical rotation). Based on the liquidus onset temperatures of these DSC scans, the optical purities are found to be 97 % and 80 %. Note that optical rotation studies require *ca.* 100-200 mg of sample while DSC experiments require 5-10 mg of sample.

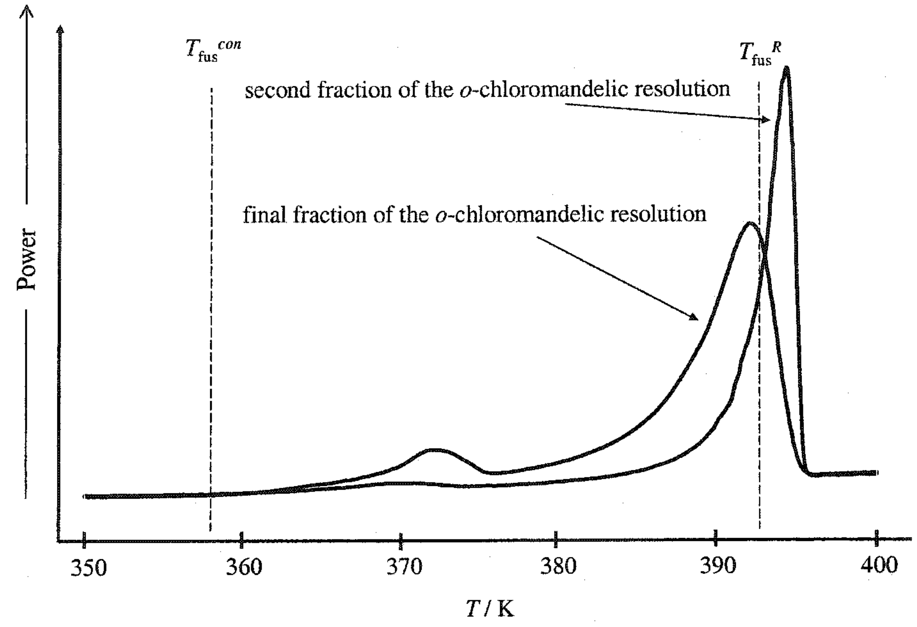

Figure 5.9 DSC scans of partially resolved *o*-chloromandelic acid samples.

The DSC studies showed that *o*-fluoromandelic acid was resolved more efficiently than *o*-chloromandelic acid. Valente *et al.*(227) have found two crystal types for (1*R*,2*S*)-(-)-ephedrine *o*-chloromandelate and one crystal type for (1*R*,2*S*)-ephedrine *o*-fluoromandelate. Polymorphic behaviour possibly hinders the resolution efficiency of *o*-chloromandelic acid. The resolution of *o*-bromomandelic acid was not nearly as successful using this method, < 5 % *ee* based on fusion temperature. Korver *et al.*(236) have postulated that *R*-(-)-*o*-bromomandelic acid and *R*-(-)-*o*-chloromandelic acid are isomorphic; therefore, polymorphism also is a possible reason for the failure of this resolution.

The DSC scans for the crystals studied throughout the remainder of the thesis are shown in figure 5.10. The fusion values are all in good agreement with the literature, table 5.4. The narrow peaks and reproducible onset temperatures show that the final products are all crystalline. No transitions were observed in DSC scans from $T = 120$ K up to T_{fus}.

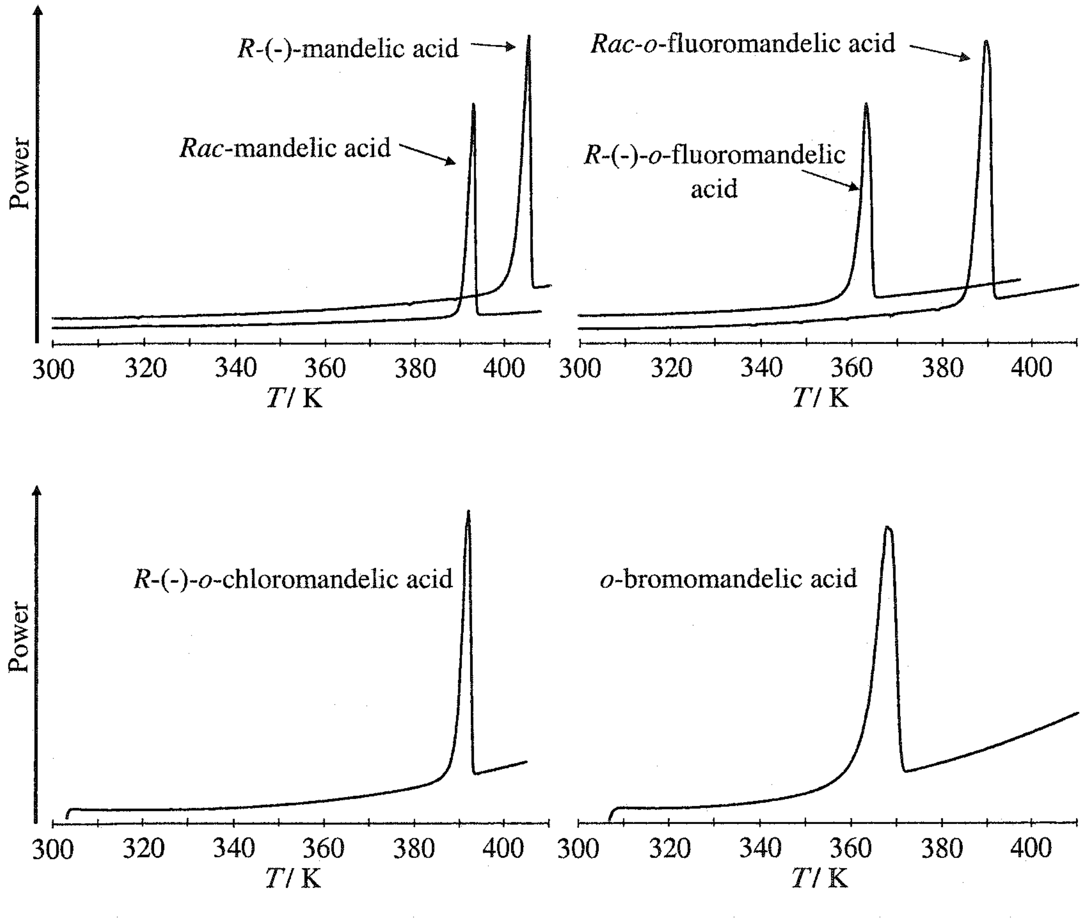

Figure 5.10 DSC scans of mandelic acid, *o*-fluoromandelic acid, *R*-(-)-*o*-chloromandelic acid and *o*-bromomandelic acid.

Table 5.4 Experimental fusion values for benzoic acid, mandelic acid, *o*-fluoromandelic acid, *o*-chloromandelic acid and *o*-bromomandelic acid.

Present results					Literature values		
No. of samples	Mass range / mg	T_{fus} / K	$\Delta_{\mathrm{fus}}H$ / kJ mol^{-1}	$\Delta_{\mathrm{fus}}S$ / J mol^{-1} K^{-1}	T_{fus} / K	$\Delta_{\mathrm{fus}}H$ / kJ mol^{-1}	Ref.
			Benzoic acid				
31	11-18	395.6 ± 0.4	18.0 ± 0.2	45.5 ± 0.5	395.5 ± 0.2	17.97 ± 0.04	229
			Rac-Mandelic acid				
17	3-12	393.0 ± 0.4	25.9 ± 0.5	65.9 ± 1.3	392	25.1	196
					393.4	25.6	221
					393.8	26.8	198
					392.7		225
					391		222
					394.2		223
					391		224
					391		240
			R-(-)-Mandelic acid				
13	6-12	405.5 ± 0.5	26.0 ± 0.5	64.1 ± 1.2	406	26.4	196
					404.8	24.5	221
					404.7	25.7	198
					405		225
					406.7		222
					405.9		223
					406		224
					409		214
					406		239
			Rac-*o*-Fluoromandelic acid				
8	11-21	390.1 ± 0.7	31.1 ± 0.7	76.7 ± 1.7	390	30	196
					388.3	31	200
					388		240
			R-(-)-*o*-Fluoromandelic acid				
7	10-15	364.2 ± 0.8	20.4 ± 0.2	56.0 ± 0.5	363	21	196
					361.8	19.1	215
			R-(-)-*o*-Chloromandelic acid				
7	8-10	392.5 ± 0.6	23.9 ± 1.0	60.9 ± 2.5	392.7	25	196
			Rac-*o*-Bromomandelic acid				
6	6-10	360.7 ± 0.8	20.2 ± 1.0	56.0 ± 2.8	362	21	196

Errors are calculated as twice the sample standard deviation.

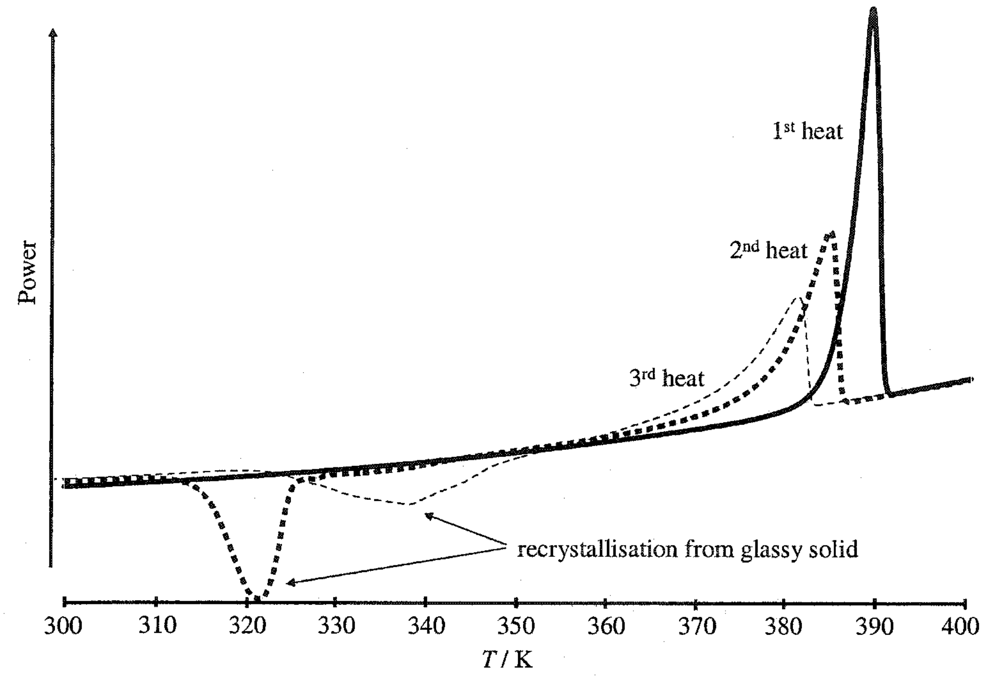

Figure 5.11 DSC heating scans of *Rac-o*-fluoromandelic acid for multiple melts.

After samples were melted then cooled, fusion peaks were not reproducible, *e.g.* *Rac-o*-fluoromandelic acid shown in figure 5.11. After samples were heated a second and third time, the scans show a partial recrystallisation before the fusion peaks. These recrystallisation peaks indicate that a glassy solid or an oil had formed after cooling. The second and third fusion peaks were broad with lower onset temperatures and lower enthalpies of fusion. When heated to $T = 400$ K and held for one minute before cooling, the *Rac-o*-fluoromandelic acid fusion temperature was lower by *ca.* 7 K and the enthalpy change was 23% smaller. A third melt showed another lowering of the fusion temperature by *ca.* 5 K and no further reduction in enthalpy change. With *Rac*-mandelic acid a second melt was *ca.* 22 K lower than the first melt and the enthalpy change was 29% smaller. Forming good crystals from a melt is not common for organics; therefore, the amorphous solids formed from the melts are not abnormal.

A second possible cause for the lower fusion temperature is decomposition. A slight decomposition of mandelic acid has been noted by other authors.(221,241,242)

Angus and Owen(241) have looked at the microanalysis of the glassy solid formed after melting mandelic acid and found: C, 64.6 %; H, 4.7 %. These values are very similar to the calculated values for a virgin sample. The authors have concluded that the analysis does not agree with the possibility of forming the ester anhydride or lactone as suggested by Bischoff and Walden(242), *i.e.*, the % carbon should increase with even a small mixture of these products. Lorenz *et al.*(221) found a mass loss of 2.8 % through thermogravimetry. Both these studies show that any decomposition is small.

The thermal analysis here is slightly different because the compounds were melted in hermetically sealed pans, which showed less than 0.29 % mass loss after cooling and puncturing. In addition, results for samples sealed in ultra high purity He(*g*) were the same as those sealed in air.

^{13}C NMR spectra for samples held at $T = 410$ K for five and 30 minutes prior to cooling, showed no additional peaks for *Rac-o*-fluoromandelic acid and some small additional peaks for *Rac*-mandelic acid, figure 5.12. Small peaks at 127.26 and 126.91 ppm were found for *Rac*-mandelic acid held at $T = 410$ K for five minutes and two smaller peaks at 128.53 and 128.97 ppm were found for *Rac*-mandelic acid held at $T = 410$ K for 30 minutes. These decomposition products have not been assigned. It is possible that the latter two peaks are those of benzoic acid, *i.e.*, loss of CO_2. A 9.7% loss CO_2 gives 2.8 % overall mass loss, as observed in the TGA of Lorenz *et al.*(221) A 1 % mass loss of CO_2 would give the 0.29 % mass loss, as observed here. The phenyl carbons of benzoic acid are expected above 128 ppm; therefore, the two peaks at 126.91 and 127.26 ppm do not support this decomposition. These peaks also do not support the benzaldehyde product, *i.e.*, additional loss of water. Multiple heat capacity measurements of the liquids, described later, show no appreciable change over a 34 minute time period between replicate measurements (within 3 % error).

All these results show that there is little decomposition of the chemical upon melting, which is in agreement with the literature discussed. Finally, it should be noted that experimental points shown in the phase diagrams, figure 5.2, are in good agreement with the Prigogine-Defay(49) and Schröder-van Laar(40,41) equations. These equations are not applicable with a significantly decomposed liquid, due to a change in the entropy of mixing. In addition, the entropies of fusion are of a reasonable magnitude; see Chapter four.

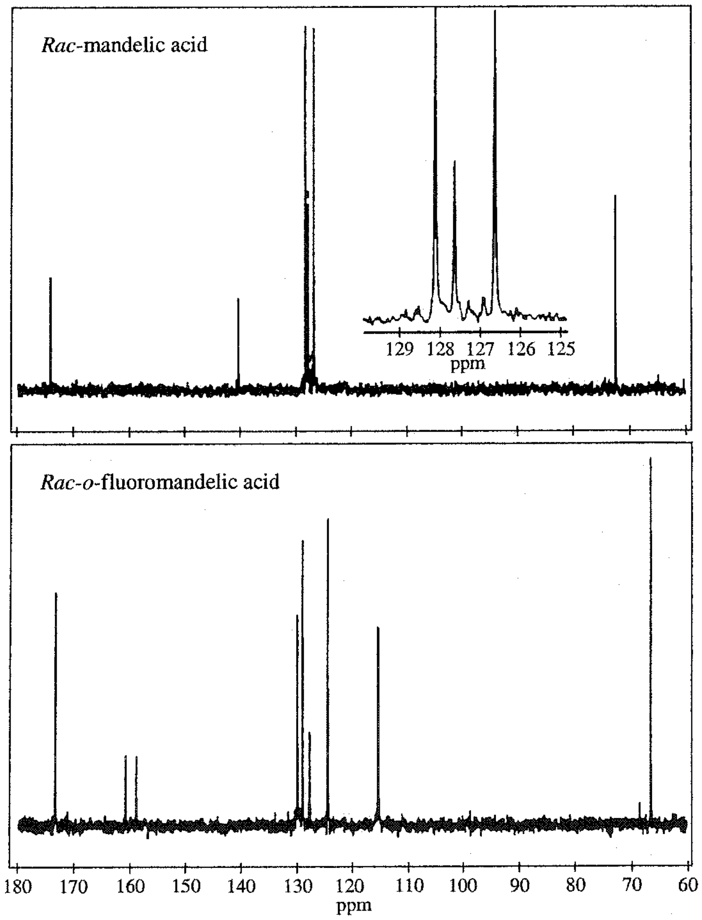

Figure 5.12 ^{13}C NMR spectra of *Rac*-mandelic acid and *Rac-o*-fluoromandelic acid after holding the hermetically sealed melt at $T = 400$ K for 5 minutes.

5.3.3 Crystal structures and first derivative properties

5.3.3.1 X-ray structures and hydrogen-bonding patterns

Mandelic acid

Summaries of the crystal structure parameters for *Rac*-mandelic acid and *R*-(-)-mandelic acid are shown in tables 5.5 and 5.6 at $T = 103$ to 296 K. The molecular structures, numbering schemes and representative packing diagrams for these crystals are shown in figures 5.13 and 5.14.

The crystal structure for *Rac*-mandelic acid was first reported by Cameron and Duffin in 1974.(243) Wei and Ward(213) later redetermined and evaluated previous structure determinations by comparing the interatomic parameters to X-ray and neutron diffraction studies of α-hydroxyacetic acid. Patil *et al.*(214) have reported the crystal structure for *R*-(-)-mandelic acid. For comparison, the cell parameters of Wei and Ward(213) and Patil *et al.*(214) are shown in tables 5.5 and 5.6 respectively. Fischer and Profir(244) have reported a different metastable *Rac*-mandelic acid structure at $T = 299$ K; however, they note that the modified structure rearranges to the more stable Pbca *Rac*-mandelic acid structure at $T = 318$ K.

Table 5.5 Summary of X-ray structure and refinement results for *Rac*-mandelic acid.

	Present results						Ref.(213)
T / K	103±1	143±1	153±1	183±1	223±1	296±1	295
Crystal	I	I	II	I	I	III	
diffractometer	AFC5R	AFC5R	AFC8	AFC5R	AFC5R	AFC5R	
Space Group	Pbca	Pbca	Pbca	Pbca	Pbca	Pbca	Pbca
a / Å	9.353(4)	9.402(4)	9.410(2)	9.535(4)	9.621(4)	9.948(3)	9.953(2)
b / Å	15.867(5)	15.931(5)	15.910(3)	15.993(4)	16.075(4)	16.162(3)	16.183(3)
c / Å	10.236(5)	10.200(5)	10.190(2)	10.067(5)	9.963(6)	9.957(3)	9.669(2)
V / Å^3	1519(1)	1528(1)	1525.6(4)	1535.2(9)	1540.8(9)	1552.5(7)	1557.4(6)
Z	8	8	8	8	8	8	8
ρ_{calc} / g cm^{-3}	1.330	1.323	1.324	1.316	1.312	1.302	1.298
R	0.039	a	0.047	a	a	0.039	0.087
O1H1-O3 / Å	1.9		1.9			1.9	1.91(7)
O2H2-O1 / Å	1.8		1.7			1.7	1.69(8)

Cell setting is orthorhombic; [a] only cell parameters obtained.

Table 5.6 Summary of X-ray structure and refinement results for *R*-(-)-mandelic acid.

	Present results											Ref.(214)
T / K	103±1	128±1	143±1	173±1	183±1	213±1	223±1	253±1	263±1	296±1	296±1	295
Crystal	I	II	I	II	I	II	I	II	I	II	I	
diffractometer	AFC5R	AFC8	AFC5R	AFC8	AFC5R	AFC8	AFC5R	AFC8	AFC5R	AFC8	AFC5R	
Space Group	$P2_1$	$P2_1$	$P2_1$	$P2_1$	$P2_1$	$P2_1$	$P2_1$	$P2_1$	$P2_1$	$P2_1$	$P2_1$	$P2_1$
a / Å	8.387(3)	8.398(2)	8.481(5)	8.460(1)	8.490(2)	8.506(2)	8.534(5)	8.557(1)	8.588(5)	8.604(2)	8.621(4)	8.629(1)
b / Å	5.860(3)	5.858(1)	5.858(3)	5.8585(8)	5.854(3)	5.858(1)	5.857(3)	5.8610(8)	5.856(2)	5.845(1)	5.855(2)	5.861(1)
c / Å	15.049(3)	15.053(3)	15.099(3)	15.092(3)	15.112(4)	15.123(3)	15.125(3)	15.152(2)	15.154(3)	15.150(3)	15.170(3)	15.185(2)
β / °	103.05(2)	103.05(1)	102.89(3)	102.92(1)	102.98(2)	102.89(1)	102.84(3)	102.81(1)	102.80(2)	102.77(1)	102.80(2)	102.76(1)
V / Å^3	720.6(4)	721.4(2)	731.2(5)	729.0(2)	731.9(4)	734.6(2)	737.0(5)	741.0(2)	743.1(5)	743.0(3)	746.7(5)	749
Z	4	4	4	4	4	4	4	4	4	4	4	4
ρ_{calc} / g cm^{-3}	1.402	1.401	1.382	1.386	1.381	1.376	1.371	1.364	1.360	1.360	1.354	
R	0.037	0.056	a	0.048	a	0.038	a	0.046	a	0.072	a	0.035
Molecule A												
O1H1-O3 / Å		1.9		1.9		1.9		2.35[c]		c		2.16(3)
O2H2-O1 / Å		1.7		1.7		1.7		1.6		1.7		1.83(2)
Molecule B												
O1H1-O3 / Å		2.1		2.1		2.0		1.9		2.0		2.21(3)
O2H2-O1 / Å		1.7		1.7		1.7		1.4[c]		1.7		1.88(2)
O1H1-O3[b] / Å		2.1		2.2		2.3		2.3		2.3		2.19(3)

Cell setting is monoclinic; [a] only cell parameters obtained; [b] intramolecular hydrogen bond; [c] abnormal OH bonds indicate less confidence in the hydrogen location.

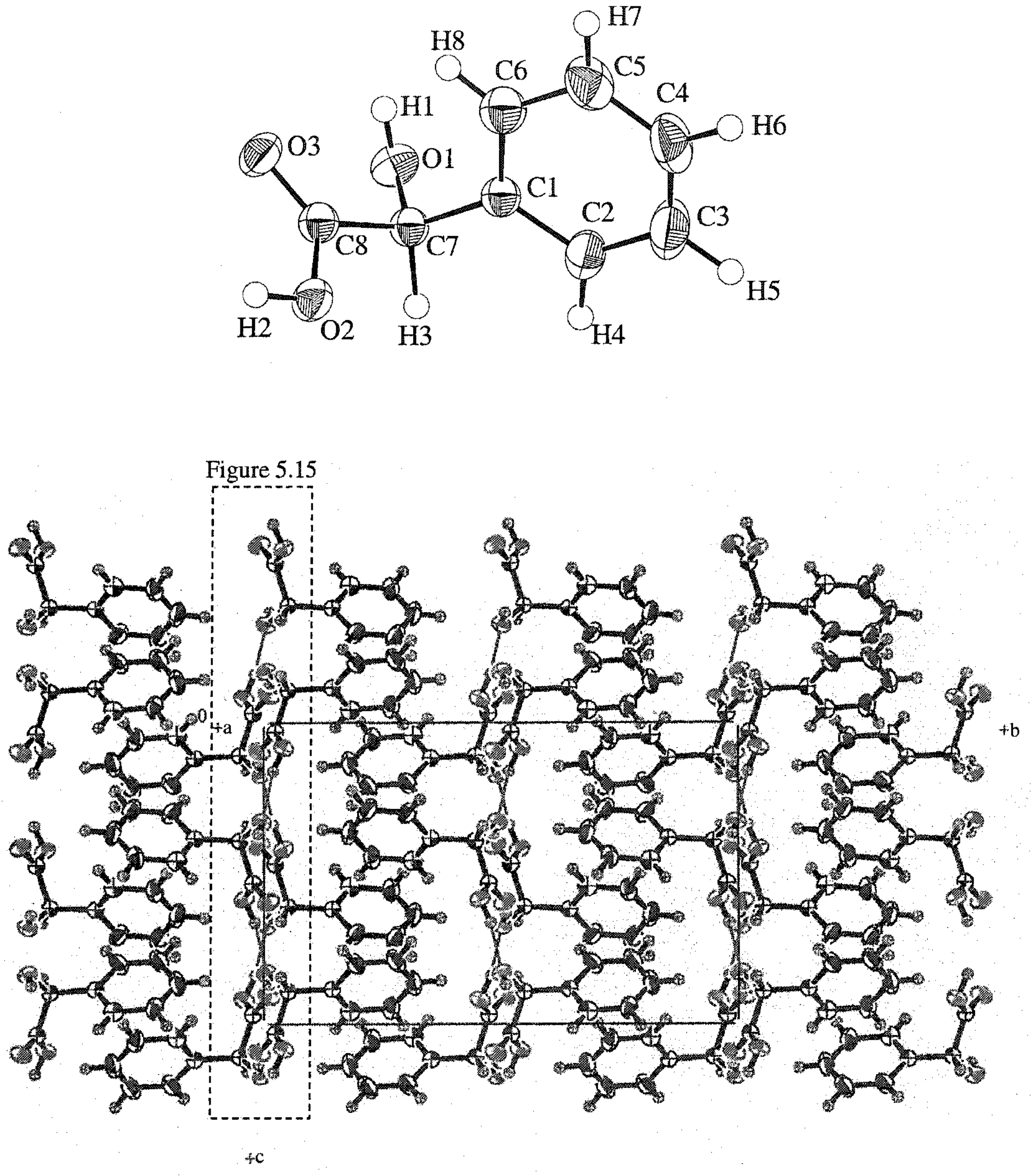
H7
H8
C6
C5
C4
H6
H1
O3
O1
C1
C2
C3
C8
C7
H5
H2
O2
H3
H4
Figure 5.15
0
+a
+b
+c

Figure 5.13 Molecular structure, numbering scheme and representative packing diagram for *Rac*-mandelic acid. $T = 153$ K; —— shows the unit cell; ----is the hydrogen-bonding plane shown in figure 5.15.

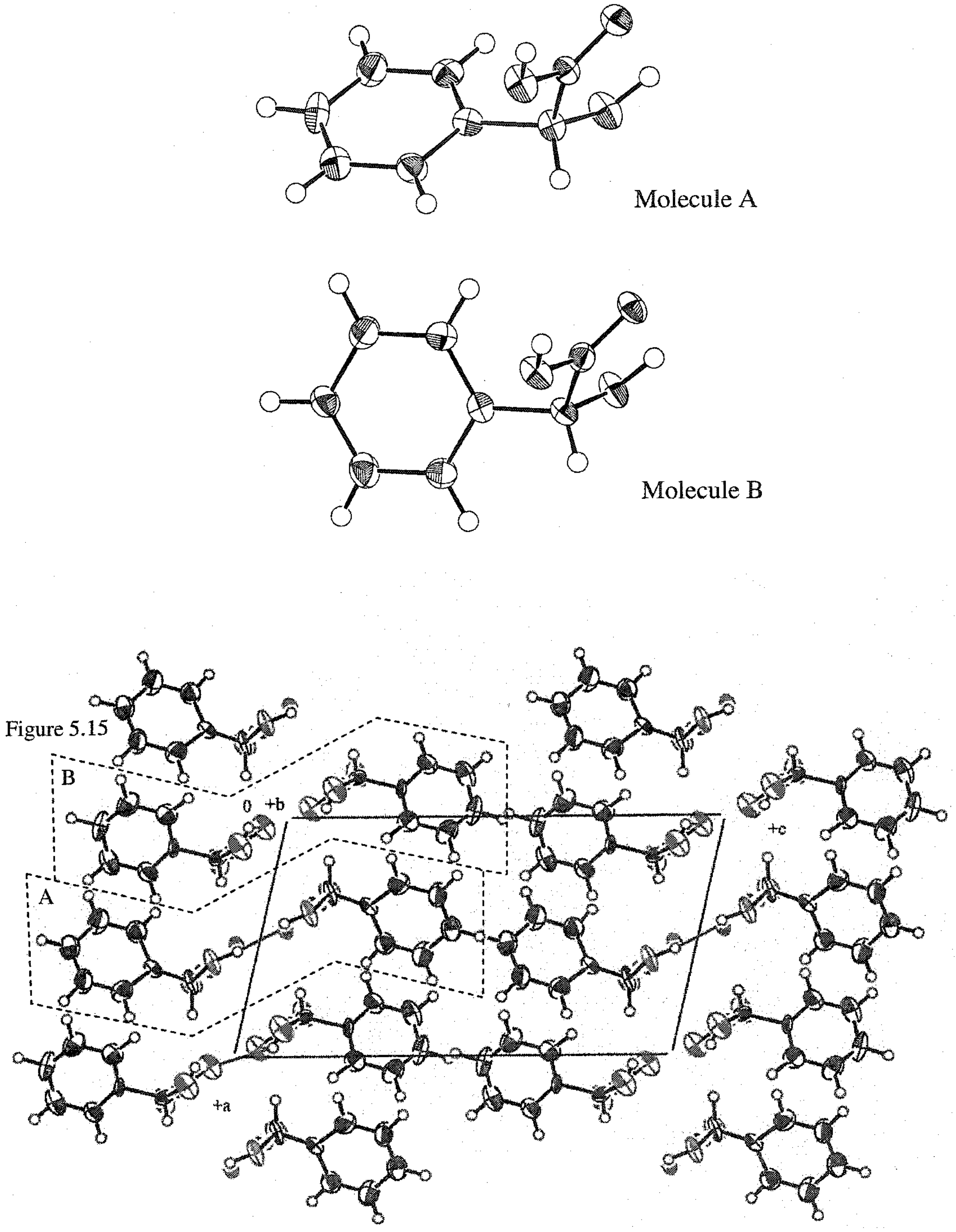
Molecule A
Molecule B
Figure 5.15
B
A
0
+b
+c
+a

Figure 5.14 Molecular structure and representative packing diagram for *R*-(-)-mandelic acid. *T* = 128 K; labels are given in figure 5.13; —— shows the unit cell; ---- is the hydrogen-bonding plane shown in figure 5.15.

The modified structure of Fischer and Profir(244) was originally thought to be the metastable formation of the conglomerate.(245) This structure was formed by controlling the cooling rate for recrystallisation from water. IR measurements showed that the crystal was the same as the optically pure crystals and that optically pure crystals grown using the same technique were the same structure as those described here.(245) The modified racemic structure was later found to be in the $P2_1/c$ space group and involves hydrogen-bonding patterns similar to the optically pure crystals. This study exemplifies why X-ray diffraction and vibrational spectroscopy are complementary. Recently Profir and Rasmuson(246) have found that these metastable racemic crystals can be grown from acetic acid solvent at fast cooling rates, but recrystallisations from other solvents, or from acetic acid at slow cooling rates, results in the more stable *Rac*-mandelic acid, Pbca.

Hydrogens were located and not refined in the some of the structures given here. A thorough hydrogen-bonding study was not completed, since the main goal was to obtain cell parameters at various temperatures. However, the hydrogen patterns and agree with the descriptions given by Li(247) and Larsen and Marthi.(215) A brief discussion of these patterns is given here.

The mandelic acids have two possible hydrogen-bonding donor groups, O1H1 and O2H2, and all three oxygens, O1, O2 and O3, can act as hydrogen-bonding acceptor atoms. Of the possible acceptors, all but O2 are commonly found acceptors in the hydrogen-bonding networks of the mandelic acids.(215) In addition, the torsional angle involving O3C8-C7O1 is normally small.(215) From the *ab inito* results of Chapter four, Mulliken charges were calculated for these atoms (B3LYP/6-31G(d,p)). The calculated charges for the minimised structures are as follows: O1 = -0.5507 *e*; O2 = -0.4706 *e*; O3 = -0.4731 *e*; H1 = 0.3248 *e*; H2 = 0.3321 *e*. Hydrogen bond distances, expressed as hydrogen to acceptor oxygen, have been reported in tables 5.5 and 5.6. The most electronegative of the possible acceptor oxygens, O1, was found to be a hydrogen bond acceptor in both *Rac*-mandelic acid and *R*-(-)-mandelic acid. Both donor groups are actively hydrogen bonding in these compounds. The hydrogen bonds of the racemic crystal are near 180°, whereas molecule B of the optically pure crystal has multiple acceptors for at *ca.* 150° and 100° for intra- and intermolecular O1H1-O3 bonds, respectively.

As shown in figure 5.13 and 5.14, there are extensive hydrogen-bonding networks (arrays) within these crystals. There is an interest in classifying hydrogen-bonding patterns for organics using graph sets.(248) Graph sets describe the combination of basic repeated units (motifs or sets) of hydrogen bonds: S, self; D, finite set; R, ring set; C, chain set. The geometric repetition of these sets, by ribbons, columns, or sheets describes a network of hydrogen bonds. The stacking of networks describes the hydrogen-bonding pattern. One of the overall goals of graph sets is to provide standardised compilations of hydrogen-bonding patterns, where pattern stability or frequency can be assessed and applied in calibration of empirical potentials. The hydrogen-bonding motifs of the mandelic acid crystals are shown in figure 5.15.

The *R*-(-)-mandelic acid crystal structure contains ribbons of hydrogen bonds, C(5)C(5) and S(5)C(5)C(5), parallel to the ***b*** axis, while the racemic crystal shows a more extensive corrugated sheet of rings parallel to the *ac* plane. The R(10) rings of the racemic crystal are held together by C(5) chains and are related by inversion symmetry, *i.* Li(247) has discussed the mandelic acid crystal patterns using the structures reported by Wei and Ward(213) and Patil *et al.*(214) Note that Li(247) has used different priority rules; therefore, assigned graph sets are S(5)R(8)R(8) and R(10)R(22), but the patterns are the same.

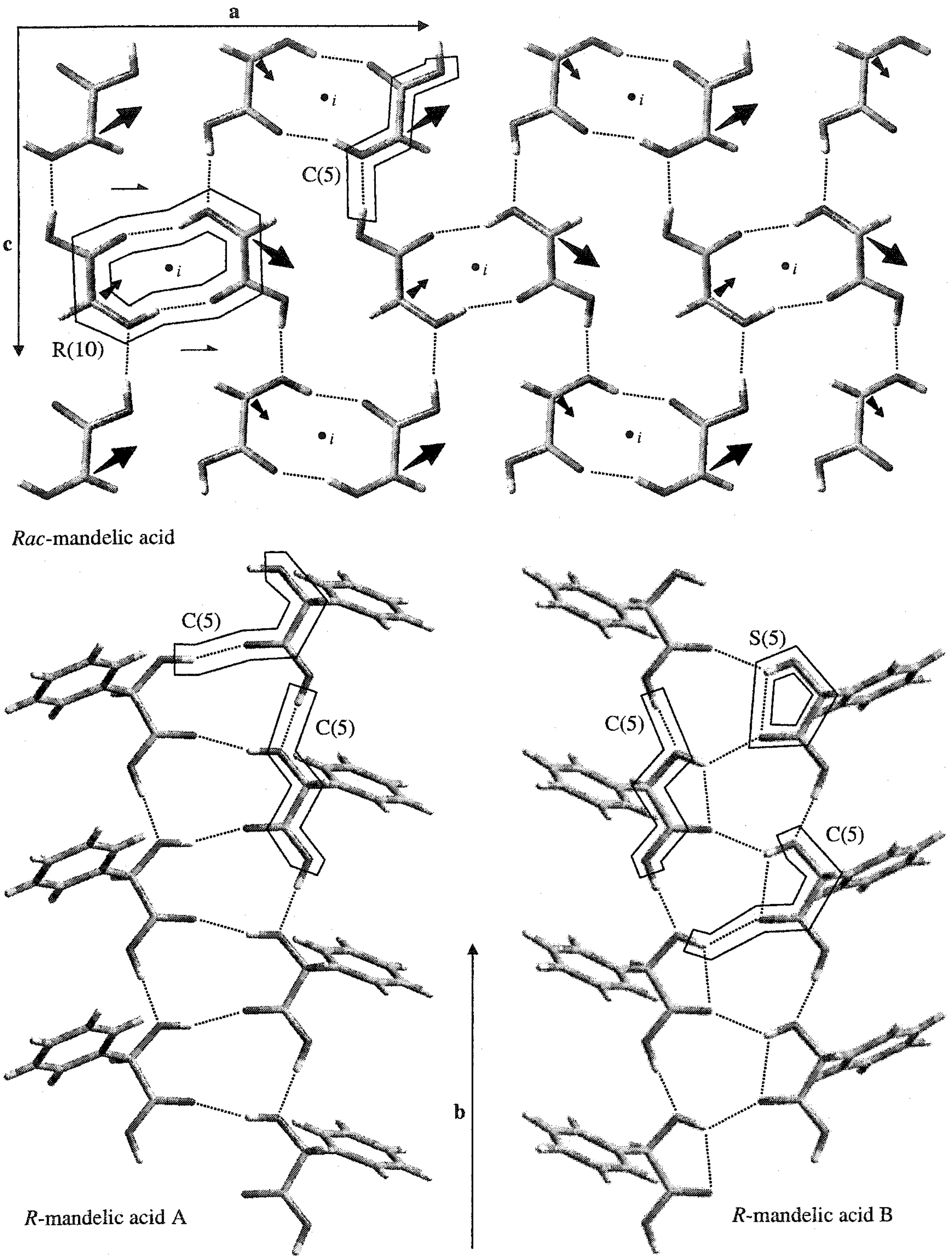
a
c
C(5)
R(10)
i
Rac-mandelic acid
C(5)
C(5)
S(5)
C(5)
C(5)
b
R-mandelic acid A
R-mandelic acid B

Figure 5.15 Hydrogen-bonding patterns of the mandelic acid crystals. The projections are illustrated in figures 5.13 and 5.14. Arrows in the racemic hydrogen-bonding motif show where the absent rings project out of, or into, the plane of the page.

Li(247) has noted a pseudo 2_1 symmetry relationship between the C(5)C(5) ribbons in the optically pure crystal, which would be 2_1 if there were not two conformers located in the unit cell. The metastable *Rac*-mandelic acid structure of Fischer and Profir(244) has a very similar hydrogen-bonding structure with inversion symmetry, which is the likely reason for the IR spectra being the same. Based on the hydrogen locations found in the structures here, the different conformers are involved in two distinguishable hydrogen-bonding ribbons. The distinguishing feature is an intramolecular S(5) ring involved in the hydrogen-bonding ribbon of molecule B. The pattern shows bifurcated hydrogen bonds, where there is competition between the intra- and intermolecular hydrogen bonds. Li's figure 3.14 shows the latter pattern and not the projection of the other ribbon involving molecule A. Larsen and Marthi(215) also have found pattern differences between the hydrogen-bonding ribbons of molecules A and B using the same structural data.(214) These authors have assigned a C(4) chain for the molecule A ribbon.

Li(247) has suggested that the hydrogen-bonding pattern of the optically pure crystal is more stable, because the fusion temperature of the optically pure crystal is higher than that of the racemic crystal. As noted by Brock *et al.*(51) and throughout the discussion in Chapter two and four, the fusion temperature of the racemic crystal should be compared to the conglomerate fusion temperature and not the optically pure fusion temperature. Therefore, the racemic crystal is more stable than the optically pure crystal near the fusion temperatures.

In addition to a more extensive hydrogen-bonding network in the racemic crystal, 2-D versus 1-D, the phenyl rings of for the *Rac*-mandelic acid and *R*-(-)-mandelic acid crystals have herringbone-type stacked phenyl ring planes. Both these herringbone stacked phenyl ring planes are parallel to the hydrogen-bonding patterns. The difference is that there is only one herringbone plane in the racemic crystal which includes molecules projecting out either side to a hydrogen-bonding plane, whereas the optically pure crystal shows two herringbone stacking planes with the involved molecules of each plane belonging to the same hydrogen-bonding plane. The phenyl rings of the *Rac*-mandelic acid are slightly bent, such that they do not fit straight into the herringbone stack like those in the *R*-(-)-mandelic acid crystal. The phenyl ring stacking plans are more interpenetrating in the *R*-(-)-mandelic acid crystal than those in the racemic crystal.

o-Fluoromandelic acid

Summaries of the crystal structure parameters for *Rac*-*o*-fluoromandelic acid and *R*-(-)-*o*-fluoromandelic acid are shown in tables 5.7 and 5.8 at $T = 103$ to 296 K. All these crystals were measured using the AFC5R. The molecular structures, numbering schemes and representative packing diagrams for these crystals are shown in figures 5.16 and 5.17. The racemic crystals were found in the more common $P2_1/c$ space group and the optically pure crystals were found in the same space group as the optically pure unsubstituted mandelic acid, $P2_1$. Once again, two distinguishable molecules were found in the unit cell of the optically pure compound. The calculated Mulliken charges for the minimised molecular structure of *o*-fluoromandelic acid are as follows: O1 = -0.5095 *e*; O2 = -0.4879 *e*; O3 = -0.4437 *e*; H1 = 0.3087 *e*; H2 = 0.3257 *e*, F = -0.2828 *e*. The largest difference here is that O1 is less electronegative that other substituted mandelic acids. The charge has been transferred to the chiral carbon.

Rac-*o*-fluoromandelic acid forms a different hydrogen-bonding pattern from that of *Rac*-mandelic acid and the other substituted mandelic acids. It also is the most stable relative to its conglomerate compared to the other halogen-substituted mandelic acids; $T_{\text{fus}}^{Rac} - T_{\text{fus}}^{con} = 63$ K versus $T_{\text{fus}}^{Rac} - T_{\text{fus}}^{con} = 21$ to 48 K for the other for the other halogen-substituted mandelic acids listed in table 5.1. The pattern reveals cyclic dimers, $R^2_2(8)$, involving the acid group, O2H2-O3. With the unsubstituted mandelic acid crystals, the hydroxyl hydrogen, H1, was adjacent to O3 and able to hydrogen bond with the same molecule using the O3 acceptor. With *Rac*-*o*-fluoromandelic acid, H1 is turned further away from the acid group and the intermolecular O1H1-O1 hydrogen bonds form chains which link the dimers together, C(2) related by 2_1. These linked dimers form corrugated hydrogen-bonding planes parallel to the ***bc*** plane.

Larsen and Marthi(215) found hydrogen bonding of molecules A with A and B with B for *R*-(-)-*m*-fluoromandelic acid and *R*-(-)-*p*-fluoromandelic acid, but not for *R*-(-)-*o*-fluoromandelic acid. This is in agreement with the structures reported here; however, there is a close intramolecular O1H1-F distance found here. This is shown by the Ortep diagrams shown in figure 5.17. This suggests that, as for *R*-(-)-mandelic acid, *R*-(-)-*m*-fluoromandelic acid and *R*-(-)-*p*-fluoromandelic acid crystals, there are competing intramolecular and intermolecular hydrogen bond interactions.

Table 5.7 Summary of X-ray structure and refinement results for *Rac*-*o*-fluoromandelic acid.

	Present results						Ref(200)
T / K	103±1	143±1	183±1	223±1	263±1	296±1	122±1
Crystal	I	I/II[b]	I	I	I	III	
diffractometer	AFC5R	AFC5R	AFC5R	AFC5R	AFC5R	AFC5R	
Space Group	$P2_1/c$		$P2_1/c$	$P2_1/c$	$P2_1/c$	$P2_1/c$	$P2_1/c$
a / Å	8.436(5)	8.427(8)	8.434(5)	8.435(5)	8.436(5)	8.425(1)	8.424(1)
b / Å	5.467(4)	5.492(2)	5.519(4)	5.548(4)	5.578(4)	5.605(1)	5.4766(7)
c / Å	15.974(4)	15.986(9)	15.984(4)	15.989(4)	15.995(4)	15.975(1)	15.959(2)
α / °		90.41(7)					
β / °	95.94(3)	95.89(6)	95.93(3)	95.92(3)	95.91(3)	95.908(9)	95.96(1)
γ / °		89.90(9)					
V / Å^3	732.8(6)	735.9(7)	740.1(6)	744.2(6)	748.5(6)	750.4(2)	732.3(3)
Z	4	4	4	4	4	4	4
ρ_{calc} / g cm^{-3}	1.542	1.535	1.527	1.518	1.510	1.506	1.543
R	0.035	a	a	a	a	0.028	0.040
O1H1-O1	1.6					1.6	1.87(2)
O2H2-O3	2.1					2.2	2.10(1)

Cell setting is monoclinic for all but *T* = 143±1 K; [a] only cell parameters obtained; [b] cell parameters checked with two crystals, one where the temperature was held at *T* = 103 ± 1 K for the first measurement and the second was measured first at *T* = 143 ± 1 K.

Table 5.8 Summary of X-ray structure and refinement results for *R*-(-)-*o*-fluoromandelic acid.

	Present results							Ref(215)
T / K	103±1	143±1	183±1	223±1	263±1	296±1		122±1
Crystal	I	I	I	I	I	II		
diffractometer	AFC5R	AFC5R	AFC5R	AFC5R	AFC5R	AFC5R		
Space Group	$P2_1$	$P2_1$	$P2_1$	$P2_1$	$P2_1$	$P2_1$		$P2_1$
a / Å	8.349(2)	8.351(2)	8.350(2)	8.355(2)	8.363(3)	8.375(2)		8.356(2)
b / Å	10.811(2)	10.855(2)	10.902(4)	10.958(4)	11.025(4)	11.080(2)		10.842(2)
c / Å	8.529(2)	8.533(2)	8.539(3)	8.549(3)	8.560(3)	8.580(1)		8.544(2)
β / °	94.14(2)	94.02(2)	93.92(2)	93.73(2)	93.53(2)	93.39(1)		94.13(2)
V / Å^3	767.8(3)	771.7(3)	775.5(4)	781.0(4)	787.8(4)	794.9(2)		772.0(3)
Z	4	4	4	4	4	4		4
ρ_{calc} / g cm^{-3}	1.472	1.464	1.457	1.447	1.434	1.422		1.464
R	0.049	a	0.049	a	a	0.036		0.029
O2AH2A-O1B	1.8		1.8			2.0		1.68(3)
O2BH2B-O3A	1.8		1.8			1.8		1.77(2)
O1AH1A-O3B	1.9		1.9			1.8	(-O1B)	1.87(2)
O1BH1B-O1A	1.9		1.9			2.0	(-O3A)	2.08(2)
O1AH1A-FA[b]	2.3		2.3			2.1		

Cell setting is monoclinic; [a] only cell parameters obtained; [b] intramolecular non-contact distance.

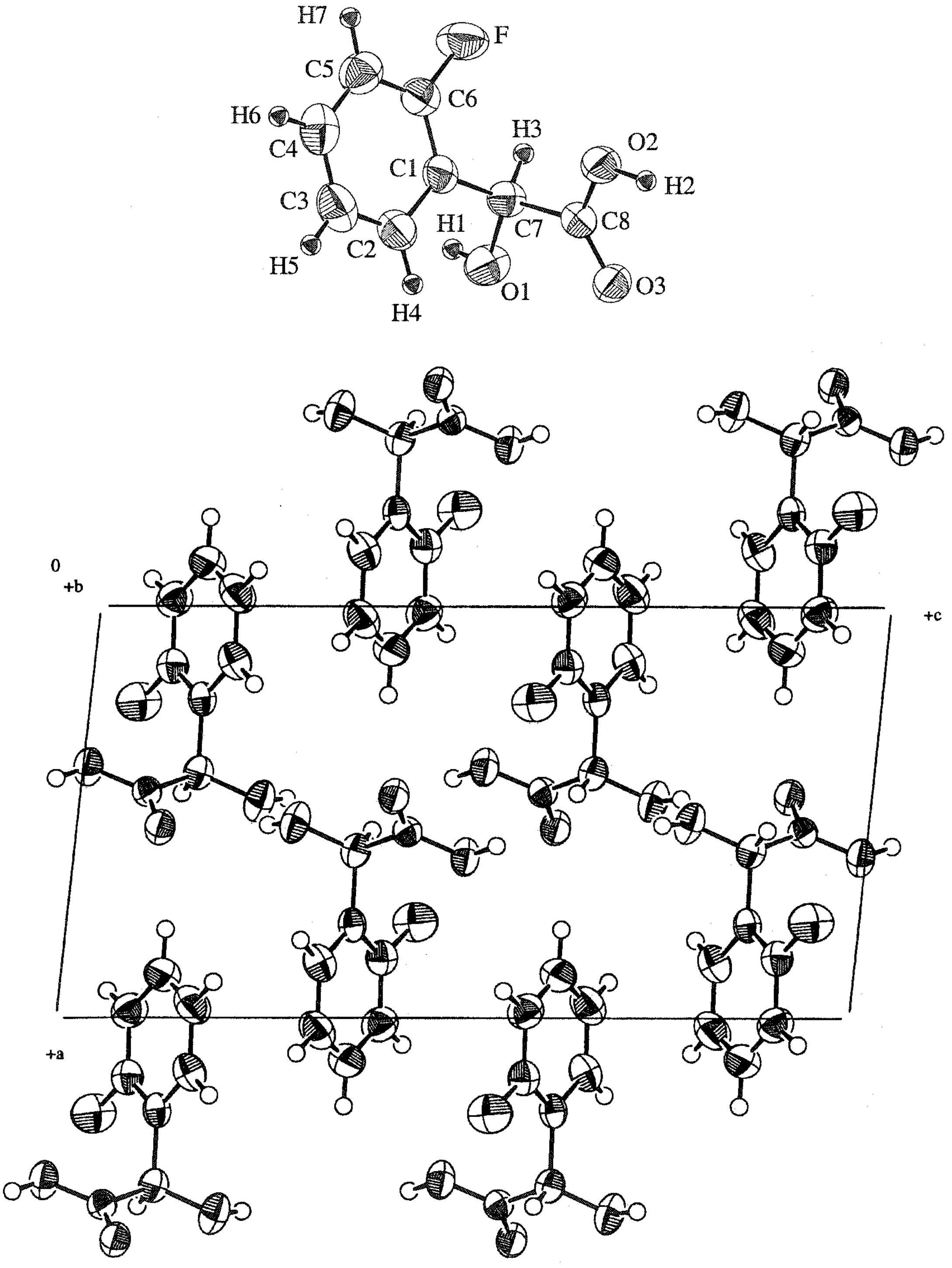
H7
F
C5
C6
H6
H3
O2
C4
C1
H2
C3
H1
C7
C8
H5
C2
O1
O3
H4
0
+b
+c
+a

Figure 5.16 Molecular structure, numbering scheme and representative packing diagram for *Rac-o*-fluoromandelic acid. $T = 296$ K; —— shows the unit cell

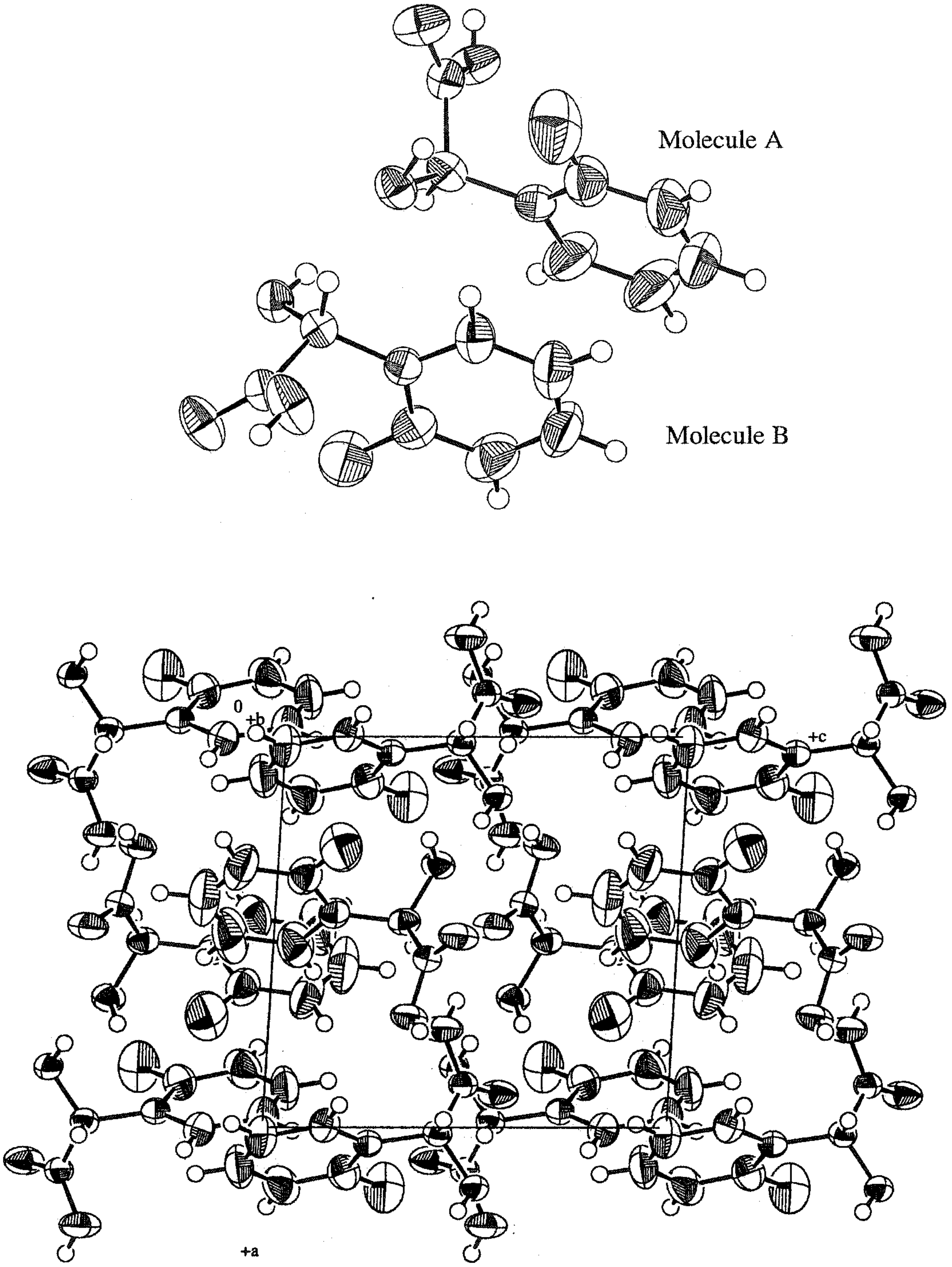
Molecule A
Molecule B
0
+b
+c
+a

Figure 5.17 Molecular structure and representative packing diagram for *R*-(-)-*o*-fluoromandelic acid. *T* = 296 K; labels are given in figure 5.14; —— shows the unit cell.

As assigned by Larsen and Marthi,(215) the intermolecular hydrogen-bonding motif of *R*-(-)-*o*-fluoromandelic acid consists of finite hydrogen bonds, D, of the type O2AH2A-O1B, O2BH2B-O3A, O1AH1A-O1B and O1BH1B-O3A. The hydrogen locations found in these crystals show finite hydrogen bonds of the type O2AH2A-O1B, O2BH2B-O3A, O1AH1A-O3B and O1BH1B-O1A. Motifs agree with the assignment of four finite hydrogen bonds between A and B conformers, but not A with A or B with B. There is no separation of phenyl ring overlap planes, as for *R*-(-)-mandelic acid crystal.

o-Chloromandelic acid

A summary of the crystal structure parameters for *R*-(-)-*o*-chloromandelic acid is shown in table 5.9 for $T = 173$, 253 and 296 K. The molecular structure and representative packing diagram for these crystals are shown in figure 5.18. Once again, two distinguishable molecules are found in these optically pure crystals and there is a lack of phenyl ring overlap, similar to the *R*-(-)-mandelic acid crystals. The calculated Mulliken charges for the minimised molecular structure of *o*-chloromandelic acid are as follows: O1 = -0.5498 *e*; O2 = -0.4612 *e*; O3 = -0.4762 *e*; H1 = 0.3265 *e*; H2 = 0.3329 *e*, Cl = -0.0154 *e*.

The hydrogen bond locations suggest that the hydrogen-bonding pattern is the same as *R*-(-)-*o*-fluoromandelic acid. However, the chlorines are not adjacent to the O1H1 groups of the same molecule; therefore, competing intramolecular interactions with the chlorines are not evident. The bond angle of the O2AH2A-O1B is *ca.* 145° with bond length of *ca.* 2.2 Å, which suggests that this bond is weak and bifurcated as in the other optically pure crystals. Korver *et al.*(236) have suggested that the *R*-(-)-*o*-chloromandelic acid crystal structure is similar to that of *R*-(-)-*o*-bromomandelic acid, because both show carbonyl stretching vibrations at $\nu = 1690$ and 1720 cm^{-1} in the IR spectra. In contrast, they have found only one carbonyl band for *R*-(-)-*o*-fluoromandelic acid;(236) however, figure 5.8 shows two carbonyl bands for the *R*-(-)-*o*-fluoromandelic acid crystals prepared here.

Table 5.9 Summary of X-ray structure and refinement results for *R*-(-)-*o*-chloromandelic acid.

T / K	173±1	253±1	296±1
Crystal	I	I	II
diffractometer	AFC8	AFC8	AFC5R
Space Group	$P2_1$	$P2_1$	$P2_1$
a / Å	8.117(2)	8.153(1)	8.163(1)
b / Å	7.550(1)	7.582(1)	7.617(1)
c / Å	13.919(3)	13.914(2)	13.9005(7)
β / °	105.81(2)	105.58(1)	105.378(6)
V / Å^3	820.7(3)	828.4(2)	833.3(1)
Z	4	4	4
ρ_{calc} / g cm^{-3}	1.510	1.496	1.487
R	0.059	0.064	^{a}0.025
O2AH2A-O1B	2.0		2.2
O2BH2B-O3A	1.4		1.7
O1AH1A-O3B	1.9		1.9
O1BH1B-O1A	1.7		1.8

Cell setting is monoclinic; crystal I was crystallised from acetone by T. S. Cameron and crystal II was crystallised from benzene. No structures for *R*-(-)-*o*-chloromandelic acid have been found in the literature.

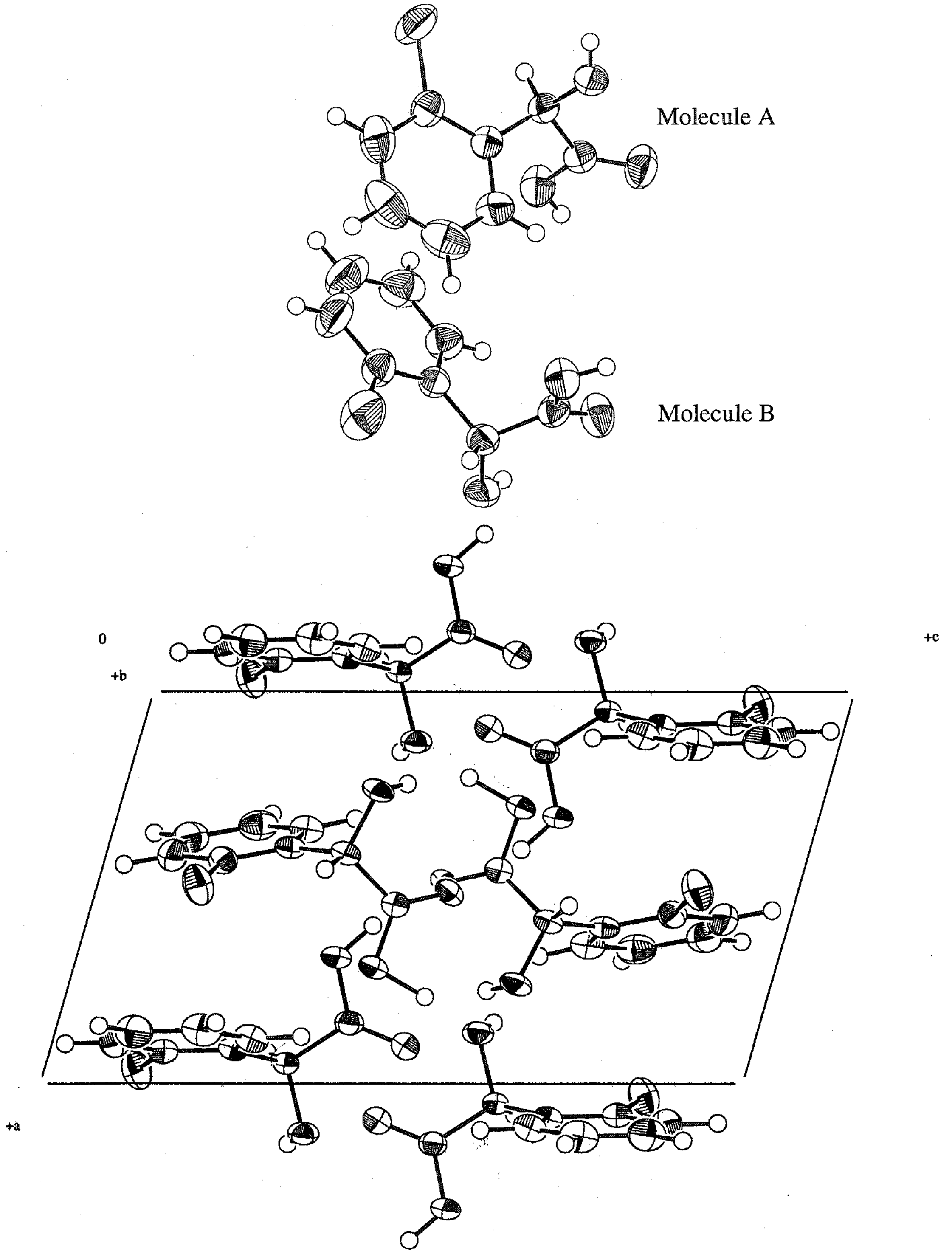
Molecule A
Molecule B
0
+b
+c
+a

Figure 5.18 Molecular structure and representative packing diagram for *R*-(-)-*o*-chloromandelic acid. *T* = 173 K; —— shows the unit cell.

o-Bromomandelic acid

Korver *et al.*(236) have reported X-ray analysis of *R*-(-)-*o*-bromomandelic acid and two configurations were found in each unit cell. No subsequent publication of the full structure was found in the literature or the CSD. The fusion temperature was lower than the racemic crystal fusion temperature reported by Collet and Jacques.(196) They suggested that the optically pure *o*-chloromandelic acid and *o*-bromomandelic acid are isomorphous, because their IR spectra were nearly identical.(196) To confirm this, they looked at the binary melting of a 1:1 mixture of *o*-chloromandelic acid and *o*-bromomandelic acid of opposite enantiomers; however, they found a solid solution.

As discussed briefly in the first chapter, a solid solution enantiomeric system is classified as an anomalous racemate (pseudoracemate) and not a true racemic crystal. Although less common, these types of crystals have been studied.(3) Collet and Jacques(196) concluded that *o*-bromomandelic acid forms a very low relative stability true racemate, based on a comparison of the IR spectra. This is a common technique when the fusion temperature is close to the conglomerate fusion temperature. The IR spectra obtained in the present work showed that there is a difference between the racemic mixture of *o*-bromomandelic acid (recrystallised from benzene) and the optically pure *o*-chloromandelic acid. The X-ray structure obtained from one of these crystals showed a twinned crystal and a 3:1 ratio of enantiomer layers.

Anomalous racemates with 3:1 compound stoichiometries have been reported in the literature in combination with a true racemic crystal and with no racemic crystal, *e.g.*, malic acid(249) and naringenin [2,3-dihydro-5,6-dihydroxy-2-(4-hydroxy-phenyl)-4H-1-benzopyran-4-one].(250) The latter of these examples forms a conglomerate of 3:1/1:3 crystals. This appears to be the case with the racemic mixture of *o*-bromomandelic acid. This also is in agreement with the different IR and Raman spectra for the racemic case.

If the resolution attempts of *o*-bromomandelic acid had not failed, the complete phase diagram could have been studied; however, using the optically pure fusion temperatures reported by Collet and Jacques,(196) the 3:1 crystals are within experimental error of the calculated conglomerate fusion temperature. Another possibility is that the sample is impure; however, multiple recrystallisations and sublimation did not change the fusion temperature and the NMR spectrum shows only the expected peaks. The IR and Raman also do not show any abnormal peaks. There is a possibility that *o*-bromomandelic acid forms a solid solution under the conditions used here, therefore, explaining the resolution failure.

Torbeev *et al.*(251) have discussed the racemic twinning of optically pure crystal layers for enantiomeric ammonium salts. These twinned crystals are found to depend on growth rate and nucleation conditions. None of the additional solvents or growth conditions used for *o*-bromomandelic acid resulted in crystallographic quality crystals, although the fusion temperatures were consistent. Regardless of the correct explanation, this work has found that growing *o*-bromomandelic acid crystals is more difficult and problematic than mandelic acid, *o*-fluoromandelic acid and *o*-chloromandelic acid.

5.3.3.2 Thermal expansion

In Chapters three and four, thermal expansion and isothermal compressibility were discussed in reference to the difference between the constant pressure heat capacity and the constant volume heat capacity; see equation 3.11. As experimental heat capacities are reported in this thesis, one objective of having X-ray crystal parameters at various temperatures was to estimate the thermal expansion.

Where heat capacities and other crystal properties are difficult to measure as tensor properties, thermal expansion is often measured for three different lattice directions. A general expression for the linear thermal expansion coefficient is given by

$$\alpha_l = \frac{1}{l}\left(\frac{\partial l}{\partial T}\right)_P, \tag{5.2}$$

where l can be any crystallographic direction. The volumetric expansion coefficient is given by replacing l with volume, V; see equation 3.12. By the convention adopted earlier in the thesis, the volumetric expansion coefficient is denoted by dropping the subscript altogether, *i.e.*, α. The axial expansion terms for a crystal can be used to calculate other tensor properties where the relationships are dependent on the space group.

Thermal expansion arises from anharmonicity of the lattice potentials.(147) Therefore at low temperatures where the zero-point energy is approached, the potential wells become harmonic and the thermal expansion becomes zero. All the crystals studied here are at temperatures above $T = 100$ K. At these higher temperatures, all thermal expansion was found to be either linearly correlated with temperature or not significantly correlated with temperature. Thus, correlation coefficients were obtained by using an empirically fit equation of the type $l = d_1 + d_2T$, where l is the unit cell length of $\boldsymbol{a}$, $\boldsymbol{b}$ or $\boldsymbol{c}$. The thermal expansion is then calculated by

$$\alpha_l = \frac{d_2}{d_1 + d_2T} \quad . \tag{5.3}$$

Correlations are shown in figures 5.19, 5.20 and 5.21. Normally coefficients of expansion are reported in the more practical way of allowing the linear or the volume denominator to be the constant room temperature value. This was the method of reporting thermal expansion coefficients in table 5.10. Using this convention equation 5.3 becomes $\alpha_l = d_2 / l^{298\mathrm{K}}$.

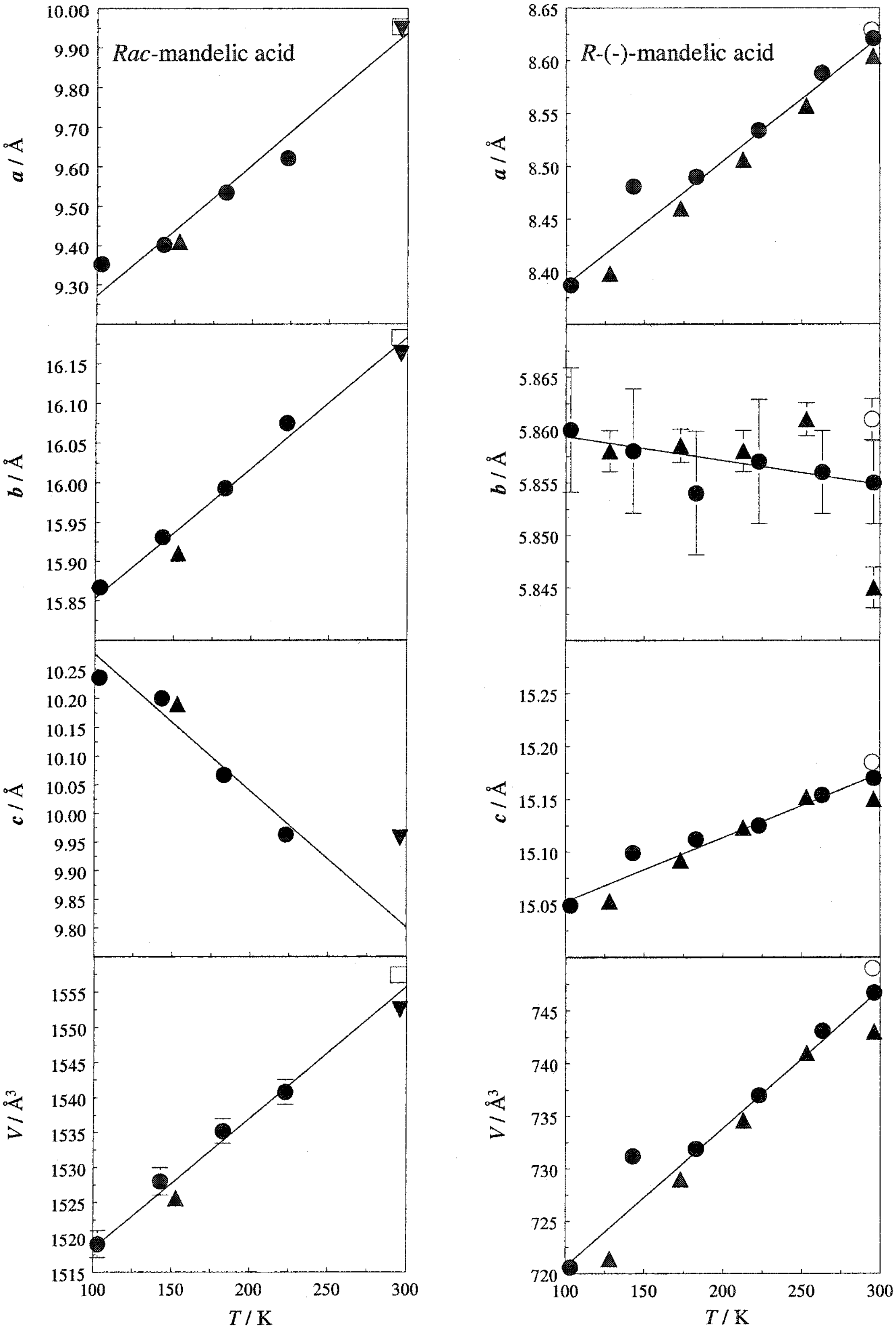

Figure 5.19 Crystallographic parameters at various temperatures for mandelic acid crystals. •, crystal I; ▲, crystal II, ▼, crystal III; □, Wei and Ward;[(213)] ○, Patil *et al.*[(214)] The visibility of error bars depends on the total parameter change (scale of *y*-axis).

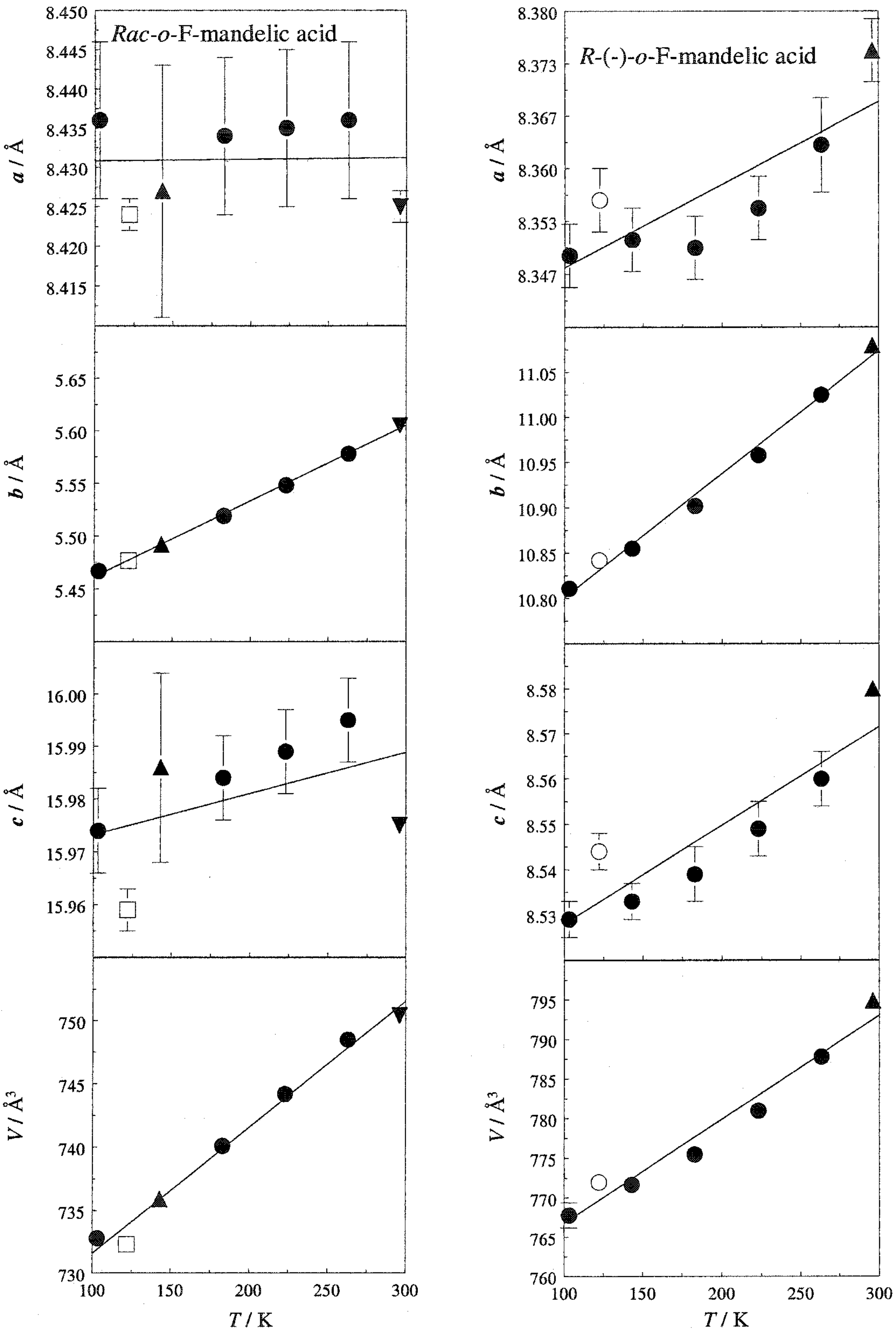

Figure 5.20 Crystallographic parameters at various temperatures for *o*-fluoromandelic acid crystals. ●, crystal I; ▲, crystal II, ▼, crystal III; □, Larsen and Marthi;[200] ○, Larsen and Marthi.[215] The visibility of error bars depends on the total parameter change (scale of *y*-axis).

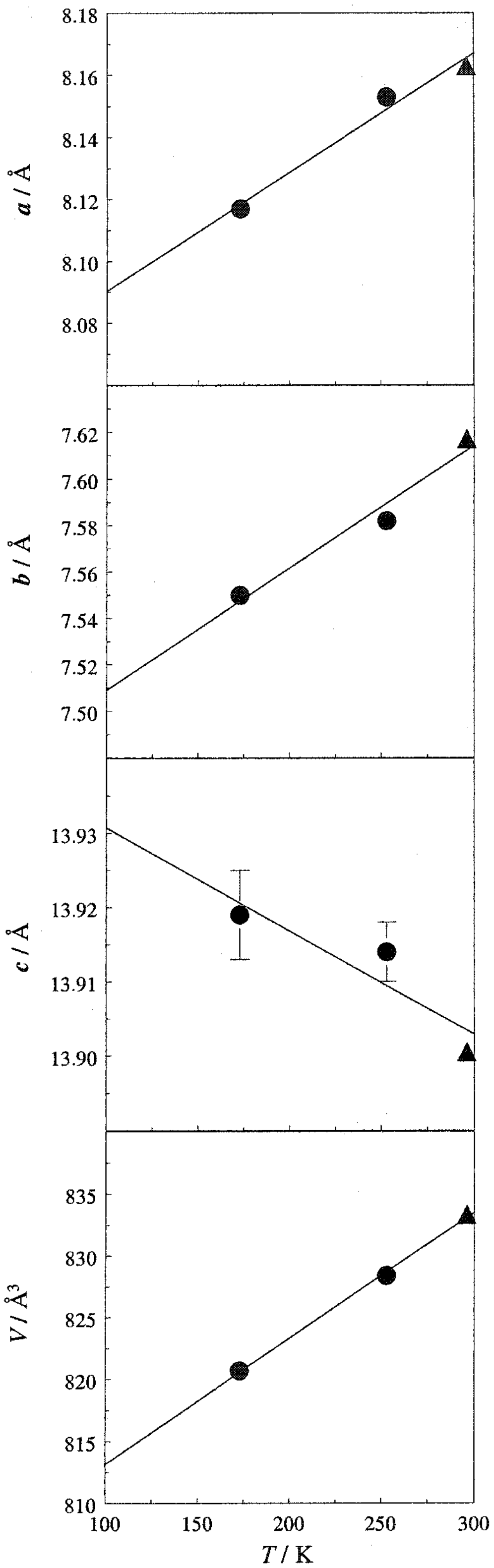

Figure 5.21 Crystallographic parameters at three temperatures for *o*-chloromandelic acid crystals. ●, crystal I; ▲, crystal II. The visibility of error bars depends on the total parameter change (scale of *y*-axis).

Table 5.10 The estimated linear and volumetric expansion properties of mandelic acid, *o*-fluoromandelic acid and *o*-chloromandelic acid crystals, and resulting values of (C_p-C_V).

	Rac-X-H	*R*-(-)-X-H	*Rac*-(-)-*o*-F	*R*-(-)-*o*-F	*R*-(-)-*o*-Cl
$d_{1,V}$ / (10^{-4} m^3 mol^{-1})	1.129 ± 0.004	1.065 ± 0.008	1.086 ± 0.004	1.132 ± 0.008	1.209 ± 0.009
$d_{2,V}$ / (10^{-8} m^3 mol^{-1} K^{-1})	1.41 ± 0.18	1.98 ± 0.32	1.50 ± 0.16	2.08 ± 0.34	1.53 ± 0.30
α_a / (10^{-4} K^{-1})	3.35 ± 0.54	1.36 ± 0.18	----	0.13 ± 0.08	0.47 ± 0.30
α_b / (10^{-4} K^{-1})	1.02 ± 0.12	----	1.28 ± 0.04	1.23 ± 0.10	0.69 ± 0.60
α_c / (10^{-4} K^{-1})	-2.42 ± 1.06	0.40 ± 0.08	----	0.25 ± 0.10	----
$V^{298\text{ K}}$ / (10^{-4} m^3 mol^{-1})	1.171 ± 0.004	1.124 ± 0.008	1.131 ± 0.004	1.194 ± 0.008	1.255 ± 0.009
α / (10^{-4} K^{-1})	1.20 ± 0.16	1.77 ± 0.28	1.33 ± 0.14	1.66 ± 0.28	1.22 ± 0.21
κ_0 / GPa	5.7 ± 2.6	7.0 ± 2.6	8.7 ± 2.6	6.9 ± 2.6	7.5 ± 2.6
$(C_p\text{-}C_V)^{50\text{K}}$ / J K^{-1} mol^{-1}	0.5 ± 0.3	1.2 ± 0.4	0.9 ± 0.3	1.1 ± 0.6	0.7 ± 0.3
$(C_p\text{-}C_V)^{100\text{K}}$ / J K^{-1} mol^{-1}	0.9 ± 0.5	2.5 ± 1.2	1.7 ± 0.6	2.3 ± 1.1	1.4 ± 0.7
$(C_p\text{-}C_V)^{300\text{K}}$ / J K^{-1} mol^{-1}	2.9 ± 1.5	7.4 ± 2.3	5.2 ± 1.1	6.8 ± 3.4	4.2 ± 2.1

The thermal expansion coefficients, as presented, are in large error near $T = 0$ K, because the linear relationship causes an extrapolation error, *i.e.*, any crystal volume change approaches $T = 0$ K with a slope of zero. This error affects the calculation of constant volume heat capacities from constant pressure heat capacities; however, C_p-C_V is still small small relative to C_p at lower temperatures; see Chapter four. Table 5.10 shows this C_p-C_V difference for $T = 50$, 100 and 300 K.

The crystal parameters for *Rac*-mandelic acid at $T = 263$ K could not be obtained. The temperature increments around this temperature are not sufficiently small to confirm or rule out a phase transition; however, the volumetric expansion coefficient (slope) seems to be well behaved and the Pbca cell is observed both below and above this temperature. Any transition is possibly related to either dynamic or static order/disorder of the hydrogens or phenyl rings. DSC scans at this temperature did not show any transition; however, DSCs often are not sensitive enough to show small or very broad thermal transitions.

In addition to this anomaly, the *c* unit cell axis of *Rac*-mandelic acid contracts upon heating, although the overall volumetric expansion is positive. Uniaxial negative thermal expansions for organic crystals, although somewhat rare, have been reported in the literature.(252) Although only three temperatures were investigated, *R*-(-)-*o*-chloromandelic acid shows a similar uniaxial negative thermal expansion. *R*-(-)-mandelic acid also shows the possibility of very small uniaxial negative thermal expansion. In these cases, the direction of contraction corresponds to same direction as O1H1-O1 intramolecular hydrogen-bonding chains. Negative thermal expansion is generally attributed to anharmonicity in low-frequency modes which involve rigid units.(252,253) The CO deformation frequencies of a C-OH group are expected at *ca.* 200 cm^{-1}; however, probably the lowest internal mode is the backbone libration of the phenyl ring. Figure 4.9 shows asymmetric potential wells, thus in the ideal gas state the rotational vibration of the phenyl ring of mandelic acid is anharmonic. This coupled with the herringbone phenyl ring stacking and the hydrogen bonding; could possibly provid the mechanism for the uniaxial negative thermal expansion.

Rac-(-)-*o*-fluoromandelic acid shows anomalous behaviour at T = 143 K. Here the crystal cell lengths are well behaved but the cell angles α and β deviate from 90°. At T =103 K and T = 183 K the unit cell is monoclinic. No anomaly was observed with DSC (T > 120 K) or in the volumetric expansion coefficient; however, both these techniques can be insensitive to small enthalpic or expansion changes, especially since there is only one set of cell parameters measured below T = 143 K. To rule out a problem with the specific crystal chosen and/or the thermal history, a second crystal was measured, where the crystal was cooled to T = 143 K, *i.e.*, the first crystal was first measured at T = 103 K. This second crystal gave similar anomalous unit cell parameters.

5.3.3.3 Isothermal compressibility

Isothermal compressibility, equation 3.13, is commonly reported is its reciprocal, the isothermal bulk modulus, κ_T:

$$\kappa_T = -V\left(\frac{\partial P}{\partial V}\right)_T, \tag{5.3}$$

Many solids of interest are at $P = 1$ atm, which is very close to $P = 0$ atm; therefore, the limiting bulk modulus at $P = 0$ K is useful, κ_0. There are not many experimental compressibility values reported for molecular organic crystals because their accurate measurement is problematic.(254,255)

King(255) has shown a useful linear correlation between bulk modulus and the packing index. For molecular crystals the packing index is defined by the ratio of the internal molecular volume and the unit cell volume, where the internal volume can be calculated from the atomic van der Waals radii.(162) Using the high precision values of King(255) a linear correlation was found to have a 2.6 GPa uncertainty at 95% confidence. This correlation was used to estimate the bulk modulii reported in table 5.9. The change in packing indices was not appreciable over the 200 K temperature range investigated; therefore, average packing indices were used. The van der Waals volumes for mandelic acid, *o*-fluoromandelic acid and *o*-chloromandelic acid are estimated to be 133, 141 and 151 Å^3, respectively.

5.4 Conclusions

The mandelic acids were identified as being good candidate compounds for experimental investigations. The true racemic and optically pure crystals of mandelic acid and *o*-fluoromandelic acid were obtained. Optically pure *o*-chloromandelic acid crystals were obtained. The racemic recrystallisation of o-bromomandelic acid resulted in a possible anomalous racemate at 3:1 ratio of enantiomers. The resolution of *o*-bromomandelic acid was unsuccessful. This is possibly due to solid state miscibility. NMR, IR, Raman, microanalysis and DSC all show that these crystals are of good quality and values obtained from these methods agree with the literature.

All crystals, except *o*-bromomandelic acid, were found to be of crystallographic quality. Some individual crystal structures were refined and non-phenyl hydrogens located by Prof. T. S. Cameron. These locations have been used to discuss the hydrogen-bonding differences among the crystals. Both the racemic crystals show 2-D hydrogen-bonding planes with *ca.* 180° hydrogen bonds and ring patterns. The optically pure crystals show evidence of bifurcated hydrogen bonds and intramolecular and intermolecular hydrogen bond competition. *R*-(-)-Mandelic acid showed more interpenetrating herring bone phenyl ring stacking planes than similar planes within *Rac*-mandelic acid. Difficulty in obtaining crystal cell parameters at one temperature shows the possibility of transitions in the *Rac*-mandelic acid and *R*-(-)-*o*-fluoromandelic acid crystals.

From cell parameter determinations, thermal expansion coefficients, bulk modulii and C_p-C_V were estimated for $T = 50$, 100 to 300 K. These values will be used to convert experimental C_p values to C_V. The estimated errors are large and statistically the C_p-C_V values are similar. However at $T = 300$ K, *Rac*-mandelic acid and *Rac*-*o*-fluoromandelic acid show a smaller C_p-C_V term than the corresponding optically pure crystals. Internal molecular contributions to expansion and compressibility are small relative to external contributions. Therefore, the C_p-C_V term is dominated by external differences, whereas the contributions to heat capacities at this temperature are affected more by number and nature of the covalent bonds in the molecule. Rather than the estimations used here, a more thorough study of the differences in bulk modulii and thermal expansions for racemic and conglomerate crystal pairs would be interesting. As shown in Chapter four, the internal contributions to C_V can be estimated using the experimental molecular vibrations; therefore, vibrational mode assignments using Raman and IR spectra are of interest.

6 INTERNAL VIBRATIONAL MODES

> *Dans les champs de l'observation, le hasard ne favorise que les esprits prepares.*
>
> *[In the field of observation, chance favours only the prepared mind.]*
>
> Louis Pasteur

6.1 Introduction

Chapter three showed how vibrational frequencies can be used to calculate internal vibrational heat capacities and Chapter four showed how external and internal frequency modes contribute to the total heat capacity for organic molecular crystals. With the vibrational spectra reported in Chapter five for *Rac*-mandelic acid, *R*-(-)-mandelic acid, *Rac*-*o*-fluoromandelic acid, *R*-(-)-*o*-fluoromandelic acid and *R*-(-)-*o*-chloromandelic acid, the internal heat capacities were calculated. In order to calculate the internal heat capacities for these crystals, the vibrational density of states needs to be described; therefore, the calculation required that the vibrational spectra be assigned.

For these mandelic acids, molecular coordinates for many normal vibrations cannot be well defined, *i.e.*, there is a lack of symmetry. However, some group frequencies can be assigned as pseudo pure vibrations, *e.g.*, phenyl ring modes. Therefore the discussion of the internal modes has been organised into discussions of six groups and their respective vibrations, ν, and deformations, δ. These include 30 substituted phenyl ring modes, three carbine modes, CH, six hydroxyl modes, $(OH)_{al}$ and $(OH)_{ac}$, one carbonyl stretch, $\nu(C{=}O)$, and 11 backbone modes, (bb or $OCCO_2$). Many of these group frequencies have been well studied in the literature where assignments are usually for either neat liquids or solutions.

6.2 Assignment tools

6.2.1 Symmetry considerations

All the space groups identified in the previous chapter are primitive and cannot be reduced. The two racemic crystals, *Rac*-mandelic acid and *Rac-o*-fluoromandelic acid, belong to space groups 61, Pbca (D_{2h}^{15}), and space group 14, $P2_1$ (C_2^2), respectively. All the optically pure crystals belong to space group 4, $P2_1$ (C_2^2). The molecular point group of any mandelic acid is C_1; therefore, the molecules can only sit on sites with the lowest symmetry. There are eight C_1 sites in the Pbca space group, four in the $P2_1/c$ space group and two in the $P2_1$ space group.

There are $3N$-6 = 51 internal modes for each unsubstituted and halogen-substituted molecule. If all internal vibrational modes are observed, there will be at least 51 observed frequencies in the vibration spectra. Those modes which are configuration dependent can show splitting in the optically pure crystal spectra. The internal peaks also are expected to be in the same vicinity for both racemic and optically pure crystal types. The latter aided in assigning internal modes. Because there is no centre of symmetry in the molecular point group or the site group, the mutual exclusion rule does not apply. By group theory all modes are assigned A.

6.2.2 Useful literature

6.2.2.1 Vibrational optical activity

Since the early investigations of Malus,(14) Arago(15) and Biot(16), the field of materials science has helped advance the understanding of optical activity. As synthetic quartz became commercially available in the early 1960's, quartz wave plates (polarisers) could be used to build circular dichroism, CD, instruments.(256) As a result, several of the studies already discussed were part of the young field of CD and optical rotary dispersion, ORD. Previous to this time, polarisers of sufficient quality were not readily available. It is now understood that optical rotary dispersion relationships are caused from molecules absorbing right and left handed polarised light with different extinction coefficients.(257) The difference in absorption-dispersion changes the relative phase shift of the light waves which can be measured with polarimetry. The sign and magnitude of the difference in absorption of right and left hand polarised light (Cotton effect) is measured by Circular Dichroism, CD.

One of the aims of early CD studies was to establish sector rules from correlations between CD spectra and absolute configuration. Applications of configuration correlation associated with the Cotton effect of the phenylcarbinols (common group $C_6H_5(CH)OH$) have been problematic because the configuration rules are rotamer dependent.(236) Generally the circular dichroism of vibrational modes is not rotamer dependent; therefore, studies on the vibrational circular dichroism, VCD, have become more relevant to understanding molecular configuration in solution. The interpretation of VCD and Raman circular intensity differential, CID, or Raman optical activity, ROA, is aided by knowledge of the vibrational assignment.(258) Literature in this area was very valuable towards assigning and accounting for internal vibrational modes discussed in this chapter.

The IR spectra of *Rac*-mandelic acid and *R*-(-)-mandelic acid have been published in the literature and show differences in the crystal types.(3) Polavarapu *et al.*(259) have studied the VCD of some phenylcarbinols. The latter study yielded arguments for the assignment of the CH deformation mode, δ(CH), for racemic mandelic acid in DMSO. By studying the effects of hydrogen bonding within carboxylic acid dimers in carbon tetrachloride, the carboxylic acid modes of racemic mandelic acid, $\nu(OH)_{ac}$ and $\nu(C{=}O)$, have been assigned.(237,260) Only discussions of these three modes for mandelic acid have been found in the literature. VCD studies also have indicated that coupling can be problematic with the absolute assignment of internal vibrational modes. This is somewhat expected since C-OH, C-COOH and C-ph bond vibrations, by normal coordinate analysis method, are considered skeletal vibrations involving the $OCCO_2$ group.(261)

6.2.2.2 Substituted benzenes

Another valuable area of the literature is the assignment of substituted benzenes. Benzene modes are the most numerous in mandelic acid and while some are coupled to the backbone modes, most are distinguishable. Benzene has a total of 30 normal vibrational modes; however, degeneracies arising from the high symmetry of non-substituted benzene reduces the observable vibrations to 20. Substitution or reduction of the symmetry allows for all 30 modes to be observed. The modes that are substituent sensitive have been thoroughly studied and described in the literature.(261)

The 30 modes for *mono*-substituted benzene, where the substituent's atomic mass is less than 25 g mol^{-1}, are shown schematically in figure 6.1.(261) The assignment numbers are those given in the extensive compilation published by Varsányi(262) and are numbered from 1 to 20 to reflect the similarity to the 20 normal modes of benzene. Varsányi's(262) assignment numbers are based on the serial numbers of Wilson.(263)

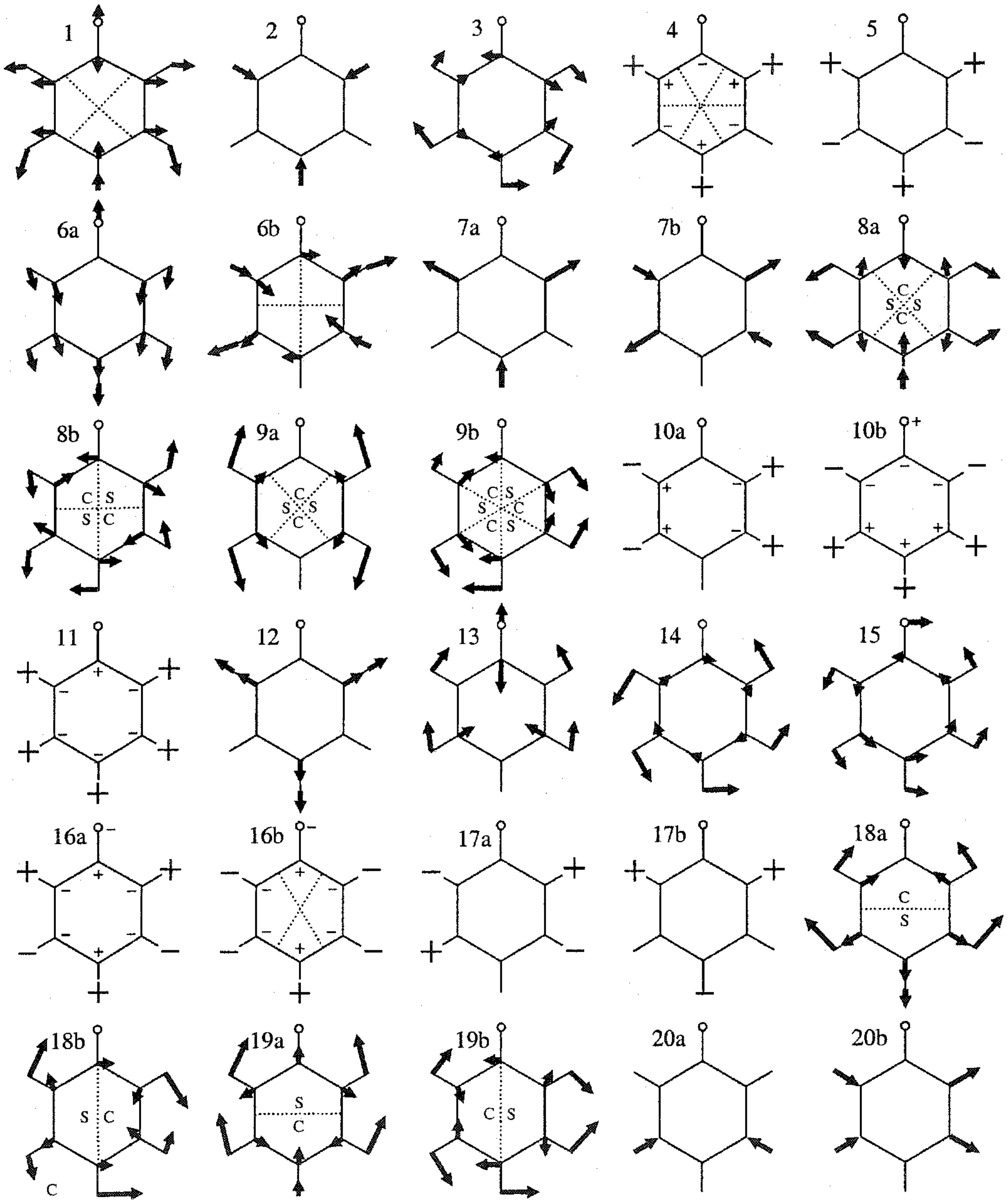
1
2
3
4
5
6a
6b
7a
7b
8a
8b
9a
9b
10a
10b
11
12
13
14
15
16a
16b
17a
17b
18a
18b
19a
19b
20a
20b
C
S
+
−

Figure 6.1 The 30 vibrational modes of *mono*-light substituted benzene. Vector magnitudes, sector compressions, C, and sector stretching, S, are based on the schematic drawings of Lin-Vien *et al.*(261) Vibrational mode serial numbers are those of Varsányi(262) and Wilson.(263)

For interpretation convenience, Varsányi(262) has described modes as being tangential, radial and out-of-plane vibrations. In other words, modes are distinguished between in-plane deformations, vibrations and out-of-plane deformations. From 700 assigned spectra, Varsányi(262) was able to find similarities and further categorise substituted benzene molecules based on the substitution position and on the substituents being heavy or light. A heavy substituent was defined as the any atom (atom bonded directly to the phenyl ring) with an atomic mass greater than 25 g mol^{-1}. A light substituent was defined as the any atom with an atomic mass less than 25 g mol^{-1}. Exceptions included the trifluoride, -CF_3, and sulfinylamino groups, -SONX-, which behave as heavy substituents.

Mandelic acid, being a *mono*-carbon-substituted benzene, would fall under the Varsányi's(262) category of *mono*-light. In this study, assignment possibilities for mandelic acid, *o*-fluoromandelic acid and *o*-chloromandelic acid crystals were considered using all the light and heavy substituent patterns, *i.e.*, the possibility that the chiral carbon could behave like a heavy substituent in a crystal was considered. The possible assignment patterns include *mono*-light, *mono*-heavy, *ortho*-light,light, *ortho*-light,heavy and *ortho*-heavy,heavy. In order to assign mandelic acid modes, similar phenyl ring substituents were considered. The frequencies for each assigned mode have been averaged for category types by selecting as many fully or near fully assigned molecules as possible from Varsányi's(262) compilation. The averaged frequencies are reported in table 6.1.

Table 6.1 Frequencies for *mono*- and *ortho*-substituted benzene molecules as assigned by Varsányi.(262)

mono-light		*mono*-heavy		*ortho*-light,light		*ortho*-light,heavy		*ortho*-heavy,heavy	
ν / cm^{-1}	Serial	ν / cm^{-1}	Serial	ν / cm^{-1}	Serial	ν / cm^{-1}	Serial	ν / cm^{-1}	Serial
201 ± 40	10b	171 ± 24	10b	175± 27	10b	154 ± 10	10b	134 ± 11	10b
342 ± 60	15	259 ± 39	15	238± 39	15	210 ± 35	15	146 ± 36	15
		335 ± 64	7a	296± 25	10a	237 ± 26	10a	215 ± 17	10a
406 ± 6	16a	402 ± 6	16a			246 ± 81	7a	274 ± 41	9b
493 ± 35	6a	458 ± 27	16b	418± 23	9b	409 ± 80	9b	324 ± 97	7b
511 ± 31	16b	615 ± 5[a]	6b	444± 14	16b	438 ± 7	16b	399 ± 61	7a
619 ± 5	6b	671 ± 21	6a	496± 39	6b	532 ± 25	6b	430 ± 6	16b
687 ± 13	4	686 ± 6	4	538± 26	16a	534 ± 29	16a	495 ± 11	16a
749 ± 11	11	744 ± 18	11	572± 19	6a	663 ± 16	6a	642 ± 10	6a
783 ± 25	1			712± 8	4	700 ± 7	4	693 ± 25	4
831 ± 11	10a	835 ± 6	10a	726± 32	1			707 ± 22	6b
887 ± 13	17b	908 ± 10	17b	753± 5	11	748 ± 5[a]	11	748 ± 7	11
957 ± 5	17a	965 ± 5[a]	17a	833± 18	12	807 ± 17	12		12
980 ± 7	5	988 ± 5[a]	5	857± 12	17a	749 ± 7	17a	856 ± 8	17a
1001 ± 5	12	1002 ± 5[a]	12	932± 10	17b	933 ± 5	17b	946 ± 13	17b
1026 ± 5	18a	1022 ± 6	18a	978± 13	5	976 ± 9	5	978 ± 5[a]	5
1080 ± 8	18b	1065 ± 6	18b	1031± 9	18b	1025 ± 8	18b	1025 ± 35	12
		1073 ± 9	1			1053 ± 10	1	1035 ± 5[a]	18b
1155 ± 5[a]	9b	1158 ± 5[a]	9b					1108 ± 15	1
1175 ± 10	9a	1177 ± 5[a]	9a	1116± 16	18a	1124 ± 9	18a	1117 ± 15	18a
1228 ± 29	13			1158± 5	9a	1158 ± 5[a]	9a	1160 ± 5[a]	9a
1300 ± 19	3	1267 ± 6	3	1205± 24	13	1233 ± 33	13		
1321 ± 12	14	1318 ± 11	14	1259± 28	7a				
1460 ± 9	19b	1435 ± 15	19b	1277± 15	3	1271 ± 18	3	1254 ± 5[a]	3
1503 ± 12	19a	1470 ± 8	19a	1304± 10	14	1273 ± 11	14	1267 ± 6	14
1589 ± 5	8b	1582 ± 16	8b	1461± 10	19a	1448 ± 7	19a	1433 ± 11	19a
1605 ± 4	8a	1587 ± 18	8a	1501± 9	19b	1477 ± 9	19b	1454 ± 16	19b
3022 ± 37	7a	3027 ± 5[a]	13	1587± 8	8a	1574 ± 9	8a	1567 ± 10	8a
3035 ± 10	20b	[b]3050	20b	1611± 10	8b	1593 ± 8	8b	1586 ± 19	8b
3039 ± 5[a]	7b	3052 ± 4	7b	[b]3017	7b	[b]3012	7b	3008 ± 6	13
3059 ± 7	2	3071 ± 5[a]	2	3026± 16	20b	3021 ± 10	20b	[b]3052	20b
3080 ± 16	20a	3083 ± 15	20a	3061± 21	2	3062 ± 6	20a	3067 ± 7	2
				3065± 6	20a	3073 ± 13	2	3097 ± 30	20a

[a]standard errors less than 5 cm^{-1} have been given a minimum of ±5 cm^{-1}; [b]where only one assignment was found, no standard error is reported; substituents on species include: $-CH_3$; $-CH_2CH_3$; $-CH(CH_3)_2$; $-NH_2$; $-OCH_3$; -F; $-CF_3$; -Cl; -Br; -I; -F,F; $-OCH_3,OCH_3$; $-NH_2,NH_2$; $-CH_3,CH_2CH_3$; $-CH_3,(CH_2)_2CH_3$; $-CH_3,CH(CH_3)_2$; $-CH_3,CHOHCH_3$; $-CH_3,F$; $-OCH_3,OCOCH_3$; CH_3,NH_2; $-NH_2,CH_2CH_3$; $-F,NH_2$; $-CH_3,Cl$; $-CH_2CH_3,Cl$; -F,Cl; $-CH_3,Br$; -F,Br; $-CH_3,I$; -F,I; $-OCH_3,Cl$; $-OCH_3,Br$; $-NH_2,Br$;-Cl,Cl; $-CF_3,Cl$; -Cl,Br; -Cl,I; -Br,Br; -Br,I; -I,I. Light substituents at those with atomic masses les than 25 g mol^{-1} and heavy subsitutents are those with atomic masses more than 25 g mol^{-1}.

6.2.3 *Ab initio* calculations

To gain further insight into mode composition, single molecule frequency calculations for unsubstituted mandelic acid and the ortho-halogen-substituted mandelic acids were completed using *ab initio* calculations. The calculated frequencies (B3LYP/6-31G(d)) described in Chapter four were compared to the patterns shown in table 6.1. The fractional contributions were not calculated; however, assignments were considered based on bond vibration amplitude, the magnitude of atomic displacement and out-of-plane bending for all atoms bonded to the phenyl ring. This was done numerically using the vectors given in the Gaussian 98(118) output files and by examining the animated vibration feature within GaussView 2.1©.(264) The frequency calculations also revealed the extensive coupling of modes.

The assigned *ab initio* frequencies for mandelic acid and *o*-fluoromandelic acid are reported in table 6.2. Because of extensive coupling, some assignments are still speculative and cannot be absolutely assigned. For these impure modes, other atomic motions also are listed in table 6.2. Qualitative information about Raman, IR and VCD activity also are included in table 6.2. These were useful in subsequent assignment of the experimental spectra. These calculated frequencies were used as aides in the assignment and are not considered to be accurate for several reasons: the error in the frequency is estimated at *ca.* 34 cm^{-1}; the calculation is applicable to the gas phase molecule; anharmonicity is ignored. Cautious interpretation of the *ab initio* results is especially important with the intensity information, where the Raman and IR intensity of the modes is expected to be different for different crystal sites and the gas phase. The frequencies for modes which are not substituent dependent are expected to be less dependent on the crystal surroundings.

Table 6.2 The *ab initio* vibrational analysis for mandelic acid and *o*-fluoromandelic acid.

mandelic acid						*o*-fluoromandelic acid					
ν / cm^{-1}	R	IR	VCD	Assn.	Other motion	ν / cm^{-1}	R	IR	VCD	Assn.	Other motion
<100	m	vw		{3·δ(bb)}	opCX	<100	m	w		{3·δ(bb)}	
208	w	m		δ(bb)	rCX	146	w	vw		15	bb
229	m	w		10b		190	m	w		10b	
308	vw	m		δ(bb)	opCC	257	w	w		10a	bb
345	m	s		15	(OH)$_{al}$	308	vw	s		δ(bb)	opCC
392	m	s		16a	(OH)$_{al}$	324	w	m		δ(bb)	opCC
406	m	s		16b	(OH)$_{al}$	351	m	s	s	16b	
449	m	m		δ(bb)		394	vw	m		9b	bb
480	m	w		δ(bb)	opCC	447	vw	m		δ(bb)	opCC
556	m	s		δ(bb)	opCC	485	w	m		δ(bb)	opCC
607	m	s	s	6b	bb, (OH)$_{ac}$	513	w	w		δ(bb)	opCC
610	m	s	s	6a	bb, (OH)$_{ac}$	530	m	m		6b	
644	m	s	vs	ν(bb)	C_6H_5	567	w	m		16a	(OH)$_{ac}$
683	w	s	s	4	(OH)$_{ac}$	614	m	s	vs	6a	bb
703	m	s	s	ν(bb)	opCH	639	m	s	s	ν(bb)	
733	m	m	s	11	bb	696	m	s		ν(bb)	tCC
828	m	vw		10a		719	vw	m		4	
836	m	w		1	bb	743	m	s		11	
861	m	s		ν(bb)	bb	769	m	m		1	bb
905	m	m		17b		838	m	w		17a	rCC
933	vw	vw		17a		862	vw	m		12	
959	vw	vw		5		882	m	s		ν(bb)	
979	vs	vw		12		912	w	m		17b	
1016	s	w		18a		943	vw	vw		5	
1058	m	s		18b	(OH)$_{al}$	1021	m	w		18b	
1093	m	vs	s	δ(OH)$_{al}$	(OH)$_{al}$	1073	m	vs	s	δ(OH)$_{al}$	(CO)$_{al}$
1142	m	vs	s	δ(OH)$_{ac}$	CH,tCC	1091	m	m		18a	
1146	m	w		9b		1143	m	m		9a	
1157	s	m		9a or 13		1149	w	vs	vs	δ(OH)$_{ac}$	
1170	m	m		13 or 9a		1172	m	s	s	13	bb,(OH)$_{al,ac}$
1221	m	s	s	δ(CH)		1217	m	m	vs	δ(CH)	
1272	m	m		δ(CH)	(OH)$_{al}$	1230	m	s	vs	7a	CH
1311	w	m		3	tCH	1251	m	m	s	3	
1323	m	s		14	CH,(OH)$_{al,ac}$	1293	m	w		14	CH
1326	m	s	s	δ(CH)	tCH,(OH)$_{ac}$	1322	m	vs		δ(OH)$_{ac}$	
1409	m	s	vs	δ(OH)$_{ac}$	CH	1335	m	m	s	δ(CH)	tCH
1443	w	m		19b		1412	m	s	s	δ(OH)$_{al}$	CH,(OH)$_{al}$
1484	vw	m		19a		1449	vw	m	s	19a	bb
1584	m	vw		8b		1484	vw	s		19b	CH
1599	s	w		8a		1585	m	m		8b	CH
1758	m	vs	s	ν(C=O)	bb	1607	s	m		8a	
2912	vs	m		ν(CH)		1765	m	vs	s	ν(C=O)	
3058	s	w		7a		2888	s	s		ν(CH)	
3065	vs	w		7b		3064	s	w		7b	
3074	vs	s		20b		3075	vs	m		20b	
3085	vs	s		2		3089	vs	s		2	
3100	vs	m		20a		3102	vs	m		20a	
3504	vs	vs	s	ν(OH)$_{al}$		3505	s	vs	s	ν(OH)$_{al}$	
3540	vs	s		ν(OH)$_{ac}$		3541	vs	s		ν(OH)$_{ac}$	

B2LYP/6-31G(d) frequencies have been scaled by the empirical factor of Scott and Radom, 0.9614.(119) Qualitative values for Raman (R), IR and VCD have been chosen based on standard deviations of intensity. Motion is denoted as follows: bb, backbone motion involving $OCCO_2$; (OH)$_{al}$ and (OH)$_{ac}$, OH on alcohol and carboxylic acid group; opCC and opCX, out-of-plane phenyl motion of CH and CX; tCH and rCX, tangential phenyl CH motion and radial CX motion.

Most of the phenyl modes are in agreement with the average values in table 6.1 for both the *mono*-light category and the *mono*-heavy category; however, if the *mono*-heavy set of serials is chosen, then OH and CH vibration and deformation modes are not all accounted for. There is extensive motion shown by these groups for many of the modes. For example, three δ(CH) modes have been assigned and one $\delta(OH)_{al}$ mode has not been assigned. The total of four deformation modes for these two groups is still expected; however, the mixing suggests that δ(CH) motions are the largest contributing motion for all three of these modes.

6.2.4 Deuterated mandelic acids

In addition to the synthesis and growth of crystals discussed in the previous chapter, a brief description of some additional experimental work is provided here. To help in identify modes affected by (OH) vibration and deformation motions, the deuterated samples of racemic mandelic acid and *o*-fluoromandelic acid were prepared and their vibrational spectra were obtained.

Deuterated samples of racemic mandelic acid and *o*-fluoromandelic acid were prepared by dissolving 250 mg samples in 10 mL D_2O (Canadian Isotopes, D-175, Lot. L233P2), *ca.* 0.3 mol %. After 48 hours the solvent was evaporated. Assuming complete random exchange between the deuterium and hydrogen at a time less than 48 hours, 99.7 % of the hydroxyl and acetic acid hydrogens have been estimated to be replaced by deuterium. Neat solid samples were characterised by DSC and Raman spectroscopy, using the same experimental procedures outlined in Chapter five (DSC scan at 167 mK s^{-1}). The Raman spectra for the deuterated solids are shown in figure 6.2.

The DSC scan of racemic deuterated *o*-fluoromandelic acid showed a fusion peak at $T_{fus} = 388.3$ K and $\Delta_{fus}H = 29$ kJ mol^{-1}. The DSC scan of racemic deuterated mandelic acid

$T_{\text{fus}} = 391.4$ K and $\Delta_{\text{fus}}H = 24$ kJ mol^{-1}. These values are slightly smaller than the protonated fusion values, table 5.1. The DSC scan of deuterated *Rac*-mandelic acid also showed a small second peak at $T = 357.0$ K with $\Delta H = 5$ kJ mol^{-1}. This small peak is *ca.* 10 K below the calculated conglomerate fusion temperature for the protonated sample, Table 5.1.

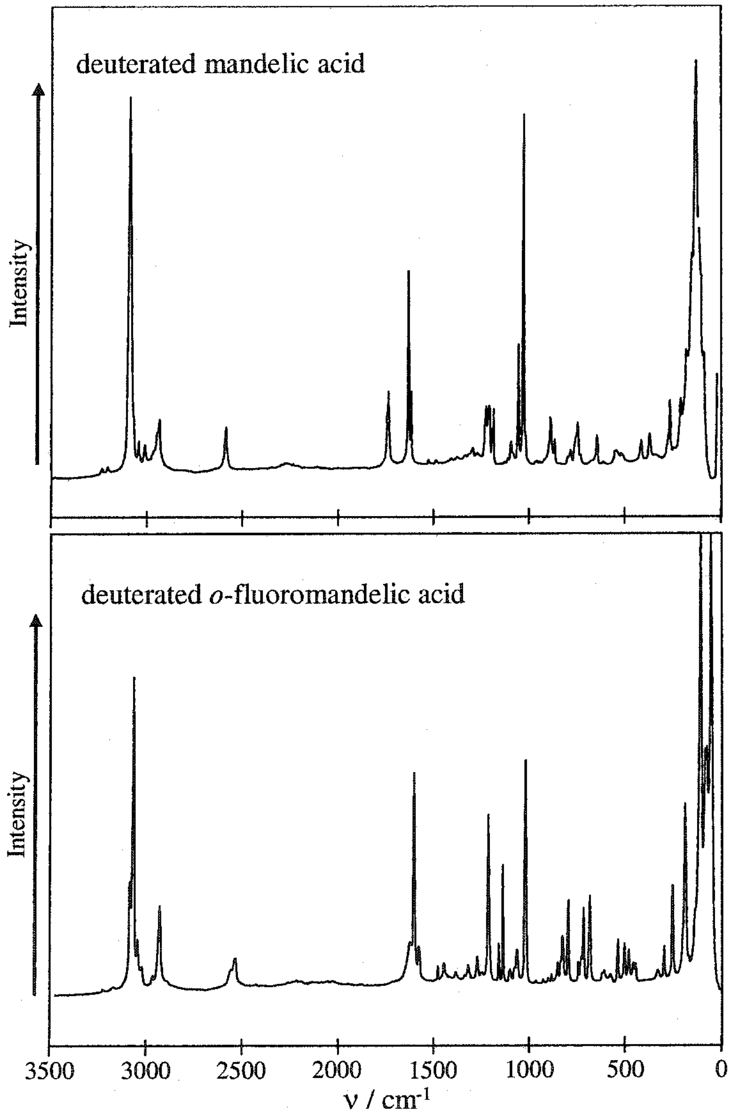

Figure 6.2 Raman spectra of racemic deuterated mandelic acid and *o*-fluoromandelic acid.

6.3 Assignment tables and density of internal vibrational states

All vibration mode assignments and qualitative peak evaluations for mandelic acid, *o*-fluoromandelic acid, *o*-chloromandelic acid and *o*-bromomandelic acid crystals are given in tables 6.3, 6.4 and 6.5. Many of the peaks are split in the optically pure crystals and not split in the racemic crystals. This splitting of peaks is indicative of conformation effects and hydrogen bond differences. Small shifts in peaks, $\Delta_{\mathrm{Rac}}\nu$, can be observed for the mandelic acid and *o*-fluoromandelic acid systems. These shifts are caused by the molecules being in different crystals. All $\Delta_{\mathrm{Rac}}\nu > 4$ cm^{-1} are shown in the tables and show that the largest differences are in the fingerprint region, $\nu < 1000$ cm^{-1}.

Because the aim was to calculate internal heat capacities and not all vibrations are uniquely assigned, the frequencies have been weighted to ensure that the total number of internal vibrations per molecule is 51 (19×3-6). Internal molar heat capacities have been calculated by modifying equation 3.16:

$$C_{V,\mathrm{int}} = R\sum_{i=1}^{m} n_i \frac{x_i^2 e^{x_i}}{(e^{x_i}-1)^2}, \tag{6.1}$$

where m is the total number of observed frequencies, n_i is the scaling factor for peak i and x_i is defined by equation 3.17. Thus the density of internal vibration states has been fixed, such that $\Sigma n_i = 51$. This calculation is utilised in Chapter seven.

Tables 6.3, 6.4 and 6.5 show the weights used for each assignment. If only one assignment has been made for a mode, then the weight is unity, *e.g.*, 19b in all spectra. If there are two peaks (splitting denoted by '}' in the tables), the weight corresponds to ½ for each peak, *e.g.*, ν(C=O) is assigned a weight of 1 for all tables, but the peak is split into two peaks for all spectra except *Rac*-mandelic acid. Most weights are at unity which provides only a slightly different density of vibration states than the other option of scaling the complete unassigned spectra by the same factor.

Table 6.3 Assignments of the vibrational spectra for *Rac*-mandelic acid and *R*-(-)-mandelic acid.

Rac-mandelic acid			*R*-(-)-mandelic acid						
ν / cm^{-1}	R	IR	ν / cm^{-1}	R	IR	Assn.	*n*	$\Delta_{Rac}\nu$	Deuterated ν / cm^{-1}
						Total	51		
117	vs		126	sh		δ(bb)	1	9	113
122	vw		151	sh		δ(bb)	1	29	133
153	m		170	m		δ(bb)	1	17	161
210	m		186	m		δ(bb)	1	-24	187
218	sh		223	w		10b	1	5	220
275	w	w	245	s		δ(bb)	1	-30	242
295		w	257	w	w	δ(bb)	1	-38	
335	m	m	322	w	s	15	1	-13	315
362		m	346	m	vw	16a	1	-16	343
402	w	w	386	w	m	16b	1	-16	388
464	m	w	492	w	m	δ(bb)	1	-28	490
498	s	s	524	m	w	δ(bb)	1	26	519
608	sh	s	594	m br	w	6b	1	-14	580
617	s	sh	616	s	m	6a	1		615
683	w br	s	645	m	m	} ν(bb)	1	-38	645
			668		m			-15	
697	vw	s	692		s	} 4	1	-5	
			703	w br	m			6	703
732	s	s	722	sh	s	} 11	1	-10	718
			733	s	m				722
768	m	m	756	s	w	} ν(bb)	1	-12	753
			770	w	m				771
842	m		837	m	m	10a	1	-5	838
856	s	m	861	s	m br	1	1	5	860
886		m	(886)			ν(bb) CCOopstr	1		890
909	w	vw	908	m	vw	17b	1		916
933	w	w	934	m	m	17a	1		938
990	sh	w	989	m	vw	5	1		989
1004	vs	m	1003	vs	vw	12	1		1003
1030	s	m	1026	s	vw	18a	1		1027
1060	w	vs	1063	m	vs	18b	1		1065
1078	w	m	1079	w	m	} δ(OH)$_{ac}$	1		1079
1106		w	1097	vw	s			-9	1096
1155	s	vw	1157	s	vw	9b	1		1155
1179	sh		1177	s	vw	9a	1		1177
1183	s		1164	s		δ(XH)	4/5	-19	1164
1192	s	s	1191	s	s	13	1		1198
1225	m	s	1201	sh		δ(CH)	4/5	-24	1238
1253	m	m	1246	m br	s	3	1	-7	1266
1284	m	s	1286	m	m	14	1		1283
1298	w	m	1307	m	m	δ(XH)	4/5	9	1305
1343	w	m	1348	m	w	δ(CH)	4/5	5	1345
1375	w	s	1375		s	δ(CH)	4/5		1379
1397	w		1402	w	vw	} δ(OH)$_{ac}$	1	5	
1446	w	sh	1439	w	sh			-7	
1453	w	s	1456	w	vs	19b	1		1457
1498	vw	m	1497	w	s	19a	1		1496
1587	s	m	1588	s		8b	1		1588
1603	vs	m	1604	vs		8a	1		1603
1717	s	vs	1714	s	vs	} ν(C=O)	1		1709
			1724		vs			6	

continued…

Table 6.3 Continued.

Rac-mandelic acid			*R*-(-)-mandelic acid						
ν / cm^{-1}	R	IR	ν / cm^{-1}	R	IR	Assn.	*n*	$\Delta_{Rac}\nu$	Deuterated ν / cm^{-1}
2972	s		2909	m		$\}$ ν(CH)	1	-63	2903
			2980	m				8	2979
3009	m		3010	M		7a	1		3011
3034	m	vw	3039	w		20b	1	5	3038
3048	m		3048	sh		7b	1		3049
3063	vs		3059	vs		2	1		3060
3071	sh	vw	3067	sh		20a	1		3068
3171	w		3173	w		2·8b overtone			3172
3199	w		3202	w		2·8a overtone			3203
3392	vw	s	3445	vw	s	$\nu(OH)_{al}$	2	53	2556, 2240

Qualitative intensity includes: very weak, vw; weak, w; medium, m; strong, s; very strong, vs; broad, br; shoulder, sh. Brackets, ν(bb) near 886 cm^{-1} is not observed for *R*-(-)-mandelic acid, but was applied in calculations from the *Rac*-mandelic acid observation. *n* is for calculation of $C_{V,\mathrm{int}}$ using equation 6.1.

Table 6.4 Assignments of the vibrational spectra for *Rac*-*o*-fluoromandelic acid and *R*-(-)-*o*-fluoromandelic acid.

Rac-*o*-F-mandelic acid			*R*-(-)-*o*-F-mandelic acid						
ν / cm^{-1}	R	IR	ν / cm^{-1}	R	IR	Assn.	*n*	$\Delta_{Rac}\nu$	Deuterated ν / cm^{-1}
						Total	51		
135	vs		125	vs		δ(bb)	1	-10	134
164	m		157	sh		15	1	-7	162
195	w		195	m		10b	1		193
214	s		222	m	s	δ(bb)	1	8	213
250		w	234	w		δ(bb)	1	-16	
280	s	s	274	m	m	10a	1	-6	277
290		w	288	m	m	δ(bb)	1		
325	s	s	330	w	m	δ(bb)	1	5	319
365	m	s	345	s	s	16b	1	-20	351
407	vw		411	m	s	9b	1		
466	m	m	464	m	s	δ(bb)	1		466
483	m	m	501	m	m	δ(bb)	1	18	477
500	m	m	513	m		δ(bb)	1	13	499
522	m	s	534	s	m	6b	1	12	521
557	s	m	552	s	m	16a	1	-5	555
599	m	s	612	m	m	6a	1	13	590
638	m	s	667	m br	m	ν(bb)	1	29	625,635
713	s	s	710	m	sh	$\}$ 4	1		700
			717	s	s			7	733
748	vs	vs	743	vs	s	$\}$ 11	1	-5	745
			752	w	vs				
760	m	m	764	m		1	1		760
818	s	s	790	s	s	$\}$ 12	1	-28	813
			822	m	m				
853	s	w	854	w	w br	17a	1		853
869	m	m	863	w	m	$\}$ ν(bb)	1	-6	868 900
			885	w	m			16	
			906		m			37	
918	s	s	926	m br	m	ν(bb)	1	8	918
948	w	m	945	w		$\}$ 17b	1		944
			950	w	m				

continued…

Table 6.4 Continued.

Rac-o-F-mandelic acid			*R*-(-)-*o*-F-mandelic acid						
ν / cm^{-1}	R	IR	ν / cm^{-1}	R	IR	Assn.	*n*	$\Delta_{\mathrm{Rac}}\nu$	Deuterated ν / cm^{-1}
981	w		982	vw	w	5	1		981
992	w		992	vw					
1032	vs	w	1031	vs	m	18b	1		1033
			1038	vs				6	
1077	m	s	1076	m	vs	$\delta(\mathrm{OH})_{\mathrm{ac}}$	1		1080
			1085	m	sh			8	1091
1110	m	s	1107	m	m	18a	1		1112
1150	s	m	1159	s	m	9a	1	9	1150
1171	m	m	1186	w	s	13	1	15	1172
1211	m		1205		m	δ(CH)	1	-6	1228
1228	s	m	1224	s	m	7a	1		
1243		m	1235	s	m	δ(XH)	1	-8	1265
1263	m	m	1252	m	m	3	1	-11	
1284	m	m	1294	m	w	14	1		1283
1306		m	1305		w	δ(XH)	1		
1328	m	w	1322	vw	w	δ(CH)	1	-6	1350
			1342	w	m			14	
1375	vw	m	1379	w	s	δ(CH)	1		1398
1420	w	w	1443	w br		$\delta(\mathrm{OH})_{\mathrm{ac}}$	1	23	
1475	m							-32	
1457	m	s	1463	w	vs	19a	1	6	1558
1488	m	s	1493	w	s	19b	1	5	1488
1585	m	m	1590	m	m	8b	1	5	1590
1614	s	w	1615	vs	m	8a	1		1614
1642	m br		1697	m br	s br	ν(C=O)	1	55	1635
1709		vs	1746	w	vs			37	
1924		vw	1928		w	5+5			
1958		vw	1960		w	5+17b			
2931	s		2916	m		ν(CH)	1	-15	2931
2941	sh		2976	s				35	2969
3022	w		3025	m		20b	1		3022
3047	m		3067	vs		7b	1	20	3047
3067	vs		3078	sh		2	1	11	3067
3086	s		3091	s		20a	1	5	3086
3175	vw		3114	sh		2.8b overtone?			3175,3225
3225	vw	br	3226	w		$\nu(\mathrm{OH})_{\mathrm{al}}$	2	-198	2040,2240
3424		br	3338		s br			-121	2568,2542

Qualitative intensity includes: very weak, vw; weak, w; medium, m; strong, s; very strong, vs; broad, br; shoulder, sh. *n* is for calculation of $C_{V,\mathrm{int}}$ using equation 6.1.

Table 6.5 Assignments of the vibrational spectra for *R*-(-)-*o*-chloromandelic acid and racemic *o*-bromomandelic acid.

R-(-)-*o*-Cl-mandelic acid			*Rac-o*-Br-mandelic acid				
ν / cm^{-1}	R	IR	ν / cm^{-1}	R	Assn.	*n* (*R-o*-Cl)	*n* (*R-o*-Br)
					Total	51	51
117	vs				a	4/5	
129	sh		126	vs	a	4/5	8/9
146	m		139	sh	a	4/5	8/9
175	m		164	s	a	4/5	8/9
190	m		176	s	a	4/5	8/9
205	sh		215	m	a	4/5	8/9

continued...

Table 6.5 Continued.

R-(-)-*o*-Cl-mandelic acid			*Rac*-*o*-Br-mandelic acid					
ν / cm^{-1}	R	IR	ν / cm^{-1}	R		Assn.	*n* (*R*-*o*-Cl)	*n* (*R*-*o*-Br)
221	m	m	236	w		a	4/5	8/9
232	m		257	vw		a	4/5	8/9
250	sh	m	285	sh		a	4/5	8/9
304	w	s	295	s		a	4/5	8/9
325	w	m	325	s		a	4/5	8/9
349	w	m	345	s		a	4/5	8/9
402	vs	m	386	m		a	4/5	8/9
419	s	m	404	m		a	4/5	8/9
450	m	s	447	m		a	4/5	8/9
487	m	m				a	4/5	
502	sh	w	492	m		a	4/5	8/9
523	s	w	516	s		a	4/5	8/9
537	s	w	523	s		a	4/5	8/9
607	m	m	608	m		a	4/5	8/9
633	m	m	627	m		ν(bb)	1	1
664	m	m	637	m		6a	1	1
692	vs	s	677	s		4	1	1
725	m	s	726	vw		ν(bb)	1	1
749	m	vs	749	s	vs	11	1	1
763	m	sh	763	m		}17a	1	1
			772	vw				
851	s	m	855	s		}12	1	1
862	s	m	872	sh	w			
932	m	s	922	w	w	17b	1	1
946	m	s	949	w	w	ν(bb)	1	1
979	w	w	983	vw		}5	1	1
992	w		991	vw				
1035	vs	s	1025	s	w	18b	1	1
1048	s	s	1046	vs	w	1	1	1
1072	m	vs	1070	m		}$\delta(OH)_{ac}$	1	1
1087	w	sh	1087	w				
1125	m	s	1120	m		18a	1	1
1156	s	m	1162	s		9a	1	1
1191	s	s	1189	s		}13	1	1
			1196	sh				
1215	m	vs	1224	m		δ(XH)	1/3	2
1251	w	w	1251	w		3	1	1
1266	vw	m				δ(XH)	1/3	
1280	w	w	1279	w		14	1	1
1295	vw	m				δ(XH)	1/3	
1311	m	w				}δ(CH)	1	
1319	m							
1367	w	sh	1312	m		δ(CH)	1	1
1377		s	1384		m br	δ(CH)	1	1
1422	vw	m	1429		sh	$\delta(OH)_{ac}$	1	1
1446	vw	s	1441		vs	}19a	1	1
1464		s						
1478	s	sh	1471	w		19b	1	1
1576	s	m	1569		vw	8a	1	1
1595	vs	m	1591		vw	8b	1	1
1696	m br	vs	1668	w br	m	}ν(C=O)	1	1
1745	m	vs	1720	m	m			
1923		w				5+5		
1954		w				5+17b		

continued…

Table 6.5 Continued.

R-(-)-*o*-Cl-mandelic acid			*Rac*-*o*-Br-mandelic acid					
ν / cm^{-1}	R	IR	ν / cm^{-1}	R		Assn.	*n* (*R*-*o*-Cl)	*n* (*R*-*o*-Br)
2928	m		2950	w		ν(CH)	1	1
2987	m		2983					
3017	w		3016	w		7b	1	1
3028	w		3050	sh		20b	1	1
3063	vs	m	3059	vs		20a	1	1
3082	s	m	3078	s		2	1	1
3093	sh		3088	s				
3150	w		3137		vw	2.8a		
3190	w	s br	3179		vw	2.8b		
3379		s	3150		br	ν(OH)$_{\mathrm{al}}$	2	2

Qualitative intensity includes: very weak, vw; weak, w; medium, m; strong, s; very strong, vs; broad, br; shoulder, sh. a denotes any one of 8·δ(bb), 6b, 7a, 9b, 10a, 10b, 15, 16a and 16b. *n* is for calculation of $C_{V,\mathrm{int}}$ using equation 6.1.

6.4 Discussion

6.4.1 Phenyl ring modes

In the absence of the other crystal spectra, it was possible to assign the mandelic acid crystal spectra using the *mono*-heavy or the *mono*-light scheme, because of an additional peak found near 1200 cm^{-1} and the two schemes differ very little in frequency. It was not possible to assign the spectra of *o*-fluoromandelic acid and *o*-chloromandelic acid crystals with the *ortho*-light,heavy and *ortho*-heavy,heavy schemes; therefore, the chiral substituent was assumed to be in the light category for the mandelic acid crystals. This is in agreement with the empirical rules of Varsányi(262) and the *ab initio* gas phase assignments.

Most phenyl mode assignments agree with the averaged frequencies from the assignments of Varsányi.(262) For example the carbon-carbon tangential stretching modes of 19a, 19b, 8b and 8a are all within the expected range for the protonated and deuterated molecules. In addition, all the pure CH stretching modes are found near the expected frequencies (7b, 20a, 20b and 2).

Deformation modes of the phenyl ring are expected to be well coupled to the backbone modes, *i.e.*, under a different assignment scheme all the carbons of the phenyl ring can be considered part of the backbone or skeleton. This complicates the assignment of the out-of-plane skeletal vibrations 16a and 16b and the radial vibrations 6a and 6b. These vibrations have different symmetries and were straight forward to identify from the *ab initio* studies. However, the order of the serial assignments is different from the order given by Varsányi.(262) The four modes for these crystals were assigned based upon the order found through the *ab initio* studies and their proximity to the true benzene modes 6 and 16. The phenyl assignments for these modes can be rearranged without changing the applied weight to the heat capacity calculations.

The out-of-plane deformation mode 4 is another phenyl mode which is coupled to the backbone modes and is expected to be substituent dependent, based on the sextant ring bending shown in figure 6.1. In contrast to the previous deformation modes, the mode 4 assignment is in very good agreement with the assignments of Varsányi(262) and shows splitting in both the *R*-(-)-mandelic acid and *R*-(-)-*o*-fluoromandelic acid crystals, but not the respective racemic crystal pairs. This is in agreement with the two rotamers shown in the crystal structures.

Other peaks, such as mode 14 are complicated by being in the δ(OH) deformation wave number region. Assignments of phenyl modes, similar to mode 14, were based on substituent trends, assignment of other deformation peaks based on deuterated spectra, peak breadth and literature assignments.

For *o*-chloromandelic acid and *o*-bromomandelic acid, peaks under *ca.* 600 cm^{-1} are very difficult to distinguish. The *ortho*-light,heavy pattern in this region shows large variances in frequencies and fewer assigned spectra were available for the averages shown in table 6.1. Therefore, many of the peaks were not assigned. Using the condition that $\Sigma n_i = 51$, all peaks in these lower regions were given the same weight.

6.4.2 Carbine and hydroxyl modes

The first ever reported VCD measurement in the liquid state was by Holzwarth *et al.*(265) who found that the carbine vibration was optically active, ν(CH) = 2920 cm^{-1}. Freeman *et al.*(266) also investigated the solution VCD of several species in an effort to find conformation rules. Of note were their assignments for *S*-methylmandelic acid, sodium *S*-(+)-mandelate and *o*-acetylmandelic acid which were ν(CH) = 2910 cm^{-1}, 2900 cm^{-1} and 2960 cm^{-1}, respectively. These values are in good agreement with the assignments reported here.

Aside from the CH stretching modes of the phenyl ring above 3000 cm^{-1}, the *Rac*-mandelic acid spectra show only one CH stretching vibration at 2972 cm^{-1}. The coupling to conformational and dimer effects causes the splitting of this peak in the other crystals. The extensive coupling of OH and CH motion was observed in the *ab initio* study and in solution by Marcott *et al.*(267)

The assignment of the carbine deformation modes has been somewhat controversial.(268) The assignment is difficult, because non-hydrogen bonded aliphatic alcohols in dilute solution show one deformation mode at *ca.* 1250 cm^{-1} and in spectra of hydrogen bond associated alcohols, this normal carbine deformation peak is replaced by a two broad peaks at 1410 and 1330 cm^{-1}. The doublet is now understood to occur because of mixing with the δ(OH) and δ(CH) frequencies; however, isotopic studies were originally confusing because all the bands shift when the hydroxyl hydrogen is replaced with deuterium. Based on the coupling explanations of Stuart and Sutherland,(268) the carbine and hydroxyl group also can be discussed as one group, CHOH,(269) *i.e.*, with asymmetric and pseudo symmetric deformation modes.

Cassanas *et al.*(269) have assigned the following peaks for hydrogen bonded aqueous lactic acid. The carbine assignments proposed by Cassanas *et al.* (269) and Stuart and

Sutherland(268) are all near or above 1300 cm^{-1}. In contrast to these assignments, Polavarapu *et al.*(259) have assigned δ(CH) = 1187 cm^{-1} by deuterating the carbine hydrogen of racemic mandelic acid. Previous to assigning the band for mandelic acid, Polavarapu *et al.*(270) have found that, for several phenylcarbinols, a band at 1200 ± 20 cm^{-1} had a large enough VCD intensity to use for enantiomer correlation relationships. However, as noted Polavarapu *et al.*(259) the deformation is not pure and should have contributions from other OH modes. It appears as if the whole region above around 1300 cm^{-1} shifts with the deuteration of these groups (figures 5, 6 and 7 of Polavarapu *et al.*(259)).

Barron *et al.*(271) have used *ab initio* calculations in combination with ROA to assign the spectra of alanine. They found two modes at frequencies above 1300 cm^{-1} and several modes below 1300 cm^{-1} with substantial δ(CH) contributions. Barron *et al.*(271) have noted that while a large VCD absorption can be associated with the δ(CH) mode, it does not need to be the major contribution to the vibrational mode.

The assignment of *ab initio* modes showed that three modes have significant carbine deformation motion. Based on the latter discussion and the *ab initio* assignments, there can be three carbine deformation assignments for the crystals. In addition a peak near 1400 cm^{-1} has been assigned $\delta(OH)_{ac}$ (consistent with hydrogen bonding). The second $\delta(OH)_{ac}$ is assigned at a lower frequency. With a weight of unity applied to all assigned peaks in this region, the other peaks have been ambiguously assigned as δ(XH), where X = O or C. The weights for the ambiguously assigned peaks have been fixed to agree with the expected total of deformation modes for $(OH)_{al}$, $(OH)_{ac}$ and (CH).

6.4.3 Backbone modes

Backbone modes have been assigned by observed trends and eliminating the phenyl ring modes, which are easier to assign. Under the current assignment scheme, all the backbone modes appear to be assigned only at lower frequencies. Under different assignment schemes for alcohols and carboxylic acids, often a ν(CO) mode is assigned at a frequency near 1200 cm^{-1}, *i.e.*, asymmetric $OCCO_2$ backbone stretch. Using the assignment scheme presented here, this asymmetric stretch of the backbone is assigned as phenyl mode 13, which is the bond stretch from the chiral carbon to the phenyl ring, figure 6.1.

The carbonyl stretch is easily assigned and has been discussed briefly in Chapter five. Cover *et al.*(236) have used the splitting of the carbonyl stretch to determine that *o*-bromomandelic acid was included as two conformers in the crystal. This splitting is observed in all spectra here, except *Rac*-mandelic acid. It is worth noting that this splitting occurs in the *Rac*-(-)-*o*-fluoromandelic acid spectra because of the carboxylic acid dimers. The latter shows that the splitting of the carbonyl stretch alone is not a conclusive test for multiple conformers.

Skeletal deformation modes are difficult to assign. The expected number of skeletal deformations left to be assigned was calculated by difference between the 51 expected internal vibrational modes per molecule and the modes which have been assigned. By assuming that no external modes are observed in the spectra, the weights, n_i, have been fixed as described before. This assumption allows for simplistic calculations. Given sufficient confidence in the backbone deformation modes, some of these lower frequencies could have been assigned as external optical modes. At this time the identification of external modes is not possible. Many external modes would be expected below *ca.* 100 cm^{-1} where peaks have not been observed due to instrumental limitations. Typically inelastic neutron scattering experiments are better for observing these low frequency modes.

6.5 Conclusions

The vibrational spectra of *Rac*-mandelic acid, *R*-(-)-mandelic acid, *Rac*-*o*-fluoromandelic acid, *R*-(-)-*o*-fluoromandelic acid, *R*-(-)-*o*-chloromandelic and *o*-bromomandelic acid crystals have been accounted for and weighted for internal heat capacity calculations. The majority of the vibrations observed in both Raman and IR have been assigned with the use of various assignment aids, such as single molecule *ab initio* calculations and discussions of CD spectra given in the literature. The splitting and shifting of assigned modes agrees with the different crystal molecular environments provided within the racemic and optically pure crystals of mandelic acid and *o*-fluoromandelic acids. Crystal assignments show that the common chiral substituent of the mandelic acids behaves like a light substituent based on the categories of Varsányi.(262)

7 EXPERIMENTAL HEAT CAPACITIES

> *A theory is the more impressive the greater the simplicity of its premises, the more different kinds of things it relates, and the more extended its area of applicability. Therefore the deep impression that classical thermodynamics made upon me. It is the only physical theory of universal content which I am convinced will never be overthrown, within the framework of applicability of its basic concepts.*
>
> Albert Einstein

7.1 Introduction

No previous low-temperature ($T < 300$ K) heat capacity results for true racemic and optically pure crystal pairs have been found in the literature, although measurements have been reported for enantiomers which form solid solutions.(272) The heat capacities of mandelic acid and *o*-fluoromandelic acid crystal pairs would provide an independent calculation of the thermodynamics of forming a true racemic crystal from a conglomerate. These calculations will be compared to the calculations outlined in Chapters two and four. In addition, the heat capacities of all four of these crystals, combined with those of *R*-(-)-*o*-chloromandelic acid crystals, are used to compare thermal properties associated with cohesive crystal forces, *i.e.*, the effective Debye temperatures are compared.

In this chapter three types of calorimeters are described. These are a commercial power compensation DSC, an in-house built adiabatic calorimeter and a commercial relaxation calorimeter. The advantages and disadvantages are discussed and their accuracy and precision have been evaluated by measurements of calorimetry standards. Because the aim was to calculate the relative stability of two crystal types, equation 2.34, the accuracy of the measurements is important to determine the enthalpy and entropy change for forming the racemic crystals from their corresponding conglomerates:

$$\Delta_{\mathrm{Rac}}H = \Delta_{\mathrm{Rac}}H^{T=T_{\mathrm{fus}}^{con}} + \int_{T=T_{\mathrm{fus}}^{con}}^{T}[C_p^R(cr) - C_p^{Rac}(cr)]\mathrm{d}T \tag{7.1}$$

and

$$\Delta_{\mathrm{Rac}}S = -\int_{T=0K}^{T}\frac{C_p^R(cr) - C_p^{Rac}(cr)}{T}\mathrm{d}T\,. \tag{7.2}$$

In equation 7.1, $T = T_{\mathrm{fus}}{}^{con}$ is the reference temperature and in equation 7.2, $T = 0$ K is the reference temperature. $\Delta_{\mathrm{Rac}}H$ at $T = T_{\mathrm{fus}}{}^{con}$ can be found using equation 2.34, because $\Delta_{\mathrm{Rac}}G$ is known with high accuracy from the previous calculations.

7.2 Experimental techniques

7.2.1 Differential scanning calorimeter (DSC)

One of the most accessible types of calorimetry is DSC. As introduced in Chapter five, the Perkin-Elmer Pyris 1 power compensation DSC was used for this work. A basic schematic for a power compensation DSC is given in figure 7.1. This type of DSC consists of two similar furnaces within the same heat sink. The heat sink can be cooled using ice or liquid nitrogen. Each furnace is heated with a platinum wire resistor and temperature is measured with a platinum resistance thermometer. In this thesis work, aluminium hermetically sealed pans were used with all samples (Perkin Elmer, 0219-0062). As per figure 7.1, the reference furnace contains an empty pan and the sample furnace contains a pan from the same batch and filled with sample.

The power supplied to each furnace, $P = P_{\mathrm{average}} + \Delta P$, is determined by the proportional feedback controls. One control aims to heat both furnaces at a fixed scanning rate using an average power, P_{average}, and the other control adjusts the difference in power, ΔP, to keep both furnaces at the same temperature. Therefore, if the heat capacity in one cell changes, the difference in power must change to maintain the same temperatures. Large heat capacity changes, such as at a transition, will cause a larger difference in supplied power. When the power differential is plotted against temperature, the extrapolated onset temperature of the peak is the temperature of the transition. The integration of the power peak provides the enthalpy change for the transition. Both temperature and power scales must be calibrated. Some calibration information for this calorimeter has been shown in figure 5.3.

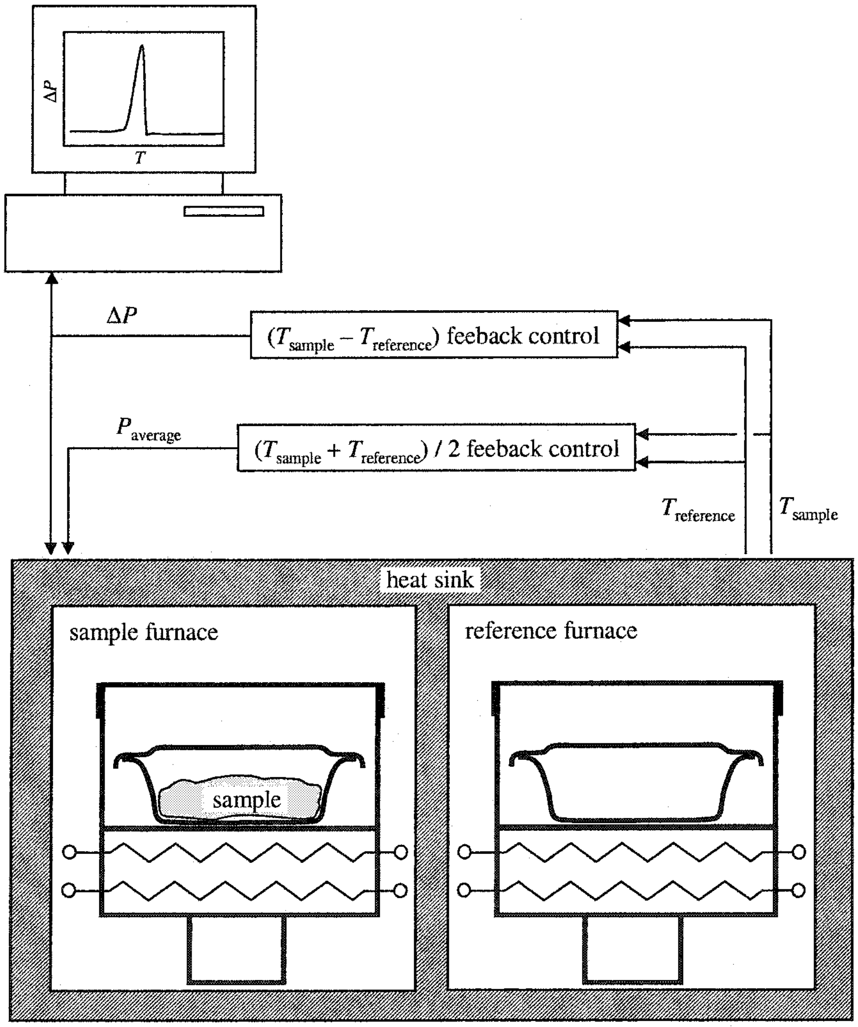
ΔP
T
ΔP
(T_sample − T_reference) feeback control
P_average
(T_sample + T_reference) / 2 feeback control
T_reference
T_sample
heat sink
sample furnace
reference furnace
sample

Figure 7.1 A schematic of a power compensation DSC.

A power compensation DSC has advantages over other types of DSCs because heat conduction is fast, higher scanning rates can be used and the temperature difference between the furnaces is minimal. Heat capacities determined using any type of DSC are not as accurate as other methods because the sample and pan contact changes depending on the sample type and the consistency of the pan placement. The advantages are that the sample mass is smaller than for adiabatic calorimetry and DSCs generally are able to be operated over large temperature ranges.(273) The DSC temperature range used in this thesis was T = 298 to 425 K.

There are several methods for determining heat capacities using a DSC. The two most common are the scanning method and the enthalpic method.(274) These two methods are different in terms of data analysis, but not calorimeter operation. The enthalpic method was used in this thesis.

Figure 7.2 shows a typical DSC scan for the enthalpic method. Two pans were selected from the same batch. The reference pan was placed in the right furnace and the sample pan was placed in the left furnace. The DSC was programmed to settle at $T = T_{\text{initial}}$ for t = 240 s. After settling, the program ramped the temperature to $T = T_{\text{final}} = T_{\text{inital}} + 10$ K at a scan rate of 40.0 mK s^{-1}. After t = 240 s at $T = T_{\text{final}}$, the temperature was raised to the next temperature by the same procedure. The heat used to achieve the temperature rise was calculated by numerically integrating, over time, the area between ΔP and the baseline, ΔP(baseline). Here the baseline was interpolated based on no heat capacity difference or thermal lag difference between the two furnaces. The initial and final ΔP(baseline) was determined by averaging data within the last 120 s before the temperature rise is initiated, as shown in figure 7.2.

The calorimeter was then opened and a sample (8-65 mg) was hermetically sealed in the sample pan. The same program and data analysis was performed to determine the heat difference with the sample sealed in the sample pan. The difference in the integrated areas from the two runs, $\Delta\Delta P$, was scaled by a calibration factor, f, determined from the reference heat capacity of Calorimetry Conference synthetic sapphire.(287) The calibrated heat was then divided by the temperature change to obtain the heat capacity of the sample,

$$C_p = \frac{\int_0^{t=490s} f[\Delta\Delta P(\text{sample} + \text{pan and empty pan}) - \Delta\Delta P(\text{empty pans})]\mathrm{d}t}{T_{\text{final}} - T_{\text{initial}}}. \quad (7.3)$$

In equation 7.3, $t = 0$ s is the initiation time of the temperature ramp and $t = 490$ s is the initiation time of the next temperature ramp. The temperature calibration for a scanning rate of 0 mK s^{-1} was approximated by the temperature calibration at 40 mK s^{-1}; see figure 5.3. Various temperature intervals, larger than $\Delta T = 10$ K, also were investigated; however, the accuracy of the heat capacities was not appreciably different. Standard samples of indium (Perkin-Elmer) and Calorimetry Conference benzoic acid (NBS-49) were measured to determine the accuracy of the method.

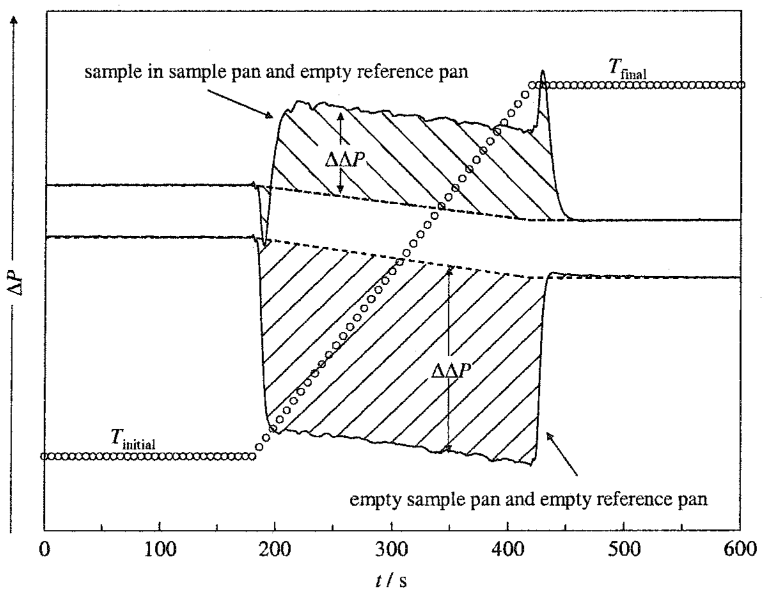

Figure 7.2 A typical DSC heat capacity scan using the enthalpic method.

7.2.2 Adiabatic calorimeter

Custom made adiabatic calorimeters are generally more accurate than DSCs. The disadvantage is the amount of sample required. Precision and accuracy are compromised when the heat capacity of the sample is small compared to the heat capacity of the addendum or sample vessel. The size and heat capacity of the addendum are limited by the sizes of the components required for the measurement, such as accurate thermometers.

The automated heat pulse adiabatic calorimeter was built in-house and has been described by Van Oort and White.(275) A condensed description is given here, with an outline of the experimental procedure that was used. The calorimeter, shown schematically in figure 7.3, is considered a small sample adiabatic calorimeter, where the sample vessel can hold up to 5 cm^3 of liquid or solid sample. The vessel is made of copper and is gold-plated to resist reaction with samples. A 0.5 mm indium wire o-ring is used to hermetically seal the vessel, where the indium wire ring sits in a groove on the top surface of the vessel.

During operation the sample vessel sits within a copper heater/thermometer assembly. Temperature is measured using a four wire platinum resistance thermometer (4 to 380 K, LakeShore Cryotronics, 12.1 mm, Pt-103, 100 Ω at $T = 273$ K). The resistance is monitored as a ratio with a standard 100 Ω resistor at room temperature. The resistance ratio is determined using a 1 mA current in the forward and reverse direction. Low-temperature varnish (GE 7031) is used to hold the thermometer in place in a small cylindrical cavity which extends up from the bottom of the assembly. The heater consists of double silk wound Karma wire (2.6 m, 590 Ω). Varnish also is used to hold the heater in place, which is wound bifilarly around the heat/thermometer assembly. Current is supplied to the heater using a constant DC voltage supply. The sample vessel and the heater/thermometer assembly are hung from the lid of the adiabatic shield by a nylon filament loop.

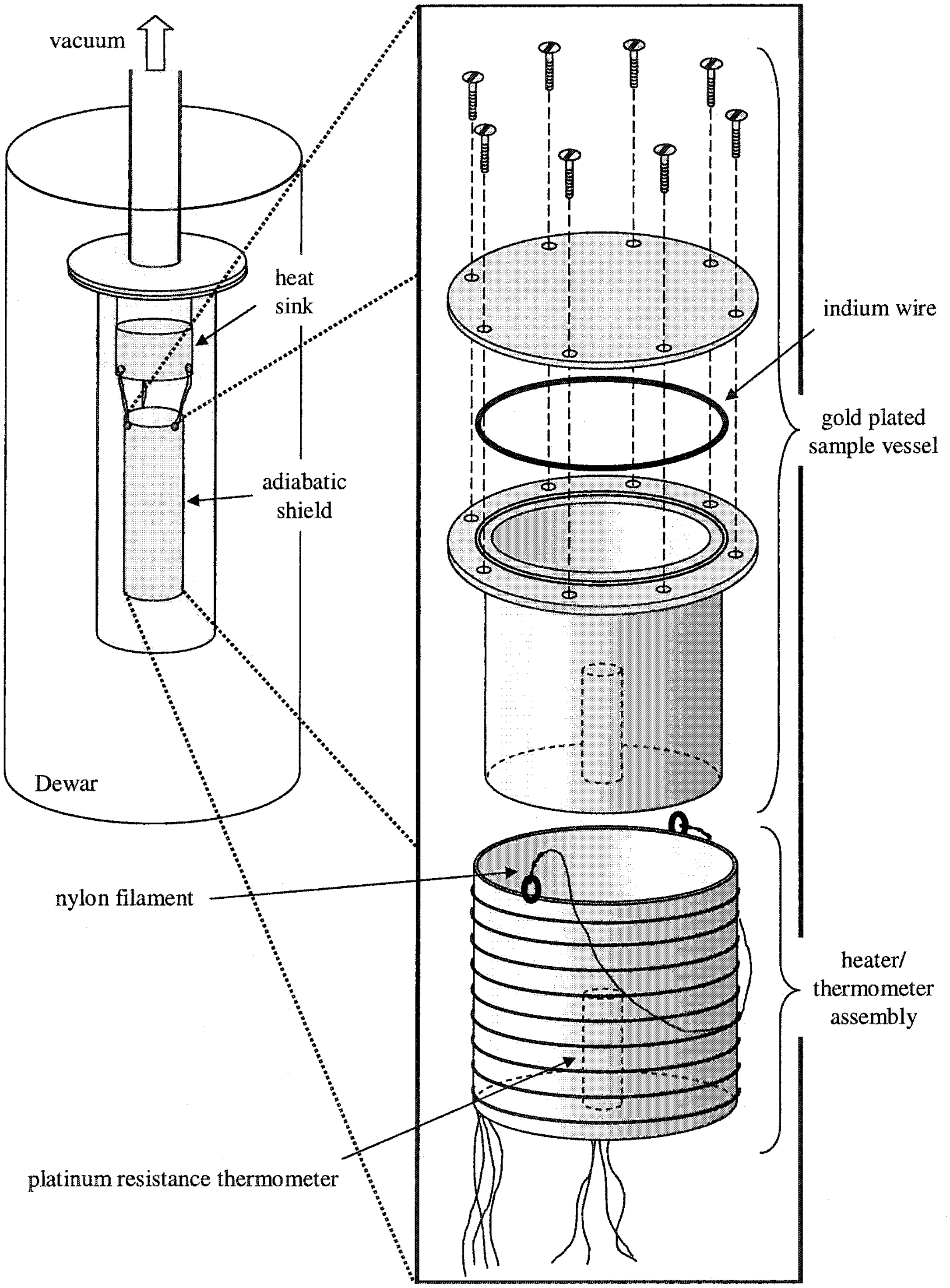
vacuum
heat sink
adiabatic shield
Dewar
nylon filament
platinum resistance thermometer
indium wire
gold plated sample vessel
heater/ thermometer assembly

Figure 7.3 Schematic of the small sample adiabatic calorimeter.

Quasiadiabatic conditions are maintained using an adiabatic shield with its own heater. The shield temperature is controlled proportionally based on the temperature difference between the shield and heater/thermometer assembly. The proportional component of the controller (set point) is adjusted as the system temperature changes. The temperature difference between the shield and the heater/thermometer assembly is measured using a copper-constantan thermocouple. The shield heater is a bifilary wound manganin wire (15 m, 100 Ω).

All voltage and resistance measurements were made using a Hewlet Packard 3465A digital voltimeter. All masses have been measured to within 0.1 mg. The respective sample, sample vessel, sample vessel lid, vessel screws and indium wire o-ring were stored within a vacuum desiccator. The desiccator was released to an ultra high purity helium atmosphere and the sample was loaded and sealed in the sample vessel. The helium atmosphere sealed within the sample vessel was required for adequate thermal contact with the sample. The sample vessel containing sample with known mass was put under vacuum for at least 12 hours and the mass was measured again. The sample vessel was then placed in the heater/thermometer assembly with a small amount of Apiezon T grease to ensure good thermal contact. The assembly was hung from the lid of the adiabatic shield using the nylon filament loop shown in figure 7.3. The adiabatic shield was then hung from the heat sink using three similar nylon filaments.

All leads were soldered using thermal-free solder (70.44% Cd + 29.56 Sn) to minimise electromotive force. The calorimeter chamber is evacuated to a pressure less than $p = 1$ mPa. Once low pressure has been achieved, the Dewar is slowly filled with either liquid nitrogen or liquid helium cryogen.

A typical heat pulse sequence is shown in figure 7.4. The heat pulse method began by adjusting the set-point of the shield controller, until the temperature drift was less than

50 μK s^{-1}. A resistance ratio, which was subsequently converted to temperature, was collected every *ca.* 45 s for 32 to 90 minutes prior to applying a DC current to the heater (heat pulse). The heat input, $q = (V^2/R)t$, was controlled by varying both the voltage and time of the pulse. The voltage applied was measured in triplicate at the start, mid-point and end of the pulse. The resistance of the heater was measured in triplicate before and after the pulse. Resistance ratios were then collected every *ca.* 45 s for an additional 32 to 90 minute time period after the heat pulse. The resistance ratios before and after the pulse, excluding a short relaxation region, were used to linearly extrapolate to the mid-point time of the pulse. These extrapolations provided initial and final resistance ratios which were converted to initial and final temperatures.

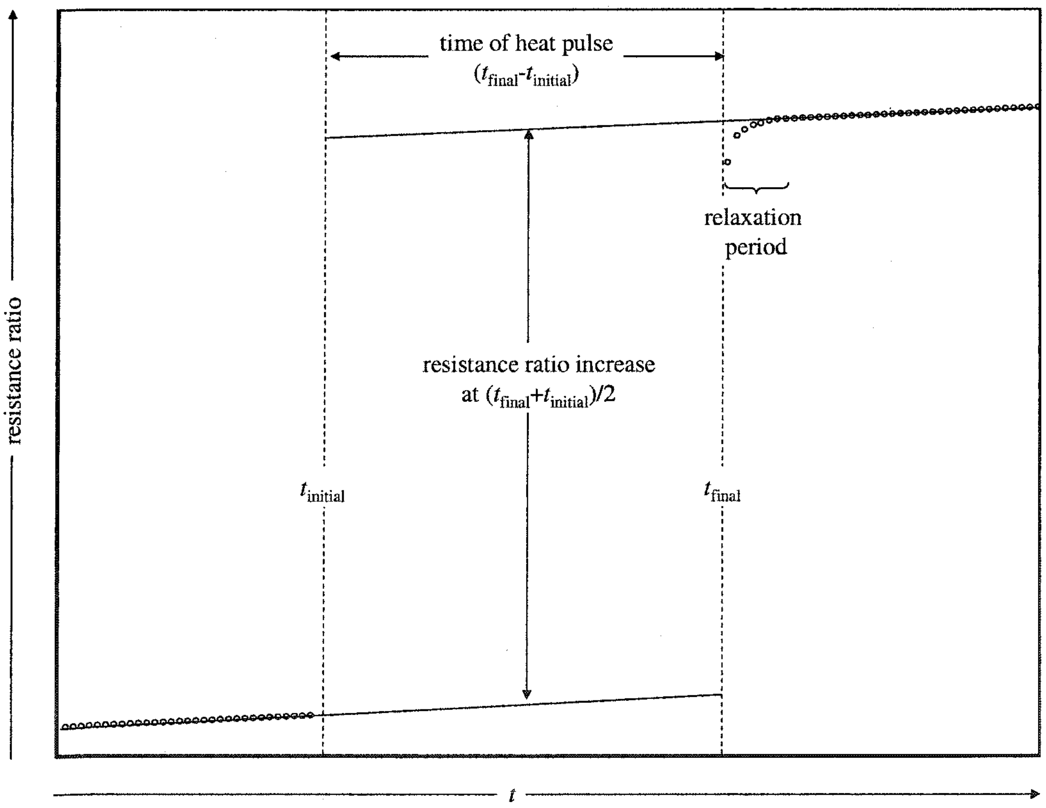
time of heat pulse
(t_{final}-t_{initial})
relaxation period
resistance ratio increase at (t_{final}+t_{initial})/2
t_{initial}
t_{final}
resistance ratio
t

Figure 7.4 A typical adiabatic calorimeter heat pulse sequence.

The total heat capacity of the sample was calculated as

$$C_p((T_{\text{inititial}} + T_{\text{final}})/2) = \frac{q}{T_{\text{final}} - T_{\text{initial}}} - C_p(\text{empty vessel})\,. \tag{7.4}$$

where the heat capacity of the empty vessel, C_p(empty vessel), has been determined previously and a quadratic spline fit was used as stored within a custom made computer program. The accuracy and precision of this calorimeter was not determined in this thesis but has been determined previously(275,276) and is discussed later in this chapter.

7.2.3 Relaxation calorimeter

The third type of calorimeter used was a commercial relaxation calorimeter, which is an accessory of the Quantum Design Physical Properties Measurement System, PPMS. This relaxation calorimeter consists of a very small platform which is in thermal contact with a sample of unknown heat capacity and has a weak thermal link to a constant temperature, T_0, heat sink, figure 7.5. The small sample and the platform are heated to some temperature $T = T_0 + \Delta T$ and then allowed to relax or decay back down to T_0. $\Delta T/T_0 = 2\%$ for measurements made in this thesis.

The advantage of relaxation calorimetry is the small sample size, 1 - 100 mg. Relaxation calorimeters are faster than heat pulse calorimeters and typically used more at lower temperatures, $T < 100$ K.(147,277,278) The two techniques complement each other. However, poor thermal contact between the sample and the platform can limit the accuracy of the relaxation measurement technique. The Quantum Design PPMS has the advantage of being able to achieve a lower temperature than the other two calorimeters described in this chapter, $T = 0.4$ K.

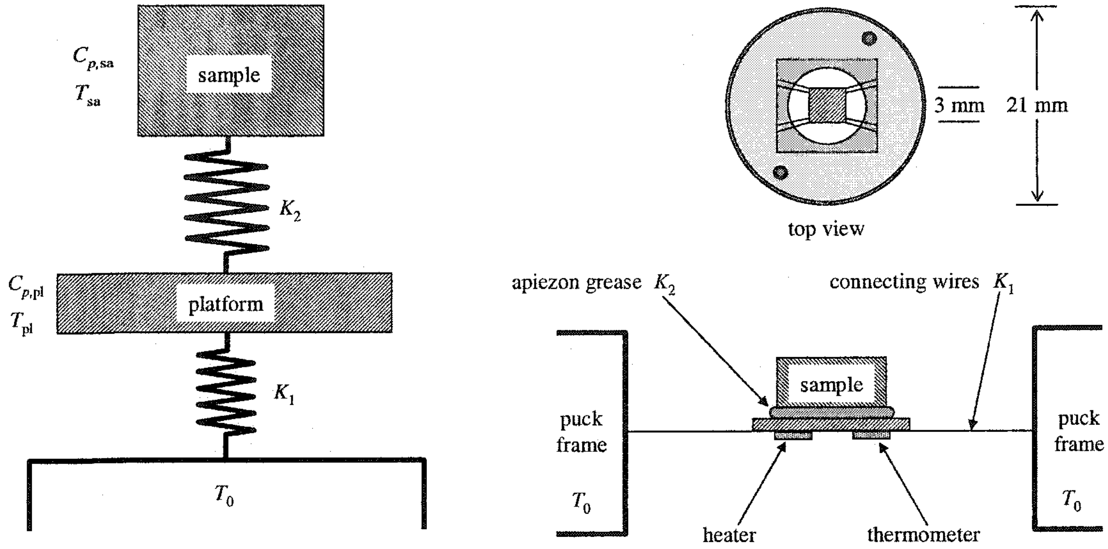
$C_{p,\text{sa}}$
T_{sa}
sample
K_2
$C_{p,\text{pl}}$
T_{pl}
platform
K_1
T_0
3 mm
21 mm
top view
apiezon grease K_2
connecting wires K_1
puck frame
T_0
sample
heater
thermometer
puck frame
T_0

typical relaxation calorimeter

Quantum Design Puck

Figure 7.5 Schematic of the PPMS relaxation calorimeter. $C_{p,\text{sa}}$, heat capacity of sample; $C_{p,\text{pl}}$, heat capacity of platform; T_{pl}, platform temperature; T_{sa}, sample temperature; T_0, heat sink (puck frame) temperature; K_1, thermal conductance between sample and heat sink; K_2, thermal conductance between sample and platform.

Various pucks are available for the PPMS. These pucks are plugged into the sample chamber within a Dewar from above. The PPMS relaxation calorimeter accessory consists of a 3×3 mm sapphire platform which is attached to the puck using 8 thin wires, figure 7.5. A thin film heater and a Cernox sensor™ (Lakeshore Cryotronics) is attached to the back of the platform and a radiation shield fits over the top of the puck. The system is evacuated to a pressure of *ca.* 12 μPa.

To measure a heat capacity using the relaxation calorimeter, the empty platform is first considered. The temperature rise is kept small so that the heat capacity of the platform, $C_{p,\text{pl}}$, and the thermal conductivity of the connecting wires, K_1, can be assumed to be constant. When the power being input to the platform is discontinued, the temperature decay of the platform, $T_{\text{pl}}(t)$, is described by

$$T_{\text{pl}}(t) = T_0 + \Delta T e^{-t/\tau_1}, \tag{7.5}$$

where the time constant $\tau_1 = C_{p,\mathrm{pl}} / K_1$ and T_0 is the heat sink temperature. Equation 7.5 is the solution to a heat-balance differential equation. If a sample is put on the platform with very good thermal contact, $K_2 >> K_1$, the time constant must include the heat capacity of the sample, $\tau_1 = (C_{p,\mathrm{pl}} + C_{p,\mathrm{sa}}) / K_1$.

Often the thermal contact of the sample and platform is not good enough to ensure that $K_2 >> K_1$; therefore, the temperature decay involves two exponential terms,

$$T_{\mathrm{pl}}(t) = T_0 + Ae^{-t/\tau_1} + Be^{-t/\tau_2} \tag{7.6}$$

The time constants, τ_1 and τ_2, are calculated from $C_{p,\mathrm{pl}}$, $C_{p,\mathrm{sa}}$, K_1, and K_2. The PPMS records the decay over two time constants, $2\tau_1$, and uses the analytical curve-fitting procedure of Hwang *et al.*(278)

Thermal contact between the sample and the platform is made using high vacuum Apiezon grease. Two measurements are required for this method. The first measurement is a decay sequence with the platform and grease. This measurement is modelled with a single time constant, equation 7.5, to obtain $C_{p,\mathrm{pl}}$ and K_1. A second measurement is made at the same temperature with the sample in contact with the grease and platform. The method of Hwang *et al.*(278) is used to analyse the decay and calculate $C_{p,\mathrm{sa}}$ and K_2 from τ_1, τ_2 and the known $C_{p,\mathrm{pl}}$ and K_1. Because this method is rapid, three replicate measurements are made at each temperature.

Puck serial number 451 was used for all heat capacity measurements reported here. The contact grease used was Apiezon N, which is recommended by Quantum Design for the temperature region 0.3 to 300 K. Apiezon N has good thermal transport properties, a low vapour pressure and is inert; however, it has a glass transition like anomaly at *ca.* 215 K and a peak transition at *ca.* 290 K.(279) Apiezon T, used with the adiabatic calorimeter, also has a broad phase transition in this region.(280) The accuracy of calorimeter Puck 451 has been checked here by measuring the heat capacity of three Calorimetry Conference sapphire crystals and National Institute of Standards and Technology, NIST, copper reference material (RM 5), as discussed in the next section.

A modified relaxation method was required to measure the heat capacities of the mandelic acid crystals for two reasons: (1) mandelic acid has a high vapour pressure and (2) the crystals are very small and must be in good thermal contact with the platform. A flow chart of the method steps with a schematic of the calorimetric set-up is shown in figure 7.6.

In this method, four measurements were made with the same temperature range and system parameters. The first measurement was the normal platform and contact grease measurement, as described before. The second measurement was for a hermetically sealed aluminium DSC pan (Perkin-Elmer, Kit No. 0219-0062, *ca.* 20 μL), where the inside of the pan was coated with Apiezon N. This measurement provided the heat capacity for the addenda vessel. Afterwards, the platform contact grease on the bottom of the pan was carefully cleaned and the addenda mass was checked to ensure that no grease had been lost from inside. The sample was then imbedded in the grease within the pan and the pan was sealed. Vigorous shaking of the pan ensured that the small crystals were in contact with the grease. A second heat capacity measurement of the platform and some new platform contact grease was made. The fourth and final heat capacity measurement was for the sample and Apiezon N grease sealed within the pan and in contact with the platform. This final measurement provided the total heat capacity, where the sample heat capacity was calculated from the difference between the total heat capacity and that of the pan and grease addenda heat capacity. Schnelle *et al.*(279) have developed a similar method for measuring the heat capacities of powdered samples in glass ampoules.

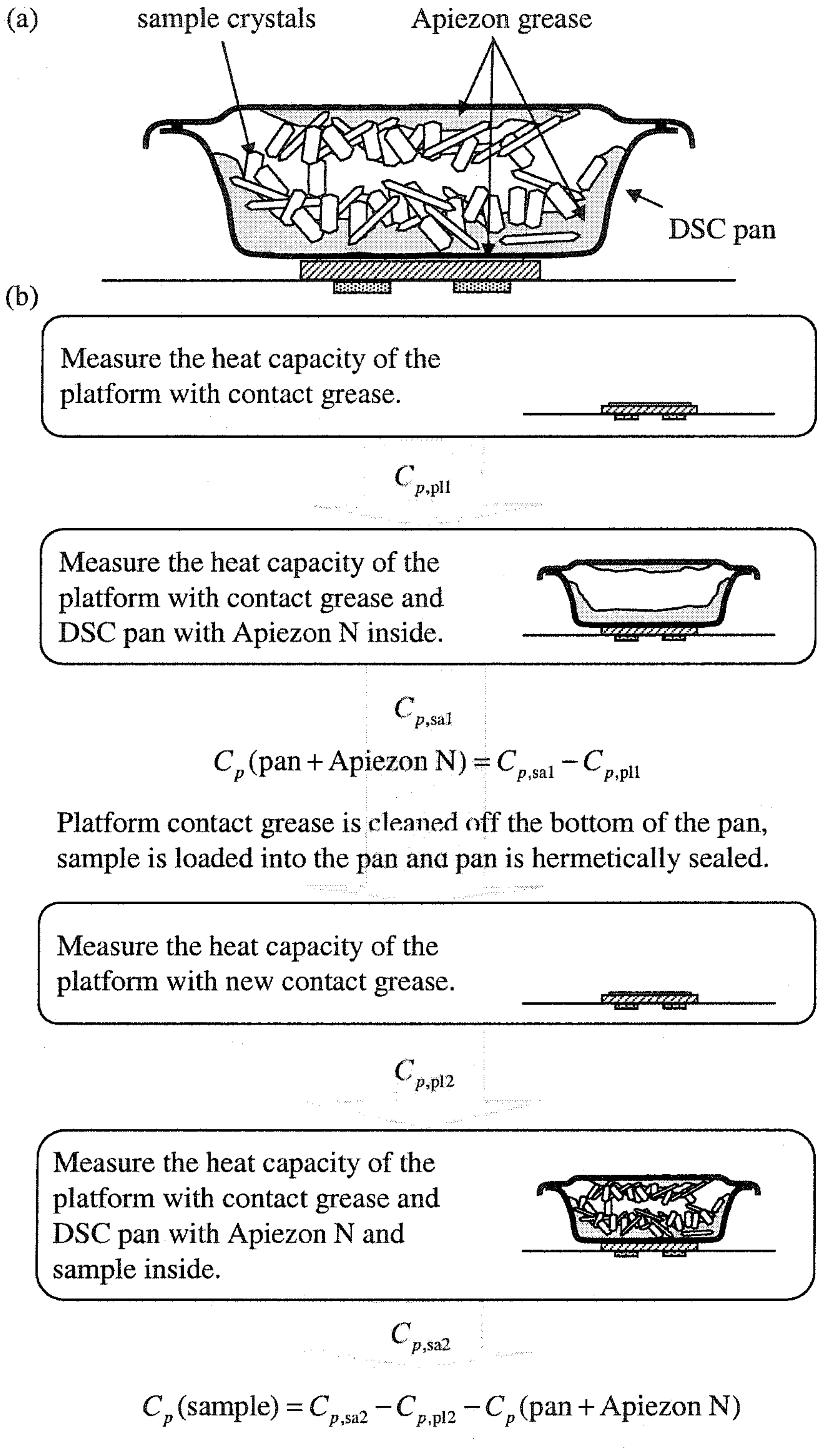

Measure the heat capacity of the platform with contact grease.

$C_{p,\text{pl1}}$

Measure the heat capacity of the platform with contact grease and DSC pan with Apiezon N inside.

$C_{p,\text{sa1}}$

$$C_p(\text{pan} + \text{Apiezon N}) = C_{p,\text{sa1}} - C_{p,\text{pl1}}$$

Platform contact grease is cleaned off the bottom of the pan, sample is loaded into the pan and pan is hermetically sealed.

Measure the heat capacity of the platform with new contact grease.

$C_{p,\text{pl2}}$

Measure the heat capacity of the platform with contact grease and DSC pan with Apiezon N and sample inside.

$C_{p,\text{sa2}}$

$$C_p(\text{sample}) = C_{p,\text{sa2}} - C_{p,\text{pl2}} - C_p(\text{pan} + \text{Apiezon N})$$

Figure 7.6 The modified heat capacity measurement method for volatile organic solids with the PPMS relaxation calorimeter and a Perkin-Elmer DSC pan. (a) schematic of addenda and sample; (b) experimental steps. $C_{p,\text{pl1}}$, heat capacity for first platform measurement; $C_{p,\text{sa1}}$, heat capacity for first addenda measurement; $C_{p,\text{pl2}}$, heat capacity for second platform measurement; $C_{p,\text{sa2}}$, total heat capacity measurement.

The advantage this method was that it could be used to measure the heat capacities of volatile molecular organic solids at very low temperatures and does not require high temperature to seal the sample vessel. The disadvantage is that the sample heat capacity uncertainty is large at the higher temperatures, because of the thermal transitions of the Apiezon N and the low sample mass. The accuracy of this method was checked by measuring the heat capacity of Calorimetry Conference benzoic acid (NBS-49); see next section. During the development of the method, heat capacities were measured for several samples of Apiezon N grease and aluminium, the materials used to form the addenda. These heat capacities also have been compared to literature values. Although each sample has been measured after the measurement of its addendum, the addendum heat capacity was calculated to check for major discrepancies and identify any problems.

7.3 Evaluations of calorimetric techniques

7.3.1 Addenda materials

7.3.1.1 Aluminium

The addenda for the modified PPMS measurement method included the puck platform, an aluminium hermetically sealed DSC pan and a substantial amount of Apiezon N grease. During the evaluation of this method, two types of pans were measured before loading with grease or sample. The first type was the hermetically sealable DSC pan described in the procedure. The second type was a non-hermetically sealable aluminium DSC pan, evaluated for measurements of non-volatile powders. Technical support staff at Perkin-Elmer have, through the manufacturing department, communicated that DSC pans are > 99% pure aluminium (communicated to the author on May 13, 2004). The heat capacities determined for these pans are shown in figure 7.7.

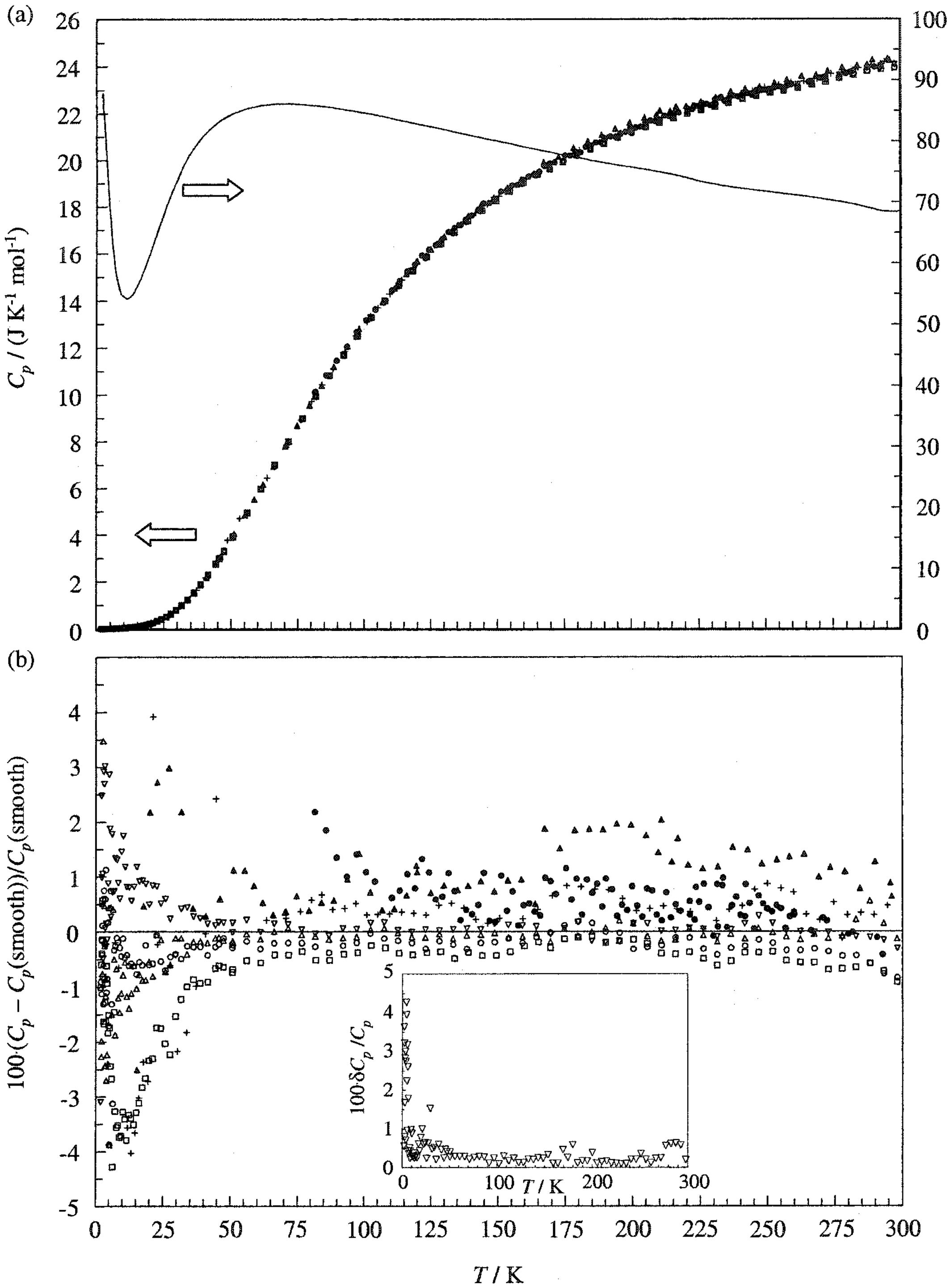

Figure 7.7 DSC pans and aluminium heat capacities. (a) Heat capacities and relative sample contribution to total heat capacity measurement; (b) (large graph) relative heat capacity differences from smoothed data and (small graph) estimated errors for aluminium Perkin-Elmer DSC pans measured with the PPMS; ○ 27.717 ± 0.020 mg non-hermetically sealable pan; □ 25.442 ± 0.007 mg non-hermetically sealable pan; Δ 24.711 ± 0.006 mg hermetically sealable pan; ∇ 25.143 ± 0.005 mg hermetically sealable pan. Pure aluminium data: ● Takahashi *et al.*;(281) ■ Leadbetter;(282) + Downie and Martin;(283) ▲ Giauque.(284) C_p(smooth) has been calculated using the polynomial fits of the hermetically sealable pan data, Δ and ∇. Errors, (b) (inset), have been estimated using standard propagation of error for three replicate measurements of the sample platform and the platform with the sample.

Figure 7.7(b) shows that the estimated errors calculated from the replicate measurements are *ca.* 30 % smaller than the reproducibility shown by the relative differences plot. These errors are based on the larger of: (1) the error calculated by the χ^2 statistic supplied by the Quantum Design program, or (2) a standard propagation of error based on twice the standard deviation of the addenda heat capacities, total heat capacity measurement and sample mass.

The representative literature data for pure aluminium(281-284) are *ca.* 1-2 % greater than measured data for the aluminium pans for $T > 50$ K and 1-4 % greater for $T < 50$ K. Figure 7.7(b) shows that the precision is *ca.* 1.0 % for $T > 50$ K and *ca.* 4% for $T < 50$ K. At $T < 50$ K, the hermetically sealable pans show a slightly better reproducibility at half this precision. These data show that both types of aluminium pans have a very similar heat capacity and agree well with literature heat capacities for pure aluminium.

Relative to the platform and additional samples, the contribution from the aluminium pans to the total measured heat capacity is large, *e.g.*, figure 7.7(a) shows that the aluminium pans are the source of more than 50% of the total measured heat capacity. The confidence in the reproducibility of the heat capacity for the pans is important for calculating the heat capacity of a pan with Apiezon N grease. The modified method required four runs in total: (1) platform, (2) pan with Apiezon N, (3) platform again and (4) pan with Apiezon N and sample. Therefore, the calculation of contributions from the pan and Apiezon N was used to identify instrumental problems during all four of these runs and to assess the relative contributions from all materials for the total heat capacity measurement.

7.3.1.2 Apiezon N

As noted with the results for the aluminium pans, knowledge of the heat capacity contribution from Apiezon N was required. The heat capacities of Apiezon N and Apiezon T are shown in figure 7.9. The heat capacity for Apiezon N has been evaluated by Schnelle *et al.*(279) and shows two anomalies at $T > 200$ K. Westrum *et al.*(280) have measured the heat capacity of Apiezon T and found one broad transition in this same temperature range. Kreitmann *et al.*(285) has found that both Apiezon N and T have significant increases in their thermal conductance at these transition points. Westrum *et al.*(280) have noted that the heat capacity over this transition region was not reproducible to within 2 %.

Figure 7.8(a) shows that the measurements made using Puck-451 are *ca.* 5-8 % lower than the spline fit interpolation of Schnelle *et al.*(279) for $T > 160$ K. As noted by Schnelle *et al.*(279) generations of Apiezon grease can have slightly different heat capacities. In addition the transitions cause the larger differences in heat capacities for $T > 200$ K.

The Apiezon N measured in this thesis work all came from the same tube and the results were reproducible within 10 % for $T < 10$ K, 4% for $T = 10$ to 40 K, 1 % for $T = 40$ to 160 K, and 3 % for $T > 160$ K. Figure 7.8(b) shows more scatter for $T = 175$ to 200 K. During the measurement of the 6.423 mg sample of Apiezon N, the DSC pan lid lost its good thermal contact at *ca.* 185 K. The heat capacities in this region show a larger disagreement. With the DSC pans, other problems have arisen, such as pans sliding off the contact grease and poor sample thermal contact inside the pans.

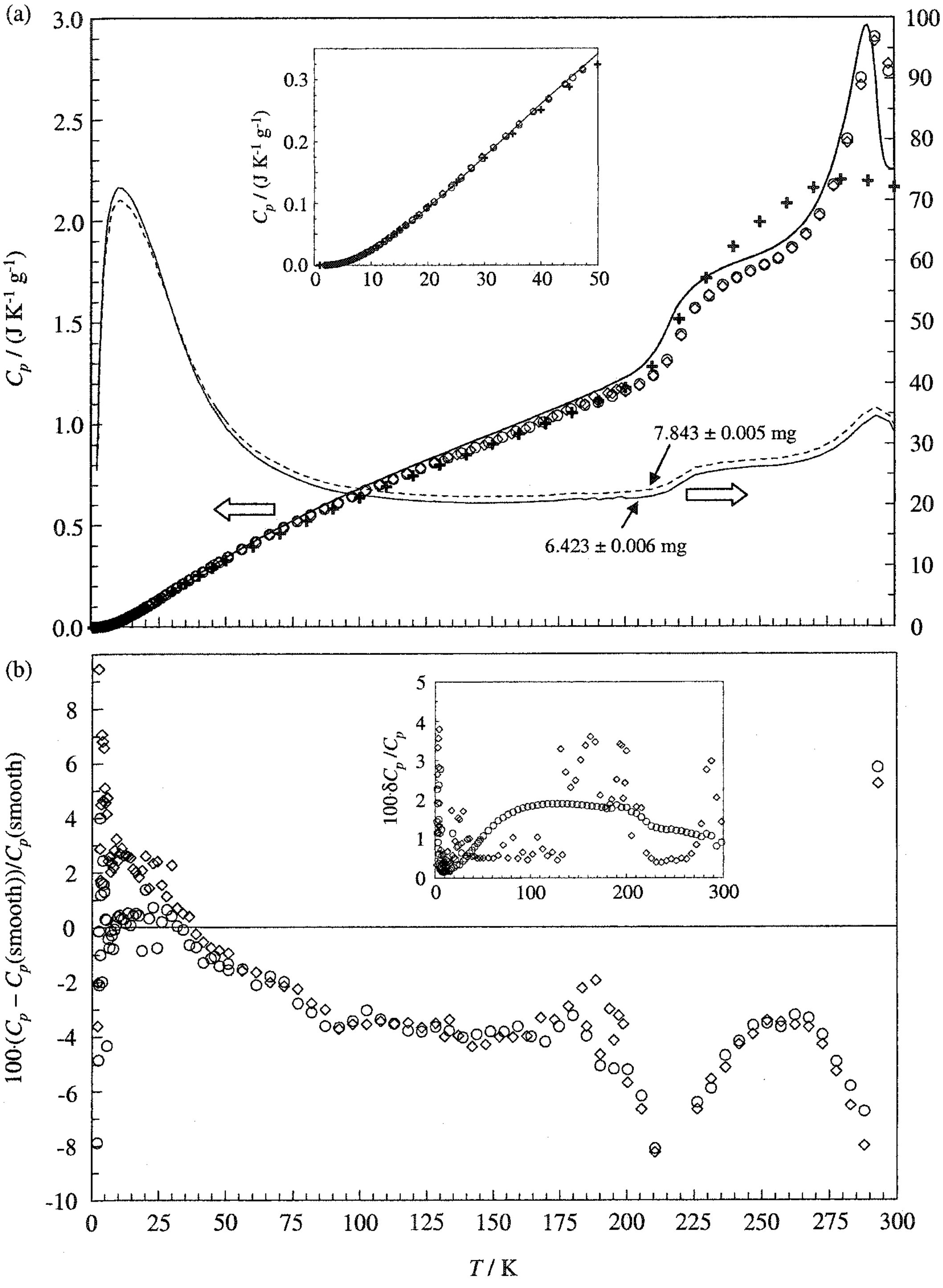

Figure 7.8 Apiezon grease heat capacities. (a) Heat capacities and relative sample contribution to total heat capacity measurement; (b) (large graph) relative heat capacity differences from smoothed literature data$^{(279)}$ and (inset) estimated errors for Apiezon N measured with the PPMS. ◇ 6.423 ± 0.006 mg Apiezon N; ○ 7.843 ± 0.005 mg Apiezon N. Literature data: + Apiezon T, Westrum *et al.*$^{(280)}$; C_p(smooth), shown as —— in (a) left axis, has been calculated using the polynomials and quadratic spline fit for Apiezon N of Schnelle *et al.*$^{(279)}$

Figure 7.8(b) shows that the total heat capacity is dominated by the pan contribution at the higher temperatures, $T > 60$ K, and by the Apiezon N grease at the lower temperatures, figure 7.9. This has the potential to cause a problem during the evaluation of any sample heat capacity. Problems can arise through mass errors or thermal contact. Due to the Quantum Design fitting procedure, if the thermal contact is compromised, the heat capacity measurements are systematically lower than they should be.

7.3.2 Calorimetry standard materials

7.3.2.1 Sapphire

Calorimetry Conference sapphire has been used as a calibrant for the DSC method and a standard for the relaxation calorimeter. Lashley *et al.*(277) have examined the accuracy of heat capacity measurements using the Quantum Design PPMS relaxation calorimeter. They have shown an accuracy of ± 3 % for $T < 4$ K and ± 5 % for $T > 4$ K. Because the heat capacity is additive, $C_p(\text{total}) = C_{p,sa} + C_{p,pl}$, the heat capacity of the sample must be substantial compared to the addenda for accurate measurements. This also is true for the adiabatic calorimeter. The heat capacity values and information for sapphire are shown in figure 7.9.

All heat capacity comparisons have been made after conversion to the 1990 International Temperature Scale, ITS-90.(286) Relative differences shown in 7.9(b) were calculated from the smoothed equations for sapphire reported by Ditmars *et al.*(293) and Fugate and Swenson.(292) Archer(287) has reported smoothed values (spline fit) for the National Institute of Standards and Technology, NIST, based on ITS-90. Archer's values(287) also have been shown in figure 7.9(b) along with values reported by Ditmars and Douglas,(288) Sorai *et al.*,(289) Viswanathan(290) and White and Minges.(291)

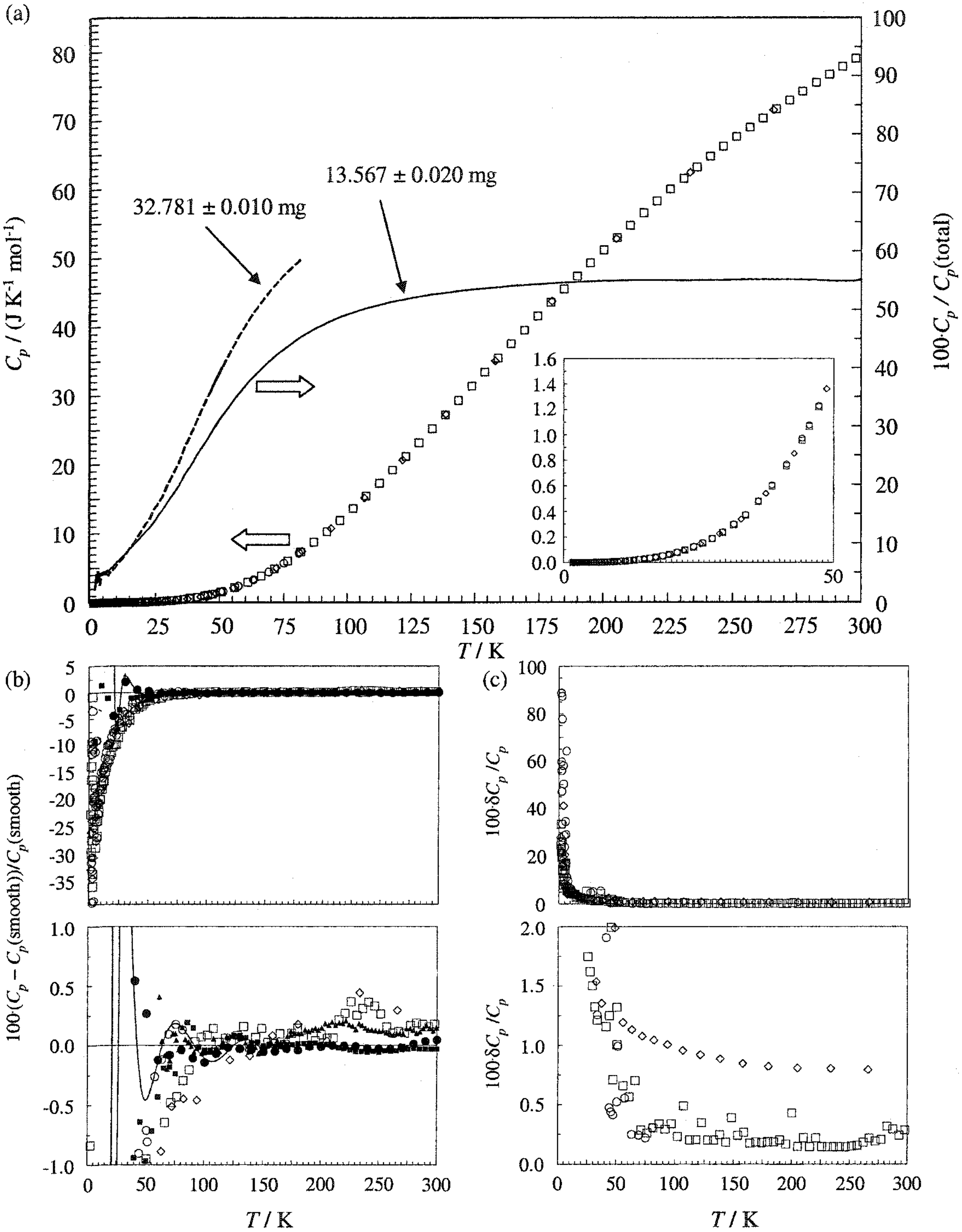

Figure 7.9 Sapphire standard heat capacities. (a) Heat capacities and relative sample contributions to total heat capacity measurements; (b) relative heat capacity differences from smoothed literature data$^{(293,292)}$ and (c) estimated errors for sapphire measured with the PPMS. ◇ 15.180 ± 0.020 mg crystal; □ 13.567 ± 0.020 mg crystal; ○ 32.781 ± 0.010 mg crystal. Literature data: ● Archer;$^{(287)}$ ■ Ditmars and Douglas;$^{(288)}$ ▲ Sorai *et al.*;$^{(289)}$ in (b), ---- Viswanathan;$^{(290)}$ in (b), —— White and Minges.$^{(291)}$ C_p(smooth) has been calculated using the equations of Fugate and Swenson$^{(292)}$ for $T < 30$ K and Ditmars *et al.*$^{(293)}$ for $T > 30$ K. Errors, (c), have been estimated using standard propagation of error for three replicate measurements of the sample platform and the platform with the crystal. (b) and (c) are shown with two different scales to show more details.

The literature values compared in figure 7.9(b) cannot be considered exhaustive. As Castanet(294) has noted, there were over 220 reports dealing with the thermodynamic properties of sapphire by 1984. Those used here are those which show either measured or smoothed heat capacities below $T = 70$ K. The heat capacities measured using Puck-451 for the Quantum Design PPMS show accuracy and precision of *ca.* 0.5 % for $T > 80$ K and *ca.* 1 % for $60 < T / \mathrm{K} < 80$. While the reproducibility is good at the lower temperatures, the accuracy is difficult to evaluate. Sapphire is not a good heat capacity reference material at $T < 60$ K, because the heat capacity is very small and the errors for smoothed literature data are large.(277,287) However, the recommended smoothed data of Ditmars and Douglas(288) agree well with the PPMS data reported here at the lower temperatures. Figure 4 of Lashley *et al.*(277) shows a similar deviation from Archer's data(287) for $T < 60$ K. The reproducibility of the PPMS data is much better than the 40 % deviation from the smoothed data for $T < 60$ K.

Again measurements were made in triplicate and the estimated errors were calculated and are shown in figure 7.9(c). The relative estimated errors reflect the precision of the data, which in this case are similar to the accuracy.

7.3.2.2 Copper

Copper is an acceptable heat capacity standard at low temperature, whereas sapphire is not. The copper reference material measured here was obtained from NIST (>99.999%, RM 5) and is from the same batch as that measured by Lashely *et al.*(277) using a PPMS. The heat capacities and other measurement information are given in figure 7.10.

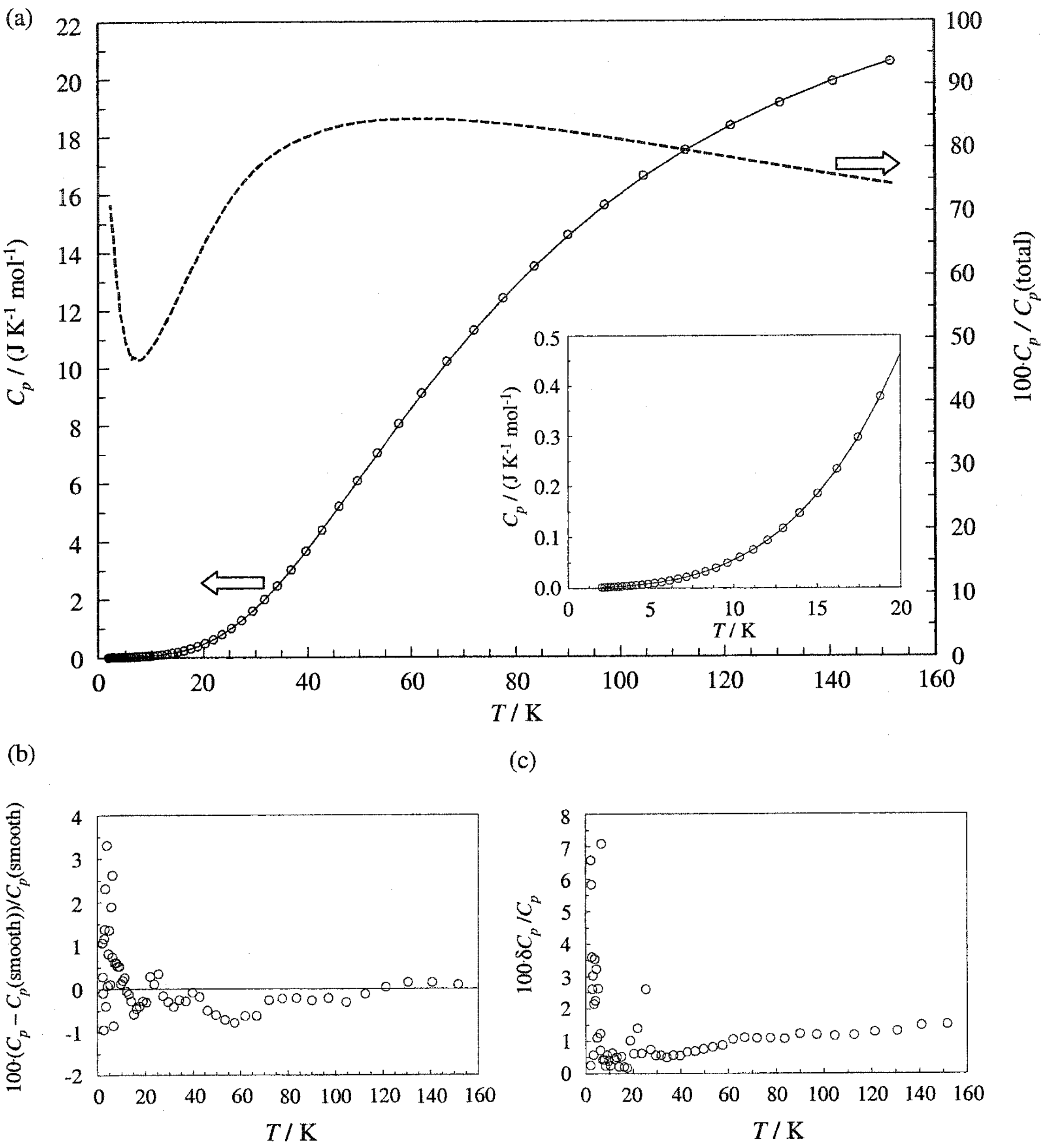

Figure 7.10 Copper standard heat capacities. (a) Heat capacities and relative sample contributions to total heat capacity measurement, (b) relative heat capacity differences from NIST recommended smoothed data$^{(295,296)}$ and (c) estimated errors for RM 5 copper measured with the PPMS. ○ 41.422 ± 0.005 mg. C_p(smooth), —— in (a) and baseline in (b), have been calculated using the NIST recommended smoothed data of Furukawa *et al.*$^{(295)}$ for $T > 25$ K and the equation of Osborne *et al.*$^{(296)}$ for $T < 25$ K. Errors, (c), have been estimated using standard propagation of error for three replicate measurements of the sample platform and the platform with the sample.

Figure 2 of Lashley *et al.*$^{(277)}$ shows an accuracy better than 4 % for copper measured with the PPMS for $T = 2$ to 300 K. Figure 7.10(b) shows that the heat capacities measured with Puck 451 are accurate to within 4% for T < 10 K and within 1% for T = 10 to 80 K when compared against the NIST recommended values.$^{(295,296)}$ Accuracy for T > 80 K is in agreement with the sapphire measurements, *ca.* 0.5%.

Estimated errors were calculated and are shown in figure 7.10(c). The precision of the copper data agree with the accuracy at $T > 60$ K and the precision is higher than the observed accuracy at $T < 60$ K.

7.3.2.3 Benzoic acid

Benzoic acid is a common reference material for adiabatic calorimeters. Van Oort and White$^{(275)}$ used Calorimetry Conference benzoic acid to evaluate the small sample adiabatic calorimeter used here, figure 7.11. The calorimeter was found to be accurate to within 0.5 % with 50 % of the total measured heat capacity being from the sample contribution at the higher temperatures. Only two measurements were made from 50 to 60 K and none were made for $T < 50$ K. For $T < 50$ K the sensitivity of the resistance thermometer is not as good; hence, heat capacities from this adiabatic calorimeter at the lower temperatures are not as accurate.

More recently this adiabatic calorimeter was used by Bessonette and White$^{(276)}$ to measure the heat capacity of NaOH. The latter study showed an agreement with the literature to within 1.2 % with 45% of the total measured heat capacity being from the sample contribution at $T = 250$ K.

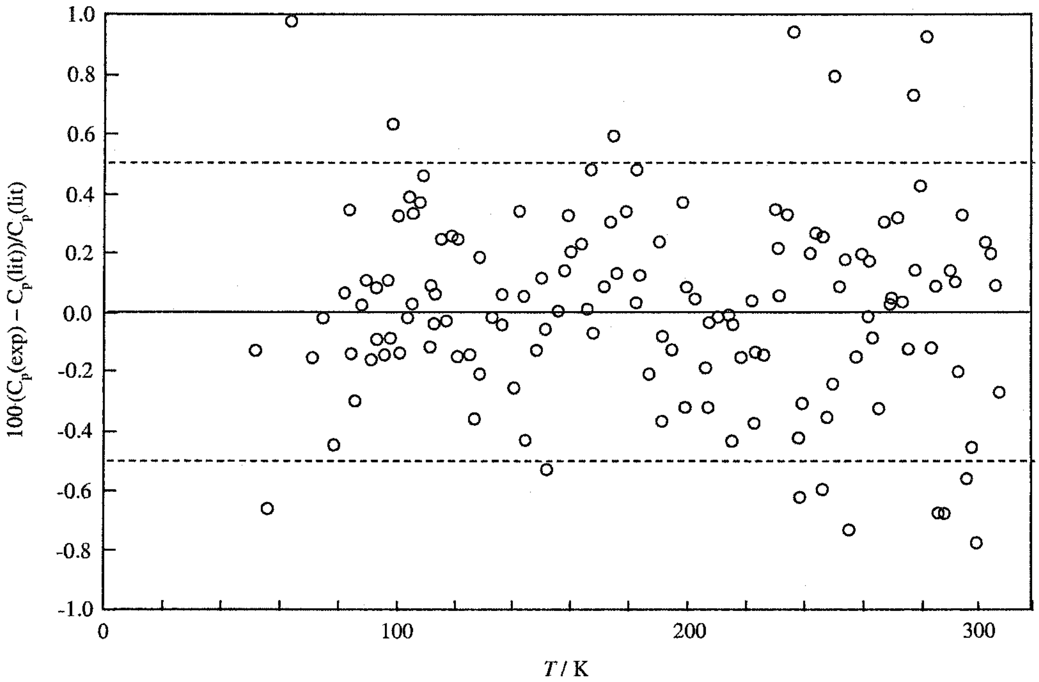

Figure 7.11 The relative difference between the measured heat capacity of benzoic acid using the adiabatic calorimeter and those reported in the literature.(159) This is a reproduction of figure 2 of Van Oort and White.(275)

Heat capacities for the same batch of Calorimetry Conference benzoic acid (NBS-49) were measured using the PPMS and DSC. As with the adiabatic calorimeter, the modified PPMS method requires that the addenda heat capacity be known, *i.e.*, pan, Apiezon N and platform. Because there is a large amount of grease and a large mass of aluminium in the addenda, organic samples are not expected to contribute the majority of the total heat capacity. The contributions over a large temperature range are shown in figure 7.12 for a measurement of 9.525 ± 0.009 mg benzoic acid and 5.899 ± 0.009 mg Apiezon N grease in a 25.143 ± 0.005 mg DSC pan. Uncertainties in the addenda contributions can significantly affect the sample heat capacity determination. This also is true for the adiabatic calorimeter.

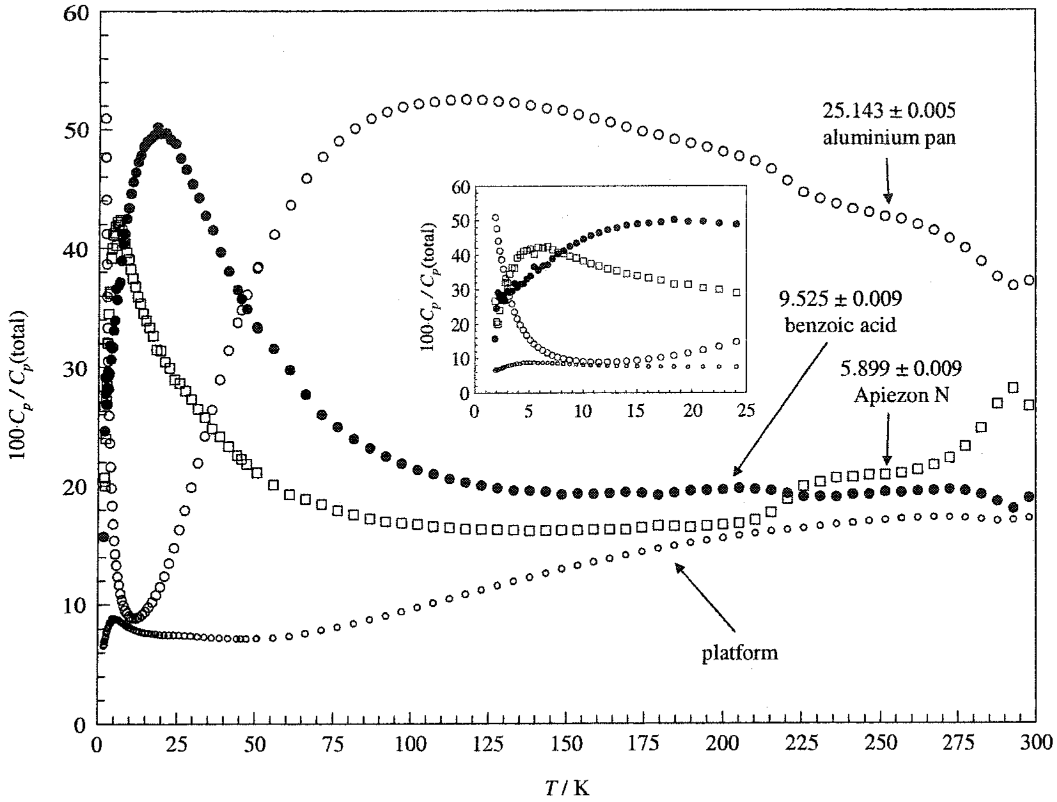

Figure 7.12 The relative contributions for the PPMS determination of the total heat capacity measurement of benzoic acid and Apiezon N grease in a hermetically sealed aluminium DSC pan. The inset shows an expansion of the lower temperature region.

Addenda measurements in this thesis were measured as complete units, Apiezon N in the pan without the sample; see figure 7.6. The corresponding measurements for addenda were reported previously with the measurement of Apiezon N grease. Recalculation of multiple addenda measurements shows a precision of 0.5%. With this estimated error and the relative contributions, the estimated sample heat capacity error due to addenda measurement error was calculated. The total sample uncertainty was calculated using standard propagation of error, using the error due to addenda measurement and the error estimated through the standard deviations of replicate sample and addendum measurements.

Estimated errors using the DSC were calculated as the twice the sample standard deviation, where each replicate measurement corresponds to a different sample.

The estimated error data for Calorimetry Conference benzoic acid measured with the PPMS and the DSC are shown in figure 7.13 along with the heat capacities and deviations from smoothed literature. To aid in interpreting the figure, raw literature data have been excluded from figure 7.13(a) and all are given the same symbol in figure 7.13(b), +.(289,297-299)

Figure 7.13(b) shows that the heat capacities measured with the PPMS agree with the literature to within *ca.* 2% for $T = 50$ to 250 K. This accuracy decreases to *ca.* 10% at the lowest temperatures and increases to 5% for $T > 250$ K. The estimated errors shown in figure 7.13(c) show the calculated precision of these measurements was 10 % for $T < 20$ K, 2% for $T = 200$ to 160 K and 2-6 % for $T > 160$ K. The calculated reproducibility for these higher temperature measurements reflects the two transitions in the Apiezon N and the issue of poor thermal contact at *ca.* 190 K.

There are many comparisons of heat capacities measured using a DSC in the literature. Two notable studies are those of Mraw and O'Rourke(300) and Callanan *et al.*(301) who have measured organic samples in the same Perkin-Elmer hermetically sealed pans used here. Mraw and O'Rourke(300) found an accuracy of 2% for $T = 300$ to 370 K and Callanan *et al.*(301) have found the same accuracy for $T = 130$ to 355 K. The DSC measurements of benzoic acid also agree with the literature with a 2 % error range for sample masses of 12.0 to 12.8 mg. The liquid heat capacities, not shown in figure 7.13(b), also agree with the values of Ginnings and Furukawa(159) to within 5%. Solid benzoic acid recrystallised from the melt showed no appreciable difference in heat capacity before and after melting.

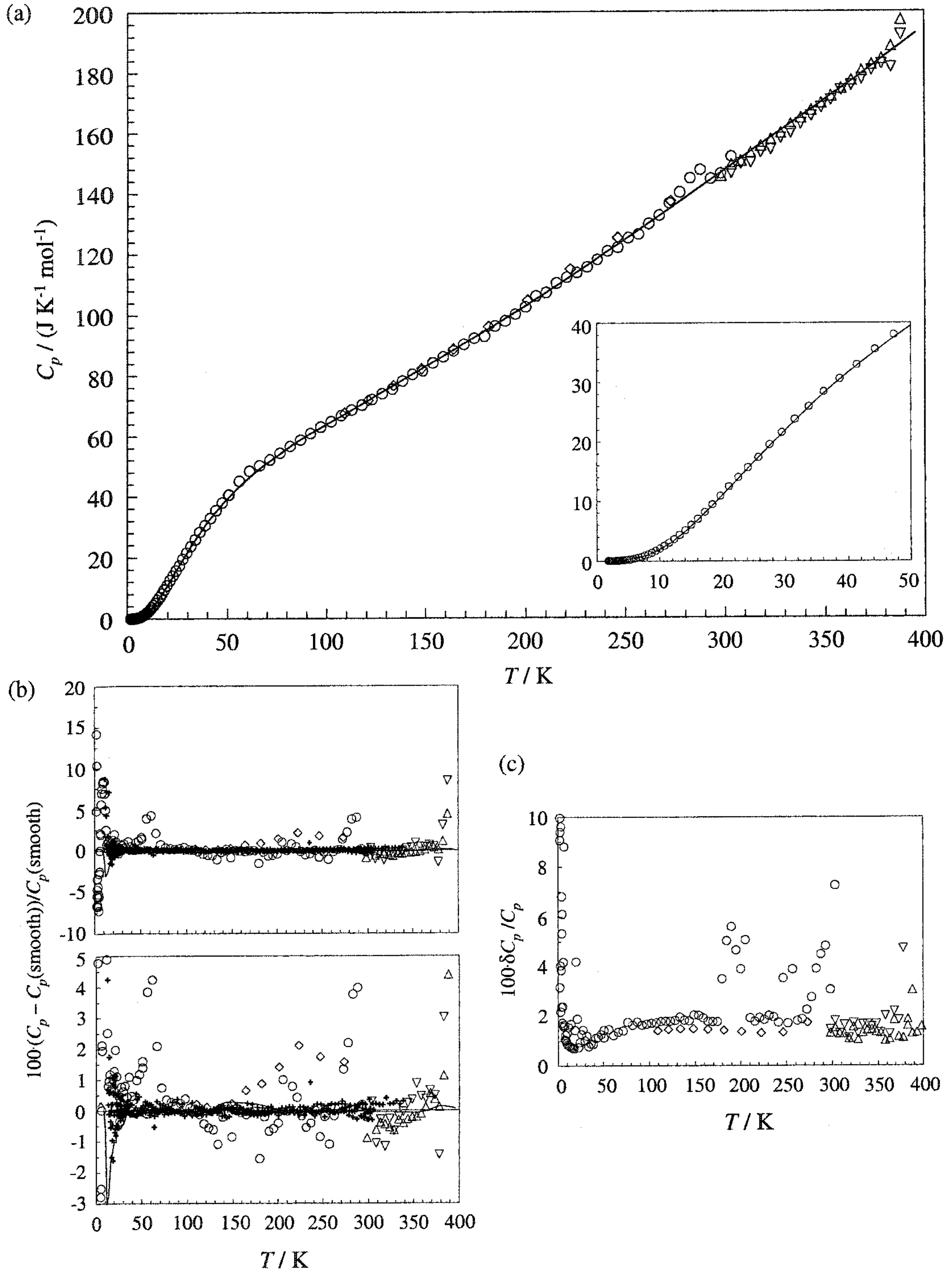

Figure 7.13 Benzoic acid standard heat capacities. (a) Heat capacities from PPMS and DSC, (b) relative heat capacity differences from smoothed literature data(159, 289, 297-299) and (c) estimated errors for Calorimetry Conference benzoic acid. ◊ 8.758 ± 0.013 mg (PPMS); ○ 9.525 ± 0.006 mg (PPMS); Δ 12.109 to 12.784 mg (DSC); ∇ 12.6 to 12.8 mg (DSC after melting). Literature data: + Tatsumi *et al.*,(297) Moriya *et al.*,(298) Cole *et al.*,(299) Sorai *et al.*;(289) —— Ginnings and Furukawa.(159) Literature data have been smoothed using multiple centred quadratic equations (not spline fit, because there are no knot points).

7.3.2.4 Indium

Some heat capacities were measure above and near the fusion temperature of benzoic acid using the DSC. Due to the vapour pressure of benzoic acid at this temperature, it is not the best heat capacity standard. Because indium was being used as a temperature calibrant for the DSC, the heat capacities of indium also were measured using the DSC. These measurements are compared to the adiabatic calorimeter data of Grønvold(302) in figure 7.14. The heat capacities measurements show an accuracy of *ca.* 3 % for $T = 298$ to 425 K for sample masses from 28 to 67 mg.

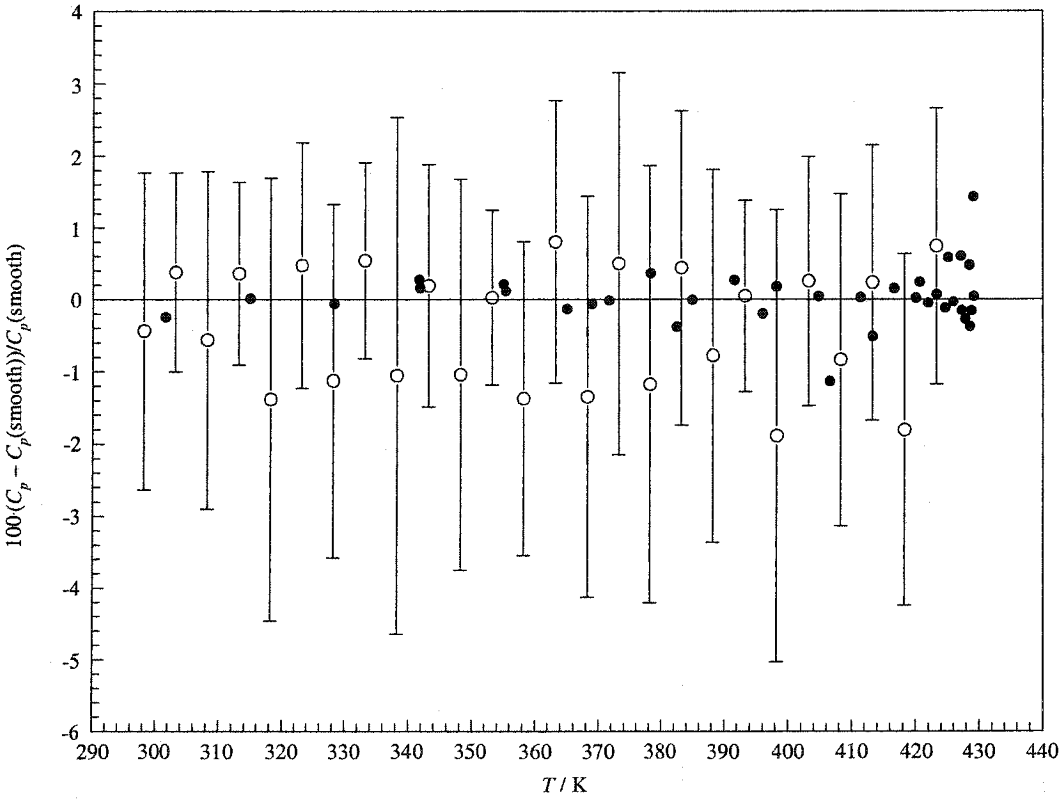

Figure 7.14 The relative DSC heat capacity differences from smoothed literature data(302) for indium. ○ DSC for samples from 28 to 67 mg; ● adiabatic calorimetric data of Grønvold.(302) Errors calculated as the twice the sample standard deviation of replicate measurements.

7.3.3 Conclusion for calorimetric standards

PPMS: Sample directly on platform

Using the normal method of measurement with the PPMS relaxation calorimeter accessory with the sample directly on the platform, the accuracy and precision of heat capacities measurements made with Puck 451 was determined by measuring Calorimetry Conference sapphire and NIST RM 5 copper standard. Heat capacities for Calorimetry Conference sapphire show accuracy of *ca.* 0.5 % for $T > 80$ K. Heat capacities for the NIST copper standard show accuracy of *ca.* 4 %. for $T = 1.86$ to 10 K, *ca.* 1 % for $T = 10$ to 80 K and *ca.* 0.5 % for $T = 80$ to 150 K. The random error or calculated reproducibility of these measurements was slightly better than the accuracy, and systematic errors associated with poor thermal contact and sample mass measurement were not significant. These references measured for Puck 451 showed better precision and accuracy than the 5% certified by Quantum Design.

The accuracy and precision for the normal PPMS method agree with those for the adiabatic calorimeter for $T > 50$ K. Both these methods have been evaluated with a sample contribution of > 40 % of the total heat capacity.

PPMS: modified method for volatile organic samples

A new method for measuring volatile organic samples within an aluminium DSC pan and Apiezon N grease was developed. Using this method, heat capacities for Calorimetry Conference benzoic acid were found to be accurate to within *ca.* 10 % for $T = 1.86$ to 20 K, 2% for $T = 20$ to 160 K and 2-6 % for $T > 160$ K. The calculated precision for $T > 60$ K is in agreement with the accuracy. Precision was estimated using systematic errors due to small sample contributions to the total heat capacity and random errors due to addenda measurements and the total heat capacity measurements.

The modified PPMS method, like the adiabatic calorimeter, requires that the sample contributes a significant portion of the total heat capacity. There are more sources of systematic and random error with the modified PPMS method, *i.e.*, the method requires two platform measurements, the pan and Apiezon N measurement and measurement of the sample sealed inside the pan. The advantage for the modified PPMS method is the ability to measure a sample of small mass and to obtain heat capacities for $T = 1.86$ to 50 K.

Adiabatic calorimeter

An earlier study with the small sample adiabatic calorimeter found the calorimeter to be accurate to within 0.5 % with 50 % of the total measured heat capacity being from the sample contribution for $T = 50$ to 300 K.(275) The resistance ratio sensitivity to temperature change, $\mathrm{d}RR/\mathrm{d}T$, is small for $T < 50$ K and causes more uncertainty in the ΔT measurement by adiabatic calorimetry. In comparison to the normal PPMS method, the adiabatic calorimeter heat capacities are of similar quality; however, for the modified method for organic samples the adiabatic calorimeter heat capacities are better. This is due to a large addenda heat capacity contribution for the modified PPMS method, where the sample contribution to the total heat capacity is not large at higher temperatures.

Errors for subsequent measurements in this thesis were calculated by assuming 0.25 % error in the addendum spline fit interpolation and 0.25% error in the total heat capacity measurement. This error was considered constant for $T = 50$ to 315 K and based on the smallest contribution to the total heat capacity, $100 \cdot \delta C_p/C_p = 0.354$ / (smallest fraction of sample contribution to total heat capacity). This gives an error which is ca. 0.2% larger than the accuracy found for the benzoic acid standard.

DSC enthalpic method

DSC heat capacities for Calorimetry Conference benzoic acid were found to be accurate to within *ca.* 2 % for $T = 300$ to 370 K. DSC heat capacities for indium were found to be accurate to within *ca.* 3 % for $T = 300$ to 420 K. The precision calculated from standard deviations of multiple sample measurements were found to agree with this accuracy. This method also requires that as much sample as possible be sealed in the pan. The advantage is the ability to obtained heat capacities for $T > 300$ K.

Overall

All three instruments have improved precision with more sample. It is possible to get much more sample into the adiabatic calorimeter; however, the addenda has a larger heat capacity. For heat capacity measurements of volatile organics the PPMS is best for $T = 1.86$ to 50 K. The adiabatic calorimeter heat capacities for volatile organics are best for $T = 50$ to 320 K and for non-volatiles, which can be placed directly on the platform of the PPMS, the two instruments are similar. For heat capacities at $T > 315$ K the DSC is the best instrument, *i.e.*, the adiabatic calorimeter and the PPMS have not been evaluated at $T > 300$ K.

Heat capacities measures by either the PPMS or adiabatic calorimeter method must be evaluated for error, based upon sample contribution to the total heat capacity. The error analysis for individual samples indicates which calorimeter data are more robust. This is only necessary for $T = 50$ to 300 K, because above and below this range the DSC and PPMS are the best instruments. More sample in the PPMS can extend the range of good heat capacities to some temperature at $T > 50$ K.

7.4 Heat capacity measurements for mandelic acids

7.4.1 Heat capacity data

The experimental heat capacities for *Rac*-mandelic acid, *R*-(-)-mandelic acid, *Rac*-*o*-fluoromandelic acid, *R*-(-)-*o*-fluoromandelic acid and *R*-(-)-*o*-chloromandelic acid are reported in tables 7.1, 7.2, 7.3, 7.4 and 7.5, respectively. All but *R*-(-)-*o*-chloromandelic acid (which was determined by PPMS and adiabatic calorimeter only) include data using the adiabatic calorimeter, the modified PPMS method and the enthalpic DSC method. Estimated errors are included in these tables.

The actual constant pressure heat capacity for a solid is slightly less than the measured heat capacity because samples are sealed under their own vapour pressure. As an example, the heat capacity for solid benzoic acid is 0.2 % less than the experimental measurement of the solid under its vapour pressure for $T = 370$ K. The reported heat capacities were not corrected for this difference, because the correction is much smaller than the estimated reproducibility of the measurements.

Table 7.1 Experimental heat capacities for *Rac*-mandelic acid.

T / K	C_p / J K^{-1} mol^{-1}	T / K	C_p / J K^{-1} mol^{-1}	T / K	C_p / J K^{-1} mol^{-1}	T / K	C_p / J K^{-1} mol^{-1}
adiabatic calorimeter (2.4819 ± 0.0005 g)^a							
25.56	17.8	76.69	62.3	137.03	94.0	220.84	130.2
28.56	22.3	78.72	62.9	139.53	95.5	224.68	132.7
29.54	22.1	82.75	65.2	141.73	96.8	224.91	133.5
31.75	25.5	83.16	66.6	144.28	97.3	227.24	134.1
32.15	23.7	85.64	66.2	146.50	98.5	230.08	134.7
33.38	28.8	86.59	65.0	148.98	100.0	231.21	135.3
34.56	27.5	87.86	69.7	151.25	101.2	233.71	138.1
35.46	30.1	90.23	69.9	153.69	102.0	234.51	138.1
36.83	32.1	90.24	70.2	155.99	102.4	237.24	138.3
36.89	32.7	92.57	72.3	157.44	103.7	240.18	140.8
39.09	36.3	93.76	71.8	158.41	105.1	244.29	142.3
39.11	35.7	94.88	71.3	161.70	106.6	245.19	145.1
40.28	40.1	95.29	73.9	164.27	107.1	246.63	143.7
41.35	43.1	97.18	73.5	164.86	107.4	250.47	147.0
42.43	41.0	97.29	76.7	168.49	108.9	254.04	147.8
43.39	38.8	99.52	75.3	171.06	110.9	255.47	147.7
43.42	39.2	100.39	77.5	171.53	110.8	255.50	148.4
44.86	44.5	101.96	77.2	175.27	113.1	260.70	152.0
46.12	46.3	104.21	76.7	177.84	114.8	265.67	153.9
47.10	43.7	105.51	77.0	178.23	115.4	265.69	153.2
50.15	47.1	106.63	78.1	182.38	116.8	269.01	154.7
50.90	47.1	108.89	80.0	184.66	119.6	271.10	155.5
53.33	49.8	110.60	82.0	184.91	118.4	276.35	159.5
55.72	52.1	111.30	82.2	189.07	119.3	278.89	161.2
56.93	53.5	113.53	82.4	191.39	120.4	279.35	161.0
59.27	52.5	115.64	84.1	191.51	120.0	281.50	163.2
59.83	56.0	115.96	86.2	194.91	118.5	286.79	167.2
60.67	56.3	118.26	84.7	198.06	122.6	291.58	168.8
61.51	56.2	120.64	86.0	198.16	119.9	291.84	171.2
64.35	56.5	120.70	86.9	201.53	121.1	297.23	175.1
64.67	57.8	122.96	86.4	204.73	123.3	302.92	180.1
66.95	58.2	125.34	88.1	204.87	124.2	303.34	178.6
67.76	57.5	125.61	88.0	208.10	124.2	307.59	180.1
69.79	60.4	127.63	88.9	211.44	128.4	314.57	185.7
70.62	58.1	130.10	91.0	211.54	127.8	314.70	186.3
71.01	59.8	130.62	91.4	214.48	129.0		
74.11	59.6	132.30	90.7	218.05	129.4		
74.54	59.2	134.83	93.5	218.20	129.7		
DSC (8-10 mg)							
303.15	183.7±4.7	343.15	203.6±3.6	383.15	236.5±2.5	413.15	346.8±5.3^l
313.15	189.9±4.3	353.15	208.2±0.6	383.15	330.6±3.8^l		
323.15	194.4±3.4	363.15	214.8±1.2	393.15	333.5±3.1^l		
333.15	200.9±4.9	373.15	221.1±3.0	403.15	338.7±3.4^l		
PPMS (5.161 ± 0.009 mg)							
1.859	0.0091±0.0009	10.74	4.71±0.07	55.88	54.4±1.3	189.85	126.7±6.1
1.994	0.029±0.009	11.49	5.55±0.06	61.03	57.5±1.4	194.98	129.0±5.8
2.129	0.037±0.012	12.29	6.50±0.11	66.18	60.3±1.6	200.13	126.8±8.9
2.280	0.045±0.007	13.15	7.53±0.12	71.34	63.2±2.6	205.27	132.0±8.5
2.441	0.050±0.003	14.06	8.71±0.11	76.48	66.2±1.9	210.44	134.8±5.5
2.614	0.061±0.011	15.04	10.0±0.2	81.63	68.8±2.1	215.56	136.3±5.7
2.793	0.066±0.004	16.09	11.4±0.1	86.78	72.0±2.4	220.73	139.8±6.3
2.986	0.091±0.006	17.21	12.9±0.1	91.93	74.4±2.3	225.88	141.6±5.0
3.197	0.108±0.005	18.41	14.8±0.1	97.08	76.4±2.5	231.02	144.2±4.9
3.421	0.140±0.005	19.70	16.2±0.3	102.24	79.2±2.6	236.18	145.5±6.2

continued…

Table 7.1 continued

T / K	C_p / J K^{-1} mol^{-1}	T / K	C_p / J K^{-1} mol^{-1}	T / K	C_p / J K^{-1} mol^{-1}	T / K	C_p / J K^{-1} mol^{-1}
3.664	0.185±0.005	21.07	18.6±1.0	107.38	82.2±2.7	241.33	150.5±5.0
3.918	0.208±0.014	22.54	19.6±2.5	112.53	84.3±2.9	246.47	149.4±9.7
4.191	0.274±0.006	24.11	22.7±0.6	117.70	87.3±3.0	251.62	153.3±10.4
4.481	0.356±0.010	25.79	24.3±0.4	122.85	89.8±3.0	256.75	160.3±5.2
4.793	0.460±0.018	27.59	26.6±0.6	128.00	92.8±3.2	261.89	160.5±5.4
5.128	0.581±0.011	29.52	27.8±0.3	133.15	94.9±3.2	267.03	162.3±5.8
5.481	0.763±0.013	31.57	31.3±0.4	138.31	98.1±3.5	272.15	165.2±6.7
5.864	0.891±0.028	33.77	33.7±0.5	143.47	101.1±3.4	277.27	166.0±8.3
6.268	1.08±0.04	36.13	36.3±0.5	148.62	104.3±3.5	282.42	165.7±12.0
6.714	1.30±0.02	38.65	38.7±0.6	153.78	107.2±3.7	287.53	165.6±15.0
7.171	1.58±0.03	41.35	41.4±0.7	158.95	108.8±3.7	292.67	171.3±14.7
7.670	1.94±0.03	44.23	44.1±0.8	164.13	110.8±3.7	297.79	180.3±10.6
8.204	2.32±0.03	45.57	45.4±0.9	169.29	114.4±3.8	303.19	184.8±6.5
8.776	2.79±0.03	47.32	46.9±0.9	174.44	117.5±3.9		
9.388	3.32±0.04	50.59	50.0±1.0	179.59	119.6±4.8		
10.04	3.97±0.06	50.72	50.0±1.0	184.70	122.8±4.8		

[a] Adiabatic heat capacity error estimated at 1.7% for $T > 50$ K and > 2 % for T < 50 K. *l* denotes liquid.

Table 7.2 Experimental heat capacities for *R*-(-)-mandelic acid.

T / K	C_p / J K^{-1} mol^{-1}	T / K	C_p / J K^{-1} mol^{-1}	T / K	C_p / J K^{-1} mol^{-1}	T / K	C_p / J K^{-1} mol^{-1}
adiabatic calorimeter (2.5140 ± 0.0005 g)[a]							
29.38	19.0	72.80	60.5	171.08	109.8	246.09	148.3
30.69	20.4	74.87	60.1	174.85	112.1	250.20	150.8
32.57	24.1	77.60	62.7	178.27	113.9	250.34	151.3
33.00	24.7	79.63	64.6	181.55	115.1	256.58	155.1
33.89	24.8	84.21	65.3	184.96	116.3	260.37	154.9
34.89	27.2	86.62	66.9	188.23	117.9	264.89	157.9
35.58	28.1	88.88	69.6	191.54	119.5	264.95	158.4
36.57	27.9	91.32	71.0	194.95	120.5	266.36	159.2
37.58	31.6	93.61	72.4	198.21	121.9	271.24	161.0
37.97	30.8	95.89	73.2	201.26	122.7	271.52	159.8
38.14	31.1	98.28	75.4	201.72	124.4	276.86	162.5
39.19	34.7	100.52	76.8	202.10	124.6	277.89	164.3
40.89	37.4	102.97	76.9	203.12	123.4	278.15	163.7
41.04	39.3	105.29	78.1	204.81	126.8	278.23	165.1
41.77	38.6	107.71	77.0	205.04	125.9	282.90	167.0
41.85	39.2	110.14	81.1	206.95	126.7	285.11	165.5
44.35	40.2	112.33	82.5	208.52	131.1	288.85	173.0
45.38	40.6	114.85	84.2	208.95	131.9	289.29	174.1
46.01	41.3	116.88	84.6	210.97	133.3	291.10	173.7
46.17	40.5	119.48	84.6	211.41	133.3	291.25	173.1
48.97	43.5	121.44	87.1	212.93	129.8	293.74	174.6
49.84	44.6	124.24	87.0	214.84	133.6	295.75	174.6
50.54	44.4	125.98	88.9	215.56	132.2	297.92	178.0
50.55	44.6	131.23	90.9	216.78	132.8	300.28	178.3
55.13	49.7	135.77	93.2	217.91	133.7	301.87	179.2
55.35	49.7	138.64	94.6	218.77	133.1	302.83	180.1
55.77	49.9	140.29	95.6	222.57	135.5	304.30	182.3
55.78	49.9	143.36	97.1	224.48	135.2	306.31	184.4
60.92	54.3	144.83	98.1	226.15	137.5	307.01	179.9
61.09	54.6	148.01	99.6	229.43	140.8	311.21	186.2
61.35	54.7	149.39	100.0	231.05	140.6	312.73	189.8
61.72	53.7	152.61	101.1	232.84	139.9	314.59	193.0
65.59	57.0	154.98	100.5	236.13	143.6	316.30	190.5

continued…

Table 7.2 continued

T / K	C_p / J K^{-1} mol^{-1}	T / K	C_p / J K^{-1} mol^{-1}	T / K	C_p / J K^{-1} mol^{-1}	T / K	C_p / J K^{-1} mol^{-1}
65.76	56.8	157.23	102.7	237.53	146.7	322.45	191.1
66.00	57.1	161.56	105.1	239.75	144.2		
67.34	58.2	163.41	106.1	243.88	147.9		
70.33	59.9	168.19	107.1	244.76	147.8		
DSC (8-10 mg)							
303.15	184.5±2.9	333.15	206.1±2.5	363.15	227.4±3.2	403.15	342.4±6.5^{l}
313.15	191.6±4.2	343.15	211.7±2.5	373.15	238.4±3.4	413.15	348.0±7.8^{l}
323.15	198.3±2.9	353.15	218.7±3.4	383.15	251.6±5.0		
PPMS (5.430 ± 0.011 mg)							
2.067	0.065±0.003	7.200	1.07±0.02	25.02	19.7±0.2	107.16	83.1±2.6
2.293	0.065±0.003	7.979	1.43±0.02	27.75	23.0±0.3	118.90	88.8±2.9
2.299	0.067±0.006	7.986	1.45±0.04	27.77	23.2±0.3	118.91	88.7±3.1
2.544	0.071±0.005	8.853	1.91±0.04	30.79	26.9±0.5	131.93	95.8±3.2
2.554	0.075±0.005	8.862	1.94±0.05	30.81	26.9±0.5	131.93	96.3±3.1
2.822	0.088±0.007	9.822	2.56±0.04	34.15	30.8±0.4	146.38	103.3±3.3
2.828	0.093±0.002	9.831	2.59±0.04	34.17	31.0±0.6	146.41	104.1±3.3
3.132	0.103±0.010	10.90	3.40±0.04	37.89	35.2±0.6	162.47	113.2±3.5
3.137	0.109±0.003	10.91	3.45±0.09	37.91	35.3±0.6	162.49	113.2±3.6
3.476	0.124±0.007	12.09	4.41±0.06	42.05	39.6±0.7	180.29	118.4±3.7
3.483	0.135±0.013	12.10	4.46±0.05	42.07	40.0±0.7	180.30	118.1±3.7
3.862	0.172±0.010	13.41	5.68±0.07	46.66	44.7±0.8	200.03	127.7±3.8
3.869	0.173±0.005	13.42	5.73±0.10	46.68	44.7±0.9	200.04	126.9±4.4
4.281	0.209±0.038	14.87	7.19±0.08	51.77	50.4±1.1	221.89	140.6±6.4
4.294	0.236±0.013	14.88	7.23±0.08	51.79	50.4±1.1	221.91	142.0±4.6
4.755	0.300±0.046	16.50	9.08±0.28	70.71	63.1±1.7	246.19	152.1±5.3
4.757	0.312±0.014	16.51	8.73±1.15	70.73	63.0±1.8	246.21	152.4±4.5
5.270	0.411±0.010	18.31	11.1±0.3	78.46	67.1±2.0	273.07	169.5±6.4
5.277	0.418±0.020	18.32	11.2±0.2	78.46	67.1±1.9	273.09	167.8±6.5
5.840	0.566±0.016	20.32	13.9±0.8	87.05	71.5±2.3	303.08	183.7±6.8
5.846	0.575±0.017	20.33	13.6±0.5	87.05	71.6±2.1	303.12	188.5±6.8
6.492	0.659±0.375	22.54	16.7±0.3	96.59	77.3±2.4		
6.493	0.761±0.030	22.55	16.7±0.3	96.59	77.5±2.4		
7.193	1.05±0.04	25.00	19.5±0.2	107.16	83.4±2.8		

[a] Adiabatic heat capacity error estimated at 1.7% for $T > 50$ K and > 2 % for $T < 50$ K. *l* denotes liquid.

Table 7.3 Experimental heat capacities for *Rac-o*-fluoromandelic acid.

T / K	C_p / J K^{-1}mol^{-1}	T / K	C_p / J K^{-1}mol^{-1}	T / K	C_p / J K^{-1}mol^{-1}	T / K	C_p / J K^{-1}mol^{-1}
			adiabatic calorimeter (3.6304 ± 0.0005 g)^{a}				
27.82	17.9	89.59	71.4	151.19	107.6	212.81	140.5
30.60	21.9	90.17	74.0	153.37	108.2	217.84	143.1
34.40	26.4	92.26	73.9	156.68	108.8	222.99	147.0
37.47	30.7	95.20	75.0	158.76	111.3	228.31	148.9
38.39	32.3	97.80	76.3	162.10	113.4	233.15	152.5
41.64	37.2	100.88	78.8	164.09	113.8	238.62	156.7
42.54	37.7	103.41	80.6	167.18	115.4	243.09	157.5
46.60	40.5	106.59	81.8	169.45	117.2	249.03	160.9
48.10	42.8	109.03	83.5	172.31	119.1	253.17	165.3
53.07	46.5	112.18	86.1	174.87	119.0	259.29	166.4
54.96	48.3	114.61	87.6	177.68	122.1	263.03	170.2
59.76	53.1	117.69	89.2	180.27	124.3	269.56	175.1
61.86	54.1	120.14	91.1	182.98	123.9	275.84	177.5
67.92	59.0	123.43	91.5	185.61	125.8	280.58	183.9
68.88	57.4	125.81	93.0	188.25	126.8	287.57	186.1
71.50	61.0	129.16	95.2	190.93	128.8	291.04	189.0
73.28	61.9	131.45	96.6	193.57	129.9	295.53	192.1
77.17	64.3	134.67	98.1	196.35	131.4	300.01	194.1
79.00	66.0	136.91	99.6	196.97	130.9	302.05	195.9
82.80	68.5	140.16	101.8	198.90	133.1	306.00	197.7
83.97	67.6	142.33	102.6	201.77	134.6	306.29	199.3
84.75	69.4	142.45	103.2	204.20	136.6		
86.78	70.3	145.67	104.4	207.40	137.4		
88.31	71.9	147.99	106.1	209.42	138.9		
			DSC (10-12 mg)				
303.15	195.5±6.7	333.15	215.0±8.9	363.15	235.3±9.0	393.15	347.2±5.5^{l}
313.15	200.9±6.2	343.15	221.4±9.7	373.15	246.8±9.7	403.15	356.6±11.8^{l}
323.15	208.0±7.8	353.15	227.2±7.4	383.15	346.2±10.6^{l}		
			PPMS (6.104 ± 0.008 mg)				
1.867	0.012±0.001	7.190	1.21±0.03	27.75	22.6±0.3	107.18	86.8±2.9
2.064	0.019±0.006	7.976	1.61±0.04	30.79	26.1±0.4	118.92	93.3±3.3
2.290	0.029±0.002	8.851	2.18±0.04	34.16	30.2±0.5	131.95	101.4±3.4
2.541	0.036±0.003	9.819	2.87±0.04	37.90	34.2±0.6	146.40	109.6±3.6
2.819	0.056±0.002	10.89	3.74±0.06	42.06	38.5±0.7	162.46	118.3±3.8
3.129	0.081±0.003	12.09	4.81±0.06	46.67	43.4±0.9	180.29	130.7±4.1
3.474	0.122±0.004	13.41	6.15±0.09	51.78	48.1±1.1	200.03	143.3±4.7
3.856	0.175±0.058	14.88	7.73±0.10	57.45	53.4±1.3	221.90	155.2±6.6
4.280	0.241±0.005	16.50	9.46±0.25	63.74	58.2±1.6	246.20	169.6±5.8
4.746	0.336±0.011	18.31	11.5±0.2	70.73	63.8±1.8	273.06	185.2±7.8
5.265	0.466±0.015	20.32	13.7±1.3	78.48	68.7±2.1	303.07	190.8±12.6
5.835	0.642±0.023	22.54	17.3±0.4	87.07	74.4±2.4		
6.488	0.923±0.015	25.01	19.7±0.8	96.61	80.5±2.6		

[a] Adiabatic heat capacity error estimated at 1.4% for $T > 50$ K and > 2 % for $T < 50$ K. l denotes liquid.

Table 7.4 Experimental heat capacities of *R*-(-)-*o*-fluoromandelic acid.

T / K	C_p / J K^{-1} mol^{-1}	T / K	C_p / J K^{-1} mol^{-1}	T / K	C_p / J K^{-1} mol^{-1}	T / K	C_p / J K^{-1} mol^{-1}
adiabatic calorimeter (2.9999 ± 0.0005 g)[a]							
27.87	21.4	80.84	68.9	162.98	112.6	239.08	159.4
30.81	25.1	84.55	70.7	166.26	115.3	241.75	163.1
31.59	27.0	85.66	72.6	168.82	116.9	244.41	162.7
34.58	31.6	85.74	71.2	172.12	119.3	247.04	165.0
34.93	30.0	88.20	73.2	174.72	121.3	249.69	165.3
35.67	30.8	91.74	75.6	177.98	122.9	252.42	166.9
38.26	35.3	94.18	76.5	180.58	124.0	253.58	167.2
39.05	37.8	97.68	78.8	183.68	126.2	255.08	168.6
39.71	38.3	100.39	80.8	186.39	127.4	257.81	172.6
42.62	41.5	103.67	81.7	189.34	129.4	260.73	173.2
42.64	40.4	106.54	83.0	190.09	129.9	264.03	176.9
44.24	42.9	109.66	85.7	192.24	131.2	267.86	175.4
45.68	44.7	112.51	87.8	195.38	132.6	270.23	181.5
46.69	44.4	115.60	89.0	195.83	132.7	275.89	181.5
49.50	46.7	118.45	90.4	198.10	133.7	276.16	181.7
49.61	46.5	121.57	91.5	201.51	135.3	279.04	188.0
51.03	47.6	124.44	93.5	205.93	137.7	280.35	189.0
54.29	50.0	127.52	94.7	207.19	139.9	284.68	187.0
55.54	51.8	130.79	96.4	209.11	139.9	289.30	191.8
56.22	52.9	133.44	97.6	211.73	141.1	290.34	192.2
59.16	55.4	136.80	100.2	214.65	142.6	292.04	192.3
61.40	57.0	139.40	101.1	217.41	144.5	296.37	198.5
64.22	58.4	142.70	103.3	220.16	145.3	297.36	198.5
66.31	60.4	145.33	104.1	222.88	149.5	299.98	200.5
69.14	61.9	148.62	105.9	225.56	150.0	304.97	202.1
71.19	63.4	151.26	107.9	228.28	150.9	305.44	202.7
74.04	64.1	154.56	109.4	230.98	152.6	310.45	207.0
76.01	65.8	157.11	109.2	233.67	154.8	313.33	208.7
79.30	68.0	160.46	111.9	236.38	156.1	313.68	208.5
DSC(9-11 mg)							
303.15	205.9±5.9	333.15	228.9±5.1	363.15	335.5±7.7^{l}	393.15	348.9±8.5^{l}
313.15	212.6±5.1	343.15	245.4±7.1	373.15	340.7±5.8^{l}	403.15	354.9±10.2^{l}
323.15	219.3±6.3	353.15	331.8±7.3^{l}	383.15	344.5±8.4^{l}		
PPMS (9.878 ± 0.008 mg)							
2.066	0.024±0.001	7.982	2.22±0.04	30.79	28.6±0.4	118.92	93.0±4.7
2.296	0.034±0.001	8.855	2.89±0.04	34.16	32.5±2.3	131.94	99.8±1.8
2.550	0.046±0.001	9.823	3.68±0.05	37.90	36.8±0.6	146.39	108.3±1.9
2.825	0.068±0.001	10.90	4.68±0.07	42.06	41.3±0.5	162.46	116.7±2.3
3.135	0.098±0.002	12.09	5.84±0.07	46.67	45.9±0.5	180.28	129.3±4.6
3.480	0.151±0.003	13.41	7.27±0.08	51.79	51.0±0.6	200.00	141.5±8.7
3.867	0.221±0.004	14.88	8.93±0.09	57.45	57.4±0.9	221.87	157.3±6.1
4.288	0.321±0.006	16.50	11.0±0.1	63.75	61.1±0.6	246.14	171.4±20.2
4.755	0.469±0.009	18.32	12.8±0.2	70.73	64.4±0.6	272.98	189.8±19.2
5.272	0.652±0.012	20.32	16.0±0.3	78.48	69.5±0.9	303.03	206.6±11.3
5.842	0.890±0.016	22.54	18.5±0.3	87.06	74.7±0.8		
6.493	1.26±0.02	25.01	21.6±0.4	96.60	80.2±0.8		
7.195	1.70±0.03	27.76	25.0±0.4	107.18	86.3±10.1		

[a] Adiabatic heat capacity error estimated at 1.6% for $T > 50$ K and > 2 % for T < 50 K. *l* denotes liquid.

Table 7.5 Experimental heat capacities of *R*-(-)-*o*-chloromandelic acid.

T / K	C_p / J K^{-1} mol^{-1}	T / K	C_p / J K^{-1} mol^{-1}	T / K	C_p / J K^{-1} mol^{-1}	T / K	C_p / J K^{-1} mol^{-1}
adiabatic calorimeter (2.4971 ± 0.0005 g)[a]							
32.61	26.9	100.43	84.1	164.30	116.5	225.58	146.5
36.28	29.7	102.32	84.7	167.28	118.4	228.58	152.4
38.31	35.0	106.18	86.3	169.99	120.1	231.13	151.5
41.29	42.5	108.37	87.8	172.94	121.9	234.07	153.1
44.38	44.4	111.89	90.0	175.65	122.9	239.51	158.4
45.53	44.2	114.63	91.6	178.59	125.0	244.90	160.6
49.44	46.6	117.57	92.8	181.30	124.8	248.93	163.5
50.78	48.4	120.94	94.2	184.23	128.0	254.69	166.1
54.18	51.9	123.62	95.7	187.01	129.3	258.42	169.1
57.59	56.5	126.83	97.2	189.89	130.8	259.27	168.6
64.38	59.9	129.70	99.6	195.58	132.8	264.57	170.6
70.64	63.8	132.63	101.6	195.49	133.6	268.61	172.5
71.82	64.9	135.48	103.1	198.11	135.8	274.41	177.6
76.95	67.0	138.42	104.0	201.13	135.1	280.25	180.8
77.92	68.4	141.34	105.8	203.42	138.4	284.98	185.4
83.33	72.8	144.25	108.5	206.62	140.1	289.16	182.9
83.90	73.0	147.12	109.3	208.84	141.6	294.27	186.8
86.48	74.8	150.03	109.8	212.06	142.6	301.77	190.6
89.74	77.7	152.85	111.3	214.31	143.1	304.45	196.6
92.29	79.9	155.81	112.7	217.53	144.1	313.81	201.4
94.68	81.1	158.60	114.1	219.96	146.4		
96.25	81.4	161.54	116.2	223.10	148.5		
PPMS (3.731 ± 0.011 mg)							
2.066	0.083±0.007	7.980	2.41±0.04	30.80	31.2±0.7	118.92	96.0±5.1
2.292	0.090±0.005	8.854	3.20±0.06	34.16	35.2±0.8	131.95	103.5±5.4
2.543	0.101±0.016	9.824	4.24±0.07	37.91	39.4±1.0	146.40	112.1±5.6
2.821	0.119±0.009	10.90	5.45±0.12	42.06	43.6±1.2	162.46	120.9±5.9
3.132	0.133±0.007	12.09	6.92±0.11	46.67	78.3±1.5	180.30	134.4±7.7
3.479	0.153±0.009	13.41	8.64±0.18	51.78	43.2±1.8	200.04	144.3±6.6
3.861	0.240±0.122	14.88	10.6±0.1	57.45	57.7±2.2	221.90	155.9±8.5
4.284	0.303±0.015	16.51	12.8±0.2	63.75	62.2±2.6	246.16	173.0±8.9
2.751	0.426±0.014	18.32	15.1±0.2	70.73	67.2±2.9	273.04	179.8±10.8
5.262	0.588±0.111	20.32	18.8±0.3	78.47	72.5±3.3	303.15	203.1±9.3
5.841	0.851±0.018	22.55	20.0±1.2	87.06	77.7±3.7		
6.493	1.21±0.31	25.01	24.1±0.4	96.61	84.0±4.6		
7.193	1.74±0.03	27.76	27.3±0.8	107.18	89.8±4.6		

[a] Adiabatic heat capacity error estimated at 1.8% for $T > 50$ K and > 2 % for T < 50 K. *l* denotes liquid.

7.4.2 Uncertainty and data assessment

The benzoic acid measurements have enabled the development of an error calculation dependent on the sample contribution to the total heat capacity and the variance in the addenda and total heat capacity measurements. This same error treatment was applied in calculating the uncertainties for the PPMS heat capacities reported in tables 7.1 through 7.5.

The adiabatic calorimeter results for mandelic acid, *o*-fluoromandelic acid and *o*-chloromandelic acid have been calculated by assuming 0.25% error in the addendum spline fit interpolation and 0.25% error in the total heat capacity calculation. This error is considered constant for $T > 50$ K and is based on the smallest sample contribution.

As noted in the introduction, the differences in the integrated heat capacities are of importance to thermodynamic calculations. Because the calorimetric techniques do not easily allow for measurements at specified temperature intervals, the density of experimental points is different for each system. Smoothed heat capacities have been interpolated from the best heat capacity measurements by fitting centred quadratic equations at specified temperature intervals. The smoothing equations were fit to the best experimental data at temperatures within 20 % of the interpolation temperature. The best data were selected based on the error analysis for each system. These selections and analyses are briefly discussed here.

Rac-mandelic acid and *R*-(-)-mandelic acid

The heat capacities, calculated errors and sample contributions to the total heat capacity for *Rac*-(-)-mandelic acid and *R*-(-)-mandelic acid are shown in figure 7.15. The difference between the heat capacity of the two crystal types is larger than the combined errors for $T < 50$ K; see figure 7.15(a). There are differences at higher temperatures and there appears to be some small anomalies. These differences and anomalous behaviour are discussed in the subsequent sections of this chapter.

Because of crystal size and morphology differences, the mandelic acid samples could not be loaded with as large a mass as the benzoic acid references. Therefore, the mandelic acid PPMS sample heat capacity contributions are less than of those for the Calorimetry Conference benzoic acid measurements and the precision is less. The sample contribution for the mandelic acid adiabatic calorimeter heat capacities are larger than those of the PPMS, but less than those measured for benzoic acid with the adiabatic calorimeter. These contributions are shown in 7.15(b), and 7.15(c) shows the calculated errors associated with these two different measurement methods. The heat capacities measured using the adiabatic calorimeter show a precision of *ca.* 1.7 % for $T > 50$ K. Accuracy is considerably worse at lower temperatures.

Figure 7.16 shows the smoothed and selected raw data for the heat capacities of *Rac*-mandelic acid and *R*-(-)-mandelic acid. The calculated errors and sample contributions to the total heat capacity show that the best heat capacity data for $T = 1.86$ to 50 K are provided by the PPMS and the best heat capacity data for T > 50 K are provided by the adiabatic calorimeter. This assessment agrees with the discussion of the overall accuracy of these instruments. To allow for some overlap of the data in the smoothing, all adiabatic calorimeter and PPMS data were included for $T = 40$ to 60 K. Note that confidence in these data is not substantially different from 1.7 % (*ca.* 2%).

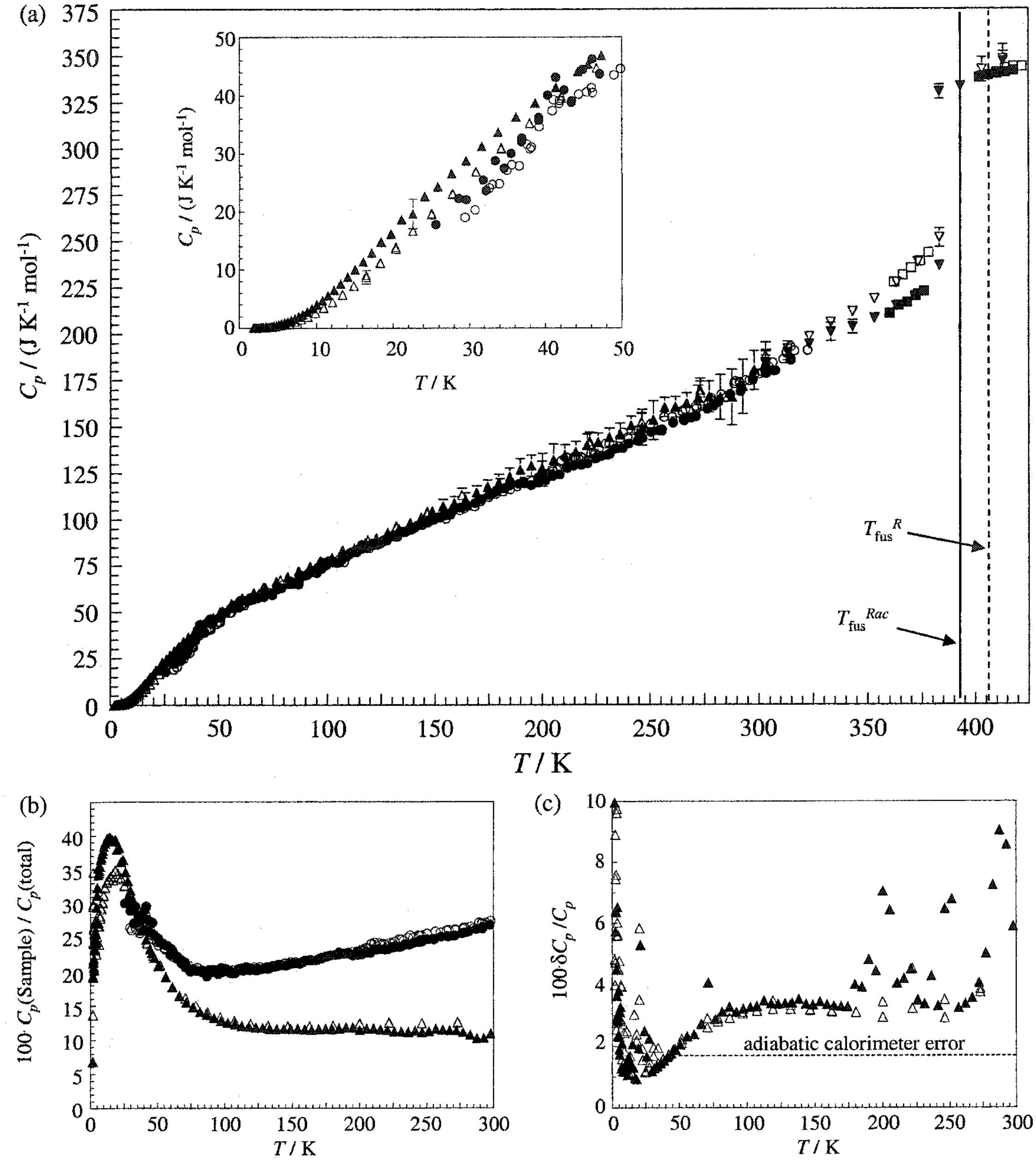

Figure 7.15 Mandelic acid heat capacities. (a) Heat capacities, (b) relative sample contributions to the total heat capacities and (c) estimated errors for *Rac*-mandelic acid and *R*-(-)-mandelic acid measured with the adiabatic calorimeter, the PPMS and the DSC. ● adiabatic calorimeter, *Rac*-mandelic acid, 2.4819 ± 0.0005 g; ○ adiabatic calorimeter, *R*-(-)-mandelic acid, 2.5140 ± 0.0005 g; ▲ PPMS, *Rac*-mandelic acid, 5.161 ± 0.009 mg; △ PPMS, *R*-(-)-mandelic acid, 5.430 ± 0.011 mg; ▼ DSC, *Rac*-mandelic acid, 8-10 mg; ▽ DSC, *R*-(-)-mandelic acid, 8-10 mg; ■ DSC, *Rac*-mandelic acid;(85) □ DSC, *R*-(-)-mandelic acid;(85) Error bars are not visible where the symbol size is larger than the calculated error.

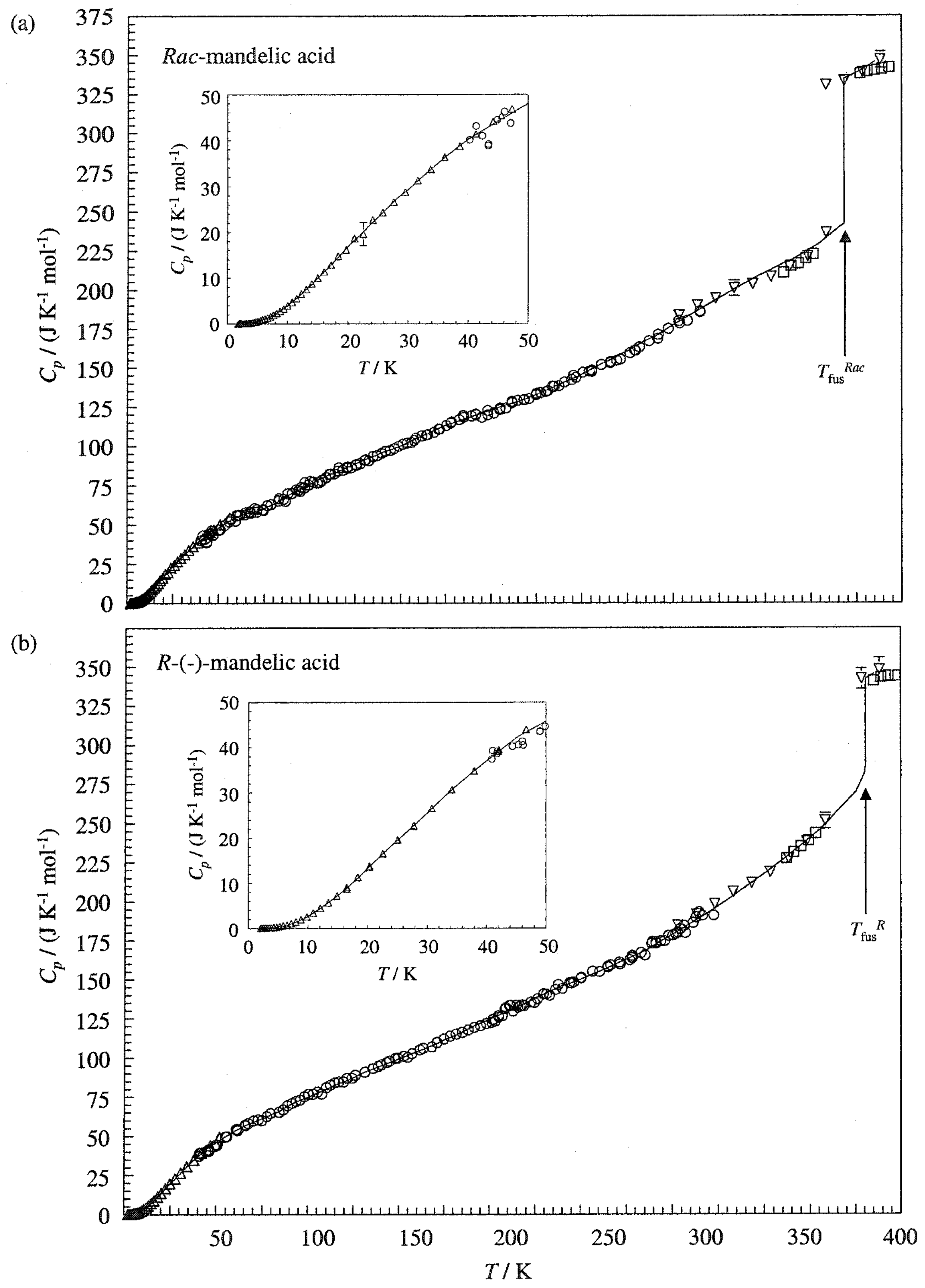

Figure 7.16 Smoothed and best experimental heat capacities for (a) *Rac*-mandelic acid and (b) *R*-(-)-mandelic acid. ○ adiabatic calorimeter; Δ PPMS; ∇ DSC; □ DSC data of Leqlercq *et al.*[85] Smoothed data are shown as solid lines. Error bars are not visible where the symbol size is larger than the calculated error.

***Rac-o*-fluoromandelic acid and *R*-(-)-*o*-fluoromandelic acid**

The heat capacities, calculated errors and sample contributions to the total heat capacities for *Rac*-(-)-*o*-fluoromandelic acid and *R*-(-)-*o*-fluoromandelic acid are shown in figure 7.17. Figure 7.17(a) shows that the heat capacity for *R*-(-)-*o*-fluoromandelic acid is greater than the *Rac*-*o*-fluoromandelic acid for $T < 125$ K and $T > 200$ K to $T_{\mathrm{fus}}{}^{R}$. There are no anomalies observed in the *o*-fluoromandelic acid heat capacities below the fusion temperature.

Figure 7.17(b) shows the relative contributions of the sample to the total measured heat capacities using the adiabatic calorimeter. It was possible to load more *o*-fluoromandelic acid samples in all three calorimeters than with the mandelic acid samples. The sample heat capacity contributions for the PPMS and adiabatic calorimeter are less than those for benzoic acid(275) and more than those for mandelic acid, with one exception. The *R*-(-)-*o*-fluoromandelic acid sample for the PPMS was similar in size and heat capacity contribution to that of the PPMS benzoic acid sample.

The heat capacities, measured using the adiabatic calorimeter, show a precision of *ca.* 1.4 % and 1.6 % ($T > 50$ K) for *Rac*-*o*-fluoromandelic acid and *R*-(-)-*o*-fluoromandelic acid, respectively. For T = 1.87 to 50 K, the PPMS provides better data. For *Rac*-o-fluoromandelic acid, the adiabatic calorimeter data at T > 50 K are more precise. From $T = 50$ to 100 K the PPMS and adiabatic calorimeter data for *R*-(-)-*o*-fluoromandelic acid show similar heat capacity contributions to the total heat capacities and similar precision; therefore, data have been included for both techniques for $T = 50$ to 100 K. Figure 7.18 shows the smoothed and selected raw data for the heat capacities of *Rac*-*o*-fluoromandelic acid and *R*-(-)-*o*-fluoromandelic acid.

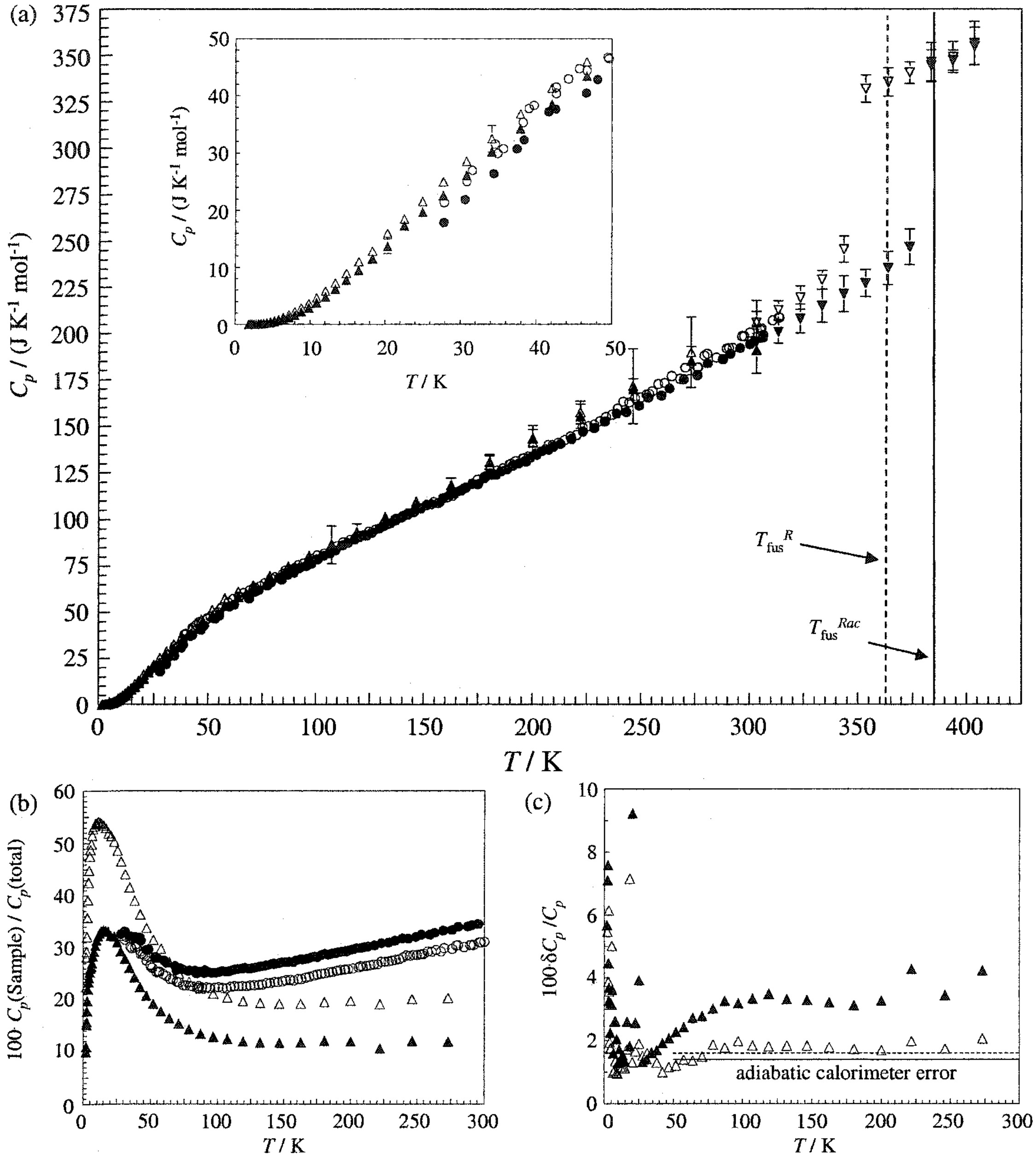

Figure 7.17 *o*-Fluoromandelic acid heat capacities. (a) Heat capacities, (b) relative sample contributions to the total heat capacities and (c) estimated errors for *Rac*-*o*-fluoromandelic acid and *R*-(-)-*o*-fluoromandelic acid measured with the adiabatic calorimeter, the PPMS and the DSC. ● adiabatic calorimeter, *Rac*-*o*-fluoromandelic acid, 3.6304 ± 0.0005 g; ○ adiabatic calorimeter, *R*-(-)-*o*-fluoromandelic acid, 2.9999 ± 0.0005 g; ▲ PPMS, *Rac*-*o*-fluoromandelic acid, 6.104 ± 0.008 mg; △ PPMS, *R*-(-)-*o*-fluoromandelic acid, 9.878 ± 0.008 mg; ▼ DSC, *Rac*-*o*-fluoromandelic acid, 10-12 mg; ▽ DSC, *R*-(-)-*o*-fluoromandelic acid, 9-11 mg. Error bars are not visible where the symbol size is larger than the calculated error.

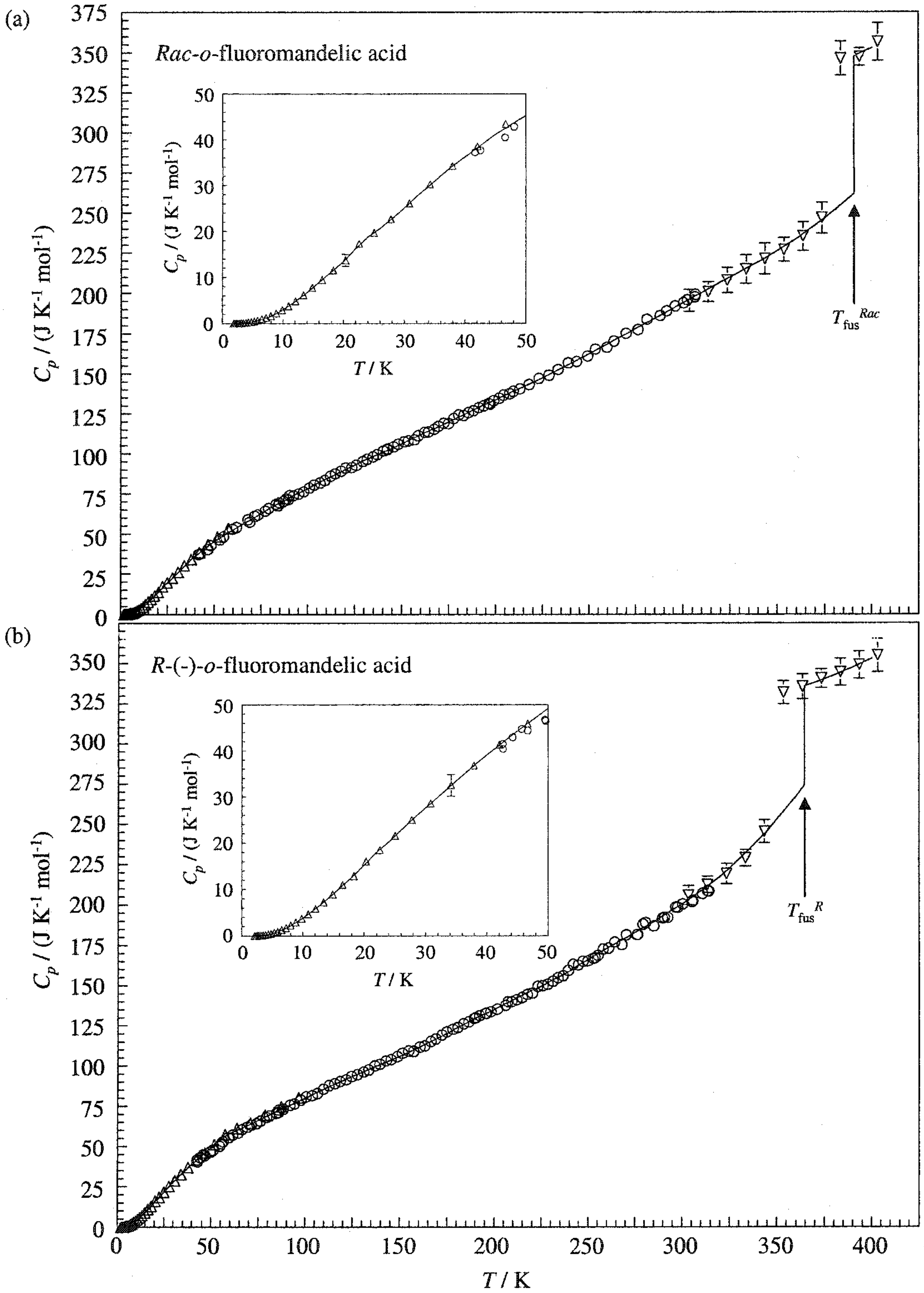

Figure 7.18 Smoothed and best experimental heat capacities for (a) *Rac-o*-fluoromandelic acid and (b) *R*-(-)-*o*-fluoromandelic acid. ○ adiabatic calorimeter; △ PPMS; ▽ DSC. Smoothed data are shown as solid line. Error bars are not visible where the symbol size is larger than the calculated error.

R-(-)-*o*-chloromandelic acid

The experimental heat capacities for *R*-(-)-*o*-chloromandelic acid also have been measured using the adiabatic calorimeter and the PPMS; see table 7.5. These heat capacities cannot be used to investigate the thermodynamics of forming the racemic crystal, because the racemic crystal was not available to investigate (*o*-chloromandelic acid is a conglomerate-forming compound). The heat capacities were measure for comparison to the heat capacities of the other four crystals. Any difference could indicate why the 1:1 enantiomeric mixture of *o*-chloromandelic acid forms a conglomerate rather than a racemic crystal.

Figure 7.20 shows the experimental heat capacities, relative sample contributions to the total heat capacity measurements and the calculated errors for *R*-(-)-*o*-chloromandelic acid. The sample heat capacity contributions for the adiabatic calorimeter are comparable to those for mandelic acid, *ca.* 18 to 25 %. Likewise, the precision also is comparable to the unsubstituted mandelic acids, *ca.* 1.8 %. The *R*-(-)-*o*-chloromandelic acid crystals are large soft platet-like crystals and it was difficult to get a large amount of sample into the DSC pan for the PPMS heat capacity measurements. Due to this small sample size, 3.731 ± 0.011 mg, the PPMS sample contributions to the total heat capacity are less than the minimum for the adiabatic calorimeter data, 14 % at $T = 50$ K; see figure 7.20 (b). The precision also is worse for the PPMS heat capacities than for those measured using the adiabatic calorimeter for $T > 50$ K.

Figure 7.20 show the smoothed and selected raw data for the heat capacities of *R*-(-)-*o*-chloromandelic acid. PPMS data were used for $T = 2$ to 60 K and adiabatic calorimeter data were used for $T = 40$ to 315 K. The overlap of data in the region of $T = 40$ to 60 K are consistent with the treatment of the heat capacity data for the unsubstituted mandelic acids.

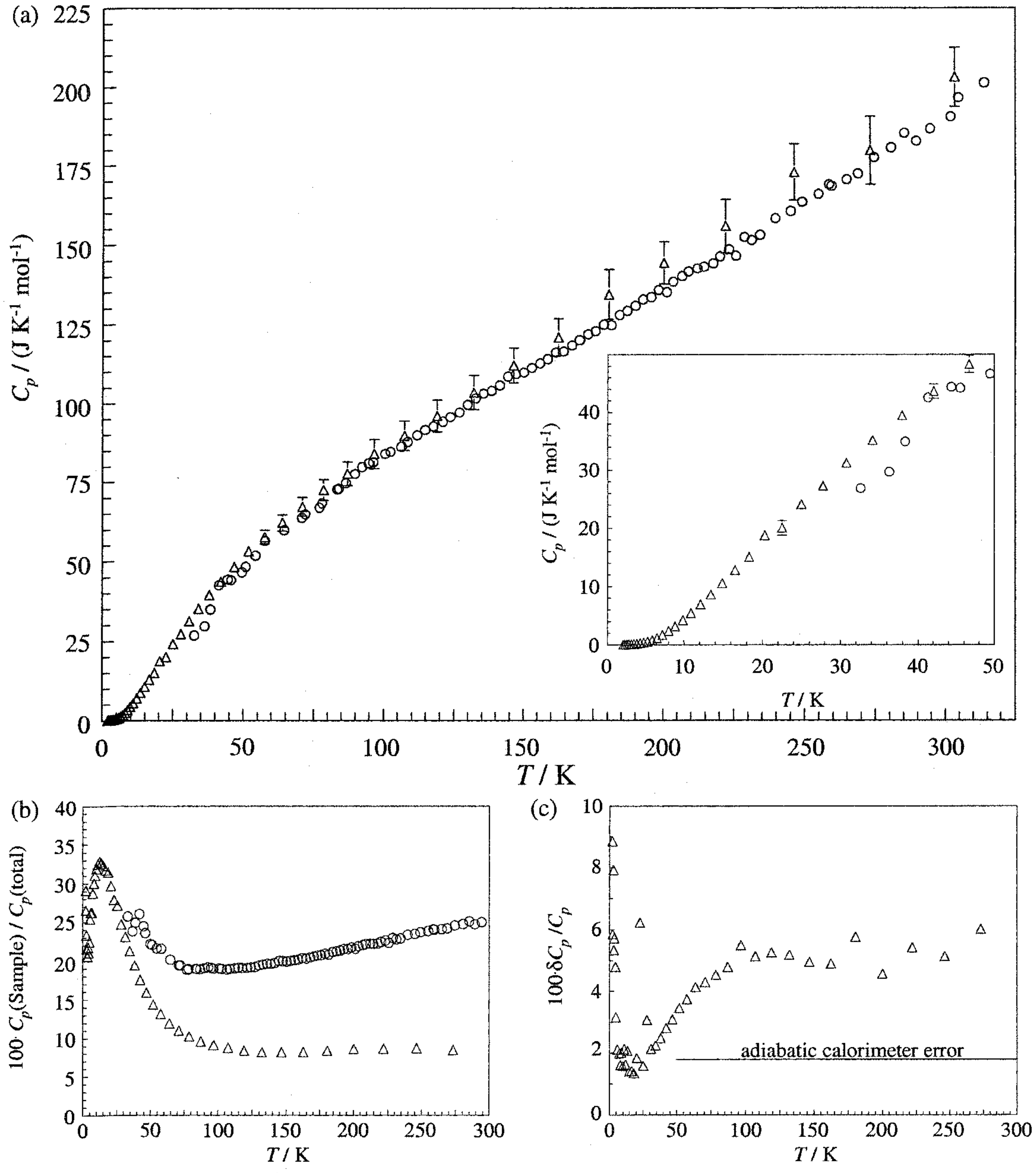

Figure 7.19 R-(-)-o-Chloromandelic acid heat capacities. (a) Heat capacities, (b) relative sample contributions to the total heat capacities and (c) estimated errors for R-(-)-o-chloromandelic acid measured with the adiabatic calorimeter and the PPMS. ○ adiabatic calorimeter, R-(-)-o-chloromandelic acid, 2.9999 ± 0.0005 g; Δ PPMS, R-(-)-o-chloromandelic acid, 3.731 ± 0.011 mg. Error bars are not visible where the symbol size is larger than the calculated error.

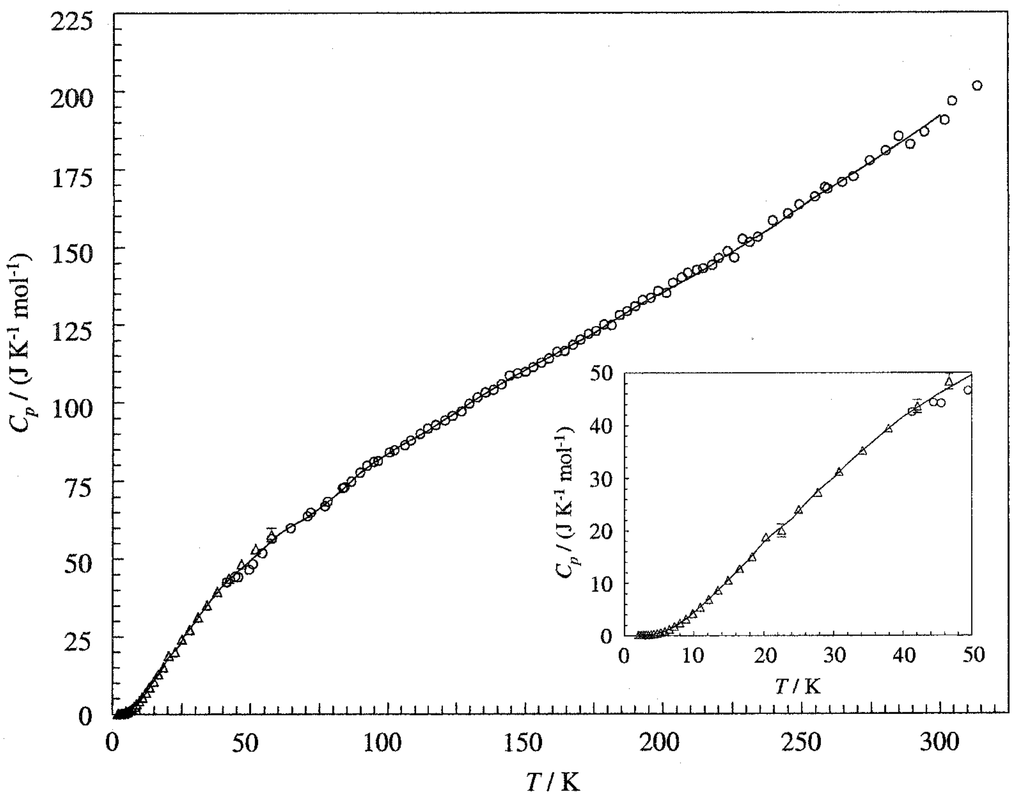

Figure 7.20 Smoothed and best experimental heat capacities for *R*-(-)-*o*-chloromandelic acid. ○ adiabatic calorimeter; Δ PPMS. Smoothed data are shown as solid line. Error bars are not visible where the symbol size is larger than the calculated error.

7.4.3 Contributions to constant pressure heat capacities

The smoothed constant pressure heat capacities, C_p-C_V contributions, internal vibrational heat capacities and external constant volume heat capacities for *Rac*-mandelic acid, *R*-(-)-mandelic acid, *Rac*-*o*-fluoromandelic acid, *R*-(-)-*o*-fluoromandelic acid, and *R*-(-)-*o*-chloromandelic acid are reported in tables 7.6, 7.7 and 7.8.

Table 7.6 Smoothed constant pressure heat capacities, constant volume heat capacities, internal vibrational heat capacities and external constant volume heat capacities for mandelic acid.*

	Rac-mandelic acid				*R*-(-)-mandelic acid			
T / K	C_p(smooth)	C_p-C_V	$C_{V,\mathrm{int}}$	$C_{V,\mathrm{ext}}$	C_p(smooth)	C_p-C_V	$C_{V,\mathrm{int}}$	$C_{V,\mathrm{ext}}$
2	0.029	0.0	0.000	0.0	0.066	0.0	0.000	0.0
4	0.234	0.0	0.000	0.2	0.182	0.1	0.000	0.1
6	0.963	0.1	0.000	0.9	0.577	0.1	0.000	0.4
8	2.17	0.1	0.000	2.1	1.46	0.2	0.000	1.3
10	3.92	0.1	0.000	3.8	2.72	0.2	0.000	2.5
12	6.14	0.1	0.000	6.0	4.39	0.3	0.000	4.1
14	8.62	0.1	0.012	8.5	6.30	0.3	0.004	6.0
16	11.2	0.2	0.044	11.0	8.30	0.4	0.015	7.9
18	14.0	0.2	0.115	13.7	10.7	0.4	0.045	10.2
20	16.9	0.2	0.247	16.5	13.3	0.5	0.107	12.7
22	19.4	0.2	0.453	18.7	15.8	0.5	0.214	15.0
24	22.1	0.2	0.745	21.1	18.4	0.6	0.379	17.4
26	24.5	0.2	1.13	23.1	20.7	0.6	0.615	19.4
28	27.3	0.3	1.59	25.4	23.1	0.7	0.927	21.5
30	29.3	0.3	2.15	26.9	25.5	0.7	1.32	23.5
32	31.7	0.3	2.77	28.6	28.1	0.8	1.80	25.5
34	34.0	0.3	3.46	30.2	30.4	0.8	2.35	27.3
36	36.1	0.3	4.21	31.6	32.7	0.9	2.99	28.9
38	38.2	0.4	5.01	32.8	35.0	0.9	3.70	30.3
40	40.2	0.4	5.85	34.0	37.0	1.0	4.47	31.5
45	44.1	0.4	8.11	35.6	42.1	1.1	6.66	34.4
50	48.0	0.5	10.5	37.0	45.8	1.2	9.14	35.5
55	51.9	0.5	13.0	38.3	49.8	1.4	11.8	36.6
60	54.9	0.6	15.6	38.8	53.3	1.5	14.6	37.2
65	57.2	0.6	18.2	38.4	56.5	1.6	17.5	37.4
70	58.5	0.7	20.8	37.0	58.9	1.7	20.4	36.8
75	60.5	0.7	23.4	36.4	61.3	1.9	23.3	36.2
80	63.1	0.8	26.0	36.3	63.7	2.0	26.1	35.7
85	66.3	0.8	28.6	36.9	66.4	2.1	28.9	35.4
90	69.9	0.9	31.2	37.8	69.9	2.2	31.7	36.0
95	72.7	0.9	33.8	38.0	72.7	2.3	34.4	35.9
100	75.6	1.0	36.3	38.4	74.7	2.5	37.1	35.2
110	81.4	1.1	41.3	39.0	80.0	2.7	42.3	35.0
120	86.1	1.2	46.2	38.7	84.9	3.0	47.3	34.6
130	91.4	1.2	51.0	39.2	90.4	3.2	52.2	35.0
140	95.9	1.3	55.8	38.7	94.8	3.5	56.9	34.4
150	100	1.4	60.5	38.2	99.3	3.7	61.7	33.9
160	106	1.5	65.2	38.9	104	3.9	66.4	33.7
170	110	1.6	70.0	39.4	109	4.2	71.1	33.5
180	115	1.7	74.7	38.6	114	4.4	75.8	33.5
190	119	1.8	79.4	37.9	120	4.7	80.5	34.4
200	123	1.9	84.2	37.0	125	4.9	85.2	34.5
210	127	2.0	89.0	35.8	130	5.2	90.0	34.7
220	131	2.1	93.9	34.6	135	5.4	94.8	35.0
230	135	2.2	98.7	34.4	141	5.7	99.7	35.4
240	141	2.3	104	34.9	146	5.9	105	35.8
250	146	2.4	108	34.8	150	6.2	109	34.6
260	152	2.5	113	36.1	155	6.4	114	34.4
270	158	2.6	118	37.0	160	6.7	119	34.5
280	164	2.7	123	38.5	165	6.9	124	34.5
290	170	2.8	128	39.1	172	7.2	129	35.7
300	178	2.9	133	41.9	179	7.4	134	37.6
310	184	3.0	138	43.7	186	7.7	139	39.7

continued ...

Table 7.6 continued

	Rac-mandelic acid				*R*-(-)-mandelic acid			
T / K	C_p(smooth)	C_p-C_V	$C_{V,\mathrm{int}}$	$C_{\mathrm{V,ext}}$	C_p(smooth)	C_p-C_V	$C_{V,\mathrm{int}}$	$C_{\mathrm{V,ext}}$
320	191	3.1	142	45.6	193	7.9	143	42.0
330	198	3.2	147	47.7	201	8.1	148	44.9
340	205	3.3	152	49.6	209	8.4	153	46.5
350	211	3.4	156	51.0	218	8.6	157	50.0
360	217	3.5	161	52.4	227	8.9	162	53.8
370	223	3.6	166	53.8	236	9.1	166	58.2
380	230	3.7	170	56.6	246	9.4	171	63.0
390	240	3.7	174	61.7	258	9.6	175	69.4
393.1	242[a]		176					
393.1	335[b]		176					
400	339		178		270	9.9	179	98.3
405.5					287[a]	10.0	181	
405.5					342[b]		181	
410	346		181		346		183	

*All heat capacity units in J K^{-1} mol^{-1}; [a] $C_p(cr)$, [b] $C_p(l)$

Table 7.7 Smoothed constant pressure heat capacities, constant volume heat capacities, internal vibrational heat capacities and external constant volume heat capacities for *o*-fluoromandelic acid.*

	Rac-*o*-fluoromandelic acid				*R*-(-)-*o*-fluoromandelic acid			
T / K	C_p(smooth)	C_p-C_V	$C_{V,\mathrm{int}}$	$C_{\mathrm{V,ext}}$	C_p(smooth)	C_p-C_V	$C_{V,\mathrm{int}}$	$C_{\mathrm{V,ext}}$
2	0.018	0.0	0.000	0.0	0.021	0.0	0.000	0.0
4	0.195	0.1	0.000	0.1	0.249	0.1	0.000	0.2
6	0.717	0.1	0.000	0.6	0.979	0.1	0.000	0.8
8	1.63	0.1	0.000	1.5	2.24	0.2	0.000	2.1
10	3.01	0.2	0.000	2.8	3.85	0.2	0.000	3.6
12	4.73	0.2	0.000	4.5	5.76	0.3	0.000	5.5
14	6.77	0.2	0.002	6.5	7.92	0.3	0.004	7.6
16	8.93	0.3	0.007	8.6	10.3	0.4	0.015	10.0
18	11.2	0.3	0.023	10.8	12.6	0.4	0.043	12.2
20	13.5	0.3	0.058	13.1	15.3	0.5	0.098	14.7
22	16.3	0.4	0.121	15.8	18.0	0.5	0.192	17.3
24	18.8	0.4	0.224	18.2	20.3	0.5	0.334	19.4
26	20.7	0.5	0.373	19.8	22.8	0.6	0.530	21.7
28	22.8	0.5	0.578	21.8	25.3	0.6	0.787	23.9
30	25.2	0.5	0.842	23.8	27.7	0.7	1.11	25.9
32	27.6	0.6	1.17	25.9	30.0	0.7	1.49	27.8
34	29.9	0.6	1.56	27.8	32.3	0.8	1.93	29.6
36	32.2	0.6	2.01	29.5	34.6	0.8	2.44	31.3
38	34.3	0.7	2.53	31.2	36.9	0.9	3.00	33.0
40	36.2	0.7	3.10	32.4	39.1	0.9	3.62	34.6
45	41.1	0.8	4.77	35.5	44.3	1.0	5.40	37.9
50	45.2	0.9	6.74	37.6	49.2	1.1	7.44	40.6
55	49.2	1.0	8.95	39.3	54.4	1.2	9.71	43.4
60	52.5	1.0	11.3	40.1	58.3	1.4	12.2	44.8
65	56.2	1.1	13.9	41.1	60.8	1.5	14.7	44.6
70	59.3	1.2	16.5	41.5	63.5	1.6	17.4	44.5
75	62.6	1.3	19.3	42.1	66.3	1.7	20.1	44.5
80	66.4	1.5	22.1	42.9	69.2	1.8	22.9	44.5
85	69.6	1.6	24.9	43.2	72.1	1.9	25.7	44.4
90	72.6	1.6	27.7	43.3	74.8	2.0	28.6	44.2
95	75.5	1.7	30.6	43.3	77.4	2.2	31.4	43.8

continued ...

Table 7.6 continued

	Rac-o-fluoromandelic acid				*R*-(-)-*o*-fluoromandelic acid			
T / K	C_p(smooth)	C_p-C_V	$C_{V,\text{int}}$	$C_{V,\text{ext}}$	C_p(smooth)	C_p-C_V	$C_{V,\text{int}}$	$C_{V,\text{ext}}$
100	78.4	1.8	33.5	43.2	80.1	2.3	34.2	43.5
110	84.6	1.9	39.2	43.5	85.7	2.5	39.9	43.3
120	90.3	2.1	45.0	43.2	91.0	2.7	45.5	42.8
130	96.0	2.3	50.7	43.0	96.2	2.9	51.1	42.1
140	101	2.4	56.3	42.2	101	3.2	56.7	41.4
150	106	2.6	62.0	41.9	106	3.4	62.2	40.7
160	112	2.8	67.5	41.7	112	3.6	67.6	40.5
170	117	2.9	73.1	41.4	117	3.9	73.0	40.5
180	123	3.1	78.6	41.1	124	4.1	78.5	41.0
190	128	3.3	84.0	41.0	130	4.3	83.8	41.6
200	134	3.5	89.4	40.9	135	4.5	89.2	41.4
210	139	3.6	94.8	40.8	141	4.8	94.5	41.8
220	145	3.8	100	40.7	147	5.0	99.8	42.4
230	150	4.0	106	40.9	153	5.2	105	42.6
240	156	4.2	111	41.4	159	5.4	110	43.4
250	162	4.3	116	42.0	166	5.7	116	44.8
260	169	4.5	121	43.0	173	5.9	121	46.5
270	175	4.7	126	44.0	180	6.1	126	47.6
280	181	4.8	132	45.0	186	6.4	131	48.8
290	188	5.0	137	46.1	194	6.6	136	51.0
300	194	5.2	142	47.5	201	6.8	141	52.7
310	201	5.4	147	48.7	209	7.0	144	55.8
320	207	5.5	152	50.2	218	7.3	151	59.5
330	213	5.7	156	51.2	228	7.5	156	65.0
340	220	5.9	161	52.6	240	7.7	161	71.6
350	227	6.1	166	54.7	253	7.9	165	80.1
360	234	6.2	171	57.4	268	8.2	170	89.5
364.2					274[a]			
364.2					336[b]			
370	243	6.4	175	61.2	338			
380	252	6.6	179	65.8	343			
390	262	6.8	184	71.1	348			
390.1	262[a]							
390.1	348[b]							
400	353				353			

*All heat capacity units in J K^{-1} mol^{-1}; [a] $C_p(cr)$, [b] $C_p(l)$

Table 7.8 Smoothed constant pressure heat capacities, constant volume heat capacities, internal vibrational heat capacities and external constant volume heat capacities for *R*-(-)-*o*-chloromandelic acid.*

T / K	C_p(smooth)	C_p-C_V	$C_{V,\mathrm{int}}$	$C_{V,\mathrm{ext}}$	T / K	C_p(smooth)	C_p-C_V	$C_{V,\mathrm{int}}$	$C_{V,\mathrm{ext}}$
2	0.082	0.0	0.000	0.1	75	66.3	1.1	26.2	39.0
4	0.256	0.1	0.000	0.2	80	69.8	1.1	29.3	39.3
6	0.924	0.1	0.000	0.8	85	73.7	1.2	32.4	40.1
8	2.43	0.1	0.000	2.3	90	77.8	1.3	35.5	41.1
10	4.43	0.1	0.000	4.3	95	80.9	1.3	38.5	41.1
12	6.79	0.1	0.000	6.6	100	83.7	1.4	41.5	40.8
14	9.39	0.2	0.008	9.2	110	88.8	1.5	47.5	39.8
16	12.1	0.2	0.031	11.9	120	94.1	1.7	53.3	39.1
18	14.8	0.2	0.083	14.4	130	100.0	1.8	59.0	39.1
20	17.9	0.3	0.184	17.4	140	105.3	2.0	64.6	38.7
22	20.1	0.3	0.348	19.5	150	110.4	2.1	70.2	38.1
24	22.3	0.3	0.588	21.3	160	115.1	2.2	75.7	37.1
26	25.2	0.4	0.913	23.9	170	119.9	2.4	81.2	36.3
28	27.9	0.4	1.33	26.1	180	125.0	2.5	86.6	35.8
30	30.2	0.4	1.83	27.9	190	130.4	2.7	92.0	35.7
32	32.7	0.4	2.43	29.8	200	135.4	2.8	97.3	35.2
34	35.1	0.5	3.11	31.5	210	140.2	2.9	103	34.6
36	37.3	0.5	3.86	32.9	220	145.6	3.1	108	34.6
38	39.5	0.5	4.69	34.3	230	151.1	3.2	113	34.7
40	41.6	0.6	5.59	35.5	240	156.6	3.4	118	34.9
45	45.9	0.6	8.07	37.2	250	162.9	3.5	124	35.9
50	49.6	0.7	10.8	38.0	260	168.6	3.6	129	36.3
55	53.8	0.8	13.8	39.2	270	174.3	3.8	134	36.8
60	57.9	0.8	16.8	40.2	280	180.1	3.9	139	37.4
65	60.9	0.9	19.9	40.0	290	185.9	4.1	144	38.1
70	63.1	1.0	23.1	39.0	300	192.0	4.2	149	39.1

*All heat capacity units in J K^{-1} mol^{-1}

Internal vibrational C_V contributions

The internal vibrational heat capacities for all these mandelic acids have been calculated from the vibrational assignments given in Chapter six. The temperature profile of the internal heat capacity contributions are approximately parallel to the total heat capacity at the higher temperatures, $T >$ *ca.* 60 K. These contributions to the total sample heat capacities are significant for $T > 20$ K.

C_p-C_V contributions

The C_p-C_V estimations for these mandelic acids have been calculated from the estimated thermal expansion, estimated isothermal compressibility and volumes given in Chapter five. The absolute error in this estimation is large, but the contribution relative to C_p is small. Most of this error is due to the error in isothermal compressibility estimations, for which there are no experimental data, and the assumption of a temperature independent thermal expansion coefficient. One guard digit has been reported in the tables for this quantity. This error reduces the confidence in calculating C_V for $T < 50$ K.

The C_p-C_V terms estimated in Chapter five contribute less than 4 % to the total heat capacity at $T = 300$ K for *R*-(-)-mandelic acid and less than 2 % for *Rac*-mandelic acid at $T = 300$ K. The contribution is less than 4 % of the total heat capacity at $T = 300$ K for *R*-(-)-*o*-fluoromandelic acid, less than 3 % for *Rac*-*o*-fluoromandelic acid at $T = 300$ K and *ca.* 2 % for *R*-(-)-*o*-chloromandelic acid at $T = 300$ K. The contribution is 1-2% of the constant pressure heat capacity at $T = 30$ K and likely overestimated at lower temperatures since a constant α has been used, whereas $\alpha \rightarrow 0$ K^{-1} as $T \rightarrow 0$ K.

External constant volume, $C_{V,\mathrm{ext}}$, contributions

The apparent external constant volume heat capacities for these mandelic acids were estimated from the constant pressure heat capacities by removal of the contributions from C_p-C_V and the internal vibrational contributions, *i.e.*, $C_{V,\mathrm{ext}} = C_p - (C_p\text{-}C_V) - C_{V,\mathrm{int}}$. These external contributions are shown in figure 7.21 and 7.22. Analogous data for $C_{p,\mathrm{ext}}$ are shown for several other molecular organic species in figure 4.4. Errors have been calculated by adding the error contributions from the sum-squared deviations for the smoothed C_p equations and errors for the C_p - C_V contributions.

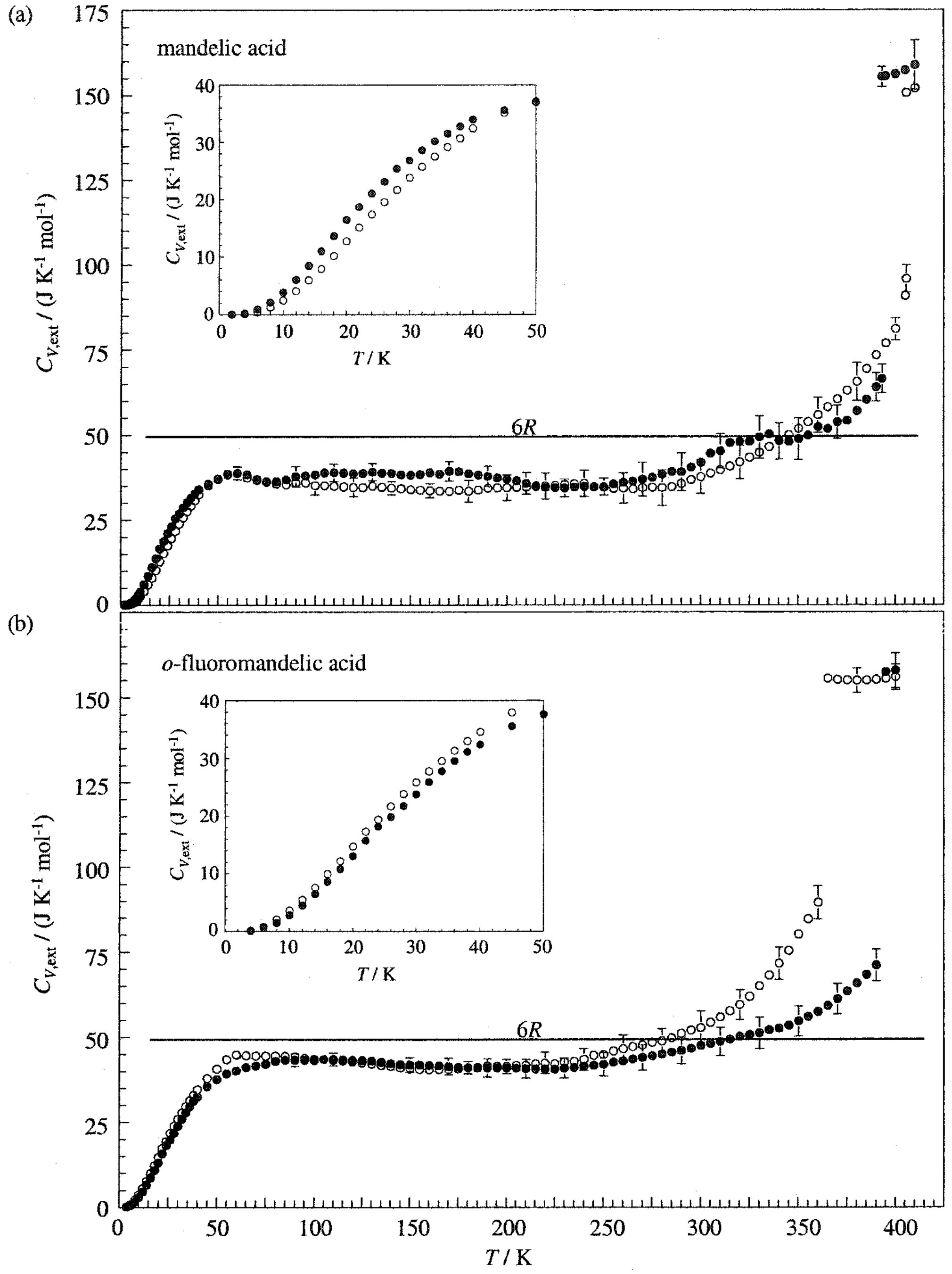

Figure 7.21 The estimated external constant volume heat capacities for (a) *Rac*-mandelic acid and *R*-(-)-mandelic acid, (b) *Rac*-*o*-fluoromandelic acid and *R*-(-)-*o*-fluoromandelic acid. ● racemic; ○ optically pure. Calculated error only is shown for selected temperatures for figure clarity.

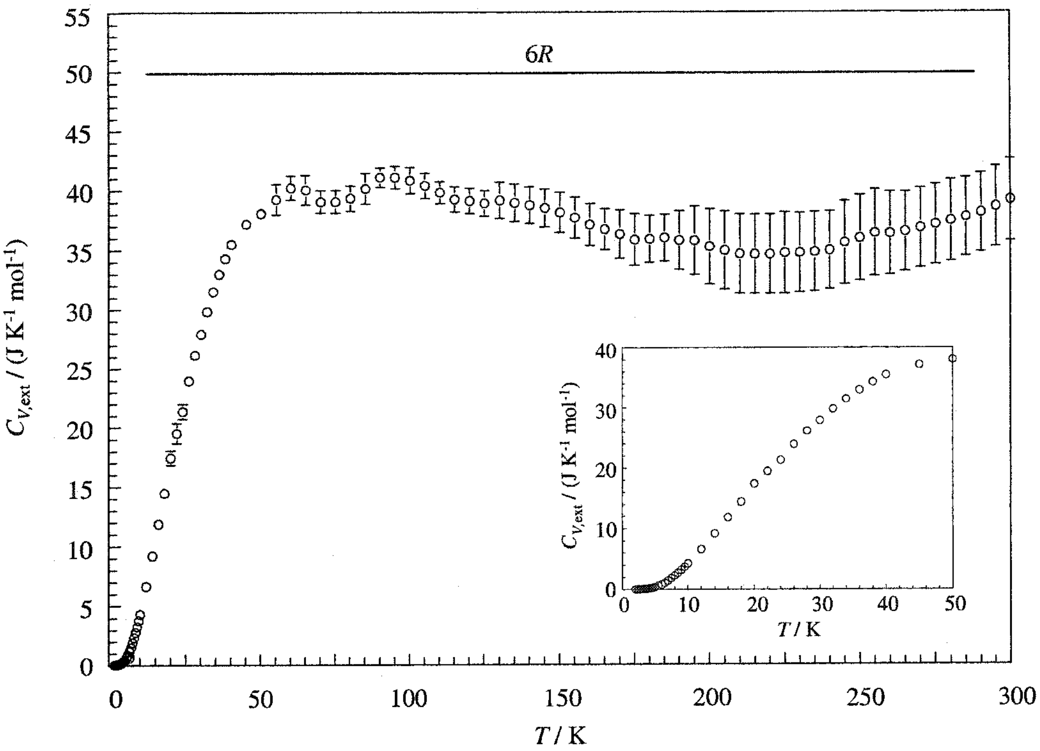

Figure 7.22 The estimated external constant volume heat capacities for *R*-(-)-*o*-chloromandelic acid.

The external heat capacities show a plateau with respect to temperature at $C_{V,\mathrm{ext}} < 6\,R$, expected at *ca.* 6 *R* from the discussion in Chapter five. This reduction from 6R is likely due to external modes being incorrectly assigned as internal modes from the vibrational spectra, *i.e.*, the low-frequency region was evenly weighted in the heat capacity calculation, because the frequencies could not be unambiguously assigned. This causes the external constant volume heat capacities to be underestimated.

A reasonable explanation for this underestimation of $C_{V,ext}$, especially at higher temperatures, is that the isothermal compressibility is likely underestimated; thus, the C_p-C_V term would be overestimated. This explanation is supported because all the crystals measured here were soft. Several attempts to press the samples into DSC pans, resulted in poor quality DSC fusion peaks. In addition, where some crystals were too large for single crystal X-ray crystallography or when they had grown together, separation resulted in poor quality crystals which could not be solved (communicated observation of the crystallographer, Prof. T. S. Cameron).

The larger heat capacities for temperatures approaching the fusion temperatures are due to premelting or crystal softening. This softening is common among organic crystals, see figure 4.4. Softening can be caused by crystal imperfections or impurities. For example, Duddu *et al.*(303) have described the inclusion of small fractions of the opposite enantiomer in crystals. These small inclusions are one type of crystal imperfection which can affect enantiomeric crystals.

Mandelic acid

In the case of the unsubstituted mandelic acids, Larsen and Stary(304) have studied the racemic and optically pure crystals by pulsed proton NMR from $T = 95$ K to T_{fus}. They observed two significant changes in the relaxation times, *ca.* 260 K for *R*-(-)-mandelic acid and *ca.* 140 K for *Rac*-mandelic acid.(304) The relaxation times were the same for both crystals at the lower temperatures, where the crystals are considered more rigid. The change in relaxation time was attributed to 180° phenyl ring flipping with rotational activation barriers of $\Delta_{\mathrm{rot}}E^{\dagger} = 63$ kJ mol^{-1} for *R*-(-)-mandelic acid and $\Delta_{\mathrm{rot}}E^{\dagger} = 33$ kJ mol^{-1} for *Rac*-(-)-mandelic acid ($\Delta_{\mathrm{rot}}E^{\dagger} = 67$ kJ mol^{-1} for solid benzene).(304)

The inflection point is observed for the total heat capacity of *R*-(-)-mandelic acid at *ca.* 280 K is close to the *ca.* 260 K observed by Larsen and Stary.(304) Figure 7.21(a) shows a lower temperature inflection point at *ca.* 175 K and some anomalous behaviour at T = 300 to 350 K for *Rac*-mandelic acid. While the lower temperature inflection point agrees with the onset of phenyl ring flipping,(304) the inflection and the higher temperature anomalous features are small when compared to the experimental errors. There is a larger premelting effect observed for *Rac*-mandelic acid than for *R*-(-)-mandelic acid, even though *R*-(-)-mandelic acid melts at a higher temperature.

At the time of the Larsen and Stary(304) study, only the *Rac*-mandelic acid crystal structure was available in the literature.(243) As discussed in Chapter five, the crystal structures of *Rac*-mandelic acid and *R*-(-)-mandelic acid show different herringbone stacking phenyl planes. Anharmonic phenyl ring motion could be the cause of both the uniaxial negative thermal expansion and the enhanced premelting. This would likely involve a twisting of the hydrogen-bonding networks which are more intermolecularly bound to the phenyl ring stacking in the *Rac*-mandelic acid crystal than they are in the *R*-(-)-mandelic acid crystal; see figures 5.13 and 5.14.

As noted in Chapter five, crystal parameters for *Rac*-mandelic acid at $T = 263$ K could not be obtained; however, the temperature increments around this temperature were not sufficiently small enough to observe a change in the volumetric expansion coefficient. The Pbca cell is observed both below and above this temperature. The unit cell volume for *R*-(-)-mandelic acid also was observed to increase slightly at $T = 143$ K; see figure 5.19. These temperatures do not seem to correspond with any events observed in the heat capacities; however, these events could have thermal contributions which are smaller than the precision of the heat capacity measurements.

***o*-Fluoromandelic acid and *R*-(-)-*o*-chloromandelic acid**

o-Chloromandelic acid shows similar ripples in the experimental heat capacities as for the mandelic acid crystals for $T = 60$ to 100 K. Note that these ripples look more significant on the scale given for the external heat capacities and there were only five heat capacity measurements from $T = 60$ to 85 K. Three possible reasons that these ripples are not part of the sample heat capacities are: (1) the liquefication of small quantities if air at $T = 60$ to 100

K, (2) the temperature derivative of the addenda heat capacity is largest in this temperature region, or (3) more heat capacity measurements would have shown the ripples to be noise.

Overall the external constant pressure heat capacities of *o*-chloromandelic acid are more similar to the unsubstituted mandelic acid crystals than they are to *o*-fluoromandelic acid, *i.e.*, the *o*-fluoromandelic acid crystals have a plateau that is closer to 6 *R*. In addition, although there were X-ray measurements only at three temperatures, there seems to be some evidence that *R*-(-)-*o*-chloromandelic acid undergoes a uniaxial negative themal expansion similar to that of *Rac*-mandelic acid.

The *o*-fluoromandelic acid heat capacities are smoother than the mandelic acid heat capacities. No significant anomalies are observed with these heat capacities. The crystal structures, reported in Chapter five, showed anomalous behaviour for *Rac*-(-)-*o*-fluoromandelic acid at $T = 143$ K. Here the crystal cell lengths are well behaved but the cell angles α and β become non-right angles (triclinic).

The larger the *ortho* substituent on the phenyl ring, the less likely the ring will undergo a flip due to steric hindrance. Although it is difficult to calculate the activation energy for this flip in the crystal lattice, the activation energy for flipping the phenyl ring was calculated for the ideal gas state using *ab inito* techniques; see figure 4.6. These are $\Delta_{\mathrm{rot}}E^{\dagger} = 10$ and 10-28 kJ mol^{-1} for the mandelic acid and *o*-fluoromandelic acid molecules, respectively. Note that the ring on mandelic acid can turn 360°C with the same 10 kJ mol^{-1} activation barrier, whereas the *o*-fluoromandelic acid phenyl ring is hindered by two different activation barriers, one at 10 kJ mol^{-1} and other at 28 kJ mol^{-1}. The latter corresponds to the fluorine passing closest to the α-oxygen or hydroxyl group.

7.4.4 Debye analysis

The $C_{V,\mathrm{ext}}$ contributions for $T < 50$ K can be used to calculate effective Debye temperatures for the studied crystals. Effective Debye temperatures are related to the external crystal forces, where a larger effective Debye temperature corresponds to a more rigid crystal lattice. External $C_{V,\mathrm{ext}}$ for molecular organic crystals can be approximated by a 6*N* Debye function; see Chapter four. The effective Debye temperatures, with propagated error, for *Rac*-mandelic acid, *R*-(-)-mandelic acid, *Rac*-*o*-fluoromandelic acid, *R*-(-)-*o*-fluoromandelic acid, and *R*-(-)-*o*-chloromandelic acid crystals are compared in figure 7.23.

In order of smallest to largest effective Debye temperatures, figure 7.23 shows *R*-(-)-*o*-chloromandelic acid, *Rac*-mandelic acid, *R*-(-)-*o*-fluoromandelic acid, *Rac*-(-)-*o*-fluoromandelic acid and *R*-(-)-mandelic acid.

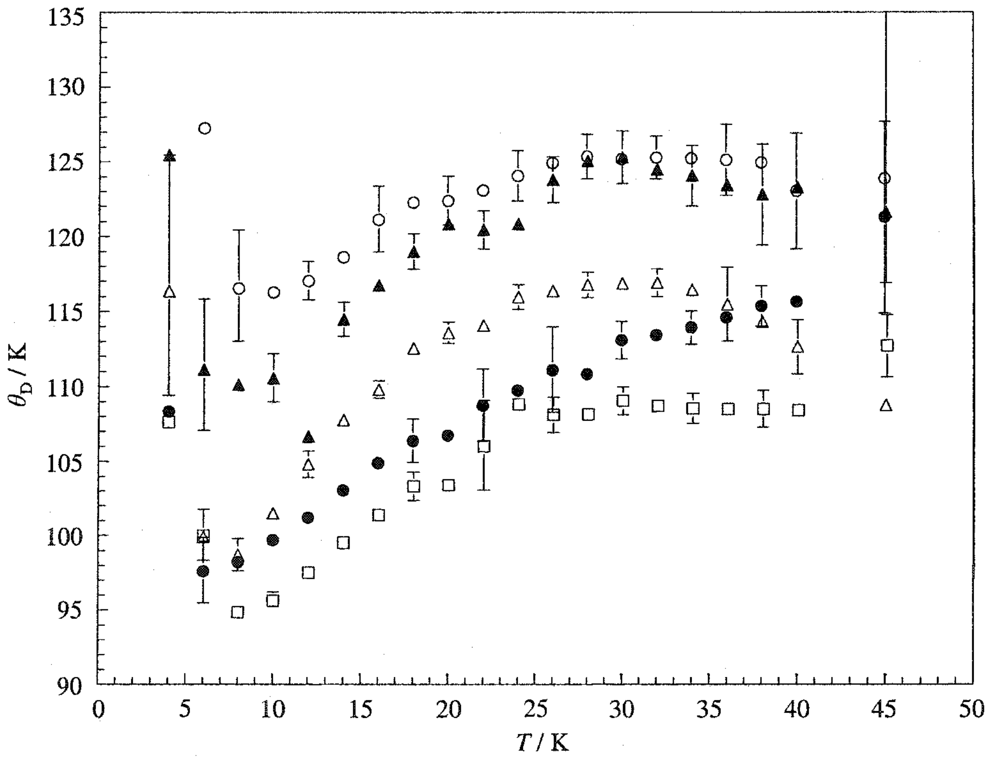

Figure 7.23 The effective Debye temperatures for *Rac*-mandelic acid, *R*-(-)-mandelic acid, *Rac*-o-fluoromandelic acid, *R*-(-)-*o*-fluoromandelic acid and *R*-(-)-*o*-chloromandelic acid. ● *Rac*-mandelic acid; ○ *R*-(-)-mandelic acid; ▲ *Rac*-*o*-fluoromandelic acid; △ *R*-(-)-*o*-fluoromandelic acid; □ *R*-(-)-*o*-chloromandelic acid. Non-symmetrical error bars shown only for selected points for figure clarity.

The effective Debye temperatures for *Rac*-mandelic acid are *ca.* 20 K lower than those of the corresponding *R*-(-)-mandelic acid. The effective Debye temperatures for *Rac*-o-fluoromandelic acid are *ca.* 10 K larger than those of the corresponding *R*-(-)-o-fluoromandelic acid. One can see that the *Rac*-mandelic acid is less rigid than its corresponding optically pure crystal, whereas *R*-(-)-*o*-fluoromandelic acid is less rigid than its corresponding racemic crystal. This is in agreement with comparing the crystal density differences and the fusion entropy differences reported in Chapter six.

The large effective Debye temperatures for *R*-(-)-mandelic acid and *Rac*-o-fluoromandelic acid are very similar. This suggests that the large relative stability of *Rac*-(-)-*o*-fluoromandelic acid relative to its conglomerate, is partially caused by a destabilisation of the conglomerate crystals. This also is shown by the small fusion entropy for *R*-(-)-*o*-fluoromandelic acid; see $\Delta_{\text{fus}}S$ values in table 5.4.

The effective Debye temperatures show that *o*-chloromandelic acid is the softest crystal of the five. This is in agreement with the discussion on loading problems for the PPMS.

7.4.5 Thermodynamic analysis and cycles

The smoothed constant pressure heat capacities have been used to obtain the numerically integrated enthalpy and entropy functions, H-H_0 and S-S_0, for *Rac*-mandelic acid, *R*-(-)-mandelic acid, *Rac*-*o*-fluoromandelic acid, *R*-(-)-*o*-fluoromandelic acid and *R*-(-)-*o*-chloromandelic acid; see equations 3.1 and 3.2. These values can be used for any thermodynamic cycle containing the pure species; therefore, the functions and along with a Gibbs energy function are often published in tables as $(H$-$H_0)/T$, S-S_0 and -$(G$-$G_0)/T$ at regular temperature intervals. Tables 7.9, 7.10 and 7.11 are these types of tables.

Table 7.9 Thermodynamic functions for mandelic acid crystals.*

	Rac-mandelic acid			*R*-(-)-mandelic acid		
T / K	$(H-H_0)/T$	S-S_0	-(G-G_0)/T	$(H-H_0)/T$	S-S_0	-(G-G_0)/T
2	0.007	0.014	0.007	0.016	0.033	0.016
4	0.056	0.080	0.023	0.061	0.101	0.040
6	0.225	0.296	0.072	0.161	0.242	0.081
8	0.546	0.722	0.176	0.358	0.508	0.150
10	1.037	1.383	0.347	0.694	0.958	0.263
12	1.702	2.287	0.585	1.167	1.591	0.424
14	2.514	3.415	0.901	1.762	2.405	0.643
16	3.440	4.733	1.292	2.456	3.375	0.919
18	4.457	6.210	1.753	3.240	4.490	1.250
20	5.556	7.832	2.276	4.118	5.751	1.633
22	6.704	9.561	2.858	5.074	7.142	2.068
24	7.873	11.36	3.490	6.080	8.632	2.551
26	9.058	13.22	4.166	7.122	10.20	3.078
28	10.26	15.14	4.881	8.191	11.84	3.644
30	11.46	17.09	5.630	9.287	13.53	4.246
32	12.65	19.06	6.407	10.40	15.28	4.880
34	13.84	21.05	7.210	11.53	17.07	5.544
36	15.02	23.05	8.034	12.66	18.89	6.234
38	16.18	25.06	8.877	13.79	20.74	6.949
40	17.33	27.07	9.737	14.93	22.62	7.685
45	20.09	32.03	11.94	17.76	27.37	9.607
50	22.69	36.89	14.20	20.51	32.13	11.62
55	25.17	41.64	16.48	23.15	36.86	13.70
60	27.52	46.29	18.77	25.67	41.50	15.83
65	29.72	50.78	21.06	27.98	45.96	17.98
70	31.72	55.07	23.34	30.10	50.23	20.13
75	33.58	59.17	25.60	32.10	54.38	22.28
80	35.34	63.16	27.82	34.01	58.42	24.41
85	37.07	67.09	30.02	35.83	62.36	26.53
90	38.79	70.98	32.19	37.63	66.26	28.63
95	40.50	74.83	34.33	39.40	70.12	30.71
100	42.19	78.64	36.45	41.12	73.90	32.78
110	45.50	86.13	40.63	44.42	81.27	36.85
120	48.68	93.41	44.73	47.59	88.44	40.86
130	51.76	100.5	78.74	50.66	95.45	44.79
140	54.75	107.4	52.69	53.66	102.3	48.65
150	57.63	114.2	56.57	56.55	109.0	52.45
160	60.46	120.8	60.38	59.37	115.6	56.19
170	63.25	127.4	64.13	62.14	122.0	59.88
180	66.03	133.8	67.82	64.87	128.4	63.51
190	68.71	140.2	71.46	67.59	134.7	67.09
200	71.33	146.4	75.06	70.32	140.9	70.62
210	73.89	152.5	78.60	73.03	147.1	74.12
220	76.38	158.5	82.09	75.74	153.3	77.58
230	78.84	164.4	85.54	78.44	159.4	81.01
240	81.31	170.3	88.95	81.15	165.6	84.40
250	83.78	176.1	92.32	83.82	171.6	87.77
260	86.29	181.9	95.66	86.47	177.6	91.11
270	88.83	187.8	98.96	89.10	183.5	94.42
280	91.41	193.6	102.2	91.73	189.4	97.71
290	94.03	199.5	105.5	94.37	195.3	101.0
300	96.69	205.4	108.7	97.07	201.3	104.2
310	99.45	211.4	111.9	99.82	207.3	107.4

continued …

Table 7.9 continued

	Rac-mandelic acid			*R*-(-)-mandelic acid		
	$(H-H_0)/T$	S-S_0	$-(G$-$G_0)/T$	$(H-H_0)/T$	S-S_0	$-(G$-$G_0)/T$
320	102.3	217.4	115.1	102.6	213.3	110.7
330	105.1	223.5	118.3	105.5	219.3	113.9
340	108.0	229.5	121.5	108.4	225.5	117.1
350	110.8	235.5	124.7	111.4	231.7	120.2
360	113.6	241.5	127.8	114.5	237.9	123.4
370	116.5	247.5	131.0	117.6	244.2	126.6
380	119.4	253.5	134.1	120.9	250.7	129.8
390	122.4	259.6	137.3	124.2	257.2	133.0
393.1	123.3	261.5	138.2			
393.1	189.2	327.4	138.2			
400	191.8	333.3	141.6	127.7	263.9	136.2
405.5				129.7	267.7	137.9
405.5				193.9	331.8	137.9
410	195.4	341.8	146.4	195.5	335.5	140.0

*All functions in $\mathrm{J\ K^{-1}\ mol^{-1}}$

Table 7.10 Thermodynamic functions for *o*-fluoromandelic acid crystals.*

	Rac-*o*-fluoromandelic acid			*R*-(-)-*o*-fluoromandelic acid		
T / K	$(H-H_0)/T$	S-S_0	$-(G$-$G_0)/T$	$(H-H_0)/T$	S-S_0	$-(G$-$G_0)/T$
2	0.004	0.009	0.004	0.005	0.010	0.005
4	0.044	0.059	0.016	0.054	0.073	0.019
6	0.168	0.221	0.053	0.226	0.294	0.068
8	0.412	0.543	0.131	0.565	0.740	0.175
10	0.788	1.049	0.261	1.055	1.406	0.350
12	1.302	1.744	0.442	1.681	2.271	0.590
14	1.937	2.622	0.685	2.418	3.317	0.899
16	2.676	3.663	0.987	3.256	4.528	1.272
18	3.495	4.841	1.346	4.171	5.877	1.706
20	4.377	6.135	1.758	5.150	7.343	2.193
22	5.331	7.548	2.217	6.196	8.926	2.731
24	6.349	9.071	2.723	7.275	10.59	3.315
26	7.379	10.65	3.272	8.374	12.31	3.940
28	8.406	12.26	3.855	9.494	14.09	4.601
30	9.446	13.92	4.470	10.63	15.92	5.294
32	10.51	15.62	5.113	11.76	17.78	6.016
34	11.58	17.36	5.782	12.90	19.66	6.763
36	12.66	19.14	6.474	14.04	21.57	7.532
38	13.75	20.93	7.188	15.18	23.51	8.322
40	14.82	22.74	7.920	16.32	25.45	9.130
45	17.47	27.29	9.818	19.15	30.36	11.22
50	20.04	31.83	11.79	21.91	35.28	13.38
55	22.51	36.33	13.82	24.63	40.22	15.59
60	24.87	40.75	15.88	27.27	45.12	17.85
65	27.14	45.10	17.96	29.75	49.89	20.13
70	29.32	49.38	20.06	32.06	54.49	22.43
75	31.43	53.58	22.15	34.25	58.97	24.71
80	33.50	57.74	24.25	36.35	63.34	26.99
85	35.53	61.87	26.34	38.36	67.62	29.26
90	37.50	65.93	28.43	40.31	71.82	31.51
95	39.42	69.93	30.51	42.20	75.94	33.74

continued ...

Table 7.10 continued

	Rac-*o*-fluoromandelic acid			*R*-(-)-*o*-fluoromandelic acid		
T / K	$(H-H_0)/T$	$S-S_0$	$-(G-G_0)/T$	$(H-H_0)/T$	$S-S_0$	$-(G-G_0)/T$
100	41.30	73.88	32.58	44.02	79.97	35.95
110	44.96	81.65	36.69	47.56	87.87	40.31
120	48.50	89.25	40.75	50.96	95.56	44.60
130	51.93	96.71	44.77	54.24	103.1	48.81
140	55.26	104.0	48.74	57.42	110.4	52.95
150	58.49	111.2	52.67	60.51	117.5	57.01
160	61.66	118.2	56.54	63.54	124.6	61.02
170	64.78	125.2	60.37	66.54	131.5	64.96
180	67.85	132.0	64.17	69.54	138.4	68.85
190	70.89	138.8	67.92	72.54	145.2	72.69
200	73.90	145.5	71.63	75.53	152.0	76.48
210	76.88	152.2	75.31	78.51	158.8	80.24
220	79.84	158.8	78.95	81.49	165.5	83.96
230	82.78	165.3	82.56	84.47	172.1	87.65
240	85.72	171.9	86.15	87.45	178.8	91.31
250	88.67	178.4	89.71	90.46	185.4	94.94
260	91.63	184.9	93.24	93.51	192.1	98.55
270	94.61	191.4	96.76	96.59	198.7	102.1
280	97.59	197.8	100.3	99.67	205.4	105.7
290	100.6	204.3	103.7	102.8	212.0	109.3
300	103.6	210.8	107.2	105.9	218.7	112.8
310	106.6	217.3	110.6	109.1	225.4	116.3
320	109.7	223.8	114.1	112.4	232.2	119.8
330	112.7	230.2	117.5	115.7	239.1	123.3
340	115.8	236.7	120.9	119.2	246.1	126.8
350	118.9	243.2	124.3	122.9	253.2	130.4
360	122.0	249.6	127.7	126.7	260.5	133.9
364.2				128.3	263.7	135.3
364.2				184.4	319.7	135.3
370	125.1	256.2	131.1	186.7	325.0	138.3
380	128.3	262.8	134.5	190.8	334.1	143.3
390	131.6	269.4	137.8	194.7	343.1	148.3
390.1	131.6	269.5	137.9			
390.1	211.4	346.2	134.8			
400	214.8	355.0	140.2	198.6	351.9	153.3

*All functions in J K^{-1} mol^{-1}

Table 7.11 Thermodynamic functions for *R*-(-)-*o*-chloromandelic acid.*

T / K	$(H - H_0)/T$	S-S_0	-$(G$-$G_0)/T$	T / K	$(H - H_0)/T$	S-S_0	-$(G$-$G_0)/T$
2	0.021	0.041	0.021	75	35.26	62.08	26.82
4	0.079	0.131	0.052	80	37.31	66.47	29.16
6	0.230	0.337	0.107	85	39.33	70.82	31.49
8	0.578	0.792	0.214	90	41.36	75.15	33.79
10	1.139	1.538	0.399	95	43.36	79.44	36.08
12	1.884	2.547	0.663	100	45.31	83.67	38.36
14	2.771	3.784	1.013	110	49.04	91.89	42.85
16	3.769	5.212	1.443	120	52.56	99.83	47.27
18	4.843	6.789	1.946	130	55.97	107.6	51.62
20	5.992	8.504	2.512	140	59.30	115.2	55.89
22	7.175	10.31	3.138	150	62.54	122.6	60.09
24	8.344	12.16	3.813	160	65.69	129.9	64.23
26	9.528	14.05	4.526	170	68.73	137.0	68.30
28	10.74	16.02	5.276	180	71.71	144.0	72.32
30	11.96	18.02	6.058	190	74.66	150.9	76.27
32	13.18	20.04	6.868	200	77.58	157.8	80.18
34	14.39	22.10	7.704	210	80.44	164.5	84.03
36	15.60	24.16	8.560	220	83.28	171.1	87.84
38	16.80	26.24	9.436	230	86.11	177.7	91.60
40	17.99	28.32	10.33	240	88.93	184.3	95.33
45	20.85	33.47	12.62	250	91.77	190.8	99.02
50	23.54	38.50	14.96	260	94.62	197.3	102.7
55	26.10	43.42	17.32	270	97.47	203.8	106.3
60	28.57	48.27	19.70	280	100.3	210.2	109.9
65	30.94	53.02	22.08	290	103.2	216.6	113.5
70	33.16	57.62	24.46	300	106.0	223.0	117.0

*All heat capacity units in J K^{-1} mol^{-1}

In Chapter two, two thermodynamic cycles were shown for calculating the Gibbs energy, entropy and enthalpy change for forming a racemic crystal from a conglomerate. This subject is now revisited.

Using the values reported in table 7.9, the Gibbs energy, enthalpy and entropy changes for forming *Rac*-mandelic acid from a 1:1 mixture of *R*-(-)- and *S*-(+)-mandelic acids have been calculated; see the cycles in figure 2.8. The Gibbs energy, enthalpy and entropy changes for forming *Rac*-*o*-fluoromandelic acid from a 1:1 mixture of *R*-(-)- and *S*-(+)-*o*-fluoromandelic acids also have been calculated using the data in table 7.10. The results for these calculations are shown in figures 7.24 and 7.25, respectively.

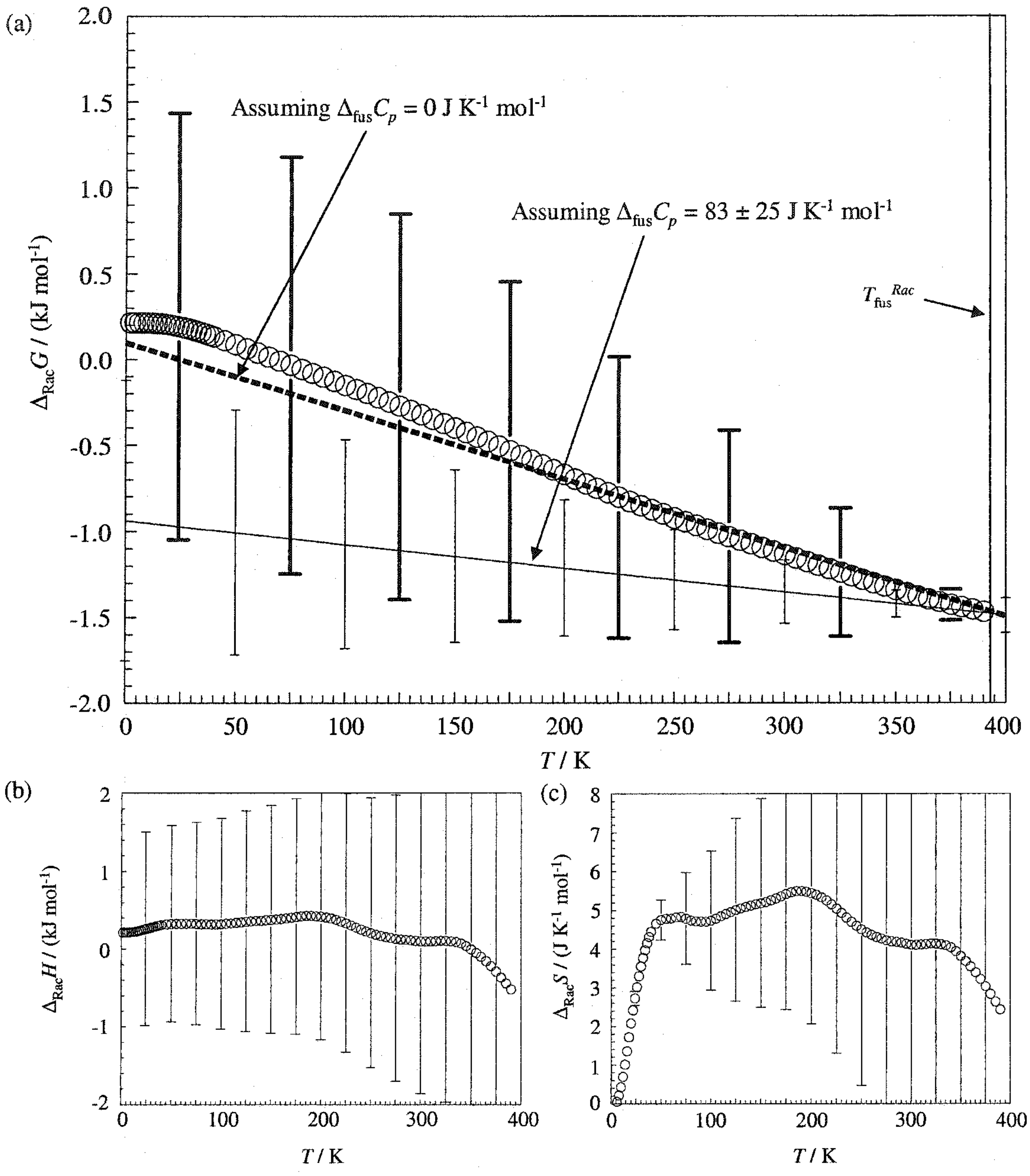

Figure 7.24 The thermodynamic changes for forming *Rac*-mandelic acid from its corresponding conglomerate. (a) Gibbs energy, (b) enthalpy change and (c) entropy change. ○ numerically integrated heat capacities; lines denote calculations completed using equations 2.34 and 2.35 and assuming $\Delta_{fus}C_p = 83 \pm 25$ (equation 4.13) or 0 J K^{-1} mol^{-1}, as indicated. Errors have been estimated by adding half of the sum-squared errors to one set of crystal heat capacities and subtracting the sum-squared errors from the other.

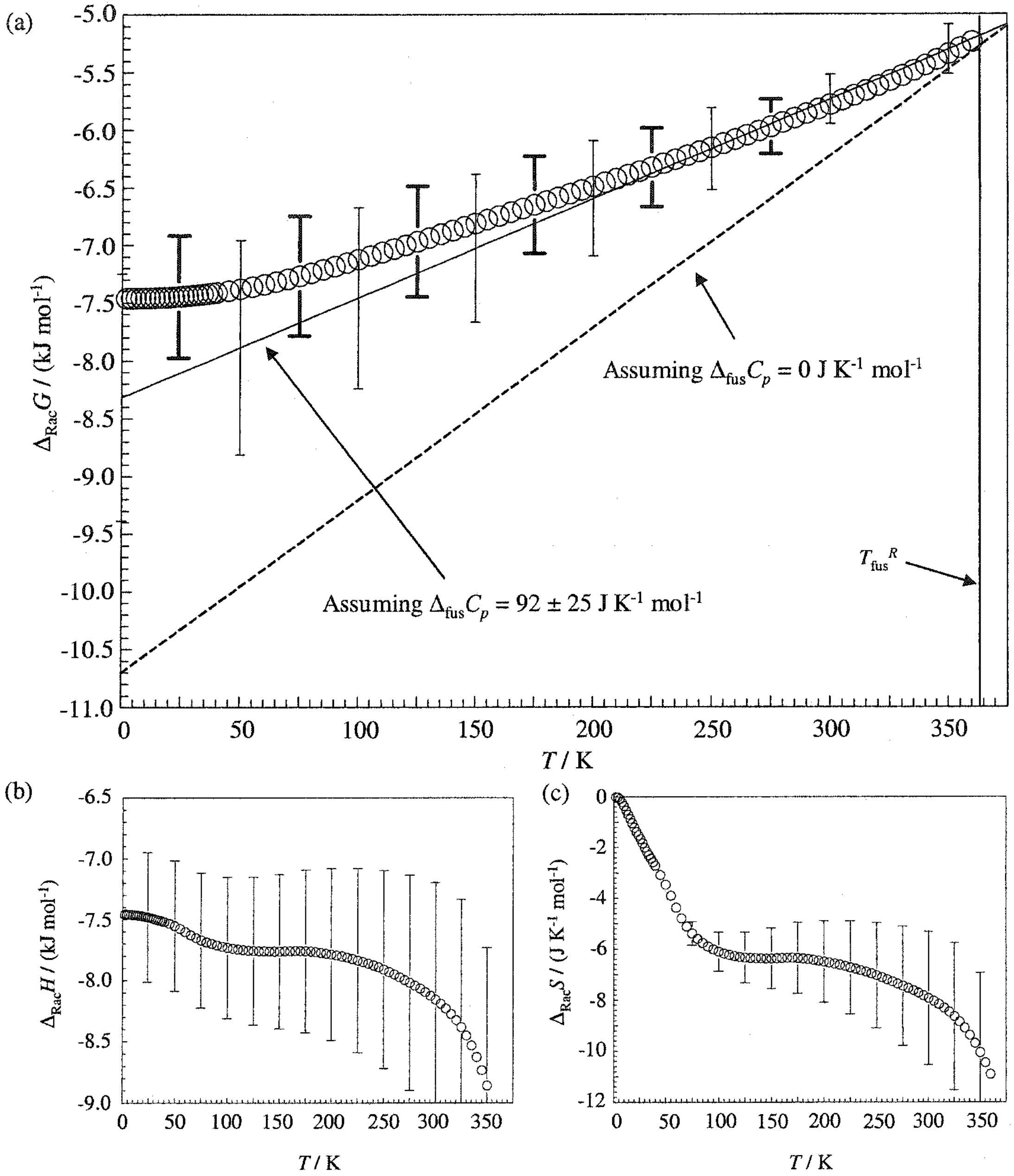

Figure 7.25 The thermodynamic changes for forming *Rac*-*o*-fluoromandelic acid from its corresponding conglomerate. (a) Gibbs energy, (b) enthalpy change and (c) entropy change. ○ numerically integrated heat capacities; lines denote calculations completed using equations 2.34 and 2.35 and assuming $\Delta_{fus}C_p$ = 92 ± 25 (equation 4.13) or 0 J K^{-1} mol^{-1}, as indicated. Errors have been estimated by adding half of the sum-squared errors to one set of crystal heat capacities and subtracting the sum-squared errors from the other.

Uncertainties for differences in the numerically integrated calculations have been estimated by adding half of the sum-squared errors (variance of experimental data to smoothed interpolation) to one set of crystal heat capacities and subtracting the sum-squared errors from the other. This calculation was repeated with opposing subtraction and addition terms, *i.e.*, the first error calculation assumes (C_p^{Rac} – 0.5 S.E., C_p^{R} + 0.5 S.E.) and the second error calculation assumes (C_p^{Rac} + 0.5 S.E., C_p^{R} – 0.5 S.E.). This error calculation grossly over estimates the total error from the integrations, as it systematically imposes the same sign of error at all temperatures, *i.e.*, assumes the worst with only 50% cancellation of error upon integration. Regardless, the calculation does give a semi-quantitative assessment of how the thermodynamic changes are affected by errors in the measurements.

One method for checking the integrated functions is to look at the differences between the entropies of the racemic and optically pure liquid, *i.e.*, at $T = T_l$ in figure 2.8. If the entropies of both crystal types are assumed to be near zero at $T = 0$ K, then $S^{\mathrm{Rac}}(l)$-$S^{\mathrm{R}}(l) \approx R \ln(2) = 5.8$ J K^{-1} mol^{-1}. From tables 7.9 and 7.10, these values were calculated to be $S^{\mathrm{Rac}}(l)$-$S^{\mathrm{R}}(l) = 6.1$ J K^{-1} mol$^{-1} \approx R \ln(2.1)$ for mandelic acid at $T = 410$ K and $S^{\mathrm{Rac}}(l)$-$S^{\mathrm{R}}(l) = 3.1$ J K^{-1} mol$^{-1} \approx R \ln(1.4)$ for *o*-fluoromandelic acid at $T = 400$ K. Note these values are subject to the experimental error and extrapolation in the fusion temperatures, fusion enthalpies and heat capacities from $T = 1.86$ to T_l for both crystal types. The fusion entropy differences alone give a propagated error of 1.8 J K^{-1} mol^{-1}. Therefore, the agreement at T_l, and hence internal consistency, is very good for both mandelic acid and *o*-fluoromandelic acid.

Also shown in figure 7.24(a) and 7.25(a) are the Gibbs energy changes calculated using the higher temperature thermodynamic cycle shown in figure 2.8, fusion cycle. These are calculated with equations 2.34 and 2.35 and only require the fusion properties reported in Chapter five. Two assumptions used with these equations, compared in Chapter four, were

$\Delta_{\text{fus}}C_p = 0$ J K^{-1} mol^{-1} and the estimation of $\Delta_{\text{fus}}C_p$, using equation 4.13; estimations were $\Delta_{\text{fus}}C_p = 83$ and 92 J K^{-1} mol^{-1} for mandelic acid and *o*-fluoromandelic acid, respectively.

In total, there are three calculation methods compared in figures 7.24(a) and 7.25(a), two fusion cycle calculations and one more time consuming, but more robust, calculation involving the integration of low-temperature heat capacities. The fusion cycle calculations of equations 2.34 and 2.35 are less robust, because of the assumption that the heat capacities of the enantiomeric crystals are the same for $T < T_{\text{fus}}$.

Rac-mandelic acid is only slightly more stable than its corresponding conglomerate; therefore the Gibbs energy change for the formation of the racemate is small. All three calculation methods agree, given the large propagated error for the small Gibbs energy change. *Rac-o*-fluoromandelic acid is more stable relative to its corresponding conglomerate than mandelic acid, and the magnitude of the Gibbs energy change on formation of the racemate is greater. The Gibbs energies calculated with the integrated heat capacity method agree with the fusion cycle calculation using the estimated $\Delta_{\text{fus}}C_p = 92$ J K^{-1} mol^{-1} but not using $\Delta_{\text{fus}}C_p = 0$ J K^{-1} mol^{-1}.

The enthalpy changes and entropy changes at selected temperatures are summarised in table 7.12.

Table 7.12 The enthalpy changes and entropy changes for forming *Rac*-mandelic acid or *Rac-o*-fluoromandelic acid from their corresponding conglomerate crystals.

		mandelic acid		*o*-fluoromandelic acid	
Calculation method	T / K	$\Delta_{\text{Rac}}H$ / kJ mol^{-1}	$\Delta_{\text{Rac}}S$ / J K^{-1} mol^{-1}	$\Delta_{\text{Rac}}H$ / kJ mol^{-1}	$\Delta_{\text{Rac}}S$ / J K^{-1} mol^{-1}
$\Delta_{\text{fus}}C_p = 0$ J K^{-1} mol^{-1}	0	0.1 ± 1.6	3.9 ± 4.0	-10.7 ± 2.7	-14.9 ± 7.4
$\Delta_{\text{fus}}C_p = 0$ J K^{-1} mol^{-1}	T_{fus}^{con}	0.1 ± 1.6	3.9 ± 4.0	-10.7 ± 2.7	-14.9 ± 7.4
$\Delta_{\text{fus}}C_p$ = estimation*	0	-0.9 ± 1.0	1.3 ± 2.5	-8.3 ± 1.1	-8.6 ± 3.2
$\Delta_{\text{fus}}C_p$ = estimation*	T_{fus}^{con}	-0.9 ± 1.0	1.3 ± 2.5	-8.3 ± 1.1	-8.6 ± 3.2
Integrated $C_{p,\text{exp}}$	0	0.2 ± 1.2	0.0	-7.5 ± 0.5	0.0
Integrated $C_{p,\text{exp}}$	100	0.3 ± 1.4	4.7 ± 1.8	-7.7 ± 0.6	-6.1 ± 0.8
Integrated $C_{p,\text{exp}}$	200	0.4 ± 1.6	5.4 ± 3.4	-7.8 ± 0.8	-6.5 ± 1.6
Integrated $C_{p,\text{exp}}$	300	0.0 ± 2.0	4.1 ± 4.8	-8.2 ± 1.0	-7.9 ± 2.6
Integrated $C_{p,\text{exp}}$	T_{fus}^{con}	-0.2 ± 2.3	3.2 ± 5.9	-8.4 ± 1.0	-8.8 ± 2.9

*Estimation = 83 J K^{-1} mol^{-1} for mandelic acid and 92 J K^{-1} mol^{-1} for *o*-fluoromandelic acid. T_{fus}^{con} = 371 K for mandelic acid and 327 K for *o*-fluoromandelic acid.

Mandelic acid

The results reported in table 7.12 show that the entropy changes for forming the racemic crystal calculated previously from fusion values are positive and not a result of calculation or experimental error; however, the entropy changes for mandelic acid are not statistically different from zero at the conglomerate fusion temperature, $T_{\text{fus}}{}^{con}$ for any of the three calculation methods. This could be a result of over estimating the error. The entropy differences are statistically postive at $T = 100$ and 200 K. Thus, *Rac*-mandelic acid is entropically more stable than its corresponding conglomerate, especially at low temperatures. Enthalpically, formation of the racemic crystal is energetically neutral at all temperatures. The calculations for this crystal system show how enthalpy changes calculated near the fusion temperatures must be interpreted with caution, if they are to be used in calibrating or interpreting empirical crystal forces, especially for $T = 0$ K, *e.g.*, molecular mechanical type calculations.

The NMR studies completed by Larsen and Stary(304) indicate that this entropic stability could be caused by the phenyl rings having more rotational freedom in the racemic crystal relative to its conglomerate.

o-Fluoromandelic acid

The enthalpy and entropy changes for forming *Rac*-*o*-fluoromandelic acid from its corresponding conglomerate, calculated by the integrated heat capacity method or the fusion cycle method using $\Delta_{\text{fus}}C_p = 92 \text{ J K}^{-1} \text{ mol}^{-1}$, are in agreement. At the conglomerate temperature, $T_{\text{fus}}{}^{con}$, the enthalpy and entropy changes calculated using these two methods are in very good agreement. The errors in the enthalpy and entropy changes using the $\Delta_{\text{fus}}C_p = 0 \text{ J K}^{-1} \text{ mol}^{-1}$ assumption are much larger than the other two methods; however, the signs of these changes are still consistent, *i.e.*, all calculations show that the

Rac-o-fluoromandelic acid is enthalpically stable and entropically unstable relative to its conglomerate. Note that the comparisons of the fusion entropies and effective Debye temperatures suggested that this is due to the optically pure crystals being more entropically stable.

The bifurcated hydrogen bonds found in *R*-(-)-*o*-fluoromandelic acid crystal structures and the strong dimer hydrogen bonding of the carboxylic acid groups found in the *Rac-o*-fluoromandelic acid crystal structure, are the likely causes of the enthalpic stabilisation and entropic destabilisation of *Rac-o*-fluoromandelic acid relative to its conglomerate. Here the dimer allows stronger intramolecular interactions and the molecular freedom is more limited in the racemic crystal. This is in agreement with the Debye analysis.

7.5 Conclusions

The objective of this chapter was to report the first heat capacity measurements for true racemic and optically pure crystal pairs from near $T = 0$ K to above T_{fus}. These measurements were made using three complementary calorimetric techniques: DSC, adiabatic calorimetry and relaxation calorimetry. Using these experimental values, previous higher temperature cycle calculations, based on fusion values, were independently tested for accuracy; see Chapter two and Chapter four.

The heat capacities of *Rac*-mandelic acid, *R*-(-)-mandelic acid, *Rac-o*-fluoromandelic acid, *R*-(-)-*o*-fluoromandelic acid and *R*-(-)-*o*-chloromandelic acid have been reported. The best data were selected from these measurements, based on error analyses of the three instruments. The best heat capacities were smoothed and the contributions to the constant volume heat capacities have been estimated; C_p-C_V contributions, internal vibrational heat capacities and external constant volume heat capacities were obtained. Although small sample sizes pushed the accuracy of the calorimetric techniques, external checks show the robust nature of the results.

No phase changes were found below the fusion temperatures, but some premelting or crystal softening was observed. The inflection points which mark the onset of this premelting for the mandelic acid crystals have been attributed to the onset of 180° phenyl ring flipping. Other small peaks and temperature ranges where heat capacities were more scattered were apparent; however, this scatter was not significantly different from the overall precision of the measurements.

The estimated external constant volume heat capacities were used to compare the effective Debye temperatures. The apparent Debye temperatures calculated from these external heat capacities were all within the range of $\theta_D = 95$ to 130 K for $T < 40$ K. Comparison of the effective Debye temperatures shows that the *R*-(-)-*o*-fluoromandelic acid and *R*-(-)-*o*-chloromandelic acid crystals are less rigid relative to the other three crystals.

The heat capacities of *R*-(-)-o-chloromandelic acid also were integrated and entropy and enthalpy functions were reported. Because *o*-chloromandelic acid is a conglomerate-forming compound, the formation of the racemic crystal could not be studied; however, the enthalpy and entropy values as a function of temperature can be used in future thermodynamic calculations. One calculation which would be of interest towards understanding resolutions, is the Gibbs energy of forming diastereomeric salts from the individual pure crystals. Here the thermodynamics of forming (1*R*,2*S*)-(-)-ephedrine *R*-(-)-*o*-chloromandelate could be compared to the thermodynamics of forming (1*R*,2*S*)-(-)-ephedrine *S*-(+)-*o*-chloromandelate.

The Gibbs energy change for forming *Rac*-mandelic acid from its conglomerate was found to be small. The enthalpy change was found to be near zero, while the entropy change was significant and positive for $T < 200$ K. For $T > 200$ K, the confidence in the entropic difference is low due to the propagation of error and similarity between the heat capacities of the two crystals. Overall, *Rac*-mandelic acid was found to be entropically more stable than its corresponding conglomerate. This entropic stability could be caused by the phenyl rings having more rotational freedom in the racemic crystal.

The same calculations for *Rac*-*o*-fluoromandelic acid and *R*-(-)-*o*-fluoromandelic acid are more robust, since the racemic crystal is much more stable relative to its conglomerate. The numerically integrated heat capacities show a similar entropy change to that of the calculation from Chapter four using the estimated $\Delta_{\mathrm{fus}}C_p$. All calculations resulted in a residual enthalpy change favouring the racemic crystal at all temperatures. *Rac*-o-fluoromandelic acid is enthalpically stable and entropically unstable relative to its conglomerate.

Both these comparisons indicate that the entropy changes for forming a racemic crystal from a conglomerate, as calculated in Chapter four, are significant. The fusion cycle calculations can be used to obtain good enthalpy and entropy changes near the fusion temperature provided that a reasonable estimate for $\Delta_{\mathrm{fus}}C_p$ is used and there is no anomalous behaviour at temperatures less than the fusion temperatures. All energy extrapolations to $T = 0$ K are in error to up to 2 kJ mol^{-1}; therefore care should be taken when interpreting residual enthalpy changes for crystals of similar stability, such as the mandelic acid crystals.

8 CONCLUSIONS AND FUTURE DIRECTIONS

> *Life is dominated by dissymmetrical actions. I can even foresee that all living species are primordially in their structure, in their external forms, functions of a cosmic dissymmetry.*
>
> Louis Pasteur, 1854

8.1 Thermodynamics of forming a racemic crystal from a conglomerate

8.1.1 Introduction

The first line of this thesis stated that ‘understanding the physical consequences of chirality or dissymmetry is fundamental to the current knowledge of any chemist.’ One observed physical consequence of molecular chirality is the experimental prevalence of racemic crystals over conglomerates. This prevalence complicates the goal of separation or resolution of enantiomers, because molecules which form racemic crystals are more difficult to resolve than those which form conglomerate crystals, 1:1 mechanic mixture of optically pure crystals.

This thesis has been directed towards understanding the enthalpy and entropy changes for forming racemic crystals from their corresponding conglomerates for many reasons: (1) the enthalpy and entropy changes can be used to interpret different interactions which influence the relative stability of the crystals, (2) enantiomeric crystals can be used to calibrate and investigate intermolecular empirical potentials for other molecular crystals, because only the crystal structure and molecular configuration is different, and (3) while the Gibbs energy change is normally in favour of the racemic crystal near the fusion temperatures, accurate enthalpy and entropy changes can be used to investigate whether the racemic crystal is favoured by equilibration at other temperatures.

8.1.2 Calorimetric techniques

In this thesis, calorimetry was the main method used for studying the thermodynamic differences between the two crystal types. A small sample adiabatic pulse calorimeter, a relaxation calorimeter and a differential scanning calorimeter were used to obtain experimental heat capacities from $T = 1.86$ to 410 K. Because three instruments were being used and one was new (the PPMS relaxation calorimeter), the calorimetric techniques were first validated by measuring and comparing the heat capacities of calorimetry standards. In addition, a modified technique for measuring the heat capacities of volatile organic samples was developed.

All three instruments were found to give improved precision with a larger sample mass. For heat capacities at $T > 315$ K the DSC was found to be the better instrument. For heat capacity measurements of volatile organics the PPMS is better for $T = 1.86$ to 50 K. The adiabatic calorimeter heat capacities for volatile organics are better for $T = 50$ to 320 K. For non-volatiles, which can be placed directly on the platform of the PPMS, the accuracy and precision of the PPMS and the adiabatic calorimeter were found to be similar for $T = 50$ to 300 K.

8.1.3 The mandelic acids

The true racemic and optically pure crystals of mandelic acid and *o*-fluoromandelic acid were obtained. Optically pure *o*-chloromandelic acid crystals were obtained. The racemic recrystallisation of *o*-bromomandelic acid resulted in a possible anomalous racemate with a 3:1 ratio of enantiomers. NMR, IR, Raman, microanalysis and DSC showed that these compounds are of good quality.

All crystals, except *o*-bromomandelic acid, were found to be of crystallographic quality. Both the racemic crystals show 2-D hydrogen-bonding planes with *ca.* 180° hydrogen bonds and ring patterns. The optically pure crystals show evidence of bifurcated hydrogen bonds and intramolecular and intermolecular hydrogen bond competition. Difficulty in obtaining crystal cell parameters at one temperature shows the possibility of anomalies in the *Rac*-mandelic acid and *R*-(-)-*o*-fluoromandelic acid crystals. In addition, a strong uniaxial negative thermal expansion was observed for the *Rac*-mandelic acid.

Low-temperature heat capacity measurements have been completed for *Rac*-mandelic acid, *R*-(-)-mandelic acid, *Rac*-*o*-fluoromandelic acid, *R*-(-)-*o*-fluoromandelic acid and *R*-(-)-*o*-chloromandelic acid. Vibrational assignments also were made for the internal modes of these crystals. The heat capacity measurements show small differences between corresponding racemic and optically pure crystals. These differences are not accounted for by the differences in the internal vibrational heat capacities; however, at lower temperatures, $T < 60$ K, the differences are observed in the effective Debye temperatures. By numerically integrating the heat capacities, enthalpy, entropy and Gibbs energy functions were reported. These values were used to calculate the enthalpy, entropy and Gibbs energy change for forming *Rac*-mandelic acid and *Rac*-(-)-*o*-fluoromandelic acid from their corresponding conglomerate crystals.

Mandelic acid

The Gibbs energy change for forming *Rac*-mandelic acid from its conglomerate was found to be small. The enthalpy difference was found to be near zero, while the entropy difference was significant for $T = 2$ to 200 K. For $T > 200$ K, the confidence in the entropic difference is low, due to the propagation of error and similarity between the heat capacities of the two crystals. Overall, *Rac*-mandelic acid was found to be entropically more stable than its corresponding conglomerate with little residual enthalpy difference at $T = 0$ K.

This entropic stability shows that racemic crystals need not be enthalpically stabilised given molecular flexibility and increased molecular freedom in the racemic crystal. The small entropic difference for the formation of *Rac*-mandelic acid causes the Gibbs energy change to be $\Delta_{\mathrm{Rac}}G = -1.4 \pm 0.2$ kJ mol^{-1} at the temperature where the conglomerate is expected, T_{fus}^{con}. This small Gibbs energy change causes the racemic crystal to melt at *ca.* 20 K above the estimated fusion of the hypothetical conglomerate.

o-Fluoromandelic acid

The apparent Debye temperature, fusion temperature, fusion enthalpy and fusion entropy show that the *Rac-o*-fluoromandelic acid is more stable relative to the corresponding conglomerate, due, in part, to a destabilisation of the *R*-(-)-o-fluoromandelic acid. The *Rac-o*-fluoromandelic acid crystals showed a different hydrogen-bonding network than those in the other crystals. Here carboxylic acid dimers are involved in the hydrogen-bonding network, whereas the R-(-)-o-fluoromandelic acid contains a bifurcated hydrogen bond network.

The calculations of the enthalpy and entropy changes for forming *Rac-o*-fluoromandelic acid from a 1:1 mixture of *S*-(-)- and *R*-(-)-*o*-fluoromandelic acid crystals, show that the racemic crystal is enthalpically stabilised and entropically destabilised. Thus, the stronger hydrogen-bonding network and limited molecular mobility causes *Rac-o*-fluoromandelic acid to be very stable relative to its conglomerate by $\Delta_{\mathrm{Rac}}G = -5.5 \pm 0.3$ kJ mol^{-1} at the estimated conglomerate fusion temperature. This causes the racemic crystal to melt at *ca.* 63 K above the estimated fusion of the hypothetical conglomerate.

The studies here have shown that strong hydrogen bonding is important in stabilising *Rac-o*-fluoromandelic acid whereas hydrogen bond preference is compromised with the phenyl ring motion in *Rac*-mandelic acid crystal. Thus it would seem that if one wants to choose molecules which are more likely to form conglomerates, soft flexible molecules with sterically demanding groups would be favourable.

8.1.4 Liquid-solid heat capacity differences

The measurements and calculations given in the final chapter are more robust than other methods for determining the entropy change for forming a racemic crystal, because of a virtually complete description of the thermodynamic properties over a large temperature range. It would be a daunting task to do these types of measurement for a large number of crystals; therefore, the usual method for calculating the Gibbs energy change for forming a racemic crystal from a conglomerate was investigated. This method uses a thermodynamic cycle which requires the fusion temperature and enthalpy of pairs of optically pure and racemic crystals. In investigating the errors for the fusion cycle calculation, it was found that the solid-liquid heat capacity differences at the fusion temperature generally are larger for chiral molecules than those for achiral molecules.

A molecular flexibility and symmetry relationship has been found for solid-liquid heat capacity differences at the fusion temperature, $\Delta_{\text{fus}}C_p$. A correlation equation suggests that the $\Delta_{\text{fus}}C_p$ value for chiral compounds could be expected to be greater than those of achiral chemicals based on simple symmetry descriptors used in calculating ideal gas properties.

8.1.5 Conclusions

Many chiral organic molecules have three or more different functional groups, which makes the comparison of different interactions difficult. For this reason several authors(3,51,198) have calculated the Gibbs energy of forming a racemic crystal from a conglomerate using the same fusion cycle used in this thesis, since fusion values are easier to locate in the literature and easier to measure, as compared to low-temperature heat capacities.

The difference with this work is that studies here have focused on the accuracy of enthalpy and entropy changes, versus simply the Gibbs energy changes. The accuracies of these values are important if the fusion cycle is to be used for comparison to molecular mechanics calculations, estimating temperatures at which the conglomerate could become the more stable crystal or for drawing general analogies about the enthalpic or entropic stability of these crystal types for many compounds. Brock *et al.*(51) identified the systematic error in these calculations and attributed the error to the assumption that $\Delta_{\text{fus}}C_p = 0\ \text{J K}^{-1}\ \text{mol}^{-1}$. In this thesis two approaches were followed: first, the $\Delta_{\text{fus}}C_p$ values were estimated through a correlation equation that was not dependent on the correlation for $\Delta_{\text{Rac}}H$ or $\Delta_{\text{Rac}}S$ values, and second, two thorough thermodynamic studies were competed for two true racemic crystal and optically pure crystal pairs.

With the first study and the estimation of $\Delta_{\text{fus}}C_p$, the values were used to recalculate the Gibbs energy, enthalpy and entropy changes for forming a racemic crystal from a conglomerate for many compounds. The systems included were predominantly from smaller compilations found in the literature. The overall conclusion is similar to the conclusion of Brock *et al.*(51) Racemic crystals appear to be enthalpically stabilised for most compounds; however, while not general, significant entropic changes were found for some individual compounds, *e.g.*, entropic contributions are significant for both the mandelic acid and *o*-fluoromandelic acid.

These calculations were shown to be robust for two systems when compared against the more thorough calculations using integrated low-temperature heat capacities. As demonstrated with the mandelic acid case, low-temperature anomalies in the heat capacities, in this case premelting, cause the residual enthalpy changes calculated using the fusion cycle equation to have a larger error.

In terms of looking at differences in molecular interactions, the thermodynamic calculations and comparisons are limited if fusion temperatures and enthalpies are not published with crystal structures. The difference in effort to add fusion values to crystal structure information is minimal with DSC. Such things as hydrogen-bonding patterns could then be evaluated to quantify their relative stability.

8.2 *Ab initio* tools and ideal gas heat capacities

The studies in Chapter three were used to present some research that was conducted outside the area of racemic and conglomerate crystal pairs, but the concepts discussed were useful tools for the subsequent studies. In particular the multiple conformations and internal rotation effects on the heat capacities of some *n*-alkanes were investigated further. It was shown that simple structural attributes can be utilized to correlate heat capacities with conformational disorder. This was the same correlation scheme used to estimate the liquid-solid heat capacity differences.

It also was shown that *ab initio* frequencies can be used to calculate ideal gas heat capacities for organic molecules, where the results are comparable to additivity methods. These types of *ab initio* frequency calculations were later used as a tool for assigning vibrational modes and for investigating the general external contributions for many solid and liquid heat capacities.

8.3 Future directions

8.3.1 Experimental studies

At the end of Chapter two a large compilation of racemic and conglomerate crystal pairs was reported. Provided with the knowledge that these calculations agree with the more thorough method of integrating low-temperature heat capacities, the enthalpy and entropy changes listed can be used to identify interesting or important compounds. One example is 1-methyl-2',6'-pipecoloxylidide (ethycaine), for which the entropy and enthalpy changes suggest that the conglomerate might be more stable than the racemic for $T < 168$ K. This calculation used the fusion data from Nemák *et al.*(199)

For the mandelic acids, the X-ray structures indicated possible transitions at temperatures where the calorimetric techniques were not as precise. It is possible that these transitions show very small thermal anomalies, especially if they involve slight changes in hydrogen-bonding environments. Neutron diffraction studies at various temperatures and over a broad temperature range can complement these studies, because neutron diffraction shows larger scattering factors for hydrogen. In addition, low-temperature vibrational spectroscopy is another complementary technique.

The solid-liquid heat capacity differences used in Chapter four were sparse for chiral compounds. A future study could aim to study the heat capacities of more chiral molecular species. One such study is the investigation of the property differences between the disubstituted fluoromandelic acids. These molecules have recently become available through Oakridge Products, Ltd. Table 8.1 shows some preliminary values for these species.

Table 8.1 Preliminary experimental fusion values for pentafluoromandelic acid and the disubstituted fluoromandelic acids.

Substitution position	σ	T_{fus} / K	$\Delta_{\mathrm{fus}}H$ / kJ mol^{-1}	$\Delta_{\mathrm{fus}}S$ / J K^{-1} mol^{-1}	$\Delta_{\mathrm{fus}}C_{p,\mathrm{exp}}$/ J K^{-1} mol^{-1}
2,3	1	455.7 ± 1.0	29.2 ± 1.0	64.0 ± 2.2	
2,4	1	399.5 ± 1.0	30.8 ± 0.6	77.2 ± 1.6	96 ± 5
2,5	1	385.4 ± 0.5	28.6 ± 0.7	74.1 ± 1.9	93 ± 6
2,6	2	421.6 ± 1.1	29.6 ± 0.3	70.2 ± 0.4	93 ± 3
3,4	1	368.7 ± 0.9	23.1 ± 1.0	62.5 ± 2.5	72 ± 30
3,5	2	408.8 ± 0.7	32.8 ± 1.5	80.2 ± 3.9	132 ± 30
2,3,4,5,6	2	395.1 ± 1.0	33.5 ± 1.0	84.9 ± 2.5	

These measurements are made for unresolved samples and the crystal structure is unknown, except for the *Rac*-3,5- and *Rac*-2,4-difluoromandelic acid. Sample obtained from Oakridge Products, Ltd.; 2,3-(004821, lot.SC 29172); 2,4-(005209, lot. V23I); 2,5-(0014823, lot. V24G); 2,6-(004824, lot. V30J); 3,4-(005212, lot. H6666); 3,5-(004826, lot. T29M); 2,3,4,5,6-(005378, lot. V24I).

The disubstituted fluoromandelic acids contain the same atoms; however, the internal symmetry numbers depend on the location of the fluorines on the phenyl ring. The X-ray structures have been solved for *Rac*-3,5-difluoromandelic acid (triclinic, P-1, $Z = 8$, $T = 233$ K) and *Rac*-2,4-difluoromandelic acid (orthorhombic, Pbca, $Z = 8$, $T = 233$ K) at DalX by Prof. T. S. Cameron and Dr. K. Robertson. This is an incomplete study, but represents an area which could be investigated further. Studies could include the resolution and comparison of heat capacities for these related molecules using the methods outlined in this thesis.

Another interesting project is the investigation of apparent molar heat capacity and apparent molar volumes of these molecules in achiral solvents. The latter project would aim to determine the differences in heat capacity for low-symmetry molecules with different internal symmetry. Thus all differences in the apparent molar properties should be symmetry related.

The fraction of the external contribution to heat capacities depends on the number of covalent bonds within the molecules; however, internal molecular contributions to expansion and compressibility are small relative to external contributions. Rather than the estimations used here, a more thorough study of the differences in bulk modulii and thermal expansion coefficients for racemic and conglomerate crystal pairs would be useful, from the perspective of identifying the differences between intramolecular forces.

8.3.2 Theoretical explorations

As discussed briefly in Chapter six, the substituent effects on the Cotton effect of mandelic acids have been investigated in the literature.(197,236,237) Mandelic acid and substituted mandelic acids have temperature dependent Cotton effects, *i.e.*, for some mandelic acids the Cotton effect in solution changes sign when the temperature is lowered from $T = 298$ K to $T = 88$ K.(236,237) This has been explained using two theories: (1) the phenyl rotamer populations change depending on temperature and (2) the rotational strength of the molecule is changed by substitution. Korver *et al.*(236) have investigated these effects using molecular orbital calculations performed using the extended Hückel method. The relaxed potential energy scans performed during this thesis research can be used for the same type of study with updated *ab initio* computational techniques.

Korver *et al.*(236) compared the minimised structure for each molecule and the rotational strength using a restricted potential energy scan, whereas a larger phase space was investigated here and vibrational frequencies for each of the four conformers were calculated. The advantages are that the conformer equilibrium can be calculated for $T > 0$ K. The latter assumes that the time scale is sufficient to allow for equilibrium. Large rotational barriers will cause this assumption to fail. Therefore a future study is to calculate the optical rotational strength of each one of these conformers; therefore, a temperature dependence of the CD can be predicted. In addition, there are two to four more minima to be investigated, *i.e.*, the conformational change associated with rotating the carboxylic acid group has not been fully investigated. Based on preliminary calculations (B3LYP/6-311G(d,p)) for the four conformations shown in figure 4.9, the energy changes for conformation changes are small and the rotamer populations do change, *i.e.*, the molecules are flexible. For example *o*-fluoromandelic acid shows a 7:1 mixture of phenyl ring rotamers at $T = 200$ K and a 4:1 mixture at $T = 300$ K. These ratios are significantly decreased with *o*-chloromandelic acid, *ca.* 20:1 at $T = 300$ K. The meta-substituted mandelic acid calculations show a 1:1 mixture at $T = 200$ K.

Other calculations were performed which involved *ab initio* cluster calculations, aimed at estimating crystal energies. A central molecule was optimized within a group of 12 closest neighbor molecules (locations were set by X-ray crystal real space matrices). Thus, the crystal energies were calculated as a sum of: (1) the energy required to deform the molecule from the minimised ideal gas conformation and (2) the energy required to move this deformed molecule into a fixed 12 molecule cluster. These calculations failed due to computation time, the requirement of higher levels of theory and large computational errors, but some of the concepts could be investigated further. Note that *ab initio* calculations do not model induction-dispersion interactions well.(305)

The formation energy differences calculated for a molecule in a racemic crystal and a molecule in an optically pure crystal were found to be of the same magnitude as the difference in the experimental enthalpy change at $T = 0$ K. This indicates that molecular prediction programs, based on molecular mechanics, require the modelling of conformationally flexible molecules. Chapter two discussed of the calculations performed by Li *et al.*,(72) which are molecular mechanical calculations involving rigid molecules. Reutzel-Edens *et al.*(212) recently calculated deformation energies by *ab initio* methods and the crystal energies by molecular mechanical methods. This is in agreement with the findings and future work outline here for flexible molecules, *i.e.*, higher molecular conformation energies can be adopted in lower energy crystals. It is my opinion that future molecular crystal programs will take the approach of Reutzel-Edens *et al.*(212) Work in this area is being pursued by Professor L. Lu at the University of Wisconsin and Professor M. D. Ward at the University of Minnesota.

As a final note, Sørenson and Larsen(306) have recently evaluated the hydrogen bonding of racemic versus optically pure mono-carboxylic acids with no other functional groups. These authors point out that studies of racemic and optically pure crystals provide the opportunity to investigate intermolecular interactions, because building units are the same. Therefore, there is no requirement of lattice energies obtained through enthalpies of sublimation. In terms of comparing and calibrating molecular mechanical potentials, both X-ray structures and the calculations similar to those performed in this thesis are necessary. Therefore, the theoretical and experimental studies are complementary. In this way, the calculation of the energy changes for forming a racemic crystal from a conglomerate using estimated values for $\Delta_{\mathrm{fus}}C_p$ can provide more robust interpretations of theoretical explorations.

8.4 Final comment

The quote at the beginning of this Chapter is interesting, especially because of the date. Perhaps, if conglomerate crystals were more common, Pasteur's discoveries would have been explored earlier. The real situation is not that straightforward and 150 years after Pasteur's comment, advances in understanding physical stereochemistry are still being made. It is my hope that this thesis has made some progress towards understanding the thermodynamic aspects of racemic and conglomerate enantiomeric crystals.

A The full Schröder-van Laar equation and an extended Prigogine and Defay equation

From equation 2.12 the chemical potential, μ_i, can be calculated at any temperature by using the heat capacity and the chemical potential for the pure species ($\mu_i = H_i^R - TS_i^R$) at $T = T_{\text{fus}}^R$ and $p = p_{\text{fus}}^R$.

$$\begin{aligned}\mu_i &= H_i^R - TS_i^R + \int_{T_{\text{fus}}^R}^{T} C_{p,i}^R \mathrm{d}T - T\int_{T_{\text{fus}}^R}^{T} \frac{C_{p,i}^R}{T}\mathrm{d}T \\ &= H_i^R - TS_i^R + C_{p,i}^R\left(T + T\ln\frac{T_{fus}^R}{T} - T_{\text{fus}}^R\right).\end{aligned} \tag{A.1}$$

Here the heat capacity, $C_{p,i}^R$, is assumed constant over a small change in temperature. Dividing by T and differentiating the function yields

$$\left[\frac{\partial \mu_i/T}{\partial T}\right]_{p,n_{j\neq i}} = -\frac{H_i^R}{T^2} + C_{p,i}^R\left(\frac{1}{T} + \frac{T_{\text{fus}}^R}{T^2}\right). \tag{A.2}$$

If the heat capacity is assumed negligible, equation A.2 is equivalent to equation 2.13.

In Chapter two, equation 2.18 equated the chemical potential of a mechanical mixture (solid) in equilibrium with an ideal mixture (liquid). Using the derivative relationships of equation A.2 and equation 2.14 the full derivative of equation 2.18 can be written,

$$\begin{aligned}&\left[-\frac{H^R(cr)}{T^2} + C_p^R(cr)\left(\frac{1}{T} + \frac{T_{\text{fus}}^R}{T^2}\right)\right]\delta T + \frac{V^R(cr)}{T}\delta p \\ &= \left[-\frac{H^R(l)}{T^2} + C_p^R(l)\left(\frac{1}{T} + \frac{T_{fus}^R}{T^2}\right)\right]\delta T + \frac{V^R(l)}{T}\delta p + R\delta\ln x_R,\end{aligned} \tag{A.3}$$

where the liquid and crystal volumes for the pure species, $V^R(l)$ and $V^R(cr)$, are assumed to be constant over a small temperature and pressure range.

The enthalpies, heat capacities and volumes in equation A.3 have been defined at a standard fusion temperature and pressure for the pure species. Therefore, one can substitute the fusion values $\Delta_{\text{fus}}H^R = H^R(l) - H^R(cr)$, $\Delta_{\text{fus}}C_p^{\,R} = C_p^{\,R}(l) - C_p^{\,R}(cr)$ and $\Delta_{\text{fus}}V^R = V^R(l) - V^R(cr)$ into equation A.3 and solve for any change in fusion temperature and fusion pressure from the standard values defined above:

$$\ln x_R = \frac{1}{R}\int_{T_{\text{fus}}^R}^{T_{\text{fus}}} \frac{\Delta_{\text{fus}}H^R}{T^2} - \Delta_{\text{fus}}C_p^R\left(\frac{T_{\text{fus}}^R}{T^2} + \frac{1}{T}\right)\mathrm{d}T - \frac{1}{RT}\int_{p_{\text{fus}}^R}^{p_{\text{fus}}} \Delta_{\text{fus}}V\mathrm{d}p\,. \tag{A.4}$$

Now,

$$\begin{aligned}\ln x_R = {} & \frac{\Delta_{\text{fus}}H^R}{R}\left(\frac{1}{T_{\text{fus}}^R} - \frac{1}{T_{\text{fus}}}\right) + \frac{\Delta_{\text{fus}}C_p^R}{R}\left(\ln\frac{T_{\text{fus}}^R}{T_{\text{fus}}} + 1 - \frac{T_{\text{fus}}^R}{T_{\text{fus}}}\right) \\ & + \frac{\Delta_{\text{fus}}V}{RT}\left(p_{\text{fus}}^R - p_{\text{fus}}\right),\end{aligned} \tag{A.5}$$

where T_{fus} and p_{fus} are the new equilibrium temperature and pressure of fusion. Equation A.5 is the full Schröder-van Laar equation.

The same derivation is done for the extended Prigogine and Defay equation, except $\delta\ln x_R$ is replaced with $(\delta\ln x_R(1-x_R))/2$ and the integration is from $x_R = 0.5$ to 0:

$$\begin{aligned}\ln 4x_R(1-x_R) = {} & \frac{2\Delta_{\text{fus}}H^R}{R}\left(\frac{1}{T_{\text{fus}}^R} - \frac{1}{T_{\text{fus}}}\right) + \frac{2\Delta_{\text{fus}}C_p^R}{R}\left(\ln\frac{T_{\text{fus}}^R}{T_{\text{fus}}} + 1 - \frac{T_{\text{fus}}^R}{T_{\text{fus}}}\right) \\ & + \frac{2\Delta_{\text{fus}}V}{RT}\left(p_{\text{fus}}^R - p_{\text{fus}}\right)\end{aligned} \tag{A.6}$$

B Lists of chemical names and cross references to CA information

Various compilations of properties are used throughout the thesis, where the molecular name corresponds to the name used by the authors of the referenced study. This was done this way because several of these names are shorter and more recognisable, *e.g.*, mandelic acid. All these names were combined into a database for this thesis. To aid a reader or perhaps follow-up investigations which will require further literature searching, these names are given with cross-references to the Chemical Cbstract names, denoted as CA. Table B.1 shows the molecular names used in the thesis with the name used by the Chemical Abstracts nomenclature and the page number of the thesis where properties of the compound are cited.

Table B.1 Chemical names cited listed with Chemical Abstract, CA, nomenclature.

Name used in cited literature	Name used by CA	Page(s)
acenaphthene	1,2-dihydroacenaphthylene	100
alprenolol	1-[(1-methylethyl)amino]-3-[2-(2-propenyl)phenoxy]-2-propanol	120
amylmercaptan	1-pentanethiol	100,112
anthracene	anthracene	98,100,112
atenolol	4-[2-hydroxy-3-[(1-methylethyl)amino]propoxy]benzeneacetamide	120
benzene	benzene	59
benzyl alcohol	benzenemethanol	100,112
benzylidenecamphor	1,7,7-trimethyl-3-(phenylmethylene)bicyclo[2.2.1]heptan-2-one	121
bevantolol	1-[[2-(3,4-dimethoxyphenyl)ethyl]amino]-3-(3-methylphenoxy)-2-propanol	121
biphenyl	1,1'-Biphenyl	100,112
bromobenzene	bromobenzene	74
m-bromomandelic acid	3-bromo-α-hydroxybenzeneacetic acid	119
o-bromomandelic acid	2-bromo-α-hydroxybenzeneacetic acid	128-
p-bromomandelic acid	4-bromo-α-hydroxybenzeneacetic acid	119
1-bromo-octane	1-bromo-octane	100,112
2-(*p*-bromophenoxy)propionic acid	2-(4-bromophenoxy)propanoic acid	119
3-(*m*-bromophenyl)hydracrylic acid	3-bromo-β-hydroxybenzenepropanoic acid	119
3-(*o*-bromophenyl)hydracrylic acid	2-bromo-β-hydroxybenzenepropanoic acid	119
butanone	2-butanone	74
trans-2-butene	(2E)-2-butene	74
butyl-*p*-aminobenzoate	butyl ester 4-aminobenzoic acid	100,112
t-butylmercaptan	2-methyl-2-propanethiol	100,112
1-butyl-2'6'-pipecoloxylidide (bupivicaine)	1-butyl-N-(2,6-dimethylphenyl)-2-piperidinecarboxamide	118
carvone	2-methyl-5-(1-methylethenyl)-2-cyclohexen-1-one	34,35
m-chloromandelic acid	3-chloro-α-hydroxybenzeneacetic acid	119
o-chloromandelic acid	2-chloro-α-hydroxybenzeneacetic acid	12-
p-chloromandelic acid	4-chloro-α-hydroxybenzeneacetic acid	119
2-(2-chloro-3-methylphenoxy)propionic acid	2-(2-chloro-3-methylphenoxy)propanoic acid	119
2-(*m*-chlorophenoxy)propionic acid	2-(3-chlorophenoxy)propanoic acid	119

continued...

Table B.1 continued

Name used in cited literature	Name used by CA	Page(s)
2-(*o*-chlorophenoxy)propionic acid	2-(2-chlorophenoxy)propanoic acid	119
3-(*m*-chlorophenyl)hydracrylic acid	3-chloro-β-hydroxy-benzenepropanoic acid	119,129,130
3-(*o*-chlorophenyl)hydracrylic acid	2-chloro-β-hydroxybenzenepropanoic acid	119,127,129
3-(*p*-chlorophenyl)hydracrylic acid	4-chloro-β-hydroxy-benzenepropanoic acid	127,129
chlorotrifluoroethene	chlorotrifluoroethene	100,112
cis-sobrerol	*rel*-(1*R*,5*R*)-5-hydroxy-α,α,4-trimethyl-3-cyclohexene-1-methanol	120
cyclohexylbenzene	cyclohexylbenzene	100,112
dibenzothiophene	dibenzothiophene	
trans-1,2-dibromoacenaphthene	1,2-dibromo-1,2-dihydroacenaphthylene	120
trans-1,2-dichloroacenaphthene	*trans*-1,2-dichloro-1,2-dihydroacenaphthylene	120
1,5-dichloro-11,12-di(hydroxymethyl)-9,10-dihydro-9,10-ethanoanthracene *trans* (*exo*)	(9αS*,10αS*,11R*,12R*)-1,5-dichloro-9,10-dihydro-11,12-dimethanol- 9,10-ethanoanthracene	121
1,5-dichloro-11,12-di(hydroxymethyl)-9,10-dihydro-9,10-ethanoanthracene *trans* (*endo*)	(9αR*,10αR*,11R*,12R*)-1,5-dichloro-9,10-dihydro-11,12-dimethanol- 9,10-ethanoanthracene	121
1,5-dichloro-9,10-dihydro-9,10-ethano-11,12-dicarbomethoxyanthracene (*exo*)	(9αS*,10αS*,11R*,12R*)-dimethyl ester 1,5-dichloro-9,10-dihydro-9,10-ethanoanthracene-11,12-dicarboxylic acid	120
1,5-dichloro-9,10-dihydro-9,10-ethano-11,12-dicarbomethoxyanthracene (*endo*)	(9αR*,10αR*,11R*,12R*)-dimethyl ester 1,5-dichloro-9,10-dihydro-9,10-ethanoanthracene-11,12-dicarboxylic acid	120
1,5-dichloro-9,10-ethanoanthracene	1,5-dichloro-9,10-dihydro-9,10-ethanoanthracene	120
9,10-dihydro-9,10-ethano-11,12-dicarbomethoxyanthracene (*exo*)	*rel*-(11*R*,12*R*)-dimethyl ester 9,10-dihydro-9,10-ethanoanthracene-11,12-dicarboxylic acid	120
11,12-di(hydroxymethyl)-9,10-dihydro-9,10-ethanoanthracene	(11*R*,12*R*)-*rel*-9,10-dihydro-9,10-ethanoanthracene-11,12-dimethanol	120
11,12-di(iodomethyl)-9,10-dihydro-9,10-ethanoanthracene	*trans*-9,10-dihydro-11,12-bis(iodomethyl)-9,10-ethanoanthracene	120
dimethylamine	N-methylmethanamine	100,112
dimethyl-O,O'-dibenzoyltartarate	(R*,R*)-dimethyl ester 2,3-bis(benzoyloxy)-butanedioic acid	121
dimethyl-O,O'-diacetyltartarate	(R*,R*)-dimethyl ester 2,3-bis(acetyloxy)butanedioic acid	120
9,10-dimethyl-9,10-dihydro-9,10-ethano-11,12-dicarbomethoxyanthracene (*exo*)	*trans*-dimethyl ester 9,10-dihydro-9,10-dimethyl-9,10-ethanoanthracene-11,12-dicarboxylic acid	121
1,1-dimethylhydrazine	1,1-dimethylhydrazine	100,112
2,2-dimethylpentane	2,2-dimethylpentane	100,112

continued...

Table B.1 continued

Name used in cited literature	Name used by CA	Page(s)
diphenyl ether	1,1'-oxybisbenzene	100,112
ephedrine	(α*S*)-*rel*-α-[(1*R*)-1-(methylamino)ethyl]benzenemethanol	122,136
ephedrine·HCl	*rel*-(α*S*)-α-[(1*R*)-1-(methylamino)ethyl]benzenemethanol hydrochloride	122
ethylacetate	ethyl ester acetic acid	74,100,112
ethylbenzene	ethylbenzene	100,112
ethyl-*p*-aminobenzoate	ethyl ester 4-aminobenzoic acid	100,112
2-ethylpentane	3-methylhexane	100,112
1-ethyl-2'6'-pipecoloxylidide (ethycaine)	N-(2,6-dimethylphenyl)-1-ethyl-2-piperidinecarboxamide	118
fechone	1,3,3-trimethylbicyclo[2.2.1]heptan-2-one	34
fluorene	fluorene	98,100,112
octafluorocyclobutane	octafluorocyclobutane	74
1,1-difluoroethane	1,1-difluoroethane	74
m-fluoromandelic acid	3-fluoro-α-hydroxybenzeneacetic acid	112,119,127
o-fluoromandelic acid	2-fluoro-α-hydroxybenzeneacetic acid	12-290
p-fluoromandelic acid	4-fluoro-α-hydroxybenzeneacetic acid	127
3-(*m*-fluorophenyl)hydracrylic acid	3-fluoro-β-hydroxybenzenepropanoic acid	127
3-(*o*-fluorophenyl)hydracrylic acid	2-fluoro-β-hydroxybenzenepropanoic acid	127
3-(*p*-fluorophenyl)hydracrylic acid	4-fluoro-β-hydroxybenzenepropanoic acid	39,112,119
furan	furan	100,112
glycerol acetonide	2,2-dimethyl-1,3-dioxolane-4-methanol	34
glycine	glycine	3
n-heptane	heptane	74
hexane	hexane	80,100,112
hexyl-*p*-aminobenzoate	hexyl ester 4-aminobenzoic acid	100,112
3-hydroxy-3-phenylbutyric acid	β-hydroxy-β-methylbenzenepropanoic acid	119
3-hydroxy-3-phenylpivalic acid	β-hydroxy-α,α-dimethylbenzenepropanoic acid	120
3-hydroxy-3-phenylvaleric acid	β-ethyl-β-hydroxybenzenepropanoic acid	120
ibuprofen	α-methyl-4-(2-methylpropyl)benzeneacetic acid	120

Continued…

Table B.1 continued.

Name used in cited literature	Name used by CA	Page(s)
1-indanol	2,3-dihydro-1H-inden-1-ol	
iopanoic acid	3-amino-α-ethyl-2,4,6-triiodobenzenepropanoic acid	122
isopropylmercaptan	2-propanethiol	100,112
limonene	1-methyl-4-(1-methylethenyl)cyclohexene	34,35
malic acid	hydroxybutanedioic acid	38,119
mandelic acid	α-hydroxybenzeneacetic acid	39
methane	methane	59
methylamine	methanamine	100,112
methyl-*p*-aminobenzoate	4-aminomethylesterbenzoic acid	100,112
α-methylbenzylamine	α-methylbenzenemethanamine	34
N,N'-*bis*-α-methylbenzylthiourea	1,3-bis(α-methylbenzyl)-2-thiourea	121
2-methyl-1,3-butadiene	2-methyl-1,3-butadiene	74
2,2,3-trimethylbutane	2,2,3-trimethylbutane	74
2-methyl-2-butanethiol	2-methyl-2-butanethiol	74
3,3-dimethyl-1-butene	3,3-dimethyl-1-butene	74
cis-1,3-dimethylcyclopentane	(1*R*,3*S*)-*rel*-1,3-dimethylcyclopentane	74
1-methyl-4-ethylbenzene	1-ethyl-4-methylbenzene	74
di-(methylethyl)ether	2,2'-oxybispropane	74
α-methyl-α-ethylsuccinic acid	2-ethyl-2-methylbutanedioic acid	34
methyllactate	methyl ester 2-hydroxy-propanoic acid	34
2-methylhexane	2-methylhexane	100,112
α-methyl-α-isopropylsuccinic acid	2-methyl-2-(1-methylethyl)butanedioic acid	34
1-methylnaphthalene	1-methylnaphthalene	74,98,100,112
2-methylnaphthalene	2-methylnaphthalene	74,98,100,112
methylnitrate	methyl ester nitric acid	100,112
4-methylphenol	4-methylphenol	74
1-methyl-2'6'-pipecoloxylidide (mepivicaine)	N-(2,6-dimethylphenyl)-1-methyl-2-piperidinecarboxamide	118
3-methylpyridine	3-methylpyridine	74
α-methylsuccinic acid	methylbutanedioic acid	8
3-methylthiophene	3-methylthiophene	73,74
naphthalene	naphthalene	98,100,112
2-(1-naphthyl)propionic acid	α-methyl-1-naphthaleneacetic acid	120

continued...

Table B.1 continued

Name used in cited literature	Name used by CA	Page(s)
2-nitrobutane	2-nitrobutane	74
2-(1-nitro-2-naphthoxy)propionamide	2-[(1-nitro-2-naphthalenyl)oxy]propanamide	120
2-(*p*-nitrophenoxy)propionic acid	2-(4-nitrophenoxy)propanoic acid	119
2-*p*-nitrophenylbutane	1-(1-methylpropyl)-4-nitrobenzene	34
nonyl-*p*-aminobenzoate	nonyl ester 4-aminobenzoic acid	100,112
norephedrine	*rel*-(α*S*)-α-[(1*R*)-1-aminoethyl]-benzenemethanol	119
norephedrine salicylate	2-hydroxybenzoic acid compd. with α-(1-aminoethyl)benzenemethanol (1:1)	119
norephedrine·HCl	*rel*-(α*S*)-α-[(1*R*)-1-aminoethyl]-benzenemethanol hydrochloride	120
octane	octane	100,112
2-octanol	2-octanol	34,35
1,4-dioxane	1,4-dioxane	74
pentyl-*p*-aminobenzoate	pentyl ester 4-aminobenzoic acid	100,112
2-pentyne	2-pentyne	74
phenanthrene	phenanthrene	98,100,112
2-phenoxypropionic acid	2-phenoxypropanoic acid	119
erthyro-phenylglyceric acid	α,β-dihydroxybenzenepropanoic acid	39
3-phenylhydracrylic acid	β-hydroxybenzenepropanoic acid	117-129
α-pinene	2,6,6-trimethylbicyclo[3.1.1]hept-2-ene	34
pindolol	1-(1H-indol-4-yloxy)-3-[(1-methylethyl)amino]-2-propanol	120
2'6'-pipecoloxylidide	N-(2,6-dimethylphenyl)-2-piperidinecarboxamide	118
piperidine	piperidine	58
propane	propane	74
1,2-propanediol	1,2-propanediol	34
propanenitrile	propanenitrile	73,74
propranolol	1-[(1-methylethyl)amino]-3-(1-naphthalenyloxy)-2-propanol	121
propranolol·HCl	1-[(1-methylethyl)amino]-3-(1-naphthalenyloxy)-2-propanol hydrochloride	121
propyl-*p*-aminobenzoate	propylester -4-aminobenzoic acid	100,112
propylbenzene	propylbenzene	100,112
1-propyl-2'6'-pipecoloxylidide (ropivicane)	N-(2,6-dimethylphenyl)-1-propyl-2-piperidinecarboxamide	118

continued...

Table B.1 continued

Name used in cited literature	Name used by CA	Page(s)
pseudoephedrine	(α*R*)-*rel*-α-[(1*R*)-1-(methylamino)ethyl]benzenemethanol	120
pseudoephedrine·HCl	*rel*-(α*R*)-α-[(1*R*)-1-(methylamino)ethyl]benzenemethanol hydrochloride	120
quartz	quartz	2,3,182
o-quinone	3,5-cyclohexadiene-1,2-dione	3
razoxane	4,4'-(1-methyl-1,2-ethanediyl)bis-2,6-Piperazinedione	120
trans-sobrerol	*rel*-(1*R*,5*S*)-5-hydroxy-α,α,4-trimethyl-3-cyclohexene-1-methanol	120
sulpiride	5-(aminosulfonyl)-N-[(1-ethyl-2-pyrrolidinyl)methyl]-2-methoxybenzamide	120
tartaric acid	2,3-dihydroxybutanedioic acid	2
tazofelone	5-[[3,5-bis(1,1-dimethylethyl)-4-hydroxyphenyl]methyl]- 4-thiazolidinone	121
1-thiahexane	1-(methylthio)butane	74
4,5-dithiaoctane	dipropyldisulfide	74
threonine	2-amino-3-hydroxybutanoic acid	34
toluene	methylbenzene	59,100,112
trichloroethene	trichloroethene	74
trimethylamine	N,N-dimethylmethanamine	59,74,100,112
1,2,3-trimethylbenzene	1,2,3-trimethylbenzene	59,100,112
1,2,4-trimethylbenzene	1,2,4-trimethylbenzene	59,100,112
1,3,5-trimethylbenzene	1,3,5-trimethylbenzene	59,100,112
triphenylmethane	1,1',1''-methylidynetrisbenzene	100,112
2,3,3-triphenylvaleric acid	β-ethyl-α,β-diphenyl-benzenepropanoic acid	121
o-tyrosine	2-hydroxyphenylalanine	8
m-xylene	1,3-dimethylbenzene	100,112
o-xylene	1,2-dimethylbenzene	100,112
p-xylene	1,4-dimethylbenzene	100,112

References

1. D. P. Craig and D. P. Mellor, *Top. Curr. Chem.* **63**, 1 (1976).
2. S. Kotha, *Tetrahedron* **50**, 3639 (1994).
3. J. Jacques, A. Collet and S. H. Wilen, *Enantiomers, racemates and resolutions*, Krieger Publishing Co. Malabar, Florida (1994).
4. R. Stosch, M. M. Welzel, S. Bauerecker and H. K. Cammenga, *Mol. Cryst. Liq. Cryst.* **312**, 285 (1998).
5. C. Fouquey and M. Leclercq, *Tetrahedron* **26**, 5637 (1970).
6. J. Madarász, D. Kozma, G. Pokol, M. Ács and E. Fogassy, *J. Therm. Anal.* **42**, 877 (1994).
7. H. K. Cammenga and M. Epple, *Angew. Chem. Ed. Engl.* **34**, 1171 (1995).
8. W. J. Sichina, *Am. Lab.* **33**, 16 (2001).
9. Z. Böcskei, C. Kassai, K. Simon, E. Fogassy and D. Kozma, *J. Chem. Soc. Perkin Trans. II* 1511 (1996).
10. S. Druot, M. N. Petit, S. Petit, G. Coquerel and N. B. Chanh, *Mol. Cryst. Liq. Cryst.* **275**, 271 (1996).
11. R. J. Prankerd and M. Z. Elsabee, *Thermochimica Acta* **248**, 147 (1995).
12. S. Houllemare-Druot and G. Coquerel, *J. Chem. Soc. Perkin Trans. II*, 2211 (1998).
13. L. Pasteur, *Société Chimique de Paris*, *(1860 & 1866)*, Translated reprint, Simpkin, Marshall, Hamilton, Kent & Co. Ltd., London (1905).
14. E. T. Malus, *Mém. Soc. Arceuil* **2**, 143 (1809).
15. D. F. J. Arago, *Mém. Inst. France Pt. 1*, 93 (1811).
16. J. B. Biot, *Mém. Inst. France Pt. 1*, 1 (1812).
17. S. F. Mason, *Molecular optical activity and the chiral discriminations*, Cambridge university press, London (1982).
18. J. B. Biot, *Mém. Acad. Sci. France* **15**, 93 (1838).
19. L. Pasteur, *Compt. Rend. Acad. Sci. Paris* **26**, 535 (1848).

20. Lord Kelvin, *Baltimore lectures (1884) on molecular dynamics and the wave theory of light*, Clay and Sons, London (1904).

21. T.M. Lowry, *Optical rotatory power*, Dover Publications, New York (1964).

22. E. Juaristi, *Introduction to stereochemistry and conformational analysis*, John Wiley & Sons, Inc., New York (1991).

23. R. S. Cahn, C. Ingold and V. Prelog, *Angew. Chem. Inter. Ed.* **5**, 385 (1966).

24. T. Graham, *Elements of Chemistry*, Bailliere, London (1842).

25. H. W. B. Roozeboom, *Z. Phys. Chem.* **28**, 494 (1899).

26. Z. J. Li and D. J. W. Grant, *J. Pharm. Sci.* **86**, 1073 (1997).

27. R. Kuroda and S. F. Mason, *J. Chem. Soc. Dalton*, 1268 (1981).

28. I. Kuzmenko, I. Weissbuch, E. Gurovich, L. Leiserowitz and M. Lahav, *Chirality* **10**, 415 (1998).

29. M. E. Jungfleisch, *J. Pharm. Chim. 5* ème Série, 346 (1882).

30. B. B. Dowling, U.S. Patent 2,898,358 (International Minerals and Chemical Corp.) C. A. **54**, 17284g (1959).

31. A. Collet, M.-J. Brienne and J. Jacques, *Bull. Soc. Chim. Fr.*, 127 (1972).

32. S. H. Wilen, A. Collet and J. Jacques, *Tetrahedron* **33**, 2725 (1977).

33. H. Nohira, M. Kai, M. Nohira, J. Nishikawa, T. Hoshiko and K. Saigo, *Chem. Lett., Chem. Soc. Japan.*, 951 (1981)

34. S. Kotha, *Tetrahedron* **50**, 3639 (1994).

35. A. Scacchi, *Atti Accad. Sci. Napoli* **4**, 250 (1865)

36. H. Suh, K. H. Park, W. P. Jensen and D. E. Lewis, *J. Chem. Ed.* **74**, 800 (1997).

37. I. Szelenyi, G. Geisslinger, E. Polymeropoulos, W. Paul, M. Herbst and K. Brune, *Drug News Perspect.* **11**, 139 (1998).

38. H. Chun, S. S. Massoud, R. Wen and I. Bernal, *Polyhedron* **18**, 3647 (1999).

39. J. K. Whitesell, R. E. Davis, M.-S. Wong and N.-L. Chang, *J. Am. Chem. Soc.* **116**, 523 (1994).

40. I Schröder, *Z. Phys. Chem.* **11**, 449 (1893).

41. J. J. van Laar, *Arch. Neerl.II* **8**, 264 (1903).

42. M. Kuhnert-Brandstätter and L. Friedl, *Mikrochimica Acta II*, 507 (1977).

43. J. P. Mathieu, *J. Raman Spectrosc.* **1**, 47 (1973).

44. J. E. Anderson and W. P. Slichter, *J. Chem. Phys.* **41**, 1922 (1964).

45. B. Chion, J. Lajzerowicz, D. Bordeaux, A. Collet and J. Jacques, *J. Phys. Chem.* **82**, 2682 (1978).

46. P. Horvath, A. Gergely and B. Noszal, *Talanta* **44**, 1479 (1997).

47. A. Collet, *Problems and wonders of chiral molecules*. Ed. M. Simonyi, 91-123, Akadémiai Kiadó, Budapest (1990).

48. C. P. Brock and J. D. Dunitz, *Mol. Cryst. Liq. Cryst.* **242**, 61 (1994).

49. I. Prigogine and R. Defay, *Chemical thermodynamics*, Translated by D. H. Everett, Longmans, Green and Co. Ltd., London (1965).

50. E. Mitscherlich, *Comt. Rend. Acad. Sci. Paris* **19**, 719 (1844).

51. C. P. Brock, W. B. Schweizer and J. D. Dunitz, *J. Am. Chem. Soc.* **113**, 9811 (1991).

52. E. Mitscherlich, *Abhandlungen Akad. Wiss., Berlin*, 427 (1819).

53. R. M. Roberts, *Serendipity, accidental discoveries in science*, John Wiley & Sons, Inc., New York (1989).

54. O. Wallach, *Liebigs Ann. Chem.* **286**, 90 (1895).

55. J. D. Roberts and M. C. Caserio, *Basic principles of organic chemistry*, Benjamin, New York (1964).

56. E. L. Eliel, *Stereochemistry of carbon compounds*, McGraw-Hill, New York (1962).

57. H. A. J. Oonk, *Phase theory: The thermodynamics of heterogeneous equilibria*, Elsevier Science Publishing Co. Ltd., New York (1981).

58. A. I. Kitaigorodskii, *Physical chemistry, Vol 29: Molecular crystals and molecules*, Academic Press, New York (1973).

59. K Marthi, S. Larsen, M. Ács, J. Balint and E. Fogassy, *Acta Cryst.* **B50**, 762 (1994).

60. C. Pedone and E. Benedetti, *Acta Cryst.* **B28**, 1970 (1972).

61. M. C. Perucaud, J. Canceill and J. Jaques, *Bull. Soc. Chim. Fr.*, 1011 (1974).

62. A. Gavezzotti, *Acc. Chem. Res.* **27**, 309 (1994).

63. A. Gavezzotti, *J. Chem. Soc. Perkin Trans II*, 1399 (1995).

64. G. Filippini and A. Gavezzotti, *Acta. Cryst.* **B49**, 868 (1993).

65. S. Coe, J. J. Kane, T. L. Nguyen, L. M. Toledo, E. Wininger, F. W. Fowler and J. W. Lauher, *J. Am. Chem. Soc.* **119**, 86 (1997).

66. S. Larsen and K. Marthi, *Acta Cryst.* **B51**, 338 (1995).

67. R. S. Berry, S. A. Rice and J. Ross, *Physical Chemistry 2nd Ed.*, Oxford University Press, New York (2000).

68. A. D. Buckingham, *Disc. of the Faraday Soc.* **40**, 232 (1965).

69. A. Gavezzotti and G. Filippini, *J. Phys. Chem.* **98**, 4831 (1994).

70. B. P. van Eijck and J. Kroon, *J. Comput. Chem.* **20**, 799 (1999).

71. H. R. Karfunkel and R. J. Gdantiz, *J. Comput. Chem.* **13**, 1171 (1992).

72. Z. J. Li, W. H. Ojala and D. J. W. Grant, *J. Pharm. Sci.* **90**, 1523 (2001).

73. M. J. Vlot, J. C. van Miltenburg, H. A. J. Oonk and J. P. van der Eerden, *J. Chem. Phys.* **107**, 10102 (1997).

74. M. J. Vlot, S. Claassen, H. E. A. Huitema and J. P. Van der Eerden, *Mol. Phys.* **91**, 19 (1997).

75. J. D. Dunitz, *Acta Cryst.* **B51**, 619 (1995).

76. G. M. Anderson and D. Q. Crerar, *Thermodynamics in geochemistry: The equilibrium model*, Oxford University Press, New York (1993).

77. S. Takagi, R. Fujishiro and K. Amaya, *J. Chem. Soc. Chem. Comm.*, 480 (1968).

78. T. Kimura, T. Ozaki and S. Takagi, *Chirality* **10**, 722 (1998).

79. T. Kimura, T. Ozaki and S. Takagi, *Enantiomer.* **6**, 5 (2001).

80. J. P. Guetté, D. Boucherot and A. Horeau, *Tetrahedron Lett.*, 465 (1973).

81. A. Horeau and J. P. Guetté, *Tetrahedron* **30**, 1923 (1974).

82. Z. Atik, M. B. Ewing and M. L. McGlashan, *J. Chem. Thermodyn.* **15**, 159 (1983).

---

83. L. Lepori, M. Mengheri and V. Mollica, *J. Phys. Chem.* **87**, 3520 (1983).

84. Z. Atik, M. B. Ewing and M. L. McGlashan, *J. Phys. Chem.* **85**, 3300 (1981).

85. M. Leclercq, A. Collet and J. Jacques, *Tetrahedron* **32**, 821 (1976).

86. K. Pettersson, *Ark. Kemi* **9**, 509 (1956).

87. J. Timmermans and M. Vesselovsky, *Bull. Soc. Chim. Belg.* **41**, 53 (1932).

88. A. Fredga and M. Matell, *Ark. Kemi* **3**, 429 (1951).

89. A. Collet and F. Vigné-Maeder, *New J. Chem.* **19**, 877 (1995).

90. K. Pettersson, *Ark. Kemi* **10**, 297 (1956).

91. S. H. Neau and G. L. Flynn, *Pharm. Res.* **7**, 1157 (1990).

92. J. H. Hildebrand, J. M. Prausnitz and R. L. Scott, *Regular and related solutions*, Van Nostrand Reinhold, New York (1970).

93. S. W. Benson and J. H. Buss, *J. Chem. Phys.* **29**, 546 (1958).

94. S. W. Benson, F. R. Cruickshank, D. M. Golden, G. R. Haugen, H. E. O'Neal, A. S. Rodgers, R. Shaw and R. Walsh, *Chem. Rev.* **69**, 279 (1969).

95. R. C. Reid, J. M. Prausnitz and B. E. Poling, *The properties of gases and liquids* 4th Ed., McGraw-Hill Inc., New York (1987).

96. S. W. Benson, *Thermochemical kinetics*, chapter2, Wiley, New York (1968).

97. B. E. Poling and J. M. Prausnitz, *The properties of gases and liquids* 5th Ed., McGraw-Hill Inc., New York (2001).

98. K. G. Joback and R. C. Reid, *Chem. Eng. Comm.* **57**, 233 (1987).

99. Y. Yoneda, *Bull. Chem. Soc. Japan* **52**, 1297 (1979).

100. T.-P. Thinh and T. K. Trong, *Can. J. Chem. Eng.* **54**, 344 (1976).

101. L. Constantinou and R. Gani, *AIChE J.* **40**, 1697 (1994).

102. K. S. Pitzer and D. W. Scott, *J. Am. Chem. Soc.* **63**, 2419 (1941).

103. K. S. Pitzer, Thermodynamics 3rd Ed., McGraw-Hill, New York (1995).

104. K. S. Pitzer and W. D. Gwinn, *J. Chem. Phys.* **10**, 428 (1942).

---

105. K. S. Pitzer, *J. Chem. Phys.* **14**, 239 (1946).

106. J. E. Kilpatrick and K. S. Pitzer, *J. Chem. Phys.* **17**, 1064 (1949).

107. J. C. M. Li and K. S. Pitzer, *J. Phys. Chem.* **60**, 466 (1956).

108. G. Ercolani, *J. Chem. Ed.* **77**, 1495 (2000).

109. Y.-Y. Chuang and D. G. Truhlar, *J. Chem. Phys.* **112**, 1221 (2000).

110. V. Hnizdo, A. Fedorowicz, H. Singh and E. Demchuk, *J. Comp. Chem.* **24**, 1172 (2003).

111. M. Mammen, E. I. Shakhnovich and G. M. Whitesides, *J. Org. Chem.* **63**, 3168 (1998).

112. D. Vedal, O. H. Ellestad, P. Klaboe and G. Hagen, *Spectrochimica Acta* **32A**, 877 (1976).

113. I. A. Hossenlopp and D. G. Archer, *J. Chem. Thermodyn.* **20**, 1061 (1988).

114. M. Karni, I. Oref and A. Burcat, *J. Phys. Chem. Ref. Data* **20**, 665 (1991).

115. O. Dorofeeva, V. P. Novikov and D. B. Neumann, *J. Phys. Chem. Ref. Data* **30**, 475 (2001).

116. T. Yamada, T. H. Lay and J. W. Bozzelli, *J. Phys. Chem. A* **102**, 7286 (1998).

117. P. Vansteenkiste, V. Van Speybroeck, G. B. Marin and M. Waroquier, *J. Phys. Chem A* **107**, 3139 (2003).

118. M. J. Frisch, G. W. Trucks, H. B. Schlegel, G. E. Scuseria, M. A. Robb, J. R. Cheeseman, V. G. Zakrzewski, J. A. Montgomery, Jr., R. E. Stratmann, J. C. Burant, S. Dapprich, J. M. Millam, A. D. Daniels, K. N. Kudin, M. C. Strain, O. Farkas, J. Tomasi, V. Barone, M. Cossi, R. Cammi, B. Mennucci, C. Pomelli, C. Adamo, S. Clifford, J. Ochterski, G. A. Petersson, P. Y. Ayala, Q. Cui, K. Morokuma, P. Salvador, J. J. Dannenberg, D. K. Malick, A. D. Rabuck, K. Raghavachari, J. B. Foresman, J. Cioslowski, J. V. Ortiz, A. G. Baboul, B. B. Stefanov, G. Liu, A. Liashenko, P. Piskorz, I. Komaromi, R. Gomperts, R. L. Martin, D. J. Fox, T. Keith, M. A. Al-Laham, C. Y. Peng, A. Nanayakkara, M. Challacombe, P. M. W. Gill, B. Johnson, W. Chen, M. W. Wong, J. L. Andres, C. Gonzalez, M. Head-Gordon, E. S. Replogle, and J. A. Pople, *Gaussian 98 (Revision A.11.2)*, Gaussian Inc., Pittsburgh, PA (2001).

119. A. P. Scott and L. Radom, *J. Phys. Chem.* **100**, 16502 (1996).

120. M. J. S. Dewar, E. G. Zoebisch, E. F. Healy and J. J. P. Stewart, *J. Amer. Chem. Soc.* **107**, 3902 (1985).

---

121. A. D. Becke, *J. Chem. Phys.* **98**, 5648 (1993).

122. A. D. Becke, *Phys. Rev. A* **38**, 3098 (1988).

123. C. Lee, W. Yang and R. G. Parr, *Phys. Rev. B* **37**, 785 (1988).

124. C. Moller and M. S. Plesset, *Phys. Rev.* **46**, 618 (1934).

125. J. P. Perdew, *Phys. Rev. B* **33**, 8822 (1986).

126. J. J. P. Stewart, *J. Comp. Chem.* **10**, 209 (1989).

127. J. P. Perdew, *Electronic Structure of Solids '91*, Ed. P. Ziesche and H. Eschrig, Akademie Verlag, Berlin (1991).

128. J. A. Pople, M. Head-Gordon and K. Raghavachari, *J. Chem. Phys.* **87**, 5968 (1987).

129. *CHETAH^{TM} Version 7.2: The ASTM computer program for chemical thermodynamic and energy release evaluation (NIST special data base 16), 4th ed.*, American society for testing and materials, West Conshohocken, PA (1998).

130. K. G. Joback, *A unified approach to physical property estimation using multivariate statistical techniques*, S. M. Thesis, Dept. Chem. Eng., Massachusetts institute of technology, Cambridge, MA (1984).

131. *NIST Chemistry WebBook*, http://webbook.nist.gov/., accessed on February 2 (2004).

132. K. S. Pitzer, *J. Chem. Phys.* **12**, 310 (1944).

133. J. D. Kemp and C. J. Egan, *J. Am. Chem. Soc.* **60**, 1521 (1938).

134. G. Wesenberg and F. Weinhold, *Int. J. Quantum Chem.* **21**, 487 (1982).

135. G. D. Smith and R. L. Jaffe, *J. Phys. Chem. A* **100**, 18718 (1996).

136. J. P. Guthrie, *J. Phys. Chem. A* **105**, 8495 (2001).

137. G. Katzer and A. F. Sax, *Chem. Phys. Lett.* **368**, 473 (2003).

138. M. A. White, D. C. MacLaren, R. A. Marriott and B.-Z. Zhan, *Can. J. Phys.* **81**, 175 (2003).

139. M. A. White, *Can. J. Chem.* **76**, 1695 (1998).

140. A. R. Ubbelohde, *Melting and crystal structure*, Oxford, London (1965).

141. S. Gracin, T. Brinck and Å. C. Rasmuson, *Ind. Eng. Chem. Res.* **41**, 5114 (2002).

---

142. D. S. Mishra and S. H. Yalkowsky, *Ind. Eng. Chem. Res.* **29**, 2278 (1990).

143. D. S. Mishra and S. H. Yalkowsky, *Pharm. Res.* **9**, 958 (1992).

144. A. Einstein, *Ann. Phys.* **22**, 180 (1907).

145. P. L. Dulong and A. T. Petit, *Ann. Chim. Phys.* **10**, 395 (1819).

146. J. B. Ott and J. Boerio-Goates, *Chemical thermodynamics: principals and applications*, Academic Press, San Diego (2000).

147. T. H. K. Barron and G. K. White, *Heat capacity and thermal expansion at low temperature*, Kluwer, New York (1999).

148. P. Debye, Ann. Phys. **39**, 789 (1912).

149. B. F. Woodfield, J. Boerio-Goates, J. L. Shapiro, R. L. Putnam and A. Navrotsky, *J. Chem. Thermodyn.* **31**, 245 (1999).

150. P. Goursot and E. F. Westrum Jr., *J. Chem. Eng. Data* **13**, 471 (1968).

151. P. Goursot and E. F. Westrum Jr, *J. Chem. Eng. Data* **13**, 468 (1968).

152. P. Goursot and E. F. Westrum Jr., *J. Chem. Eng. Data* **14**, 1 (1969).

153. J. Timmermans (Ed.) *Physico-chemical constants of pure organic compounds, Vol II*, Elsevier, New York (1965).

154. J. Timmermans (Ed.) *Physico-chemical constants of pure organic compounds, Vol I*, Elsevier, New York (1950).

155. Thermodynamics research centre. *Selected properties of hydrocarbons and related compounds*, Hydrocarbon project API 44, Texas A&M University, College Station (1965-1978).

156. J. P. McCullough, H. L. Finke, J. F. Messerly, S. S. Todd, T. C. Kincheloe and G. Waddington, *J. Phys. Chem.* **61**, 1105 (1957).

157. D. F. O'Rourke and S. C. Mraw, *J. Chem. Thermodyn.* **15**, 489 (1983).

158. H. L. Finke, J. F. Messerly, S. H. Lee, A. G. Osborn and D. R. Douslin, *J. Chem. Thermodyn.* **9**, 937 (1977).

159. D. C. Ginnings and G. T. Furukawa, *J. Am. Chem. Soc.* **75**, 522 (1953).

160. P. Goursot, H. L. Girdhar and E. F. Westrum Jr., *J. Phys. Chem.* **74**, 2538 (1970).

161. H. Saint-Martin, B. Hess and H. J. C. Berendsen, *J. Chem. Phys.* **120**, 11133 (2004).

---

162. A. Bondi, *Physical properties of molecular crystals, liquids and glasses*, Wiley, New York (1968).

163. O. K. Rice, *J. Chem. Phys.* **12**, 1 (1944).

164. P. J. Flory, *J. Am. Chem. Soc.* **87**, 1833 (1965).

165. J. Blazejowski, J. Rak and P. Skurski, *J. Therm. Anal.* **45**, 829 (1995).

166. G. Coccotti, D. Frenkel and I. R. McDonald, *Simulations of liquids and solids*, North-Holland, Amsterdam (1987).

167. S. W. Benson and E. D. Siebert, *J. Am. Chem. Soc.* **114**, 4269 (1992).

168. J. L. Dote, D. Kivelson and R. N. Schwartz, *J. Phys. Chem.* **85**, 2169 (1981).

169. C. F. Chueh and A. C Swanson, *Chem. Eng. Progr.* 69, 83 (1973).

170. Y. Maham, L. G. Hepler, A. E. Mather, A. W. Hakin and R. A. Marriott, *J. Chem. Soc., Faraday Trans.* **93**, 1747 (1997).

171. L. Pogliani, *Chem. Rev.* **100**, 3827 (2000).

172. E. Estrada, *J. Phys. Chem.* A **106**, 9085 (2002).

173. D. F. R. Gilson, *J. Chem. Ed.* **69**, 23 (1992).

174. A. Lüttringhaus and G. Vierk, *Ber.* **82**, 376 (1949).

175. J. Pirsch, *Ber.* **70**, 12 (1937).

176. J. Pirsch, *Mikrochimica Acta*, 992 (1956).

177. P. Walden, *Z. Elektrochem.* **14**, 713 (1908).

178. S. H. Yalkowsky, *Ind. Eng. Chem. Fundam.* 18, 108 (1979).

179. F. T. Trouton, *Philos. Mag.* 5th series, **18**, 54 (1884).

180. R. J. C. Brown and R. F. C. Brown, *J. Chem. Ed.* **77**, 724 (2000).

181. T. Carnelley, *Philos. Mag.* 5th series, **13**, 112 (1882).

182. T. Carnelley, *Philos. Mag.* 5th series, **13**, 180 (1882).

183. J. S. Chickos, D. G. Hesse and J. F. Liebman, *J. Org. Chem.* **55**, 3833 (1990).

---

184. J. S. Chickos, C. M. Braton, D. G. Hesse and J. F. Liebman, *J. Org. Chem.* **56**, 927 (1991).

185. Ed. D. R. Lide, *Handbook of chemistry and physics*, 81st edition, CRC press, New York (2000).

186. J. Timmermans, *J. Phys. Chem. Solids* **18**, 1 (1961).

187. R.-M. Dannenfelser, N. Surendran and S. H. Yalkowsky, *SAR and QSAR in Env. Res.* **1**, 273 (1993).

188. R.-M. Dannenfelser and S. H. Yalkowsky, *Ind. Eng. Chem. Res.* **35**, 1483 (1996).

189. G. D. Rockwell, T. B. Grindley, K. C. Smith and M. A. White, *J. Phys. Chem. B* **106**, 12311 (2002).

190. H. N. V. Temperley, *J. Res. Natl. Bur. Std.* **56**, 55 (1956).

191. H. S. Frank, *J. Chem. Phys.* **13**, 478 (1945).

192. M. Tesconi and S. H. Yalkowsky, *Handbook of property estimation methods for chemicals*, Ed R. S. Boethling and D. MacKay 3 (2000).

193. L. Qiu and M. A. White, *J. Chem. Ed.* **78**, 1076 (2001).

194. R. A. Marriott, A. W. Hakin and J. L. Liu, *J. Sol. Chem.* **27**, 771 (1998).

195. J. P. Guthrie, *Can. J. Chem* **55**, 3700 (1977).

196. A. Collet and J. Jacques, *Bull. Soc. Chim. Fr.*, 3330 (1973).

197. A. Collet and J. Jacques, *Bull. Soc. Chim. Fr.*, 3857 (1972).

198. Z. J. Li, M. T. Zell, E. J. Munson and D. J. W. Grant, *J. Pharm. Sci.* **88**, 337 (1999).

199. K. Nemák. M. Áces, D. Kozma and E. Fogassy, *J. Therm. Anal.* **48**, 691 (1997).

200. S. Larsen and K. Marthi, *Acta Cryst.* **B50**, 373 (1994).

201. S. Larsen and K. Marthi, *Acta Cryst.* **B53**, 803 (1997).

202. J. Caldwell, N. Berova, D. W. Armstrong, V. Davankov, A. F. Fell, U. Hacksell, W. Koenig, W. Lindner, Y. Okamoto, W. H. Pirkle, V. Schurig, B. Testa, I. W. Wainer and C. J. Welch, *Chirality* **12**, 1 (2000).

203. F. P. Luduena, *Ann. Rev. Pharmacol.* **9**, 503 (1969).

204. B. F. Tullar, *J. Med. Chem.* **14**, 891 (1971).

---

205. G. Bettinetti, F. Giordano, G. Fronza, A. Italia, R. Pellegata, M. Villa and P. Ventura, *J. Pharm. Sci.* **79**, 470 (1990).

206. D. Pitre, M. De Amici, M. Colombo, G. G. Gallo and M. Nebuloni, *Arch. Pharm.* **325**, 385 (1992).

207. A. Vigevani, M. Zampieri and M. Pellizzato, *J. Pharm. Biomed. Anal.* **10**, 31 (1992).

208. G. Leising, R. Resel, F. Stelzer, S. Tasch, A. Lanziner and G. Hantich, *J. Clin. Pharm.* **36**, 3S (1996).

209. S. H. Neau, M. K. Shinwari and E. W. Hellmuth, *Int. J. Pharm.* **99**, 303 (1993).

210. E. Touitou, D. D. Chow and J. R. Lawter, *Int. J. Pharm.* **104**, 19 (1994).

211. D. Petre and E. Valoti, *Arch. Pharm.* **320**, 859 (1987).

212. S. M. Reutzel-Edens, V. A. Russell and L. Yu, *J. Chem. Soc.Perkin Trans. II*, 913 (2000).

213. K.-T. Wei and D. L. Ward, *Acta Cryst.* **B33**, 797 (1977).

214. A. O. Patil, W. T. Pennington, I. C. Paul, D. Y. Curtin and C. E. Dykstra, *J. Am. Chem. Soc.* **109**, 1529 (1987).

215. S. Larsen and K. Marthi, *Acta Cryst.* **B53**, 280 (1997).

216. M. Cesario and J. Guilhem, *Cryst. Struct. Comm.* **3**, 123 (1974).

217. M. Cesario and J. Guilhem, *Cryst. Struct. Comm.* **3**, 131 (1974).

218. M. Cesario and J. Guilhem, *Cryst. Struct. Comm.* **3**, 127 (1974).

219. M. Cesario and J. Guilhem, *Cryst. Struct. Comm.* **3**, 179 (1974).

220. M. Cesario and J. Guilhem, *Cryst. Struct. Comm.* **3**, 183 (1974).

221. H. Lorenz, D. Sapoundjiev and A. Seidel-Morgenstern, *J. Chem. Eng. Data* **47**, 1280 (2002).

222. W. G. Angus and R. P. Owen, *J. Chem. Soc.*, 227 (1943).

223. M. Centnerszwer, *Z. Phys. Chem.* **29**, 715 (1899).

224. J. H. Adriani, *Z. Phys. Chem.* **33**, 468 (1900).

225. M. Kuhnert-Brandstätter and R. Ulmer, *Mikrochimica Acta*, 927 (1974).

---

226. D. Kozma, J. Sztatisz, K. Tomor, G. Pokol and E. Fogassy, *J. Therm. Anal. & Cal.* **60**, 409 (2000).

227. E. J. Valente, C. W. Miller, J. Zubkowski, D. S. Eggleston and X. Shui, *Chirality* **7**, 652 (1995).

228. H. E. Gottlieb, V. Kotlyar and A. Nudelman, *J. Org. Chem.* **62**, 7512 (1997).

229. G. Dela Gatta, M. J. Richardson, S. M. Sarge and S. Støle n, *Standards for differential scanning calorimetry*, IUPAC report for project No. 120/18/97, August 3 (2003).

230. teXan for windows version 1.06: crystal structure analysis package, Molecular Structure Corporation, The Woodlands, TX (1997-1999).

231. CrystalStructure 3.6.0: Crystal structure analysis package, Rigaku and Rigaku/MSC The Woodlands, TX (2000-2004).

232. G. M. Sheldrick, SHELXL97 (1997).

233. D. T. Cromer and J. T. Waber, *International tables for X-ray crystallography*, Vol. IV, The Kynoch Press, Birmingham, England, Table 2.2 A (1974).

234. D. C. Creagh and W. J. McAuley, *International tables for X-ray crystallography*, Vol. C, Ed. A. J. C. Wilson, Kluwer, Boston, Table 4.2.6.8 (1992).

235. D. C. Creagh and J. H. Hubbell, *International tables for X-ray crystallography*, Vol. C, Ed. A. J. C. Wilson, Kluwer, Boston, Table 4.2.4.3 (1992).

236. O. Korver, S. de Jong and T. C. van Soest, *Tetrahedron* **32**, 1225 (1976).

237. O. Korver, *Tetrahedron* **26**, 5507 (1970).

238. E. T. Kaiser and F. W. Carson, *J. Am. Chem. Soc.* **86**, 2922 (1964).

239. K. Mislow and M. Heffler, *J. Am. Chem. Soc.* **74**, 3668 (1952).

240. E. L. Compere, *J. Org. Chem.*, 2566 (1968).

241. W. R. Angus and R. P. Owen, *J. Chem. Soc.*, 249 (1943).

242. C. A. Bischoff and P. Walden, *Annalen* **279**, 118 (1894).

243. T. S. Cameron and M. Duffin, *Cryst. Struct. Comm.* **3**, 539 (1974).

244. A. Fischer and V. M. Profir, *Acta Cryst.* **E59**, 01113 (2003).

245. V. M. Profir, E. Furusjö, L.-G. Danielsson and Å. C. Rasmunson, *Cryst. Growth and Design* **2**, 273 (2002).

---

246. V. M. Profir and Å. C. Rasmunson, *Cryst. Growth and Design* **4**, 315 (2004).

247. Z. J. Li, *Implications of chirality for the physicochemical properties and crystallization of chiral drugs*, PhD thesis, University of Minnesota (1997).

248. M. C. Etter, *Acc. Chem. Res.* **23**, 120 (1990).

249. M. Andersson, A. Fredga and B. Jerslev, *Acta Chem. Scand.* **20**, 1060 (1966).

250. P. L. Cox, M Jaspars, Y. Kumarasamy, L. Nahar and S. D. Sarker, *Acta Cryst.* **E59**, o46 (2003).

251. V. Y. Torbeev, K. A. Lyssenko, O. N. Kharybin, M. Y. Antipin and R. G. Kostyanovsky, *J. Phys. Chem. B* **107**, 13523 (2003).

252. H. Birkedal, D. Schwarzenbach and P. Pattison, *Agnew. Chem. Int. Ed.* **41**, 754 (2002).

253. J. S. O. Evans, *J. Chem. Soc., Dalton Trans.*, 3317 (1999).

254. T. C. Bhadra, *Indian J. Phys.* **49**, 746 (1975).

255. H. E. King Jr., *Physica* **139**, 168 (1986).

256. R. A. Laudise, *Chem. & Eng. News* **69** , 30 (1987)

257. J. G. Foss, *J. Chem. Ed.* **40**, 592 (1963).

258. P. L. Polavarapu and H. E. Smith, *J. Phys. Chem.* **92**, 1774 (1988).

259. P. L. Polavarapu, L. P. Fontana and H. E. Smith, *J. Am. Chem. Soc.* **108**, 94 (1986).

260. N. Mori, Y. Asano, T. Irie and Y. Tsuzuki, *Bull. Chem. Soc. Japan* **42**, 482 (1969).

261. D. Lin-Vien, N. B. Colthup, W. G. Fateley and J. G. Grasselli, *Infrared and raman characteristic frequencies of organic molecules*. Academic Press, Inc., San Diego, CA (1991).

262. G. Varsányi, *Assignments for vibrational spectra of seven hundred benzene derivatives*. John Wiley & Sons, NY (1974).

263. E. B. Wilson, *Phys. Rev.* **45**, 706 (1934).

264. GaussView 2.1, Gaussian, Inc., Pittsburgh, PA (2000).

265. G. Holzwarth, E. C. Hsu, H. S. Mosher, T. R. Faulkner and A. Moscowitz, *J. Am. Chem. Soc.* **96**, 251 (1974).

266. T. B. Freedman, G. A. Balkjian and L. A. Nafie, *J. Am. Chem. Soc.* **107**, 6213 (1985).

---

267. C. Marcott, C. C. Blackburn, T. R. Faulkner, A. Moscowitz and J. Overend, *J. Am. Chem. Soc.* **100**, 5262 (1978).

268. A. V. Stuart and G. B. B. M. Sutherland, *J. Chem. Phys.* **24**, 559 (1956).

269. G. Cassanas, M. Morssli, E. Fabrègue and L. Bardet, *J. Raman Spectr.* **22**, 409 (1991).

270. P. L. Polavarapu, D. F. Michalska, J. R. Neergaard and H. E. Smith, *J. Am. Chem. Soc.* **106**, 3378 (1984).

271. L. D. Barron, A. R. Gargaro, L. Hecht and P. L. Polavarapu, *Spectrochimica Acta* **47A**, 1001 (1991).

272. T. Nagumo, T. Matsuo and H. Suga, *Thermochimica Acta* **139**, 121 (1989).

273. S. C. Mraw, *Specific heat of solids* **1-2**, 395 (1988).

274. S. C. Mraw and D. F. Naas, *J. Chem. Thermodyn.* **11**, 567 (1979).

275. M. J. M. Van Oort and M. A. White, *Rev. Sci. Instr.* **58**, 1239 (1987).

276. P. W. R. Bessonette and M. A. White, *J. Chem. Phys.* **110**, 2919 (1999).

277. J. C. Lashley, M. F. Hundley, A. Migliori, J. L. Sarrao, P. G. Pagliuso, T. W. Darling, M. Jaime, J. C. Cooley, W. L. Hults, L. Morales, D. J. Thoma, J. L. Smith, J. Boerio-Goates, B. F. Woodfield, G. R. Stewart, R. A. Fisher and N. E. Phillips, *Cryogenics* **43**, 369 (2003).

278. J. S. Hwang, K. J. Lin and C. Tien, *Rev. Sci. Instr.* **68**, 94 (1997).

279. W. Schnelle, J. Engelhardt and E. Gmelin, *Cryogenics* **39**, 271 (1999).

280. E. F. Westrum Jr., C. Chou, D. W. Osborn and H. E. Flotow, *Cryogenics* **7**, 43 (1967).

281. Y. Takahashi, T. Azumi and Y. Sekine, *Thermochimica Acta* **139**, 133 (1989).

282. A. J. Leadbetter, *Proc. Phys. Soc.* **1**, 1481 (1968).

283. D. B. Downie and J. F. Martin, *J. Chem. Thermodyn.* **12**, 779 (1980).

284. W. F. Giauque and P. F. Meads, *J. Am. Chem. Soc.* **63**, 1897 (1941).

285. M. M. Kreitman, T. Ashworth and M. Rechowicz, *Cryogenics* **13**, 32 (1972).

286. R. N. Goldberg and R. D. Weir, *Pure and Appl. Chem.* **64**, 1545 (1992).

287. D. G. Archer, *J. Phys. Chem. Ref. Data* **22**, 1441 (1993).

288. D. A. Ditmars and T. B. Douglas, *J. Res. Natl. Bur. Std.* **73A**, 401 (1971).

289. M. Sorai, K. Kaji and Y. Kaneko, *J. Chem. Thermodyn.* **24**, 167 (1992).

290. R. Viswanathan, *J. Appl. Physics* **46**, 4086 (1975).

291. G. K. White and M. L. Minges, Int. *J. of Thermophyics* **18**, 1269 (1997).

292. R. Q. Fugate and C. A. Swenson, *J. Appl. Physics* **40**, 3034 (1969).

293. D. A. Ditmars, S. Ishihara, S. S. Chang, G. Bernstein and E. D. West, *J. Res. Natl. Bur. Std.* **87**, 159 (1982).

294. R. Castanet, *High Temp.-High Pressures* **16**, 449 (1984).

295. G. T. Furukawa, W. G. Saba and M. L. Reilly, *National Standard Reference Data Series – NBS 18*, U. S. Government Printing Office, Washington, D. C. (1968).

296. D. W. Osborne, H. E. Flotow and F. Schreiner, *Rev. Sci. Instr.* **38**, 159 (1967).

297. M. Tatsumi, T. Matsuo, H. Suga and S. Seki, *Bull. Chem. Soc. Japan* **48**, 3060 (1975).

298. M. Moriya, T. Matsuo and H. Suga, *J. Chem. Thermodyn.* **14**, 1143 (1982).

299. A. G. Cole, J. O. Hutchens, R. A. Robie and J. W. Stout, *J. Am. Chem. Soc.* **82**, 4807 (1960).

300. S. C. Mraw and D. F. O. O'Rourke, *J. Chem. Thermodyn.* **13**, 199 (1981).

301. J. E. Callanan, K. M. McDermott, R. D. Weir and E. F. Westrum Jr., *J. Chem. Thermodyn.* **24**, 233 (1992).

302. F. Grønvold, *J. Therm. Anal.* **13**, 419 (1978).

303. S. P. Duddu, F. K.-Y. Fung and D. J. W. Grant, *J. Phys. D: Appl. Phys.* **26**, B41 (1993).

304. D. W. Larsen and F. E. Stary, *J. Phys. Chem.* **83**, 1758 (1979).

305. A. Gavezzotti, *J. Mol. Struct.*, 615 (2002).

306. H. O. Sørenson and S. Larsen, *Acta Cryst.* **B59**, 132 (2003).